Scanning probe microscopy and related methods

Edited by Ernst Meyer

Imprint

Scanning probe microscopy and related methods

Ernst Meyer

Editorial

Address:
Department of Physics, University of Basel, Klingelbergstr. 82,
CH-4056 Basel

Email:
Ernst Meyer - ernst.meyer@unibas.ch

This article is part of the Thematic Series "Scanning probe microscopy and related methods".

Guest Editor: E. Meyer

Since the invention of scanning tunnelling microscopy (STM) [1] and atomic force microscopy (AFM) [2], a new class of local probe microscopes has entered the laboratories around the world. Scanning probe microscopy (SPM) uses probing tips to map properties, such as topography, local adhesive forces, elasticity, friction or magnetic properties. In the emerging fields of nanoscience and nanotechnology these types of microscopes help to characterize the nanoworld. In addition, local probes can also be used to modify the surfaces and to perform lithography processes.

AFM, especially, has turned out to be a versatile instrument, which can be operated in various environments, such as liquids, gases or vacuum. High and low temperature versions are available, which allow scientists to explore a large variety of materials. The strategy is not to prepare samples according to the requirements of the microscopy technique, but to perform experiments in its most native state, e.g., to study biological material in liquids. Questions to be addressed originate from almost all scientific areas. One example is the field of molecular electronics, where single molecules are investigated in order to perform specific tasks, e.g., molecular switches, molecular transistors or even molecular processors. In this area, STM and AFM have become essential tools to characterize the structure and function of molecules on surfaces.

AFM has evolved considerably in the last few years, where new operation modes, such as non-contact force microscopy (nc-AFM), Kelvin probe force microscopy (KPFM) or friction force microscopy (FFM), were developed. One main focus is the high resolution capabilities of nc-AFM, which were drastically improved. Atomic resolution on metals, semiconductors [3] and insulators was achieved. Recently, the atomic structure of single molecules was identified by nc-AFM, which gives new opportunities to investigate the local structure of these molecules [4]. In this Thematic Series, the structure of oxides is explored by the combination of nc-AFM. Colour centres are characterized by KPFM and tunnelling spectroscopy. The arrangement of molecules on insulators is another type of application, which is discussed in the present Thematic Series. The ability to measure across phase transitions gives insight into fascinating phenomena, such as metal-superconductor transitions or metal-insulator transitions.

Another important development is related to nanomechanics, where phenomena, such as friction, wear, elasticity and plasticity are studied on an atomic scale. Atomic friction has been studied in great detail, where the main mechanism is related to atomic instabilities, which lead to the characteristic stick slip behaviour. The loading and velocitiy dependence were interpreted in terms of a thermally activated Prandtl–Tomlinson-

model [5,6]. The transition into the superlubricity regime was observed for incommensurate contacts [7] and for contacts at low loads [8]. Furthermore, the control of atomic friction was achieved by electrostatic and mechanical actuation of the nanoscale contacts [8]. In this Thematic Series, a microfabricated tribometer bridges the gap between the nanometer-scale to the micron scale of micromachinery. Mechanical actuation is used to reduce friction of these micro contacts.

An important aspect of SPM is the possibility to modify surfaces. The probing tip can be either used to push or pull atoms, molecules or particles across surfaces. These experiments give information about the local bonding and to explore friction and wear mechanisms. Two different regimes were observed, which were related to the commensurability of the contacts [9]. The manipulation of a large number of particles gives also access to the size and shapes of the particles [10] and is discussed in this Thematic Series as well.

A schematic drawing of the family of scanning probe microscopes in Figure 1 demonstrates how fast and diverse this field of research develops. I hope that this Thematic Series will help the reader to get insights in this fascinating world. Furthermore, I want to thank the colleagues for their excellent contributions.

Ernst Meyer

Basel, December 2010

References

1. Binnig, G.; Rohrer, H.; Gerber, C.; Weibel, E. *Phys. Rev. Lett.* **1983,** *50,* 120–123. doi:10.1103/PhysRevLett.50.120
2. Binnig, G.; Quate, C. F.; Gerber, C. *Phys. Rev. Lett.* **1986,** *56,* 930–933. doi:10.1103/PhysRevLett.56.930
3. Giessibl, F. J. *Science* **1995,** *267,* 68–71. doi:10.1126/science.267.5194.68
4. Gross, L.; Mohn, F.; Moll, N.; Liljeroth, P.; Meyer, G. **2009,** *325,* 1110–1114. doi:10.1126/science.1176210
5. Gnecco, E.; Bennewitz, R.; Gyalog, T.; Loppacher, C.; Bammerlin, M.; Meyer, E.; Güntherodt, H.-J. *Phys. Rev. Lett.* **2000,** *84,* 1172–1175. doi:10.1103/PhysRevLett.84.1172
6. Socoliuc, A.; Bennewitz, R.; Gnecco, E.; Meyer, E. *Phys. Rev. Lett.* **2004,** *92,* 134301. doi:10.1103/PhysRevLett.92.134301
7. Dienwiebel, M.; Verhoeven, G. S.; Pradeep, N.; Frenken, J. W. M.; Heimberg, J. A.; Zandbergen, H. W. *Phys. Rev. Lett.* **2004,** *92,* 126101. doi:10.1103/PhysRevLett.92.126101
8. Socoliuc, A.; Gnecco, E.; Maier, S.; Pfeiffer, O.; Baratoff, A.; Bennewitz, R.; Meyer, E. *Science* **2006,** *313,* 207–210. doi:10.1126/science.1125874
9. Dietzel, D.; Ritter, C.; Mönninghoff, T.; Fuchs, H.; Schirmeisen, A.; Schwarz, U. D. *Phys. Rev. Lett.* **2008,** *101,* 125505. doi:10.1103/PhysRevLett.101.125505
10. Gnecco, E.; Rao, A.; Mougin, K.; Chandrasekar, G.; Meyer, E. *Nanotechnology* **2010,** *21,* 215702. doi:10.1088/0957-4484/21/21/215702
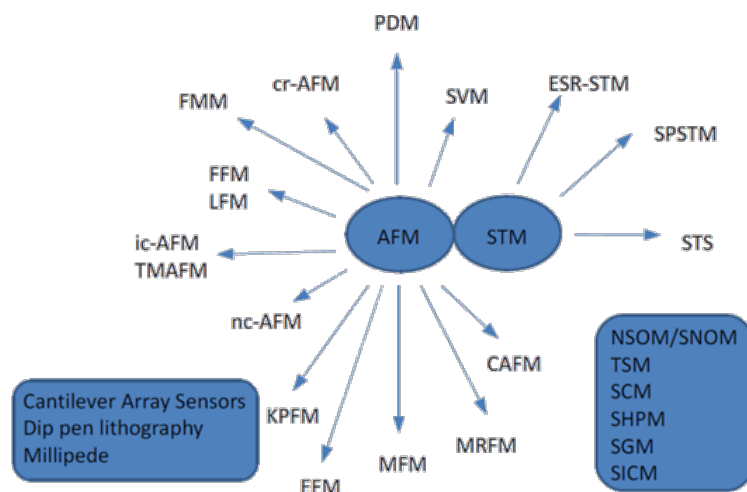
Figure 1: Scanning probe microscopy: A large familiy of microscopes, which have in common that they use local probes to characterize surfaces. AFM: Atomic Force MicroscopySTM: Scanning Tunneling Microscopy, PDM: Phase Detection Microscopy, FMM: Force Modulation Microscopy, ic-AFM: intermittent contact AFM, TMAFM: tapping mode AFM, nc-AFM: non-contact AFM, KPFM: Kelvin probe force microscopy, EFM: Electrostatic force microscopy, MFM: Magnetic force microscopy, MRFM: Magnetic resonance force microscopy, NSOM: Near-field scanning optical microscopy, SNOM: Scanning nearfield optical microscopy, TSM: Thermal scanning microscopy, cr-AFM: contact-resonance AFM, SPSTM: Spin polarized STM, SHPM: Scanning Hall probe microscopy, SGM: Scanning gate microscopy, SVM: Scanning voltage microscopy / Nanopotentiometry, ESR-STM: Electron spin resonance-STM, SICM: Scanning ion conductance microscopy, CAFM: Conductive AFM.

A collisional model for AFM manipulation of rigid nanoparticles

Enrico Gnecco

Full Research Paper

Address:
Department of Physics, University of Basel, Klingelbergstrasse 82, 4056 Basel, Switzerland; present address: IMDEA Nanociencia, Campus Universitario de Cantoblanco, Avda. Fco Tomás y Valiente 7, 28049 Madrid, Spain

Email:
Enrico Gnecco - enrico.gnecco@imdea.org

Abstract

The trajectories of differently shaped nanoparticles manipulated by atomic force microscopy are related to the scan path of the probing tip. The direction of motion of the nanoparticles is essentially fixed by the distance b between consecutive scan lines. Well-defined formulas are obtained in the case of rigid nanospheres and nanowires. Numeric results are provided for symmetric nanostars. As a result, orienting the fast scan direction perpendicular to the desired direction of motion and reducing b well below the linear size of the particles turns out to be an efficient way to control the nanomanipulation process.

Introduction

Quite soon after its invention, it became clear that atomic force microscopy (AFM) could be used not only for imaging but also for manipulating nano-objects [1,2]. This possibility has produced spectacular results and last, but not least, it has allowed the controlled manipulation of metal clusters on insulating surfaces [3] and even single atoms on semiconductors [4]. However, AFM manipulation tends to be time-consuming. A major issue is that nanoparticles are usually moved individually so that the AFM tip has to be properly positioned with respect to the particle every time. The tip is either placed on the side or on the top of the particle. Then the tip–particle interaction is

increased (by varying the tip–particle distance or the amplitude of the tip oscillations) until the particle is detached from the substrate and moved in a direction which is determined by several factors such as the scan pattern, the surface structure and the geometry of both tip and particle. Predicting the direction of motion of nanoparticles is very important, especially if it is desired to manipulate several particles at the same time. Here, we show that this is possible in simple cases of practical interest. Specifically, we assume that the AFM is operated in tapping mode (although some conclusions may be extended to contact mode), the particles are rigid and the frictional forces

between particles and substrate can be neglected when the particles collide with the tip, but they are high enough to stop the particles immediately once contact with the tip is lost. The concentration of nanoparticles on the substrate is also supposed to be low enough to prevent multiple collisions in the manipulation.

After a brief review of previous results on the manipulation of rigid nanorods, including nanospheres and thin nanowires as limit cases, we discuss symmetric nanostars as a prototype of more complex shaped particles. We show that in any case the angle of motion of the nanoparticles is precisely related to the distance *b* between consecutive scan lines. When the parameter *b* is sufficiently small, the particle tends to move perpendicularly to the scan direction. The exact relation between the angle of motion θ and the parameter *b* depends on the particle shape and can be, in principle, determined analytically. Curiously, this has a certain analogy to the scattering of sub-atomic particles, whose angle of deflection θ depends on the form of the scattering field and on the impact parameter *b* (i.e., the distance at which the particle would pass the center of the field in the absence of any interaction) [5].

Results
The model

We first consider a planar island whose profile is described by the function $r = r(\varphi)$ in polar coor-dinates or, equivalently, by a multi-value function $y = y(x)$ in cartesian coordinates. Assuming that the tip follows a raster scan pattern, the *y* coordinate of the tip varies as $Y_0 = Nb$, where *N* is the number of the scan line and *b* is the distance between consecutive scan lines (Figure 1a).
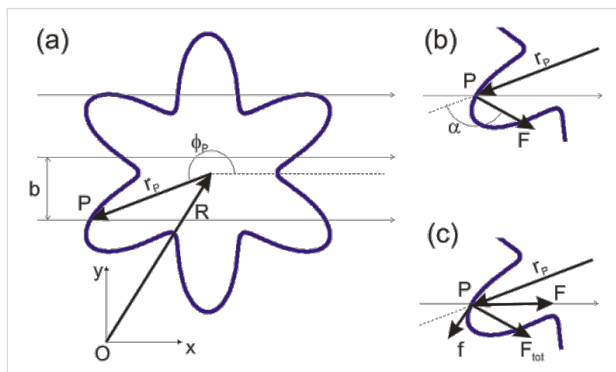

Figure 1: (a) A sharp nanotip follows a raster scan pattern with consecutive scan lines separated by a distance *b*. The tip collides with a nanoparticle (here represented by a star-shaped island) at the location *P*. (b) In tapping mode the tip oscillates in the direction *z* perpendicular to the plane of the figure and applies an impulsive force **F** perpendicular to the island profile. (c) In contact mode the force **F** is directed along the *x* axis and the total force acting on the particle will be oriented as in tapping mode only if the static friction **f** can balance the component of **F** along the island profile.

The island has a mass *M* and a moment of inertia *I* with respect to the normal axis *z* through its center of mass (COM). Here, we assume that the linear size of the island is much larger than the tip radius, so that the force **F** applied by the tip is concentrated at the point of contact *P*. We also assume that the island cannot be deformed or broken during the manipulation. In such a case, the position $\mathbf{R} \equiv (X,Y)$ of the COM and the angle of rotation Φ of the island about the normal axis *z* evolve according to the equations of motion of a rigid body:

$$\mathbf{F} = M\frac{d^2\mathbf{R}}{dt^2} , \qquad (1)$$

and

$$\mathbf{r}_P \times \mathbf{F} = I\frac{d^2\mathbf{\Phi}}{dt^2} , \qquad (2)$$

where $\mathbf{r}_P$ defines the position of the point of contact *P* with respect to the COM.

The direction of the force **F** depends on the operating mode of the AFM. In tapping mode the tip oscillates in the *z* direction with a frequency in the order of 100 kHz with an amplitude of some tens of nm. This corresponds to an average speed of some mm/s, which is well above typical scan velocities in AFM (normally in the order of 1 μm/s). Thus, the tip hits the particle almost vertically and the vector **F** is oriented perpendicularly to the island profile, i.e., at an angle $\alpha = \beta + 90°$ with respect to the *x* axis, where

$$\tan\beta = \left.\frac{dy}{dx}\right|_P = \frac{r'_P \ \sin\varphi_P + r_P \ \cos\varphi_P}{r'_P \ \cos\varphi_P + r_P \ \sin\varphi_P}$$

and *r'* is the first derivative of $r(\varphi)$ with respect to φ (Figure 1b). In contact mode the tip hits the particle along the *x* direction and the force **F** can be oriented as in tapping mode only if the static friction force **f** between tip and particle is high enough to prevent sliding along the island profile (Figure 1c).

Assuming that friction between island and substrate is also high enough to prevent any slippage of the island after a collision with the tip, Equation 1 and Equation 2 can be averaged over the short collision time Δt (in the order of $1/f$, with $f \sim 10^5$ Hz being the oscillation frequency of the tip). This leads to the equations

$$\frac{dY}{dX} = \tan\ \alpha , \qquad (3)$$

for the translation of the island and

$$\frac{d\Phi}{dR} = \frac{Mr_{\text{P}}\ \sin(\alpha - \varphi_{\text{P}})}{I}\ , \tag{4}$$

for the rotation, which can be finally integrated over the total time of interaction between tip and particle (along the given scan line). If the nanoparticle is not flat, it is easy to see that the previous analysis is still applicable provided that the particle does not roll and that its shape is not cylindrical.

Translation and wobbling of nanorods

The manipulation of a rigid nanorod formed by a cylinder (with length L) and two hemispherical caps (with radius a) is particularly instructive. Here, any possible rolling can be ignored and we can distinguish between two types of collision: (a) The tip touches the cylindrical core of the nanorod ("core" collision). (b) The tip touches one of the two hemispherical ends of the rod ("cap" collision). In case (a) the equations of motion of the nanorod can be written in the form [6]

$$\frac{d\Phi}{dY} = \frac{2M(Y_0 - Y - a\cos\Phi)}{I\sin 2\Phi}\ ,$$

and

$$\frac{dY}{dX} = -\cot\Phi\ .$$

In the case (b):

$$\frac{d\Phi}{dY} = -\frac{ML\sin(\Phi - \alpha)}{2I\sin\alpha}\ , \tag{5}$$

and

$$\frac{dY}{dX} = \tan\ \alpha\ . \tag{6}$$

In general, both core and cap collisions occur along each scan line and only numerical solutions are possible. However, a complete solution can be found in two important cases: The manipulation of a nanosphere of radius a ($L = 0$) and that of a thin nanowire of length L ($a = 0$), where only cap collisions or core collisions, respectively, occur. In the case of a nanosphere, Equation 5 and Equation 6 can be integrated leading to the following result [7]. The direction of motion of the sphere forms an angle θ with respect to the x axis (fast scan direction) given by

$$\tan\theta = -\ \frac{b}{a\left[\cos\alpha_0 + \log\tan(\alpha_0/2)\right]}\ . \tag{7}$$

The quantity α_0 is the impact angle between tip and sphere (with the exception of the very first collision) and is given by

$$\alpha_0 = \arcsin\left(1 - \frac{b}{a}\right).$$

In the case of a nanowire, the *average* direction of motion is well-defined and is given by the sim-ple formula [6]

$$\cos\overline{\theta} = \frac{b}{L}\ . \tag{8}$$

The wire oscillates perpendicularly to this direction:

$$\overline{\Phi} = \overline{\theta} + 90°.$$

Thus, Equation 7 and Equation 8 show that the directions of motion of nanospheres and nanowires manipulated by AFM in tapping mode are completely determined by the distance b between consecutive scan lines or, equivalently, by the density of scan lines $1/b$. The functions of Equation 7 and Equation 8 are plotted in Figure 2. In both cases $\theta(b)$ decreases with increasing b until the particle is lost when $b > a$ or $b > L$. Furthermore, the angle $\theta \rightarrow 90°$ when $b \rightarrow 0$. Numerical simulations show that similar conclusions are also valid for arbitrarily thick nanorods [6], although simple analytic expressions cannot, in general, be derived.

Figure 2: Angle of motion θ of a nanosphere (solid curve) and a nanowire (dashed curve) as a function of the distance b between consecutive scan lines. The parameter b is expressed in units of the sphere radius a and wire length L respectively.
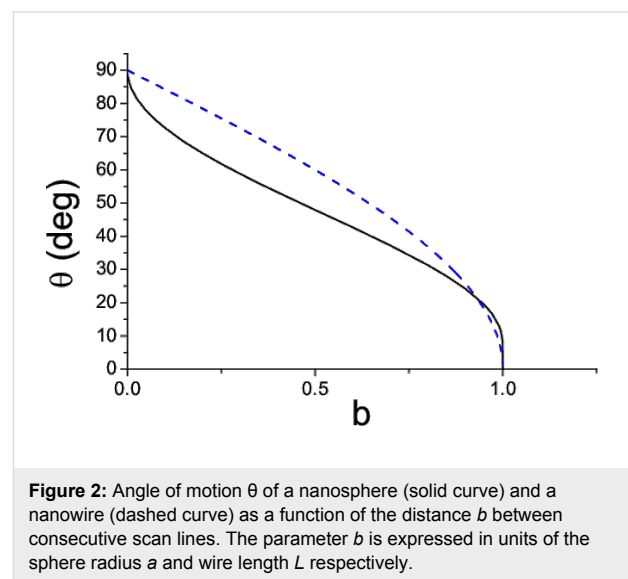
Star shaped islands: Rotational effects

As a next step we extend our analysis to more complex shapes. We consider star-shaped islands, whose profile is described by the function

$$r(\varphi) = a(1 + \sin^2 k\varphi) \,.$$

The number of branches in the island is denoted by 2k. For instance, $k = 3$ in Figure 1a. It is inter-esting to observe that both the moment of inertia I and the area A of the island are independent of k:

$$I = \sigma \int_0^{2\pi} d\varphi \int_0^{r(\varphi)} r^3 dr = \frac{867}{256} \pi\sigma a^4 \,,$$

$$A = \int_0^{2\pi} d\varphi \int_0^{r(\varphi)} r dr = \frac{19}{8} \pi a^2 \,,$$

where $\sigma = M/A$ is the area density of the island. The ratio M/I which appears in Equation 4 is thus equal to $(867/608)a^2 = 1.426a^2$. The equations of motion (Equation 3 and Equation 4) have been solved for $k = 2,3,4$ and increasing values of b until the island starts moving in the negative y direction and is lost. In Figure 3 the angle of motion $\theta = \arctan(dY/dX)$ is plotted as a function of the parameter b. The initial coordinate Y_0 of the tip along the slow scan direction was randomly chosen, with hardly any influence on the final results, except in the threshold region where the islands can be lost (and no points can be plotted). In all cases the direction of motion θ initially decreases with increasing b and, again $\theta \to 90°$ when $b \to 0$. However, the trend of the function $\theta(b)$ suddenly changes when b reaches a certain value ($b = 0.5, 0.35$ or 0.25 when $k = 2, 3$ or 4). In order to understand what happens at these points, we have also plotted the angular velocity of the particles, $d\Phi/dN$, as a func-
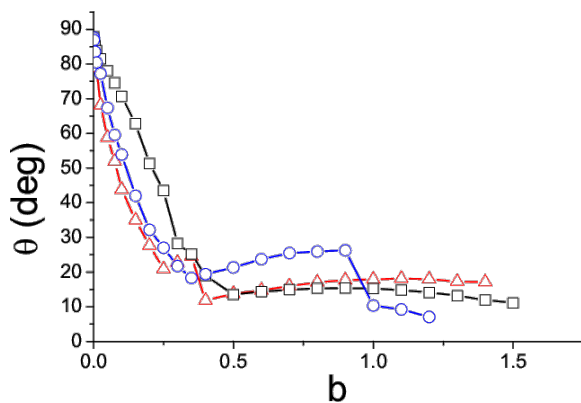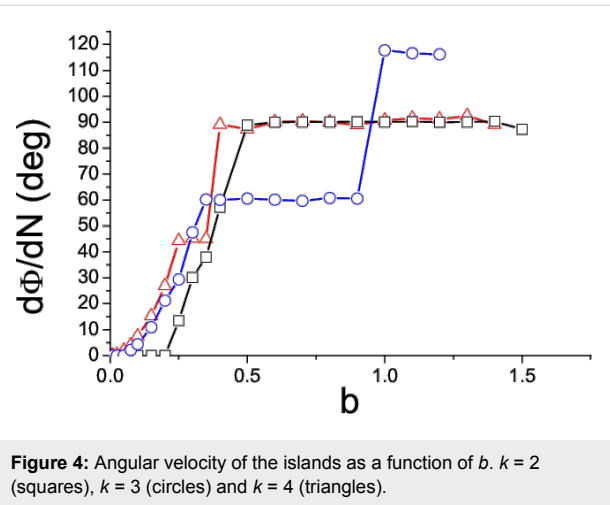

Figure 4: Angular velocity of the islands as a function of b. $k = 2$ (squares), $k = 3$ (circles) and $k = 4$ (triangles).

tion of b (Figure 4). The critical values of the parameter b correspond to the onset of rotations of $180°/k$ angles per scan line. Beyond these critical values the angular velocity remains almost constant and the function $\theta(b)$ slightly increases (Figure 3). When $k = 3$ and 4 two further critical values of b are found ($b = 0.9$ and 0.35 respectively), corresponding to rotations of $2 \times 180°/k$ angles per scan line. On the other hand, when b is small enough, the angular velocity $d\Phi/dN$ becomes negligible: Rather than rotating, the islands simply 'wobble' like the nanorods.

Discussion

The predictions of the collisional model have been experimentally verified with gold nanospheres and nanorods manipulated on silicon oxide under ambient conditions by tapping AFM [6,7]. Furthermore, we have also observed that, at least in the case of the nanospheres, the model goes beyond the restrictive hypothesis that the particles are immediately stopped after being released by the tip. This has been shown by numerical simulations, where a 'mean free path' d of the nanoparticles was introduced. If the friction force between particle and substrate decreases, and consequently the distance d increases, then the pathway of the nanoparticle fluctuates more and more, but the form of the function $\theta(b)$ remains essentially unchanged [8]. Another important point is the following. In many commercial AFMs, the tip follows a zigzag scan path rather than a raster scan path. This leads to significant variations in the impact angles between the tip and particles and to a dependence of the direction of motion on the initial position of the particles along the fast scan direction x [7]. Nevertheless, at least in the case of nanospheres, one of the previous conclusions holds: The angle of motion $\theta \to 90°$ when $b \to 0$ (in the case of a zigzag scan pattern, b can be taken as the distance between the starting points of parallel scan lines). Altogether, these observations suggest a general strategy for manipulating relatively large

Figure 3: Angle of motion θ of 2k-branched symmetric islands as a function of the distance b be-tween consecutive scan lines (in units of the length parameter a in the text). $k = 2$ (squares), $k = 3$ (circles) and $k = 4$ (triangles).

nanoparticles, i.e., in the order of or larger than the tip radius. Provided that the density of scan lines is high enough, the direction of motion of the particles can be tuned by orienting the fast scan direction *x* of the AFM *perpendicularly* to the desired direction of motion. This is much easier and more reliable than aligning the tip and moving it towards the COM of each nanoparticle, as is usually done. The rotational effects predicted by the collisional model have not yet been tested experimentally. A good benchmark would be the flower-shaped Sb islands first manipulated by Ritter et al. on HOPG and MoS_2 [9]. Possible discrepancies between theory and experiment concerning the direction of motion and angular speed of the islands could be related to the friction forces between island and substrate and even used to estimate these forces in further developments of the collisional model. Since Sb islands can be manipulated and the corresponding friction forces can be measured also in contact mode [10], the applicability of the model could also be tested under these different impact conditions. Controlling the direction of motion of arbitrarily shaped nanoparticles is important for the guided formation of nanostructures. An interesting analogy is found with AFM nanolithography. In a recent paper we have shown that the patterning of amorphous polymers can be 'tuned' by varying the scan path of an AFM tip which scratches the polymer surface while scanning [11]. Linear and 'travelling' circular ripples were formed using a raster or a circular scan path, respectively. In the same way, a desired configuration of nanoparticles could be obtained by a proper choice of the scan pattern.

Conclusion

In conclusion, we have shown that the direction of motion of nanoparticles can be controlled by AFM in a variety of significant cases. The key parameter is simply the density of scan lines in the scan path of the probe tip. Orienting the fast scan direction perpendicularly (and not parallel) to the desired direction of motion is an efficient way for manipulating the nanoparticles. With a proper choice of the scan pattern, it may be possible to reorganize an ensemble of randomly distributed nanoparticles in a well-defined arrangement.

Acknowledgements

References

1. Lüthi, R.; Meyer, E.; Haefke, H.; Howald, L.; Gutmannsbauer, W.; Güntherodt, H. J. *Science* **1994,** *266,* 1979. doi:10.1126/science.266.5193.1979
2. Schaefer, D. M.; Reifenberger, R.; Patil, A.; Andres, R. P. *Appl. Phys. Lett.* **1995,** *66,* 1012. doi:10.1063/1.113589
3. Barth, C. FANAS 2010 Conference: Friction and Adhesion in Nanomechanical Systems, Saarbrücken, Germany, Oct 25–28, 2010.
4. Sugimoto, Y.; Abe, M.; Oyabu, N.; Custance, O.; Morita, S. *Nat. Mater.* **2005,** *4,* 156. doi:10.1038/nmat1297
5. Landau, L. D.; Lifshitz, E. M. *Mechanics;* Pergamon Press: Cambridge, U.K., 1976.
6. Gnecco, E.; Rao, A.; Mougin, K.; Chandrasekar, G.; Meyer, E. *Nanotechnology* **2010,** *21,* 215702. doi:10.1088/0957-4484/21/21/215702
7. Rao, A.; Gnecco, E.; Marchetto, D.; Mougin, K.; Schönenberger, M.; Valeri, S.; Meyer, E. *Nanotechnology* **2009,** *20,* 115706. doi:10.1088/0957-4484/20/11/115706
8. Rao, A.; Wille, M. L.; Gnecco, E.; Mougin, K.; Meyer, E. *Phys. Rev. B* **2009,** *80,* 193405. doi:10.1103/PhysRevB.80.193405
9. Ritter, C.; Heyde, M.; Stegemann, B.; Rademann, K.; Schwarz, U. D. *Phys. Rev. B* **2005,** *71,* 085405. doi:10.1103/PhysRevB.71.085405
10. Dietzel, D.; Ritter, C.; Mönninghoff, T.; Fuchs, H.; Schirmeisen, A.; Schwarz, U. D. *Phys. Rev. Lett.* **2008,** *101,* 125505. doi:10.1103/PhysRevLett.101.125505
11. Gnecco, E.; Riedo, E.; King, W. P.; Marder, S. R.; Szoszkiewicz, R. *Phys. Rev. B* **2009,** *79,* 235421. doi:10.1103/PhysRevB.79.235421

The description of friction of silicon MEMS with surface roughness: virtues and limitations of a stochastic Prandtl–Tomlinson model and the simulation of vibration-induced friction reduction

W. Merlijn van Spengen[*1,2], Viviane Turq[3] and Joost W. M. Frenken[4]

Full Research Paper

Address:
[1]TU Delft, 3mE-PME, Mekelweg 2, 2628CD Delft, The Netherlands, [2]also with Falco Systems, Gelderlandplein 75L, 1082LV, Amsterdam, The Netherlands, [3]Université de Toulouse, UPS, INP, Institut Carnot Cirimat, 118, route de Narbonne, F-31062 Toulouse cedex 9, France and [4]Leiden University, LION, Niels Bohrweg 2, 2333CA, Leiden, The Netherlands

Email:
W. Merlijn van Spengen[*] - W.M.vanSpengen@tudelft.nl

* Corresponding author

Abstract

We have replaced the periodic Prandtl–Tomlinson model with an atomic-scale friction model with a random roughness term describing the surface roughness of micro-electromechanical systems (MEMS) devices with sliding surfaces. This new model is shown to exhibit the same features as previously reported experimental MEMS friction loop data. The correlation function of the surface roughness is shown to play a critical role in the modelling. It is experimentally obtained by probing the sidewall surfaces of a MEMS device flipped upright in on-chip hinges with an AFM (atomic force microscope). The addition of a modulation term to the model allows us to also simulate the effect of vibration-induced friction reduction (normal-force modulation), as a function of both vibration amplitude and frequency. The results obtained agree very well with measurement data reported previously.

Introduction

With the invention of the friction force microscope (FFM) by Mate et al. [1], it has become possible to study the friction processes on the atomic scale that count as one of the fundamental aspects of everyday friction. The FFM (an atomic force microscope (AFM) that is sensitive to the lateral forces at the tip) can probe the interactions of an (almost) atomically sharp tip with individual atoms or a small part of a crystal lattice on the Ångstrom scale. It was found that regular, repeatable stick-

slip behaviour of a contacting highest point (asperity) over the lattice of the other surface forms the very basis of the frictional processes as previously described [2,3]. To physically describe the stick-slip behaviour observed, the theories of Prandtl [4] and Tomlinson [5] were used [6,7]. This Prandtl–Tomlinson model has proven to be remarkably effective in describing atomic-scale friction.

Further research on atomic-scale friction has resulted in a wealth of information on atomic-scale friction processes, culminating in the prediction and discovery of extremely interesting processes like superlubricity (vanishing friction when crystal lattices do not match) [8,9] and thermolubricity (vanishing friction due to temperature-assisted hopping) [10,11]. Using the Prandtl–Tomlinson model and kinetic rate theory, it has been possible to describe the observed behaviour in simple theoretical terms.

The difference in length scales between the macroscopic and the atomic-scale regime is extremely important. Atomic scale friction experiments on atomically flat, non-reactive surfaces often show very low friction coefficients (e.g., ~0.01 for a tungsten tip on graphite [1]), while macroscopically, usually friction coefficients above 0.1 are encountered. Hence it is not directly clear how the atomic-scale friction coefficients relate to their macroscopic counterparts. This transition regime is also of practical significance: MEMS (micro-electromechanical systems) devices have contact forces, surface roughness and numbers of contacting asperities that position them right in this 'knowledge gap'. In addition, their commercial success is severely hampered by continuing friction and wear problems [12].

The question is now how to describe friction on the larger scale of actual MEMS devices, which pair micrometer features and nanometer-scale surface roughness with nano- to micro-Newton forces. This friction is characterized by irregular, but repeatable, stick-slip motion. Can it still be described by the Prandtl–Tomlinson model? Work on rough surface friction has centred around dynamic critical phenomena by Fisher [13,14], Chauve et al. [15], and very recently by Fajardo and Mazo [16]. Friction of rough surfaces was also extensively studied by Persson et al. [17,18] using a dedicated contact mechanics model.

This paper first reviews typical MEMS friction measurements with our fully MEMS-based tribometer, showing the irregular, but repeatable, stick-slip motion of MEMS surfaces in contact. Then we extend the common Prandtl–Tomlinson model with a stochastic component to describe the surface roughness of the sliding MEMS. This model very effectively describes the statis-

tical properties of the motion of the MEMS tribometer slider observed in several measurements. We also show the effect of vibration-induced friction reduction, both in the new theory and experiments.

Results and Discussion
MEMS tribometer friction measurements

To investigate friction on the microscale, we have developed MEMS tribometer devices that can be used to perform friction experiments between their sidewalls [19]. They consist of two perpendicular 'comb drive' linear electrostatic actuators that can move a slider in two directions (Figure 1). One comb drive is used to press the slider against a counter-surface and to vary the normal load, and the other comb drive is used to slide the slider along the other surface. Although the device is mechanically comparable to the device described by Senft and Dugger [20], the readout mechanism is completely different. We use the capacitance change of a second set of comb fingers to detect the motion of the device [21]. This allows us to measure FFM-like dynamic friction loops showing the details of the interaction. A typical result with silicon MEMS sidewall surfaces in air, containing a native oxide, is shown in Figure 2. We observe irregular, but repeatable, stick-slip, on a length scale comparable to the lateral length scale of the surface roughness (to be quantified later).
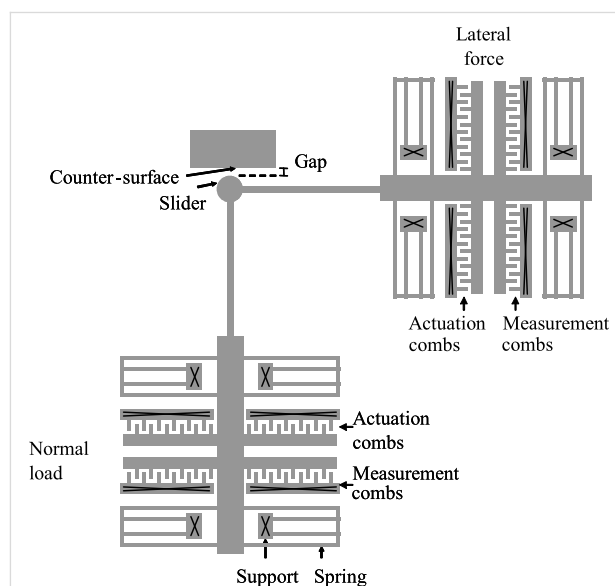
Figure 1: Schematic top view of the MEMS tribometer for studying microscale friction [19]. Several slider types have been investigated, such as the disc-shaped one in this figure. The experiments reported in the current paper have been performed with a square slider, resulting in two parallel sidewall surfaces sliding over one another. The slider surface is 20 µm by 2.0 µm, the counter-surface has the same 2.0 µm height but is much longer. Only the measurement shown in Figure 2 was performed with a small square slider of 4.0 µm by 2.0 µm. [Reprinted with permission from van Spengen, W. M.; Frenken, J. W. M. *Tribol. Lett.* **2007**, *28,* 149–156.]

Figure 2: Typical 1000-cycle-average friction loops obtained with the tribometer of Figure 1 [19], at 27 °C and a relative humidity (RH) of 30%. The sliding speed was constant at 5 µm/s. Support position 0 µm is where the loop was started every cycle. This loop is an average over 1000 scans. The fact that the slips appear sharp means that there was no significant change to their position over these 1000 scans and hence no surface changes (which would indicate wear). [Reprinted with permission from van Spengen, W. M.; Frenken, J. W. M. *Tribol. Lett.* **2007,** *28,* 149–156.]

Figure 3: Determination of the average friction force. The area enclosed by the dashed lines provides the best estimate of the typical energy dissipated during sliding. The average friction force is obtained by dividing the energy contained in the shaded area by 2·B.

Figure 4: The average friction force (determined as depicted in Figure 3) as a function of the normal load is more or less linear on the scale of MEMS devices. The tests were conducted at 27 °C and a relative humidity of 30%. The fitted friction coefficient is 0.27. Indicated are also the calculated friction force based on an exponential autocorrelation function, with blue open circles, and with the measured autocorrelation function ('real ACF'), indicated with green open triangles. The effect of the choice of autocorrelation function is very small.

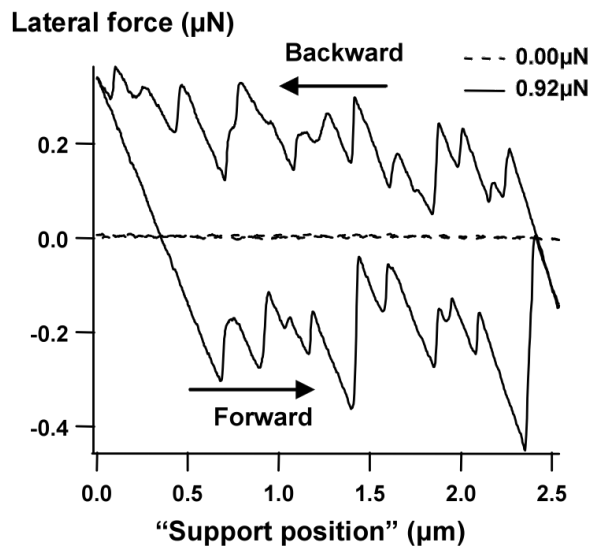To calibrate the forces measured, we need an accurate value for the spring constant of the device. This calibration has been implemented by designing two MEMS tribometers on the same chip, which have identical springs, but a known difference in mass. From the difference in resonance frequency we extract the spring constant, being 2.0 ± 0.2 N/m for the device used in this study.

The area enclosed by the friction loop corresponds to the energy dissipated during the friction process. To obtain an accurate measure for the energy dissipation, we have cut off the side lobes of the friction loop, where the device becomes stuck in one direction, taking the average lateral force only when sliding in two directions takes place (Figure 3). From this dissipated energy, we calculated the average friction force such as plotted in the succeeding graphs, by dividing this energy by the distance slid.

In the measurements used for this paper, we systematically varied the normal force, while keeping the support position speed and environmental conditions constant. This resulted in a friction force that is more or less linear in the normal force, with a friction coefficient of 0.27 at a temperature of 27 °C and 25% RH (Figure 4). The fact that the friction force becomes zero at a negative apparent normal force is due to the contribution to the effective normal load of adhesion between the two surfaces.

The new stochastic Prandtl–Tomlinson model

To describe the microscale irregular stick-slip behaviour, we have extended the well-known Prandtl–Tomlinson model [4,5,7], which is used to describe friction on the atomic scale, to include a microscale stochastic variation in the potential energy landscape. Normally, a periodic function is used, to describe the energy landscape with an atomic corrugation. In our case, the corrugations are much higher and dictated by the surface roughness. The characteristic length scale is related to the surface roughness correlation length of the MEMS sidewalls. We refer

Table 1: Comparison of the atomic-scale and stochastic Prandtl–Tomlinson models.

	atomic Prandtl–Tomlinson model	stochastic Prandtl–Tomlinson model
spring	$V_{spring} = \dfrac{1}{2}k(x - x_0)^2$	$V_{spring} = \dfrac{1}{2}k(x - x_0)^2$
surface corrugation	$V_{surface} = \dfrac{U_0}{2}\left[1 - \cos\left(\dfrac{2\pi x}{a}\right)\right]$	$V_{surface} = \xi(x)$

to our description as the 'stochastic Prandtl–Tomlinson model' (Table 1).

$\xi(x)$ is a realization of a stochastic function, where x is the space variable (position). It obeys a Gaussian distribution function linearly related to the height of the surface and an exponential autocorrelation function with correlation length λ. This 'recipe' forms the simplest description of a stochastic process. To obtain the correlation length we need a model for the variations in interaction potential that the system of two surfaces will encounter when the surfaces slide with respect to one another.

If the MEMS tribometer would be a system in which the mean distance between the surfaces during sliding would be held constant, the contact area would fully change with the surface roughness. If the normal force would be held perfectly constant, the contact area would be constant instead (assuming a constant 'bearing area' [22]) and there would be no changes in the friction except the small changes expected on the atomic scale. But at the start of a slip event, the system is out of equilibrium and hence it is expected to behave intermediately between the two extremes mentioned. The natural length and amplitude scale of $\xi(x)$ on which to expect changes are hence related to the length and amplitude scales of the surface roughness, even though the friction force is not determined by the work done against the normal force during sliding; the friction is much too high for this to be the dominating effect. In addition to the surface roughness, the elastic and inertial properties of the sliding surfaces and the whole system also contribute to the behaviour. This mode of friction is known in the literature as the 'surface topology model of stick-slip' [23].

Based on this notion that $\xi(x)$ is proportional to the surface roughness in MEMS, a measurement of the typical topology of the sidewall surface is required. We have made a special MEMS tribometer to do this, in which the counter-surface is supported with small beams and hinges instead of being directly fixed to the substrate. When the small beams are broken off with a probe needle, the counter-surface can be flipped upright and glued in place, so that conventional AFM can be used to quantitatively assess the sidewall roughness (Figure 5).
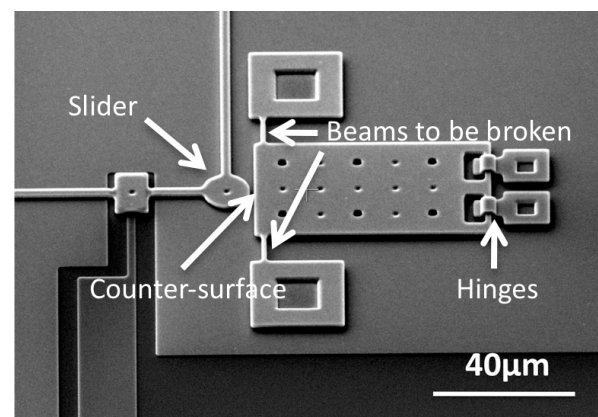
Figure 5: The counter-surface is held by two small beams. After the experiments, the beams can be broken and the counter-surface flipped upright in its hinges with a probe needle, allowing easy access with an AFM cantilever tip. The AFM has been used to measure the surface roughness (Figure 6) on the sidewall at the position where the arrow indicating 'Counter-surface' is pointing.

The AFM data show several striking features: first of all, the polycrystalline silicon MEMS sidewall surfaces coming from the MEMSCAP MUMPS process are not perfectly random (Figure 6). Instead, two areas with apparently different roughness are visible, as is some long-range waviness on the micron-scale. This surface structure is formed by the 2-step RIE (Reactive Ion Etching) process used for etching the structures from an initially continuous polycrystalline silicon film. These surface features are consistently there, from die to die, and from run to run, although they are, of course, also prone to statistical variation. As most probably, different parts of the surface will take part in the contact at the same time, and we require a 1-dimensional function; the autocorrelation function is obtained by adding all AFM scan lines taken in the direction of motion together, to obtain the graph on the right of Figure 6. This graph consists of the two different surface textures and the wiggly line separating the two. The result is an autocorrelation function with a fast, exponential decrease, and then some lower amplitude rippling that is not fully periodic but extends over a longer distance. The length scale of this ripple is most probably related to the grain size of the polycrystalline silicon that has been etched with RIE.

Figure 6: Autocorrelation function $R_{xx}(x)$ of a pristine sidewall surface measured with AFM, and theoretical exponential fit with a correlation length of 83 nm. The standard deviation on the height is 10.3 nm and the distribution is almost Gaussian. The long-range order is caused by the larger scale ripples. The result is that only one ripple may stick out significantly more than the others and hence friction is more localised than on a surface with a purely exponentially decreasing autocorrelation function. The sidewall measured with AFM is similar but not identical to the one used for the friction measurements.

Using the sidewall AFM data, we have obtained a correlation length of 83 nm in the sliding direction for one individual surface (Figure 6). At very short distances at a correlation of 0.8 and higher, the measured value deviates from the exponential curve, showing that there is a lot of variation in the interaction energy at the nanoscale as well. To define the correlation length of the interaction potential realizations $\xi(x)$, we need to take into account that there are two surfaces that both have this correlation length of 83 nm, and that the speed of change encountered when they slide over one another is then faster, and given by the square of the (normalized) individual autocorrelation functions. The correlation length of $\xi(x)$ hence is $\lambda = 41$ nm, half the correlation length of the individual surfaces.

With the exponential autocorrelation function of Figure 6, and assuming a Gaussian distribution, we can now generate multiple mathematical 1-dimensional randomly rough surfaces as realizations of the so defined stochastic function $\xi(x)$. As the correlation length is related to the surface roughness, the shape of the realization will not change with the normal load, as is also the case for the periodic Prandtl–Tomlinson model. The amplitude of $\xi(x)$ is scaled linearly with the load with the scaling factor as the single fit parameter of the model.

Friction loop simulations

The stochastic Prandtl–Tomlinson model was incorporated in an Igor Pro [24] software simulation of sliding rough surfaces

with the statistical properties taken from the measurements described above. In this simulation, first the 'surface roughness functions', typically 50, are generated using $\xi(x)$ with a scale in energy as the single fit parameter, namely the amplitude of $\xi(x)$. For every surface, the following procedure is followed. First, the support position is set to 0, this is the first point on the left hand side. Combining the surface roughness function and the parabolic potential of the spring with support position 0, the momentary energy landscape is calculated. This also defines the lateral force scale on the vertical axis. Then a contact point is defined in the same place as the support position (zero at the left hand side). This is a single point, as the effect of having two surfaces has already been incorporated in $\xi(x)$. This corresponds in a real measurement to the moment that the surfaces are brought together. Then the lowest energy point is determined, where the contact point can go monotonically (this is the essence of the Prandtl–Tomlinson model), and this point is given as the first position of the slider. From then on, every calculation cycle the support position is shifted by one point, the energy landscape is recalculated, and the lowest point in energy is evaluated where the contact point can go from its position in the previous cycle. This is repeated until the loop is completed. As a last step the trajectory of the contact point is evaluated for the first part of a second loop: from the last point in the cycle to the first time it encounters the original curve again. Indeed, the starting point of the second loop is not the same as that of the first, when the surfaces are brought into

contact in which case the initial starting position for sliding is 0. By evaluating all realizations, one after the other, both a prediction can be made for the friction force that would be encountered in a typical experiment, and how much is would differ from one experiment to the other due to variations in the contacting surfaces.

Simulated curves of the experiment of Figure 2 show a high degree of similarity to the measured data (Figure 7). The density of jumps, the typical jump length and the mean lateral force all agree well.

Friction loops for other normal loads were simulated as well. The lateral force for 50 loops and the standard deviation due to the stochastic nature of the realizations of the 'surface roughness function' $\xi(x)$ are plotted in Figure 4 together with the measurements with blue open circles. The uncertainty bars in the calculation give the 1σ variation observed for different realizations of the surface profile. We see that the curve perfectly mirrors the behaviour of the experiment in Figure 4, however the whole curve is slightly offset to the right/down compared to the experiment and shows a regime of negligible friction at low normal loads, a region that we would associate in the traditional Prandtl–Tomlinson model with 'superlubricity'. This is the case even though we have corrected for the 10 nN measured adhesion (adhesion measurements with the MEMS tribometer are detailed in [25]).
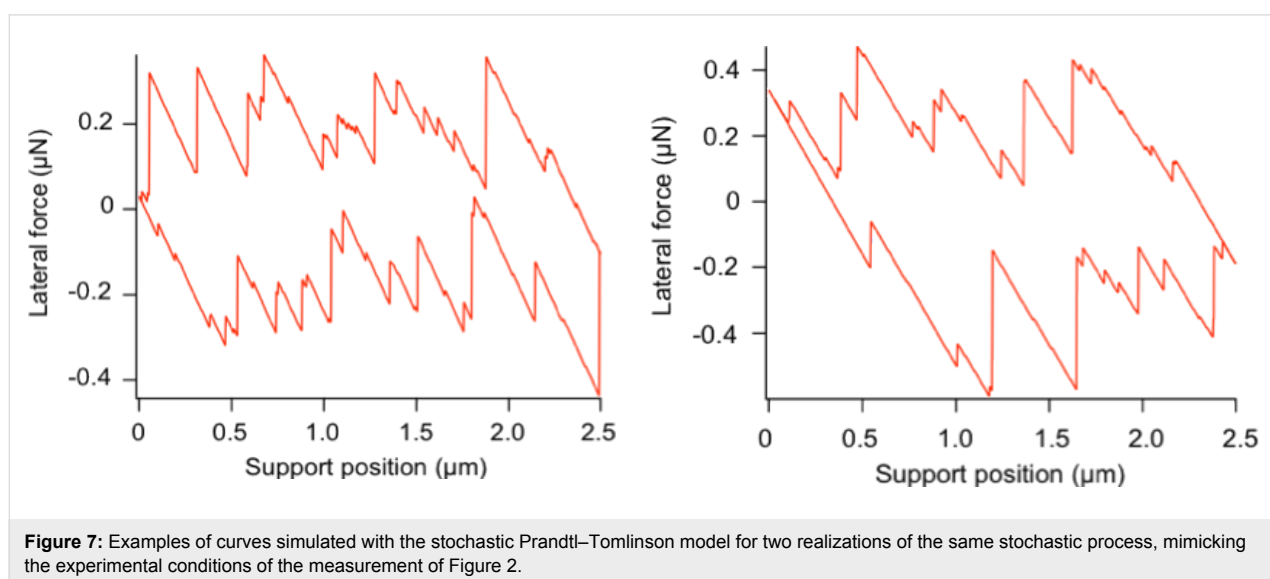
To investigate the effect of the long length scale ripples in the measured autocorrelation function on the outcome of the calculation shown in Figure 4, we have also performed the same simulation with the measured autocorrelation function instead of an ideally exponentially decaying one. These results were obtained for 25 friction loop simulations per normal force value and are shown with the green open triangles. There is no significant difference between the exponential and the 'real' autocorrelation simulations, and hence the effect of the ripples is negligible.

Because we have carried out MEMS measurements resembling force–distance curves (as described in [25]) as well as the friction measurements reported here, we are able to verify the zero-load point independent of the friction measurement. We can hence conclude that it is not allowed to shift the theoretical curve to the right to more closely fit the measurement data as one might be tempted to do, due to the assumption of the presence of a 'superlubric' regime. It seems that in hydrophilic silicon MEMS superlubricity does not take place. Instead a small extra friction force, most probably related to the water/hydrocarbons confined between and around the contacting asperities, has to be taken into account.

Just like the traditional periodic model, the stochastic Prandtl–Tomlinson model is phenomenological in the sense that it predicts the mechanical behaviour of the system, but does not say anything about the origin/amplitude of the corrugation, nor of the processes that cause the energy to really dissipate. In every slip, the stored elastic energy is suddenly released and contributes to a rise of the temperature of the sliding interface and eventually the whole MEMS device due to the thermalization of the phonons launched into the structure upon the impact of the contacting surface asperities [26].

The static shear strength itself is determined by OH-bridging forces between the surfaces, direct chemical Si–O–Si bonds between the surfaces (the rupturing of these bonds leads to wear

Figure 7: Examples of curves simulated with the stochastic Prandtl–Tomlinson model for two realizations of the same stochastic process, mimicking the experimental conditions of the measurement of Figure 2.

of the surfaces in the long run), and/or possibly liquid water meniscus strain or even gluing by confinement induced solidified water [27].

Vibration-induced lubricity simulations

The energy barriers to be overcome in typical MEMS with sliding surfaces are much too large to take advantage of thermolubricity in order to lower friction. We have recently published the results of an experimental study in which we showed that, as in the case of thermal vibrations in thermolubricity, friction in MEMS can be significantly reduced by modulating the normal force, even when the average normal force is held constant. During the moments that the normal force is below the average, it is easier for the system to slip, and if it does, less energy is dissipated due to the smaller jumps involved. In [28], we presented the experimental results and a simple analytical model to predict the corresponding friction reduction. The friction measurement as a function of normal force modulation amplitude is replicated in Figure 8. The application of high-frequency vibrations to ease sliding has been reported on the macroscale already in 1959 [29], with the most recent investigation (in-plane motion) by Popov et al. [30]. Socoliuc et al. [31] have reported on atomic-scale experiments. In the latter case, frictionless sliding can even take place when the surfaces are still in slight contact.
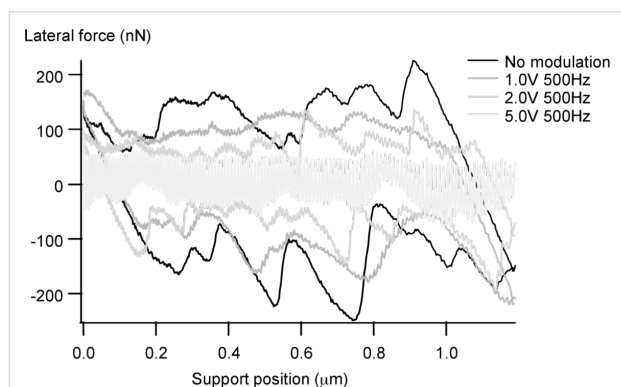
this is done is to first convert the modulation in time to a modulation in space during the sliding. The frequency of the modulation (e.g., 500 Hz) and the sliding speed (in these experiments and simulations sliding 1.2 μm back and forth in 0.5 s makes 4.8 μm/s) are combined. The spatial modulation period is then calculated as 4.8 $\mu m \cdot s^{-1}$/500 Hz = 9.6 nm. The momentary value of the corresponding sine wave is then multiplied with the energy landscape in agreement with the support position, so that one sine wave cycle is achieved for every 9.6 nm of support-position movement. The contact point can slide both forwards and backwards due to the modulation.

The result is shown in Figure 9. The similarity between the simulation and the experiment is evident. The simulation replicates even the fact that a vibrational amplitude with the frequency of the modulation is visible in the lateral force at high modulation amplitudes ('wobbling in the pits'), and that its envelope has a correlation with the surface roughness. Only in the simulation these effects are smaller than those experimentally observed, due to the fact that we are in this case close to the 'superlubric' regime in the model at low load. Figure 10 shows the expected trends of the friction reduction as a function vibration amplitude and frequency as calculated with the new model, as well as the measured curves; the agreement is excellent.

Figure 8: Modulation of the normal force at a frequency much higher than the frequency of the stick-slip events results in a significant decrease in the friction, and the appearance of a modulation signal in the lateral force. A voltage of 5.0 V is equivalent to 280 nN modulation peak–peak (linear scale) of the normal load. The average normal load is held constant at 50 nN. [Reprinted with permission from van Spengen, W. M.; Wijts, G. H. C. J.; Turq, V.; Frenken, J. W. M. *J. Adhes. Sci. Technol.* **2010,** *24,* 2669–2680.]

Figure 9: The major features of the experiment shown in Figure 8, including the amplitude reduction and the visibility of the modulation signal in the lateral force, are replicated in a simulation with the stochastic Prandtl–Tomlinson model of different modulation amplitudes. The peaks in the measurement appear blunter, most probably due to small-scale wear.

With the new stochastic Tomlinson model presented here, it is now possible to fully simulate the effect of this modulation more precisely, both as a function of modulation amplitude and modulation frequency. The effect of modulation of the normal force can be simulated by multiplying the realization of the stochastic surface corrugation with this modulation. The way

Conclusion

The new stochastic Prandtl–Tomlinson model presented in this paper is a powerful tool to describe friction of nanometer-scale rough surfaces of MEMS. Although the model is fully phenomenological (it does not describe the physical processes that give
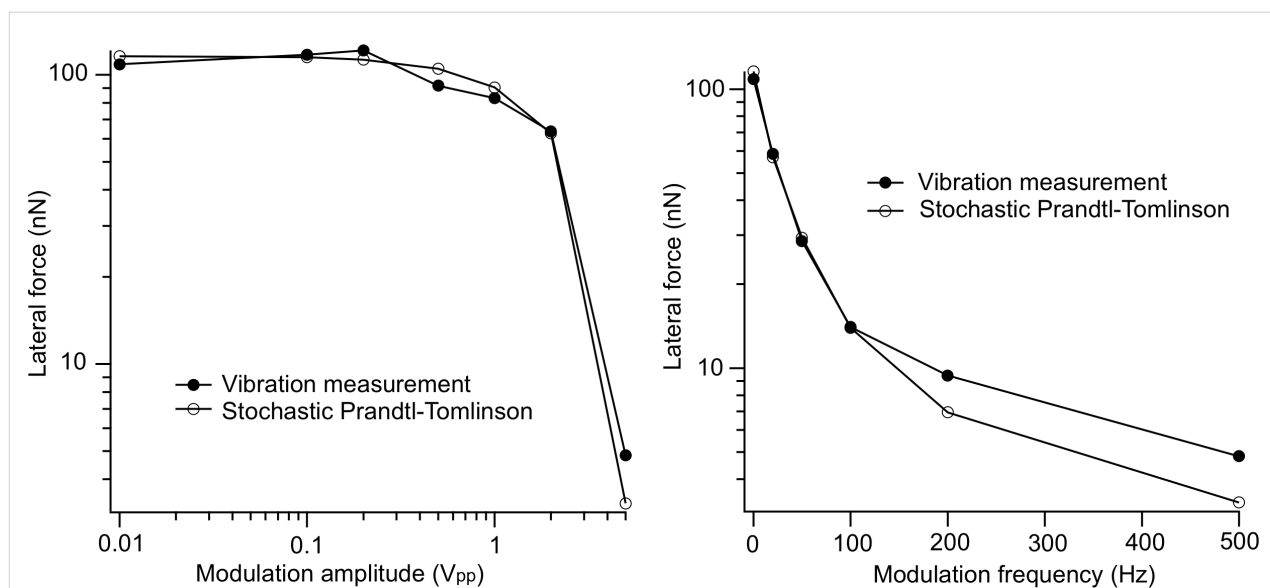
Figure 10: Calculated and measured friction reduction as a function of vibration amplitude (frequency held constant at 500 Hz, left figure) and frequency (5 V$_{pp}$ amplitude, right figure).

rise to the energy dissipation) it is able to predict the important features of the typical motion observed of a polycrystalline silicon MEMS slider as it slides against an on-chip counter-surface of same material. This proves that the overall sliding behaviour is governed by the mechanical locking statistics due to the roughness of the surfaces. We have also shown that this new model can be easily extended with a term that describes the modulation of the normal force as present in vibration-induced friction reduction strategies. This extended model predicts the critical features of the vibration experiments very well.

Acknowledgements

References

1. Mate, C. M.; McClelland, G. M.; Erlandsson, R.; Chiang, S. *Phys. Rev. Lett.* **1987,** *59,* 1942–1945. doi:10.1103/PhysRevLett.59.1942
2. Bhushan, B., Ed. *Springer handbook of nanotechnology,* 2nd ed.; Springer: Berlin, 2007; pp 791–1456.
3. Carpick, R. W.; Salmeron, M. *Chem. Rev.* **1997,** *97,* 1163–1194. doi:10.1021/cr960068q
4. Prandtl, L. Z. *Angew. Math. Mech.* **1928,** *8,* 85–106. doi:10.1002/zamm.19280080202
5. Tomlinson, G. A. *Philos. Mag.* **1929,** *7,* 905–939.
6. Zhong, W.; Tománek, D. *Phys. Rev. Lett.* **1990,** *64,* 3054–3057. doi:10.1103/PhysRevLett.64.3054
7. Meyer, E.; Overney, R. M.; Dransfeld, K.; Gyalog, T., Eds. *Nanoscience: Friction and rheology on the nanometer scale;* World Scientific: Singapore, 2002; pp 123–174.
8. Dienwiebel, M.; Verhoeven, G. S.; Pradeep, N.; Frenken, J. W. M.; Heimberg, J. A.; Zandbergen, H. W. *Phys. Rev. Lett.* **2004,** *92,* 126101. doi:10.1103/PhysRevLett.92.126101
9. Socoliuc, A.; Bennewitz, R.; Gnecco, E.; Meyer, E. *Phys. Rev. Lett.* **2004,** *92,* 134301. doi:10.1103/PhysRevLett.92.134301
10. Krylov, S. Y.; Frenken, J. W. M. *J. Phys.: Condens. Matter* **2008,** *20,* 354003. doi:10.1088/0953-8984/20/35/354003
11. Riedo, E.; Gnecco, E.; Bennewitz, R.; Meyer, E.; Brune, H. *Phys. Rev. Lett.* **2003,** *91,* 084502. doi:10.1103/PhysRevLett.91.084502
12. Kim, S. H.; Asay, D. B.; Dugger, M. T. *Nano Today* **2007,** *2,* 22–29. doi:10.1016/S1748-0132(07)70140-8
13. Fisher, D. S. *Phys. Rev. B* **1985,** *31,* 1396–1427. doi:10.1103/PhysRevB.31.1396
14. Fisher, D. S. *Phys. Rep.* **1998,** *301,* 113–150. doi:10.1016/S0370-1573(98)00008-8
15. Chauve, P.; Le Doussal, P.; Wiese, K. J. *Phys. Rev. Lett.* **2001,** *86,* 1785–1788. doi:10.1103/PhysRevLett.86.1785
16. Fajardo, O. Y.; Mazo, J. J. *Phys. Rev. B* **2010,** *82,* 035435. doi:10.1103/PhysRevB.82.035435
17. Persson, B. N. J. *J. Chem. Phys.* **2001,** *115,* 3840–3861. doi:10.1063/1.1388626
18. Persson, B. N. J.; Albohr, O.; Tartaglino, U.; Volokitin, A. I.; Tosatti, E. *J. Phys.: Condens. Matter* **2005,** *17,* R1–R62. doi:10.1088/0953-8984/17/1/R01
19. van Spengen, W.; Frenken, J. W. M. *Tribol. Lett.* **2007,** *28,* 149–156. doi:10.1007/s11249-007-9259-0
20. Senft, D. C.; Dugger, M. T. *Proc. SPIE* **1997,** *3224,* 31–38. doi:10.1117/12.284533

21. van Spengen, W. M.; Oosterkamp, T. H. *J. Micromech. Microeng.* **2007,** *17,* 828–834. doi:10.1088/0960-1317/17/4/021
22. Mummery, L. *Surface texture analysis, The handbook;* Hommelwerke: Muhlhausen, 1990.
23. Berman, A. D.; Ducker, W. A.; Israelachvili, J. N. *Langmuir* **1996,** *12,* 4559–4563. doi:10.1021/la950896z
24. *Igor Pro 6.04 analysis software;* Wavemetrics: Lake Oswego, OR, U. S. A., 2008.
25. van Spengen, W. M.; Bakker, E.; Frenken, J. W. M. *J. Micromech. Microeng.* **2007,** *17,* S91–S97. doi:10.1088/0960-1317/17/7/S05
26. Szlufarska, I.; Chandross, M.; Carpick, R. W. *J. Phys. D: Appl. Phys.* **2008,** *41,* 123001. doi:10.1088/0022-3727/41/12/123001
27. Jinesh, K. B.; Frenken, J. W. M. *Phys. Rev. Lett.* **2008,** *101,* 036101. doi:10.1103/PhysRevLett.101.036101
28. van Spengen, W. M.; Wijts, G. H. C. J.; Turq, V.; Frenken, J. W. M. *J. Adhes. Sci. Technol.* **2010,** *24,* 2669–2680. doi:10.1163/016942410X508226
29. Fridman, H. D.; Levesque, P. *J. Appl. Phys.* **1959,** *30,* 1572–1575. doi:10.1063/1.1735002
30. Popov, V. L.; Starcevic, J.; Filippov, A. E. *Tribol. Lett.* **2010,** *39,* 25–30. doi:10.1007/s11249-009-9531-6
31. Socoliuc, A.; Gnecco, E.; Maier, S.; Pfeiffer, O.; Baratoff, A.; Bennewitz, R.; Meyer, E. *Science* **2006,** *313,* 207–210. doi:10.1126/science.1125874

License and Terms

Tip-sample interactions on graphite studied using the wavelet transform

Giovanna Malegori[1,2] and Gabriele Ferrini[*1]

Full Research Paper

Address:
[1]Dipartimento di Matematica e Fisica, Università Cattolica del Sacro Cuore, I-25121 Brescia, Italy and [2]Dipartimento di Fisica, Università degli Studi di Milano, I-20122 Milano, Italy

Email:
Gabriele Ferrini[*] - gabriele@dmf.unicatt.it

* Corresponding author

Abstract

Wavelet transform analysis is applied to a thermally excited cantilever to get insights into fundamental thermodynamical properties of its motion. The shortcomings of the widely used Fourier analysis are briefly discussed to put into perspective the wavelet transform analysis, used to describe the temporal evolution of the spectral content of the thermal oscillations of a cantilever with an interacting tip. This analysis allows to retrieve the force gradients, the forces and the Hamaker constant in a measurement time of less than 40 ms.

Introduction

The non-contact atomic force microscopy (NC-AFM) is a powerful tool to study not only the surface topography, but also the mechanical and chemical characteristics of the sample at the nanoscale [1-3]. The tip of an excited cantilever is sensitive to both forces and force gradients, when approaching the sample surface. The response of the cantilever may show a modification of the oscillation amplitude, frequency, phase or damping. The measurement of these cantilever parameters allows to gain information on the physical properties of the sample with (sub-)molecular resolution [4,5]. The dynamic behavior of a weakly interacting cantilever vibrating near a resonance can be well approximated by a simple harmonic oscillator model, described by three independent parameters, resonance frequency, ω_0, amplitude at resonance, A_0, and quality factor, Q. A shift in ω_0 is related primarily to the tip-surface force gradient, A_0 to the driving force, and Q to the energy dissipation [2,6].

The thermal motion (or Brownian motion) of the cantilever's tip is connected to the local mechanical compliance via the fluctuation-dissipation theorem. The cantilever thermal fluctuations are modified by the tip-surface interaction forces: monitoring these modifications allows to reconstruct the interaction potential and

obtain information on various kinds of surface forces [7-9]. The influence of the local environment on the cantilever oscillations around the equilibrium position, detected by a quadrant photodiode in the optical beam deflection method, is usually analyzed by the Fourier transform, that represents the temporal fluctuations of the cantilever in the frequency domain. By doing so, the oscillation eigenmodes of the cantilever are displayed in the spectrum as resonance peaks. However, Fourier transform (FT) analysis is correctly interpreted (and useful) only in the case of stationary systems, i.e., the frequency spectrum must be correlated with a temporally invariant physical system. If the physical state of the system changes in time, the Fourier spectrum only displays an average of spectra corresponding to different states and so the physical information is no more correlated with a single state of the system.

There exists a powerful and well developed mathematical tool overcoming these limitations, not yet applied to analyze the dynamic force spectroscopy (DFS) data, the wavelet analysis [10,11]. In this work, we present wavelet theory as an advanced tool for the analysis and characterization of temporal traces obtained by DFS. A necessary mathematical background on wavelet theory is briefly introduced in the following sections, regarding specifically the decomposition of a one dimensional signal into its frequency components by scaled wavelet functions, known as continuous wavelet transform (CWT). Since wavelet functions are scaled according to frequency and time, such a decomposition results in the so-called *time-frequency localization*. The wavelet transform approach gives a meaningful and intuitive representation of the temporal evolution of the spectral content of an oscillating cantilever. CWT converts a one-dimensional time signal into a two dimensional time-fre-

quency representation, which displays the signal amplitude localized in time and frequency on a time-frequency plane. This is particularly useful to study transitory regimes, i.e., signal with a frequency spectrum changing during the data collection. This work will show that the tip-sample interaction forces can be quantitatively measured using CWT with acquisition times as short as few tens of milliseconds, as required for practical DFS imaging.

Since wavelets are a mathematical tool, they have been used in a number of application in different fields of science and technology to extract information from and/or denoise many different kinds of data, including – but certainly not limited to – audio signals, images, optical spectra, time series. Previously, wavelet analysis has been used in atomic force spectroscopy mainly to denoise or extract data from images [12,13], which is by far the most important application of the wavelet transform.

In the following, first we briefly illustrate the Fourier approach to analyze the time traces of the cantilever thermal oscillations collected at different separations from the surface. Successively the CWT and its use in DFS will be introduced.

Fourier analysis of the cantilever thermal fluctuations

Fourier analysis can be used to process the temporal trace of the cantilever thermal vibrations detected by a standard AFM optical beam deflection system. The power spectral density (PSD) of the time signal, extending over a temporal interval sufficiently long to assure the needed spectral resolution, reveals resonance peaks corresponding to the various oscillation eigenmodes of the cantilever beam (Figure 1). This analysis

Figure 1: Block diagram of the optical beam detection system. A typical power spectral density spectrum of the cantilever flexural modes (up to the fifth) is shown.
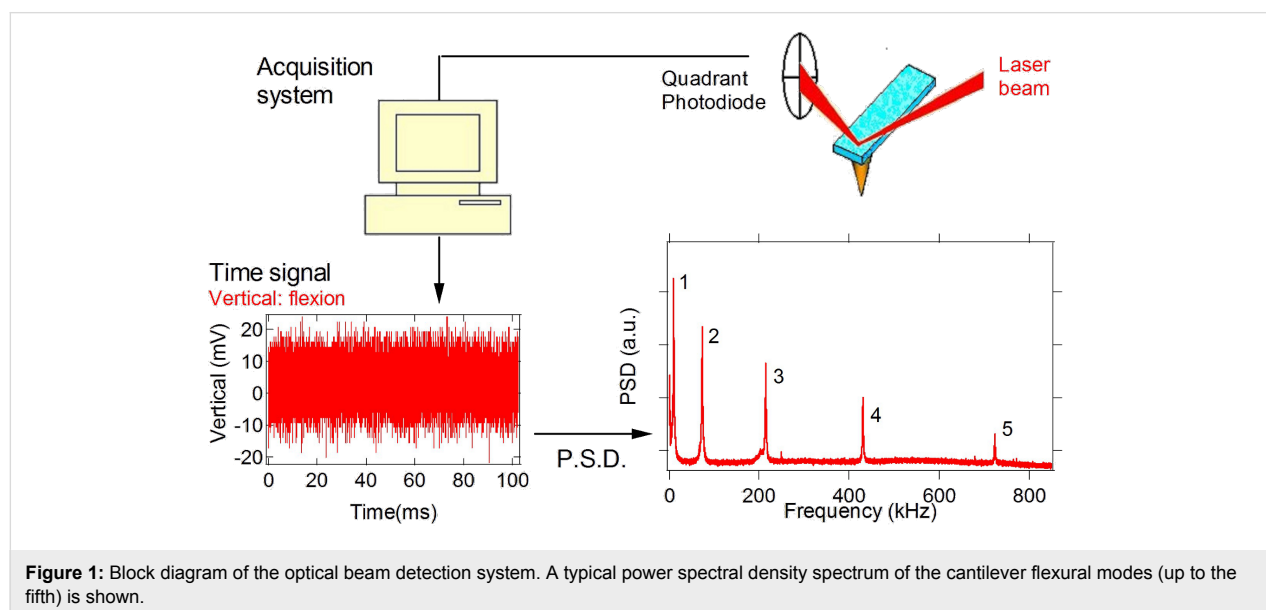
is repeated at various separations from the surface, up to the jump-to-contact distance. The force gradient of the interaction dF_{ts}/dz (where F_{ts} is the tip-sample force and z the tip-sample distance, positive along the surface normal direction) is directly evaluated by the observed frequency shift of the PSD as a function of z. Considering each flexural mode equivalent to a mass-spring system, the tip-sample interaction elastic constant $k_{ts} = -dF_{ts}/dz$ is expressed as a function of the resonant frequency as $k_{ts} = k((f_0' + f_0)(f_0' - f_0) / f_0^2)$, where f_0 is the resonant frequency of the free cantilever, f_0' is the resonant frequency of the cantilever interacting with the surface force gradients and k is the equivalent elastic constant of the mode under consideration. This relation holds if k_{ts} remains constant for the whole range of the displacements from the equilibrium position covered by the cantilever. This is usually true in the thermal regime since we are dealing with small oscillations (less than 0.2 nm) [9]. If $|k_{ts}| \ll k$ the frequency shift $\Delta f = f_0' - f_0$ is proportional to the interaction elastic constant $k_{ts} = 2k\Delta f / f_0$ [1].

From the same PSD, besides the force gradient, it is possible to measure the quality factor Q of the mode, that is determined by the relative width of the resonance peaks corresponding to the oscillation eigenmodes of the cantilever ($Q = \Delta\omega/\omega_0$). Q is usually dependent on the distance from the surface. Since the quality factor Q is connected to dissipation, important informations on the tip-sample energy exchange can be retrieved.

With this techniques force gradients and quality factors on graphite in air have been measured [9]. It was found that the attractive force gradient data are well reproduced by a nonretarded van der Waals function in the form $HR/(3z^3)$ (H is the Hamaker constant and R the tip radius of curvature), up to the jump-to-contact distance D which occurs at around 2 nm from the surface (Figure 2). In this distance range, Q is almost constant for the first and second flexural modes. This means that the interaction is conservative at distances greater than D, the first flexural mode showing an evident decrease of the Q value just before the jumps-to-contact. The dissipation mechanism related to this sharp transition is due to a local interaction of the tip apex with the surface.

In these experiments, the acquisition and storage of the photodiode time signal requires tens of seconds at each tip-sample separation. This implies that the measurements at a single spatial location (one pixel of an image) may take minutes. The long measurements duration, besides the control of thermal drifts, is not practical for imaging pourposes.

In closing this section, it is interesting to note that near the sample, the quality factor is lower than that of the free
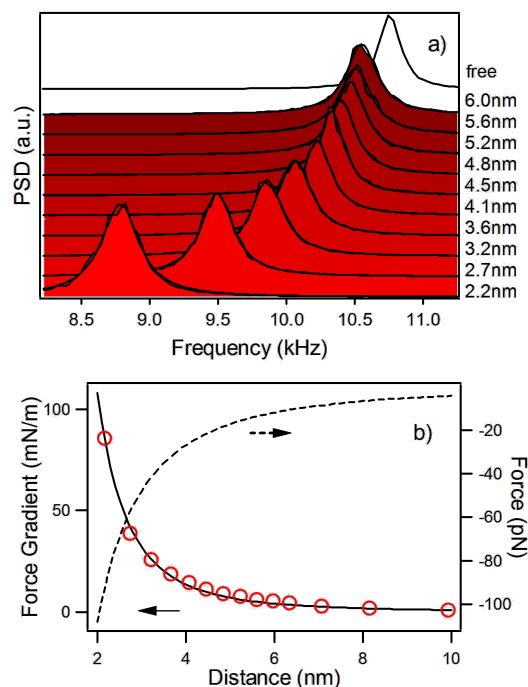
Figure 2: Results from the Fourier transform method, adapted from [9]. a) Power spectral density of the thermal fluctuations of the first flexural mode of the cantilever acquired at different tip-sample separations. A negative frequency shift of the resonant frequency is observed on approaching the graphite surface. The resonance peaks are fitted with a Lorentzian. b) The black continuous line is a fit of the van der Waals force gradient between a spherical tip and a flat surface (force gradient = $HR/3z^3$, z is the tip-sample distance) to the measured frequency shift of the first flexural mode as a function of the tip-surface separation (red circles). The dashed line is the interaction force obtained by integration.

cantilever. The decrease is due to the interaction of the rectangular beam with the sample surface. If the tip-sample separation is very small, the distance between the beam and the surface is about the tip height (nominal value $h = 20$–25 μm). When the cantilever oscillates in air or in a fluid close to a solid surface, due to a confinement effect, an increased damping is manifested as a decrease of the quality factor [14]. This effect is relevant for piezotube movements on the μm scale but not on the nm scale covered by the present measurements, where the effect of the tip-sample interaction dominates.

Continuous wavelet transform and time-frequency resolution

The FT analysis provides a frequency representation of a signal with perfect spectral resolution but without the possibility to correlate the frequency spectrum with the signal evolution in time. Instead, a time-frequency representation shows the signal evolution over both time and frequency. CWT is a refined alternative to the classical windowed Fourier analysis, providing not only the representation of the spectral energy content of the

signal at a certain time, but also the ability to adapt the resolution to the signal frequency.

A wavelet is a smooth function $\Psi(t)$ with a compact support (or a rapid decay at infinity, contrary to the Fourier basis), and zero average,

$$\int_{-\infty}^{+\infty} \Psi(t)dt = 0$$

which is translated in time by d and dilated by a positive scale parameter s,

$$\Psi_{s,d}(t) = \frac{1}{\sqrt{s}}\Psi(\frac{t-d}{s})$$

The zero average condition imply that $\Psi(t)$ is an oscillating function. The function $\Psi(t)$ is called a mother wavelet, the translated and dilated replicas $\Psi_{s,d}(t)$ are called daughter wavelets. The wavelet transform of a function of time t, $f(t)$, at the scale s and delay d is computed by correlating $f(t)$ with the daughter wavelet at the corresponding scale and delay,

$$Wf(s,d) = \int_{-\infty}^{+\infty} f(t)\Psi_{s,d}^{*}(t)dt = \int_{-\infty}^{+\infty} f(t)\frac{1}{\sqrt{s}}\Psi^{*}(\frac{t-d}{s})dt$$

The wavelet transform coefficients $Wf(s,d)$ are "resemblance" coefficients, that measure the similitude between the signal and the wavelet atoms at various scales and delays (Figure 3a).

The square modulus of the wavelet coefficients $|Wf(s,d)|^2$ is proportional to the local energy density of the signal at the given delay and scale, called the scalogram of the signal. As explained in detail below, the delay-scale representation in which wavelets are defined can be mapped into the more physical time-frequency representation to describe the signal energy localization in frequency and time. It is useful to point out that the instantaneous frequency of the signal can be traced by the so called wavelet ridges analysis of the spectrogram in the time-frequency plane. The wavelet ridges are the maxima points of the normalized scalogram [11], showing the instantaneous frequencies within the limits of the transform's resolution (the ridge analysis will be useful to represent the experimental data). When the signal contains several spectral lines whose frequencies are sufficiently apart, the wavelet ridges (i.e., the local maxima) separates each of these components during their temporal evolution, a task that cannot be performed using Fourier analysis.

To visualize the differences between the FT and CWT consider a signal $f(t) = a\cos\varphi(t)$ with time varying phase $\varphi(t)$, where $\varphi(t) = \omega_0 t$ at negative times and $\varphi(t) = \omega_0 t + \alpha t^3$ at positive times (Figure 3a). The instantaneous pulsation is the derivative of the
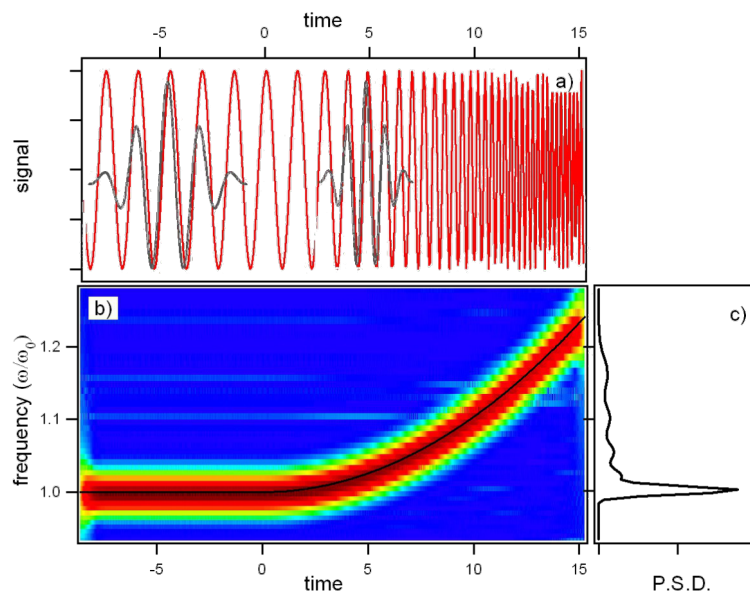
Figure 3: Comparison between the Fourier transform and the wavelet transform analysis. a) The time signal, a cosine function for negative times and a cosine with quadratic chirp for positive times. Two daughter wavelet functions with different dilations and delays are superposed to the signal to show the local resemblance between signal and wavelet. b) Wavelet transform of the temporal trace represented in a) showing the evolution of the signal frequency. The black line is the calculated instantaneous frequency. c) Fourier transform (power spectral density) of the signal represented in a). Only an average of the signal frequencies is observed.

phase $\omega(t) = \varphi'(t)$ (the black line in Figure 3b). Since FT is a time invariant operator, only an average of the time dependent spectrum is observed (Figure 3c). On the other hand, CWT approach combines the time domain and frequency domain analysis so that the evolution of each spectral component is determined. The wavelet analysis allows to extract accurately the instantaneous frequency information even for rapidly varying time series (Figure 3b).

In the remainder of this section, we higligth the main features of CWT analysis that are important when applied to the time evolution of the cantilever oscillations. Unlike FT, the basis of CWT is not unique, so it is important the choice of the wavelet basis. In this work, we use a complex mother wavelet (also called the Gabor wavelet or the Gaussian wavelet) represented as

$$\Psi(t) = \frac{1}{(\sigma^2 \pi)^{1/4}} \exp(\frac{t^2}{2\sigma^2} + i\eta t)$$

where σ controls the amplitude of the Gaussian envelope, and thus its time/frequency resolution, η the carrier frequency. Since the intrinsic time-frequency resolution in CWT is set by the atoms over which the signal is expanded, we chose this wavelet because it is particularly adapted to follow signals in time, having the least spread in both frequency and time domain and thus the best time frequency resolution.

The CWT is defined in terms of delays and scales and, as anticipated, the representation can be mapped to time and frequency. While it is immediate the connection of delay to time, some comments are useful to connect scale to frequency.

The signal relative to the vertical cantilever displacement, recorded with a digitizing oscilloscope from the optical beam deflection system photodiode, can be thought as a one dimensional string of sampling units. Each sampling unit is the value of the signal at a specific sampling time and together constitute the discretized sampled signal. A sampling unit is temporally connected to the next by a (usually) fixed sampling interval T. In this framework, the temporal parameter t in the expression of the Gabor wavelet can be regarded as a (adimensional) discrete index and likewise σ and η are adimensional wavelet parameters defining the wavelet shape over the discrete sampling string. The Gabor wavelet (adimensional) center frequency at scale s is given by $f = \eta/(2\pi s)$. It is possible to associate a pseudo frequency F (in Hz) at a scale s by considering that f is sampled with a time interval T, so that $F = f/T$. Therefore, the wavelet dilations set by the scale parameter s are inversely proportional to the frequency F.

Strictly connected to the relation between scale and frequency is the wavelet time-frequency resolution. The joint time and frequency limitations set to the analysis of the energy content of the signal leads naturally to the introduction of the Heisenberg box, associated to each analyzing wavelet. The Heisenberg box delimits an area in the time-frequency plane over which different CWT coefficients cannot be separated, providing a geometrical representation of the Heisenberg uncertainty principle (Figure 4). We adopt the commonly used definition of the measure of the uncertainty window Δ as the root-mean-square extension of the wavelet in the corresponding time or frequency space,

$$\Delta_\xi^2 = \frac{\displaystyle\int_{-\infty}^{+\infty} \xi^2 \left|\Psi(\xi - \xi_0)\right|^2 d\xi}{\displaystyle\int_{-\infty}^{+\infty} \left|\Psi(\xi)\right|^2 d\xi}$$

where ξ_0 is a translation parameter and $\Psi(\xi)$ represents the Gabor mother wavelet, expressed either in time, $\xi = t$, or circular frequency, $\xi = \omega = 2\pi F$, $\Psi(\omega) = \mathrm{FT}(\Psi(t))$.

The time-frequency resolution of the analyzing Gabor mother wavelet, used in this work, is determined by the σ parameter. The Heisenberg box associated to the mother Gabor wavelet is given by a time resolution $\Delta_t = \sigma / \sqrt{2}$ and a frequency (or pulsation) resolution $\Delta_\omega = 1/(\sqrt{2}\sigma)$. When the wavelet is subject to a scale dilatation s, the corresponding resolution has size $\Delta_{s,t} = s\Delta_t$ along time and $\Delta_{s,\omega} = \Delta\omega/s$ along frequency (Figure 4). The Heisenberg box centered at time t and frequency $\omega = 2\pi F$ is thus defined as

$$\left[t - \Delta_{s,t}, t + \Delta_{s,t}\right] \times \left[\omega - \Delta_{s,\omega}, \omega + \Delta_{s,\omega}\right]$$

As expected from the uncertainty principle, $\Delta_{s,t}\Delta_{s,\omega} = 1/2$.

It is useful to define the dimensionless parameter known as the Gabor shaping factor $G_S = \sigma\eta$ [16], which takes in to account the envelope width (temporal resolution) and the number of oscillations within the envelope width (frequency resolution). The shaping factor controls the time frequency resolution via the dimensions of the Heisenberg box (Figure 4). In fact, as it is easily seen, $\Delta_{s,t} \propto G_S$ while $\Delta_{s,\omega} \propto 1/G_S$, so that the choice of the single parameter G_S determines the shape of the Heisenberg box. An increase of G_S means more oscillations under the wavelet envelope and a larger time spread, the frequency resolution being improved and the time resolution degraded. In Figure 5 are shown the CWT of delta-like signals in time and frequency, whose time-frequency resolution is due only to the wavelet analyzing characteristics. As discussed above, it is
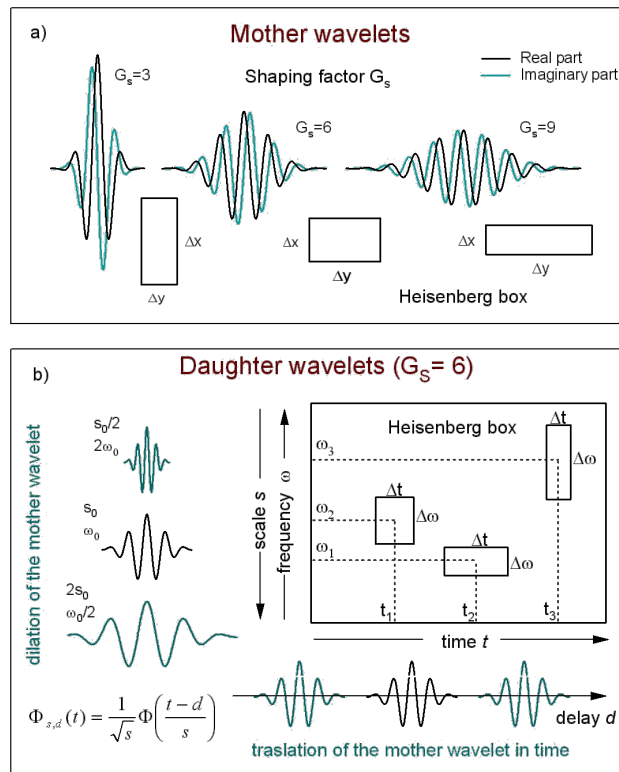
Figure 4: a) Complex Gabor wavelet with different shaping factors. An increase of G_S corresponds to more oscillations under the envelope. The "Heisenberg box" shows the relationship between the time and frequency resolution, like the uncertainty principle in quantum mechanics (adapted from [15]). b) A graphical representation of the delay and dilation transformations used in the continuous wavelet transform (adapted from [16]).
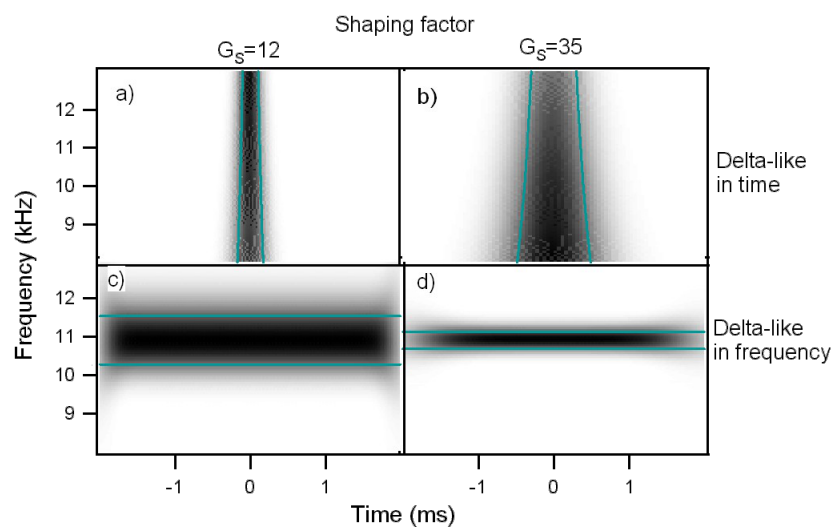
Figure 5: Continuous wavelet transform of a delta-like signal in time and a delta-like signal in frequency, analyzed with wavelets of different shaping factor, a-c) G_S = 12, b-d) G_S = 35. a-b) CWT of a delta-like function in time. The dependence of resolution on scale (frequency) is clearly shown. c-d) CWT of a delta-like function in frequency. The frequency resolution increases with the shaping factor. The degradation of the CWT resolution near the edges of the window transform is visible (edge effect).

possible to see that the frequency resolution due to the mother wavelet choice increases with G_S while the temporal resolution is degraded. The delta-like signals in time show clearly that the time resolution depends on the scale (frequency) parameter, increasing at lower scale (higher frequency). The delta-like signals in frequency also show the edge effect, a degradation of the wavelet resolution near the edges of the CWT time window due to the spectral broadening produced by the signal truncation.

Results and Discussion
Wavelet analysis of the cantilever thermal fluctuations

The wavelet analysis is applied to the force–distance curves taken with the cantilever subject to thermal fluctuations while approaching the surface. Figure 6 shows the scalogram of a 40 ms sampling of the cantilever Brownian motion around its instantaneous equilibrium position while the piezo scanner is displaced at constant velocity to move the tip towards the surface, until it jumps to contact.

The discontinuous appearance of the signal in the time-frequency representation is due to the statistical nature of the cantilever excitation. The thermal contact of the cantilever with a reservoir at temperature T implies that its mean potential energy $1/2kA_{rms}^2$ (where A_{rms} is the root mean square cantilever displacement due to thermal motion) is equal to $1/2k_BT$ by the equipartition theorem, where k_B is the Boltzmann constant and T is the temperature. Microscopically this can be regarded as the action of random thermal kicks (i.e. uncorrelated impulsive forces), a driving force with white frequency spectrum. This thermal force induces cantilever displacements from the equilibrium position, that show a marked amplitude enhancement in correspondence of the flexural eigenfrequencies. Since the cantilever is subjected also to dissipative friction forces, the amplitude response of the cantilever around a flexural resonant frequency is not delta-like, but has a finite linewidth. The PSD of the same temporal trace used for the CWT, reported in Figure 6a, shows a linewidth comparable to the frequency indetermination of the Heisenberg box of the CWT and a structure at low frequency that is reminiscent of the interaction with the surface, when for a short time the cantilever frequency is lowered.

It is interesting to clarify the origin of the "bumps" observed in the time-frequency representation. When the cantilever has a thermally activated fluctuation, each flexural mode responds as a damped harmonic oscillator whose equation of motion is $\ddot{x} + \omega_0/Q\dot{x} + \omega_0^2 x = 0$ where x is the oscillation amplitude, Q the quality factor and ω_0 the resonance frequency [17,18]. Considering for simplicity the initial conditions $x(0) = x_0$, $\dot{x}(0) = 0$ and assuming $Q \gg 1$, the solution is an exponentially decaying amplitude oscillating at the resonance frequency: $x = x_0 e^{-\omega_0 t/(2Q)} cos(\omega_0 t)$.

The energy associated to the oscillator $E(t)$ is proportional to $\dot{x}^2$ and from the above relations we see that the associated exponential energy decay time is $\tau = Q/\omega_0$. The spectral energy density of the damped oscillator ($L(\omega)$) is proportional to the square modulus of the Fourier transform of $x(t)$, $L(\omega) = |FT(x(t))|^2$. Under the assumption $Q \gg 1$, $L(\omega)$ is well approximated by a Lorentzian with a full width at half maximum of $\Delta\omega = 2\pi\Delta f = 1/\tau$.

Since the cantilever is first thermally excited and then damped to steady state by random forces that act on a much smaller time scale than its oscillation period, the characteristic response time for an isolated excitation/decay event cannot be smaller than 2τ, with an associated Lorentzian full width at half maximum of $\Delta\omega$.
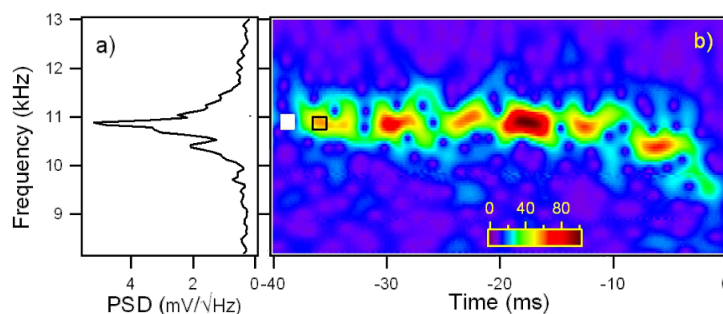
Figure 6: a) Power spectral density of the Brownian motion of the first flexural mode of the same temporal trace used for the wavelet transform on the right. b) Wavelet transform of the Brownian motion of the cantilever first flexural resonance, around its instantaneous equilibrium position, as the tip approaches the surface at constant velocity (9 nm / 40 ms = 225 nm/s). The wavelet coefficients |*Wf(f,t)*| are coded in colorscale. The origin of the time axis corresponds to the instant when the jump-to-contact occurs. The white box at the left side represents the Heisenberg box, the open box delimited by black lines represents the damped oscillator in response to an impulsive thermal excitation.

From the above reasoning, it is natural to introduce the *damped oscillator box*, a geometrical representation of the extension in the time-frequency plane of the wavelet coefficients associated to a single excitation/decay event, centered at time t and frequency ω, defined as

$$\left[t-\tau, t+\tau\right] \times \left[\omega - \Delta\omega/2, \omega + \Delta\omega/2\right]$$

The damped oscillator box, contrary to the Heisenberg box, does not represent a limitation in resolution due to the wavelet choice, but a physical representation of the damped oscillator time frequency characteristics. It is important to note that the ultimate resolution limitations imposed by the Heisenberg box associated with the analyzing wavelet could prevent the observation of the true dimensions of the damped oscillator box.

Due to their different definitions, a comment on the sizes of the Heisenberg box and the damped oscillator box is useful. The Heisenberg box dimensions are the root-mean-square extensions of the Gabor wavelet envelope (i.e., its modulus) in time and frequency. Since the Gabor wavelet evelope is a gaussian in time and frequency, its root-mean-square extension is by definition the gaussian standard deviation, i.e. the half width at $1/\sqrt{e} \approx 0.606$ of the maximum. The damped oscillator box dimension in frequency is the full width at half maximum of $L(\omega)$. In terms of the wavelet envelope (proportional to $\sqrt{L(\omega)}$), it is the full width at $1/\sqrt{2} \approx 0.707$ of the maximum. The damped oscillator box dimension in time is 2τ, where τ is the full width at $1/\sqrt{e} \approx 0.606$ of the maximum of the exponentially decaying oscillator amplitude.

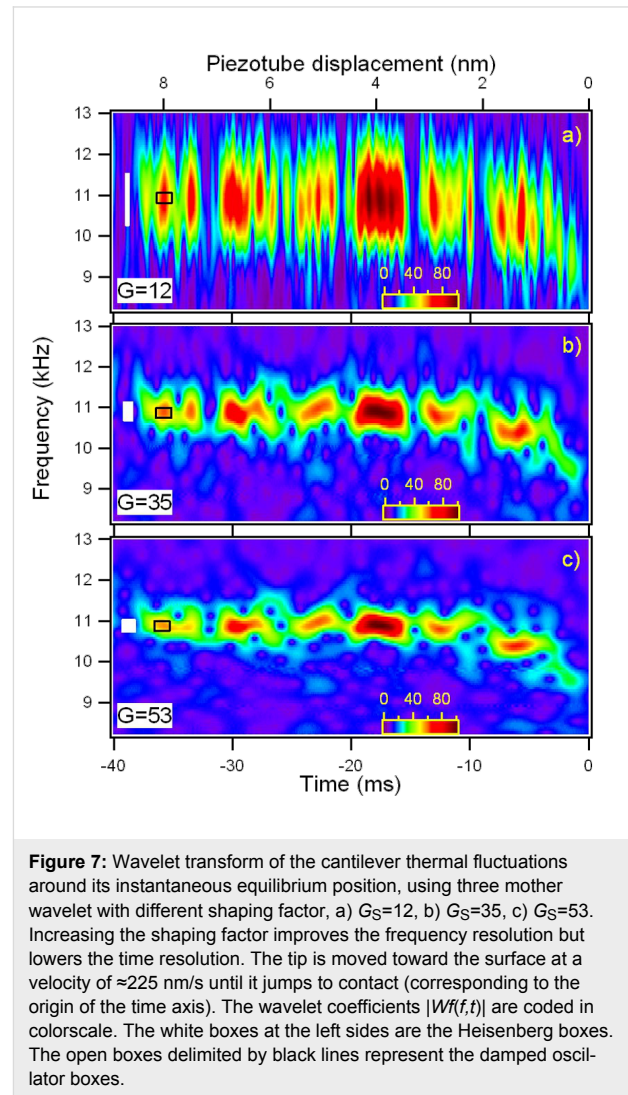We did not attempt to correct the sizes of the boxes using a single common definition because the comparisons with the experimental data in the present work are mainly qualitative. In our case $Q = 43$ and $f_0 = 10.9$ kHz for the first flexural mode, implying $\tau = 1.25$ ms and $\Delta\omega = 250$ Hz. It is important to note that the temporal and frequency width of many discrete time frequency small structures seen in the CWT of the cantilever thermal signal in Figure 7c are of the same dimensions of the damped oscillator box $2\tau \times \Delta\omega$. This observation is possible because the first flexural mode is represented with a Gabor wavelet with a shaping factor $G_S = 53$ around the resonant frequency, the Heisenberg box (1.1 ms × 290 Hz) is similar to the damped oscillator box (1.25 ms × 250 Hz). In the representation of Figure 7a and Figure 7b, the CWT has different shaping factors and thus different dimensions of the Heisenberg box (0.71 ms × 450 Hz for $G_S = 35$, Figure 7b, 0.25 ms × 1300 Hz for $G_S = 12$, Figure 7a), that allows to measure the time width of the damped oscillator structures, but not its frequency width due to limited frequency resolution. It is important to note that the temporal width of the structures is independent on the time

resolution of the wavelet, indicating that we are observing a real physical feature, that is not related to the choice of the wavelet representation. As a rule of thumb, CWT should allow to follow more easily the single-thermal-excitation-event time decay in high-Q environments and measure its frequency linewidth in low-Q environments.

Figure 7: Wavelet transform of the cantilever thermal fluctuations around its instantaneous equilibrium position, using three mother wavelet with different shaping factor, a) G_S=12, b) G_S=35, c) G_S=53. Increasing the shaping factor improves the frequency resolution but lowers the time resolution. The tip is moved toward the surface at a velocity of ≈225 nm/s until it jumps to contact (corresponding to the origin of the time axis). The wavelet coefficients |$Wf(f,t)$| are coded in colorscale. The white boxes at the left sides are the Heisenberg boxes. The open boxes delimited by black lines represent the damped oscillator boxes.

The first flexural mode frequency shift near the surface (Figure 7b) provides a complete force distance curve. The instantaneous frequency is evaluated by the wavelet ridges, the local maxima points of the normalized scalogram. In order to reduce noise effects, only maxima above a threshold are considered (see the schematic representation in the inset of Figure 8).

From the instantaneous frequency shift the gradient of the tip-sample interaction forces (dF_{ts}/dz) is retrieved, using the relations previously reported, and the time scale is converted into
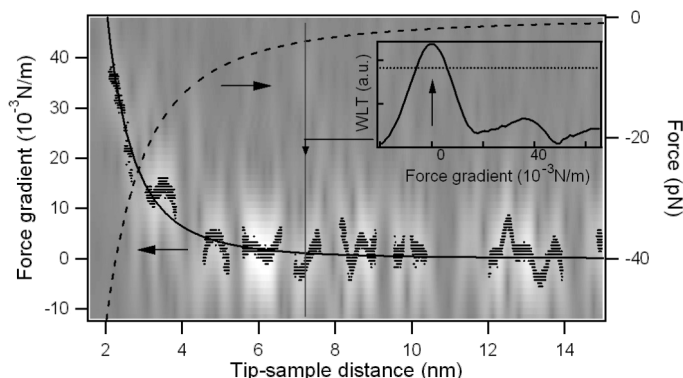
Figure 8: Force gradient versus tip-sample distance for the first flexural mode near the jump-to-contact. The wavelet ridges provide the instantaneous frequencies within the limits of the scalogram resolution. The wavelet ridges are the local maxima of the normalized scalogram above a specified threshold, as schematically shown in the inset. The threshold is represented by a horizontal line and the maximum point is indicated by an arrow for a vertical cut of the data at constant tip-sample distance. The CWT of Figure 7b is represented in gray scale on the background together with its ridges (black points). The continuous black line is an Hamaker-like force gradient function fitted to the wavelet ridges, the dashed line the force calculated by integration.

the tip-sample separation by taking into account either the piezoscanner velocity and the cantilever static deflection, to obtain a complete force gradient versus distance curve (Figure 8). The gradient data from CWT ridges are well fitted by a nonretarded van der Waals function in the form $HR/3z^{-3}$, with $HR = 1.2 \times 10^{-27}$ Jm. Using the typical values of H in graphite ($H = 0.1$ aJ), the tip radius is evaluated as $R = 12$ nm, in good agreement with the nominal radius of curvature given by the manufacturer ($R = 10$ nm). To promote this technique from proof of principle to a measurement of the Hamaker constant with a good lateral resolution, a thorough characterization of the tip radius of curvature is needed.

Finally, we note that the whole force curve is acquired in less than 40 ms, a time significantly less than that usually needed for force versus distance measurements. With an optimization of the electronics and reduction of dead times in the acquisition process, it would be possible to acquire images in which a complete information on force gradients and topography is compatible with 1–30 ms/pixel data acquisition times required for practical DFS imaging.

Conclusion

The interaction of an AFM cantilever tip with a graphite sample is measured by applying the wavelet transform analysis to its Brownian motion near the surface. The wavelet transform analysis is a mathematical tool able to analyze the instantaneous spectral content of rapidly varying signals. Using the wavelet transforms to analyze the temporal traces of the thermal motion superposed on a force-distance curve, the tip-sample interaction is measured in tens of ms, a time compatible with imaging acquisition rates. The wavelet transform technique is very promising since the analysis could be applied simultaneously to the higher flexural eigenmodes. Moreover the measurement could be carried out across the jump-to-contact transition without interruption, providing information on the elastic response of the surface.

Experimental

The experiments are carried out with an AFM [19] mounted on a massive platform suspended by springs to provide isolation from external mechanical noise. The AFM with its isolation platform are closed inside an acoustic isolation chamber. The cantilever deflection is monitored by an optical beam deflection system based on a 600 nm laser diode coupled to a monomode fiber (with a mode field diameter of 4 μm), which acts as a mode filter, giving a TEM_{00} beam output after recollimation. The collimated fiber output is focalized with an aspherical lens to a 10 μm spot on the cantilever end. A digitizing oscilloscope collects the differential outputs (left-right and top-bottom) of the four quadrant silicon diode. The overall bandwidth of the beam deflection system exceeds 1 MHz. The digitizing oscilloscope has a 8 bit vertical resolution, 250 MHz analog bandwidth, 1 Gsample/s maximum sampling rate, and a buffer memory of 128 Msample.

The silicon cantilevers average dimensions are $40 \times 460 \times 2$ μm with a typical tip radius $R = 10$ nm. The resonance frequency of the first flexural mode of the cantilever used in the experiments is $f_0 = (10.908 \pm 0.002)$ kHz, its elastic constant is $k = 0.13$ N/m [20]. For each cantilever the elastic constant is evaluated both by the Sader method [20] and the thermal noise method applied to the first flexural mode [21,22]. Both methods agree within 5%.

The piezoscanning system is based on a single scanner tube with a maximum vertical extension of 2 μm. The experiments consisted in acquiring the temporal evolution of the thermal noise as a function of the tip-sample distance. The thermal noise signal measured by the beam deflection system is sampled with the digitizing oscilloscope while the tip moves toward the surface. The piezoscanner is displaced at constant velocity of approximately 225 nm/s. The sampling time is 240 ns so that the signal string is composed by 4166 sampling points every ms of acquisition time. The CWT analysis is performed off-line.

The sample consisted of a freshly cleaved highly oriented pyrolitic graphite (HOPG) surface. All the experiments have been conducted in air, with a relative humidity of less than 50%. Figure 1 schematically shows the experimental apparatus: the electronic noise level is small enought to detect up to five flexural eigenmodes. The optical lever sensitivity is calibrated by taking the force spectroscopy curves on the hard HOPG surface, assuming a negligible indentation and thus equal distances spanned by the cantilever tip and the piezotube. The obtained sensitivity is in the range of 50–200 nm/V, depending on the cantilever type, beam position, and laser light power level. The cantilever has a 15° tilt with respect to the horizontal plane (that coincides with the sample surface), which is considered for sensitivity correction [23]. Since the laser beam position influences the effective length of the cantilever and the sensitivity, the stability of the laser alignment is carefully controlled during the measurements. From the approach force curves after the jump to contact, the tip-sample contact point is determined as the distance at which no force acts on the cantilever that is when the cantilever is not deflected.

Acknowledgements

References

1. Morita, S.; Wiesendanger, R.; Meyer, E., Eds. *Noncontact Atomic Force Microscopy;* Springer: Berlin, 2002.
2. Garcia, R.; Pérez, R. *Surf. Sci. Rep.* **2002,** *47,* 197–301. doi:10.1016/S0167-5729(02)00077-8
3. Butt, H. J.; Cappella, B.; Kappl, M. *Surf. Sci. Rep.* **2005,** *59,* 1–152. doi:10.1016/j.surfrep.2005.08.003
4. Sugimoto, Y.; Pou, P.; Abe, M.; Jelinek, P.; Pérez, R.; Morita, S.; Custance, O. *Nature* **2007,** *446,* 64–67. doi:10.1038/nature05530
5. Gross, L.; Mohn, F.; Moll, N.; Liljeroth, P.; Meyer, G. *Science* **2009,** *325,* 1110–1114. doi:10.1126/science.1176210
6. García, R.; Magerle, R.; Pérez, R. *Nat. Mater.* **2007,** *6,* 405–411. doi:10.1038/nmat1925
7. Cleveland, J. P.; Schäffer, T. E.; Hansma, P. K. *Phys. Rev. B* **1995,** *52,* R8692–R8695. doi:10.1103/PhysRevB.52.R8692
8. Roters, A.; Johannsmann, D. *J. Phys.: Condens. Matter* **1996,** *8,* 7561. doi:10.1088/0953-8984/8/41/006
9. Malegori, G.; Ferrini, G. *J. Vac. Sci. Technol., B: Microelectron. Nanometer Struct.–Process., Meas., Phenom.* **2010,** *28,* C4B18. doi:10.1116/1.3305452
10. Chui, C. K. *An Introduction to Wavelets;* Academic Press: 1992.
11. Mallat, S. G. *A Wavelet Tour of Signal Processing;* Academic Press, 1999.
12. Carmichael, M.; Vidu, R.; Maksumov, A.; Palazoglu, A.; Stroeve, P. *Langmuir* **2004,** *20,* 11557–11568. doi:10.1021/la048753c
13. Gackenheimer, C.; Cayon, L.; Reifenberger, R. *Ultramicroscopy* **2009,** *106,* 389–397. doi:10.1016/j.ultramic.2005.11.006
14. Siria, A.; Drezet, A.; Marchi, F.; Comin, F.; Huant, S.; Chevrier, J. *Phys. Rev. Lett.* **2009,** *102,* 254503. doi:10.1103/PhysRevLett.102.254503
15. Image credit: André Mouraux, Faculté de Médecine, Univ. Catholique de Louvain, Belgium.
16. Deng, Y.; Wang, C.; Chai, L.; Zhang, Z. *Appl. Phys. B: Lasers Opt.* **2005,** *81,* 1107–1111. doi:10.1007/s00340-005-1959-2
17. Albrecht, T. R.; Grütter, P.; Horne, D.; Rugar, D. *J. Appl. Phys.* **1991,** *69,* 668–673. doi:10.1063/1.347347
18. Demtröder, W. *Laser Spectroscopy,* 3rd ed.; Springer, 2003; p 60.
19. A.P.E. Research Trieste (http://www.aperesearch.com).
20. Sader, J. E.; Chon, J. W. M.; Mulvaney, P. *Rev. Sci. Instrum.* **1999,** *70,* 3967–3969. doi:10.1063/1.1150021
21. Butt, H. J.; Jaschke, M. *Nanotechnology* **1995,** *6,* 1. doi:10.1088/0957-4484/6/1/001
22. Lévy, R.; Maaloum, M. *Nanotechnology* **2002,** *13,* 33. doi:10.1088/0957-4484/13/1/307
23. Hutter, J. L. *Langmuir* **2005,** *21,* 2630–2632. doi:10.1021/la047670t

Defects in oxide surfaces studied by atomic force and scanning tunneling microscopy

Thomas König, Georg H. Simon, Lars Heinke, Leonid Lichtenstein and Markus Heyde[*]

Abstract

Surfaces of thin oxide films were investigated by means of a dual mode NC-AFM/STM. Apart from imaging the surface termination by NC-AFM with atomic resolution, point defects in magnesium oxide on Ag(001) and line defects in aluminum oxide on NiAl(110), respectively, were thoroughly studied. The contact potential was determined by Kelvin probe force microscopy (KPFM) and the electronic structure by scanning tunneling spectroscopy (STS). On magnesium oxide, different color centers, i.e., F^0, F^+, F^{2+} and divacancies, have different effects on the contact potential. These differences enabled classification and unambiguous differentiation by KPFM. True atomic resolution shows the topography at line defects in aluminum oxide. At these domain boundaries, STS and KPFM verify F^{2+}-like centers, which have been predicted by density functional theory calculations. Thus, by determining the contact potential and the electronic structure with a spatial resolution in the nanometer range, NC-AFM and STM can be successfully applied on thin oxide films beyond imaging the topography of the surface atoms.

Review
Introduction

The chemical properties of many crystal surfaces, especially oxides, are significantly influenced by defects in the perfectly ordered structure [1-5]. These defects can be impurities in the surface, interstitials, vacancies or adsorbates. Furthermore, any deviation from the crystalline pattern constitutes such a defect [6]. These defects in the pristine surface may be generated by

bombardment with particles, irradiation or contamination with adsorbates. Defects may also be generated during growth. For instance, defects in thin films may be caused by a lattice mismatch between film and substrate. This may result in a rather frequent and sometimes regular occurrence of the defects. Defect types can be conveniently classified by the dimensionality of their spatial extension, i.e., as point, line and planar defects. Apart from perturbations of the topography and the stoichiometry, most defects exhibit special electronic structures, which significantly differ from the pristine surface. In many cases, it is exactly this deviating electronic structure which produces various special properties of the surface. For example, defects are often preferred adsorption sites and hence are particularly chemically active. Electrically charged defects may enable electron transfer processes, which play an important role in chemical reactions in general and in heterogeneous catalysis in particular. A sketch of a binary oxide surface including several point defects is shown in Figure 1. These point defects could be color centers, where the site of a missing oxygen atom may be empty or occupied by one or more electrons.
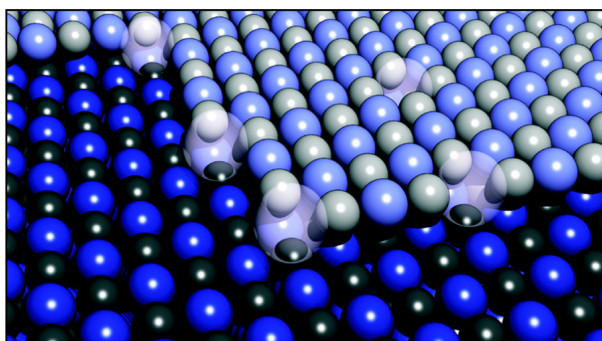

Figure 1: Model of a binary oxide surface. Point defects such as color centers, which are preferably situated at lower coordinated sites, are sketched as bright clouds.

In this publication, we review the recent work of our group, where the structure and the topography of defects in oxide surfaces was studied by non-contact atomic force microscopy (NC-AFM) and scanning tunneling microscopy (STM). Furthermore, the contact potential was determined by Kelvin probe force microscopy (KPFM). This technique has a high spatial resolution, thus avoiding averaging over various defects. Here, we confine ourselves to different point defects in magnesium oxide and to line defects in aluminum oxide. Both samples were prepared as thin films on metal supports. As a consequence, STM and scanning tunneling spectroscopy (STS) can be performed and conclusions about the electronic structure of the defects and the pristine film can be drawn. This enables a direct comparison with NC-AFM results. The application of NC-AFM

and KPFM in combination with STM and STS allows a detailed investigation of the topography as well as of the contact potential and the energetic structure of the defects.

Experimental setup: dual mode NC-AFM/STM

The employed scanning probe microscope, i.e., a NC-AFM in combination with a STM, was optimized for surface investigation on the atomic scale with spatial resolution of some picometers. Note that NC-AFM is frequently referred to as frequency modulation atomic force microscopy (FM-AFM) or dynamic force microscopy (DFM).

For the stability of tip and sample as well as for the reduction of piezo creep, piezo hysteresis, thermal drift and noise level, the setup was operated in ultrahigh vacuum (UHV) at low temperature (5 K). The resulting high stability makes atomic resolution on conductors [7] as well as on insulators [8] possible. In addition to investigations on the surface topography, site specific spectroscopy measurements can be performed [8]. The whole setup is placed in a sound absorber cabin and is carried on a wooden frame, which, in turn, is based on an active vibrational damping system. The background pressure in the UHV chamber is below 4×10^{-8} Pa. The microscope stage is cooled down with a liquid helium bath cryostat (Figure 2a). A so-called exchange gas canister is situated between microscope compartment and helium bath. The exchange gas canister is filled with helium gas to a pressure of about 1000 Pa. The helium gas establishes thermal coupling between the microscope stage inside the UHV chamber and the liquid helium inside the bath cryostat. In addition, the vibrations caused by the evaporating helium inside the bath cryostat are decoupled from the microscope.

The dual mode NC-AFM/STM sensor (Figure 2c) is situated on a tripod scanner opposite the sample. The scanner, in turn, is mounted onto a coarse approach unit (walker). The microscope stage is shown in Figure 2b. The coarse approach is driven by the shear stack piezos. If the tip-sample distance reaches the range of interatomic forces or the tunneling regime, the walker is switched off and the scan is performed by the x, y and z piezos. An additional excitation piezo oriented along z excites the tuning fork at resonance. The tuning fork sensor is presented in Figure 2c. The tuning forks were made of quartz (SiO_2) and are, therefore, piezo electric devices. Because of their very stable oscillation properties upon electric excitation, they are widely used in watches. Commercial tuning forks have often a resonance frequency of 32768 Hz ($=2^{15}$ Hz). In the employed setup, one prong of the tuning fork is glued onto the carrier. A $Pt_{0.9}Ir_{0.1}$ wire, 250 μm in diameter, is attached to the other prong as a tip. The use of a non-conducting glue electrically
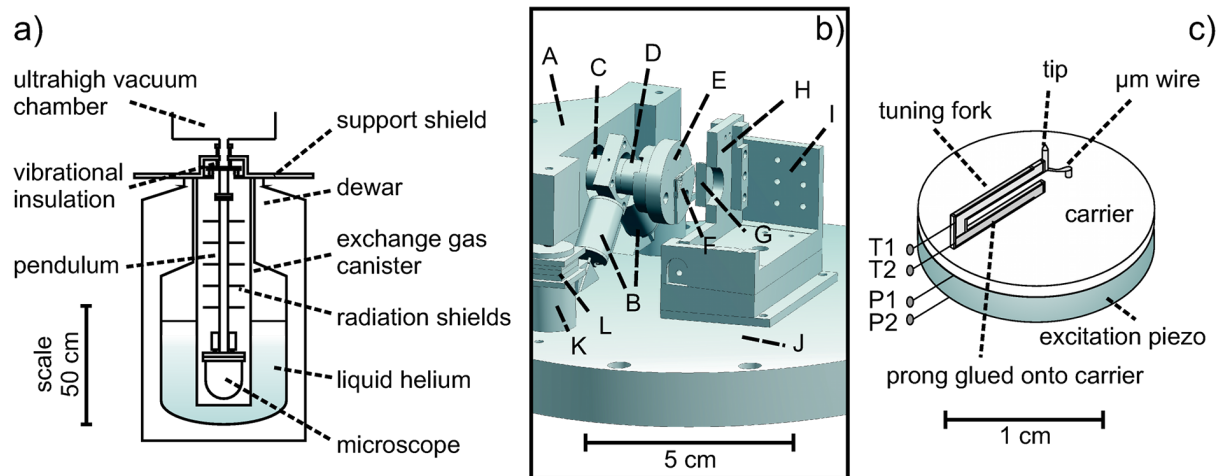
Figure 2: Experimental setup. a) Schematic of an Eigler-style bath cryostat. b) The walker unit is situated on three shear stack piezos for the coarse approach. The *x*, *y* and *z* piezos are used during the scan process. The tuning fork is located opposite the sample (only half of the sample is drawn to keep the view free to the sensor carrier). Schematic of the microscope on its support stage: (A) walker unit, (B) *x*, *y* piezo and (C) *z* piezo of the tripod scanner unit, (D) *z* dither piezo, (E) sensor carrier, (F) tuning fork assembly, (G) sample (not fully drawn), (H) sample holder (not fully drawn), (I) sample stage (not fully drawn), (J) microscope stage, (K) walker support and (L) shear stack piezos. The base plate has a diameter of 10 cm. c) The NC-AFM/STM tuning fork sensor is glued onto the carrier made of MACOR. Contacts P1 and P2 are the contacts of the excitation piezo. The signal from the tuning fork is detected via contact T1 and T2. The µm wire attached to the tip conducts the tunneling current.

insulates the tip from the tuning fork and prevents cross talk. Due to the fixed prong and the additional mass of the tip at the other prong, the resonance frequency drops to about 22 kHz.

The tuning fork is driven by the excitation piezo. Due to the piezo electric effect, the signal of the resonance frequency can be detected at the electrodes of the tuning fork. The amplitude of the signal is proportional to the oscillation amplitude of the tuning fork. The signal is so small that a low-temperature amplifier has to be placed nearby to improve the signal-to-noise ratio. In NC-AFM, the shift of the tuning fork resonance frequency Δf is used as a feedback signal to scan with constant Δf. The tip is electrically connected to a wire, 50 µm in diameter (see Figure 2c). Using this electrical contact, a bias voltage can be applied between tip and sample and a tunneling current I_t can be measured. I_t serves as a feedback signal when operating in the STM mode at constant current. While operating in one of the modes, NC-AFM or STM, the other channel can always be co-recorded. Great care was taken to ensure that both channels, NC-AFM and STM, were electrically separated from each other in order to prevent cross talk.

The great advantage of this setup is the simultaneous data acquisition of the frequency shift and the tunneling current, making it a powerful tool for high resolution real space analysis at the atomic level and merging the strengths of both techniques. The combination of both techniques enables the detection of contaminants on the tip. For instance, insulating contam-

inants cause a shift of the minimum of the Δf signal to larger tip-sample distances, whereas I_t is not influenced. In general, it is interesting to measure both signals as they complement each other and the use of the very same microscopic tip enables direct comparison. Pairs of curves from both channels recorded in a sweep in *z* direction and another one recorded at varying bias voltage are shown in Figure 3.

Spectroscopic methods: tip-sample forces in NC-AFM

In surface science, forces detectable by NC-AFM in UHV at low temperature have been classified into three main categories [9]. The first category has an electrostatic origin and covers forces between charges, also known as Coulomb forces. These forces arise from the interaction between charges, permanent dipoles and higher order moments. Polarization forces are the second category. These forces cause dipole moments in atoms or molecules, which are induced by electric fields of charges and of permanent or induced dipoles. The third category covers bonding forces, which have a quantum mechanical nature. These forces lead to charge transfer processes as involved in covalent bonding. Furthermore, this category includes the repulsive exchange forces, which are caused by the Pauli exclusion principle. These repulsive forces balance and prevail the attractive forces at very short distances. The classification into these three groups is neither rigid nor exhaustive. For example, van der Waals force, which falls into category two, is a general consequence of the zero-point energy in quantum mechanics
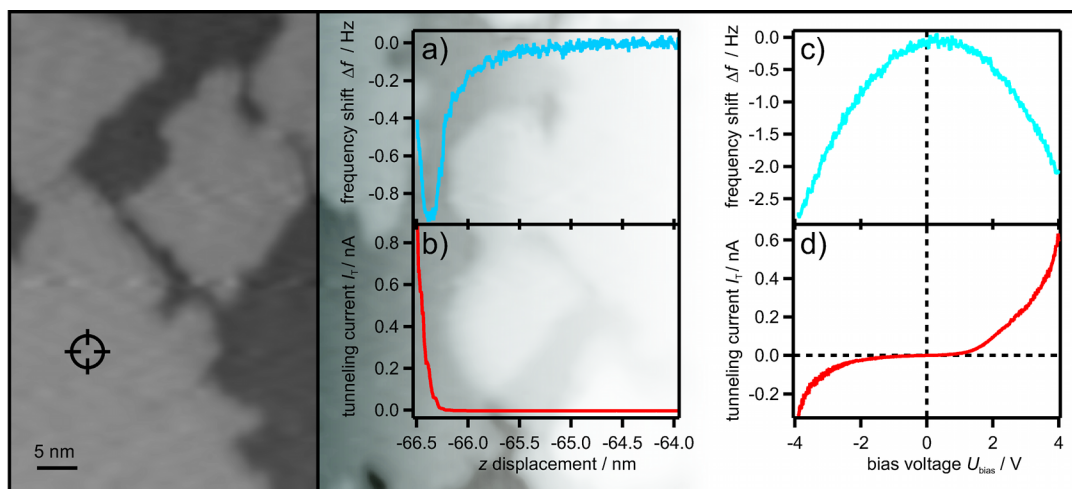
Figure 3: The same tip senses both signals. (a–d) Pairs of simultaneously recorded signal curves from the frequency shift and the current channel: (a,b) signal–distance curves at constant bias voltage, (c,d) signal–bias voltage curves at constant height. On the left-hand side, a STM image of the MgO film recorded with a bias voltage of +3.5 V and a tunneling current of 100 pA is shown. The tip position for the spectroscopy is indicated.

[10,11]. Furthermore magnetic forces, friction forces, capillary forces etc. can in principle occur in NC-AFM. These forces are not relevant in this paper, since, e.g., a magnetic tip is necessary to detect magnetic forces, or non conservative forces have to be measured to determine friction forces.

The forces relevant in this work are described below. Coulomb forces are a result of interacting charges and can be stronger than most chemical binding forces [9]. The Coulomb potential E_{Coulomb} between two charges Q_1 and Q_2 is given by

$$E_{\text{Coulomb}}(z) = \frac{Q_1 Q_2}{4\pi\varepsilon_0 \zeta z} \ , \tag{1}$$

where ε_0 is the permittivity constant, ζ is the relative permittivity or dielectric constant of the medium and z the distance between the charges. The Coulomb force F_{Coulomb} is given by

$$F_{\text{Coulomb}} = -\frac{dE_{\text{Coulomb}}}{dz} = \frac{Q_1 Q_2}{4\pi\varepsilon_0 \zeta z^2} \ . \tag{2}$$

It is well known [12] that for very small amplitudes, the shift of the resonance frequency Δf corresponds to the derivative of the tip-sample forces with respect to z. For larger amplitudes, a more general relation can be derived [12], which is not always proportional, however, strictly monotonic. Consequently, the tip-sample forces and potentials can be determined by recording Δf with NC-AFM.

Via detection of electrostatic forces, contact potentials can be determined by NC-AFM in the KPFM mode [13-16], which is

named after Lord Kelvin, who measured contact potentials in a similar way [17]. The contact potential (CP) results from the alignment of the Fermi levels of tip and sample having different work functions. The tip-sample geometry can be considered as a capacitor, resulting in the following equation for the electrostatic energy E_{el}, which together with the non-electrostatic interaction such as a Lennard-Jones potential adds to the total energy, [18,19]

$$\begin{aligned} E_{\text{el}} &= E_{\text{charge}} - E_{\text{VS}} \\ &= \frac{n^2 e^2}{2C_\Sigma} + \frac{C_1 C_2 U^2}{2C_\Sigma} - \left[ne\frac{C_1}{C_\Sigma}U + \frac{C_1 C_2 U^2}{C_\Sigma} + \frac{C_0}{2}U^2 \right] \\ &= \frac{n^2 e^2}{2C_\Sigma} - ne\frac{C_1}{C_\Sigma}U - \frac{C_1 C_2 U^2}{2C_\Sigma} - \frac{C_0}{2}U^2 \ . \end{aligned} \tag{3}$$

E_{charge} is the energy due to electrostatic charging and E_{VS} is the work done by the voltage source. Furthermore, $C_\Sigma(z) = C_1(z) + C_2$, with $C_1(z)$ is the capacity between the tip and a defect on the surface, C_2 is the capacity between the defect and the substrate and C_0 is the capacity between the tuning fork back electrodes and the surface. The voltage between tip and sample is given by

$$U = U_{\text{bias}} - \frac{\Delta\Phi_{\text{loc}}}{|e|} \ .$$

U_{bias} is the voltage applied between tip and sample, e the elementary charge, $\Delta\Phi_{\text{loc}}$ the local contact potential and n represents the number of charges e. The derivative of Equation 3 with respect to z results in the electrostatic force given by

4

$$F_{\mathrm{el}} = \frac{1}{2}\frac{\partial C_{\mathrm{S}}}{\partial z}\left(\frac{ne}{C_2} + U\right)^2 + \frac{1}{2}\frac{\partial C_0}{\partial z}U^2 \;,\qquad(4)$$

where C_{S} is given by a capacitor series $C_{\mathrm{S}} = C_1 \cdot C_2/(C_1 + C_2)$. The last term in Equation 4 can be neglected when high resolution is considered, since the electrostatic force between the substrate and the tuning fork's back electrodes integrates a large surface area [18].

In a thin oxide film on a metal support, the surface may contain charges. It is reasonable to introduce an effective contact potential $\Delta\Phi_{\mathrm{eff}}$ [20] which considers the shift of the contact potential of the pristine materials due to the charges in the surface, i.e., $\Delta\Phi_{\mathrm{eff}} = \Delta\Phi - ne^2/C_2$. This results in

$$F_{\mathrm{el}} = \frac{1}{2}\frac{\partial C_{\mathrm{S}}}{\partial z}\left(U_{\mathrm{bias}} - \frac{\Delta\Phi_{\mathrm{eff}}}{|e|}\right)^2 \;.\qquad(5)$$

Tip and sample are not directly in contact but they are electrically connected via the electronics. The electrical contact leads to an alignment of the Fermi levels of tip and sample. In Figure 4a tip and sample are not electrically connected, thus, the vacuum levels are equal and the Fermi levels do not align. In Figure 4b tip and sample are electrically connected and electrons from the material with the lower work function (here tip) flow to the material with the higher work function. The Fermi levels align and an electrical field is built up [21]. The contact potential $\Delta\Phi$ is then given by the difference in work function of the tip and of the sample surface, which may contain the studied defects. By applying a bias voltage and thus reversing the charge transfer between tip and sample, the effective contact

potential can be obtained as the point of minimal force (see Figure 4c). The advantage of KPFM compared with, e.g., photoelectron spectroscopy is the high local resolution down to single point defects or single adsorbates, instead of integrating over a square millimeter range. However, absolute values of the work function cannot be measured directly, only work function differences.

Point defects

Oxygen vacancies, also known as color centers, are electron trapping point defects and are supposed to be involved in electron transfer processes on the surface. The trapped electrons in the color centers can be transferred to adsorbates such as Au atoms. The defect-free MgO surface is quite inert while a defect rich surface shows a high and complex chemical reactivity [22]. In order to understand possible reaction pathways, a detailed characterization of color centers is highly desirable. Information about their local position and thus coordination, electronic structure, local contact potential and possible adsorbate interaction are of fundamental interest. In the following, color centers on the MgO surface are investigated in detail and classified by their charge state. From calculations it has been proposed that color centers are directly involved in chemical reactions [23,24], e.g., as adsorption sites due to more attractive defect-adsorbate interactions compared with the pristine MgO surface. It is also experimentally investigated whether color centers are attractive or repulsive in comparison to the surrounding MgO lattice.

Sample system: magnesium oxide on Ag(001)

An NC-AFM image of a perfect MgO surface is shown in Figure 5. The film is two atomic layers thick, however, films with a thickness of two to eight layers give very similar images.

Figure 4: Energetic levels. a) The Fermi levels of tip and sample when they are not electrically connected. b) Tip and sample are electrically connected and the Fermi levels align resulting in an electrostatic field. c) If the sample bias voltage corresponds the contact potential, i.e., $U_{\mathrm{CP}} = \Delta\Phi/e$, the electrostatic field is canceled.
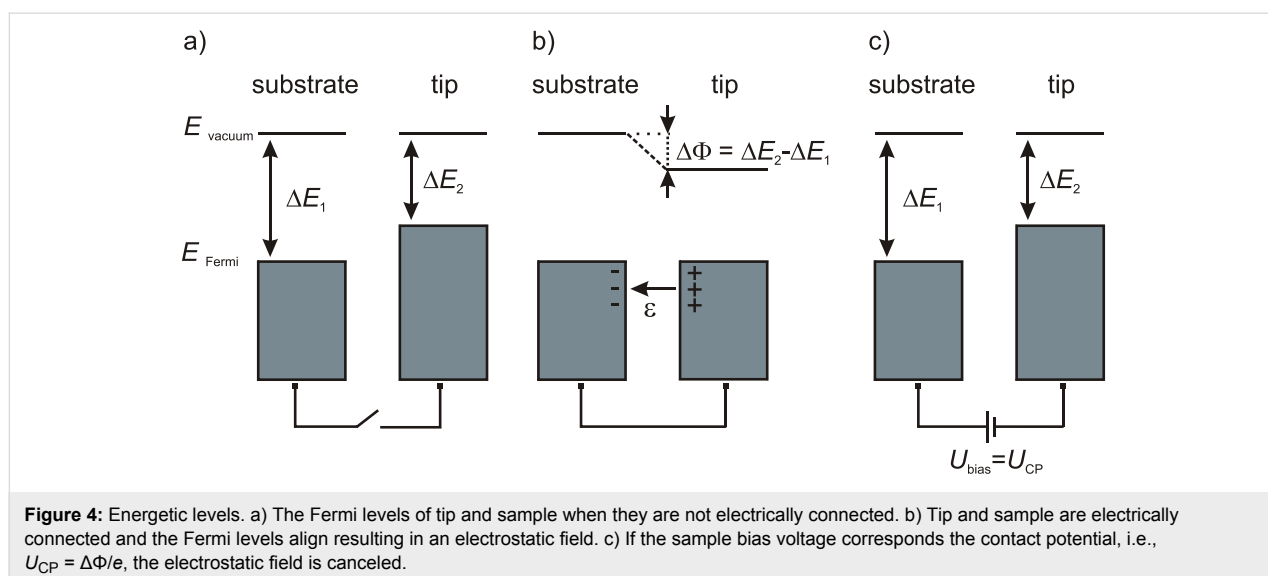
One type of ion is shown as a protrusion while the other type of ion is depicted as a depression. This is a typical finding for ionic surfaces imaged by NC-AFM [25,26]. Since the density of electrons on the MgO surface is the highest above the oxygen atoms [27], the maxima in the NC-AFM image are thought to correspond to the positions of the oxygen atoms. Furthermore, electron paramagnetic resonance (EPR) spectra have shown that the preferred adsorption sites for Au atoms are on top of the oxygen ions on the terrace of the MgO surface [26]. Assuming that the forces acting on such metal adatoms are comparable to those on the tip apex, one may conclude that a more attractive interaction occurs between the oxygen sites and the tip. This results in a contrast where oxygen atoms are imaged as protrusions in a constant Δf NC-AFM image.
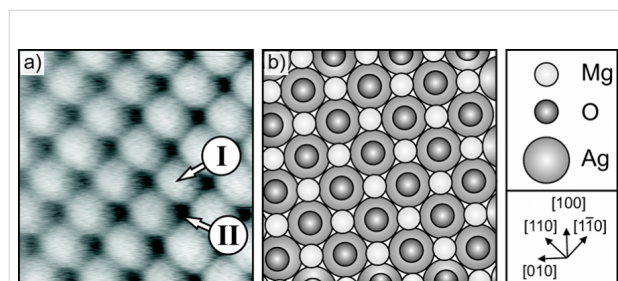

Figure 5: Magnesium oxide surface. a) Atomically resolved image recorded by NC-AFM. The position I and II indicate the two different surface atoms, oxygen and magnesium. The size is 1.5 nm x 1.5 nm and the corrugation approximately 30 pm. $\Delta f = -8.5$ Hz, $A_{osc} = 0.35$ nm. b) Schematic growth model of the MgO on Ag(001). The oxygen atoms occupy top sites, while the magnesium atoms occupy hollow sites [8].

The preparation conditions of the MgO film on Ag(001) follow a route described in [28], where a stoichiometric composition was observed. This procedure has proven its applicability in many successful preparations. The Ag(001) was sputtered with Ar^+ ions at a current density of 10 μA/cm^2 and an acceleration voltage of 800 V for 15 min. Afterwards, the Ag(001) was annealed at 690 K for 30 min. The sputtering and annealing cycle was repeated several times. Mg was evaporated from a Knudsen cell in an oxygen atmosphere of 1×10^{-4} Pa at a substrate temperature of 560 K and a deposition rate of about 1 ML of MgO/min. A certain amount of MgO can be grown onto the Ag(001) by linear extrapolation of a sub-monolayer coverage to the desired number of monolayers, assuming a constant sticking coefficient. This preparation method is only possible since the reaction kinetics of Ag with oxygen is very slow [29] compared with the reaction between Mg and O. Since the intrinsic defect density of the film is very small, color centers, such as F^0, F^+ and F^{2+}, have been generated by operating the microscope in the STM mode at high currents $I_t = 6$ nA and high voltages $U_{bias} = 7$ V or higher. Clean and well grown MgO areas have been selected to ensure defined conditions. The defects are preferentially located at kinks, corners and step edges (for an illustration see Figure 1). This means defect sites with a lower coordination number are preferred. An NC-AFM image of an MgO step edge with point defects is shown in Figure 6.

Color centers in magnesium oxide

The high local resolution of the NC-AFM image shown in Figure 5 serves as the starting point for adsorbate-defect interaction studies. The tip, representing the adsorbate, scans laterally across the defect positions at constant height along the step direction. The simultaneously measured frequency shift Δf and tunneling current I_t give insight into the local surface potential as well as into the local electronic structure. The corresponding results of such an experiment are shown in Figure 7, where the
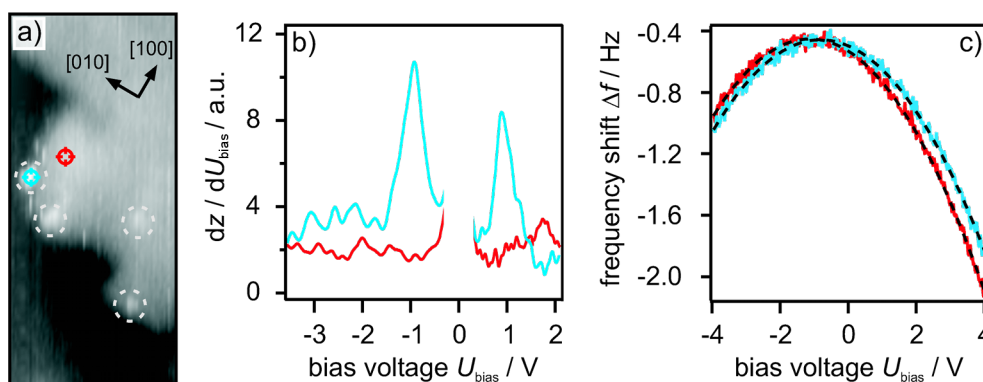
Figure 6: Spectroscopy on point defects. a) NC-AFM image of 21 nm × 9 nm measured at a frequency shift of $\Delta f = -1.6$ Hz , an oscillation amplitude of $A_{osc} = 0.34$ nm and $U_{bias} = -50$ mV. Defects are indicated by circles. The position of the spectroscopy in b) and c) is indicated red and blue. b) STS on MgO. There are no states in the MgO-film (red), whereas electronic defect states (blue) at approximately +1 V and −1 V exist. c) Frequency shift vs bias voltage spectroscopy shows a quadratic dependence at the MgO-film (red) and at the defects (blue). The maxima have different bias voltages.
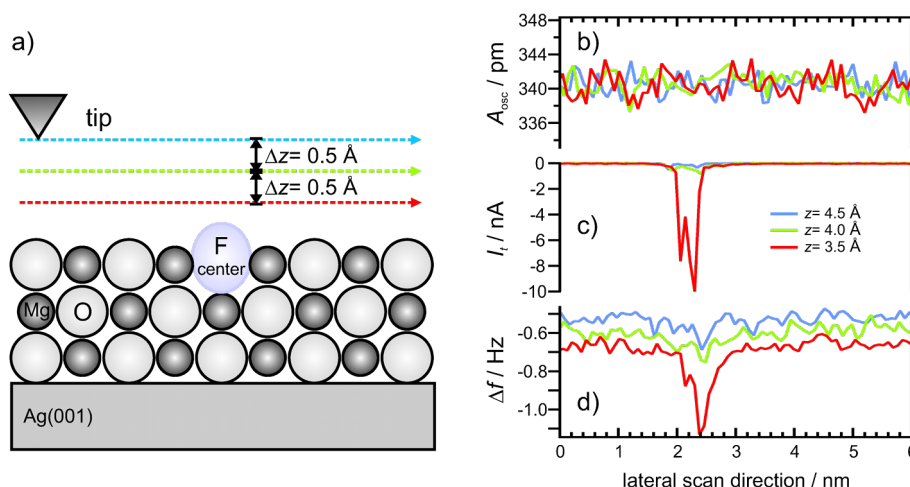
Figure 7: Dependence on tip-sample distance. Constant height line-scans across an F^0 defect situated at a step edge. The scan direction is along the step edge. The three presented channels have been measured simultaneously. The colors indicate different tip-sample distances. Note that the displacement of 4.5 Å has been chosen arbitrarily, since absolute values are generally unknown in scanning probe microscopy. b) The oscillation amplitude is constant during scan process. This excludes artefacts in frequency shift. c) The tunneling current and d) the frequency shift. Data were obtained at a bias voltage of $U_{bias} = -50$ mV.

tip scanned across an F^0 defect. The three stacked graphs show the simultaneously recorded oscillation amplitude, the frequency shift and the tunneling current. The colored traces indicate constant height scans at different tip-sample separations. At all tip-sample distances the oscillation amplitude can be considered as constant, which is a prerequisite, since the frequency shift scales with the amplitude [12].

Due to the exponential dependence of the tunneling current on the tip-sample distance, I_t vanishes at the largest separation and the shift of the resonance frequency is a consequence of the long range force background arising from electrostatic and van der Waals forces. The averaged frequency shift at the largest separation is about $\Delta f = -0.52$ Hz. By decreasing the tip-sample distance by 0.5 Å, the absolute value of the tunneling current and the frequency shift increase at the position of the defect. The tunneling current increases to $I_t = -0.5$ nA and the frequency shift to $\Delta f = -0.75$ Hz above the defect. Decreasing the tip-sample separation by another 0.5 Å results in a tunneling current of $I_t = -9.9$ nA and a frequency shift of $\Delta f = -1.13$ Hz at the defect site. Despite the decrease of 1.0 Å in tip-sample distance, the average tunneling current on the regular MgO terrace remains below $I_t = -0.05$ nA. The frequency shift changes by 0.15 Hz with decreasing tip-sample distance. This experiment demonstrates the highly attractive interaction of the tip (or adsorbate) with an F^0 center.

It has been debated in literature how color centers are imaged by NC-AFM [25,30] since a color center is a hole in the MgO lattice [22]. The observed attraction of F^0 centers originates

from the charge density of the two trapped electrons, which are located in the center of the defect site. Due to Coulomb repulsion, the trapped electrons repel each other and spill out of the defect site into the vacuum [31]. Therefore, a considerably large charge density is situated above the surface. This charge density is supposed to interact with the tip resulting in a strong attraction, as presented in Figure 7. Since the doubly occupied F^0 state is close to the Fermi level of the MgO/Ag(001) system [32], the charge density is also responsible for the strong peak in the tunneling current signal. Further insights into the interaction of tip and color center are obtained by periodic supercell DFT calculations at the level of the generalized gradient approximation as implemeted in the VASP code, which have been performed in the group of G. Pacchioni [33-35]. The $Pt_{0.9}Ir_{0.1}$ tip has been modeled by a tetrahedral Pt_4 cluster, whose geometry has been relaxed separately. The F^0 color center has been created by removing an O atom from the top layer of a three layer MgO slab. The structure of the slab with the color center has been relaxed. The tip-surface interaction energy has been computed as a function of tip-sample distance of the apical Pt_4 cluster with respect to the top layer of the MgO slab (see Figure 8d). During these calculations the separately optimized tip structure was not allowed to relax. However, the relaxation of the MgO surface has been found to be very small for the calculated distances, where no direct contact is established. The outward relaxation of the O anion at 3.5 Å is about 0.12 Å.

The results of the experimental distance dependent measurements and the corresponding theoretical results are presented in
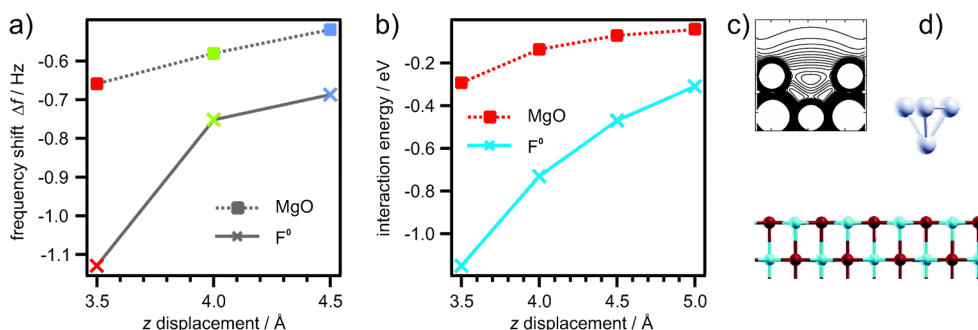
Figure 8: Dependence on tip-sample distance. a) Shift of the resonance frequency of a $Pt_{0.9}Ir_{0.1}$ tip on a regular MgO surface (squares) and above an F^0 defect site (crosses). Experimental data are derived from the constant height measurements shown in Figure 7. The frequency shift is a direct consequence resulting from potential gradients between tip and sample. The integration of the frequency shift is related to the potential energy. b) Interaction energy of a Pt_4 cluster above the O site of an MgO surface (rectangles) and above an F^0 defect center (crosses) calculated by DFT. c) The spill over of the electron charge density of an F^0 center calculated by DFT. d) The Pt_4 cluster above the MgO surface [35,36].

Figure 8. At the defect site, the tip-sample interaction increases significantly with decreasing distance. From a structural point of view the positions of the defects are "holes", i.e., missing oxygen atoms in the lattice. In the first place it is unknown which type of color center, F^0, F^+ or F^{2+}, is imaged on the MgO surface. To gain further insight into the nature of the color centers we performed high resolution KPFM measurements with single point defect resolution (Figure 6). To acquire Δf vs U_{bias} curves on top of a defect, the Δf feedback was switched off. Subsequently the frequency shift vs applied bias voltage was plotted and compared to equivalent reference measurements at the same height close to the defect. The parabolic

behavior of the frequency shift curves has been analyzed with Equation 5. The electrostatic force is always attractive. This results in the parabolic dependence of the forces (see Equation 5). The maximum of the parabola depends on the local effective contact potential $\Delta\Phi_{eff}$. It has been found that the MgO thin film shifts the Ag(001) work function and thus the contact potential by about 1.1 eV. This MgO level is set as the reference level and relative shifts are related to it. From measurements of numerous defects four different types were distinguished by their contact potential, which corresponds to the maximum position of the frequency shift vs bias voltage parabola. The results are shown in Figure 9. On the left-hand
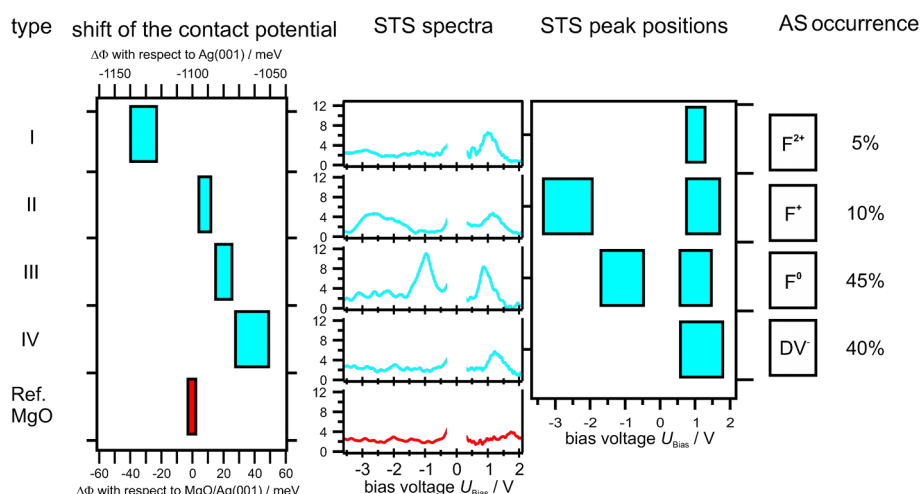
Figure 9: Color centers on MgO. The left labeling assigns numbers to the defect types. The left graph shows the relative shift of the local (effective) contact potential with respect to the MgO surface (bottom abscissa) and with respect to the Ag(001) level (top abscissa). The covered range in the shifts results from measurements with different local resolutions due to different tip structures. The energy level scheme presents the different energy levels of the defect types and their local contact potential shifts. The central graph shows STS spectra of the respective defects. The right graph presents the maxima of the STS data. The covered abscissa range accounts for the statistics of the peak positions. The assignment (AS) of defect types to color centers and negatively charged divacancies (DV⁻) according to theory as well as their relative occurrence are given on the right hand side.

side of Figure 9 the four types are indicated by numbers and the MgO reference level is given (red bar). The graph on the left-hand side represents the measured contact potential with respect to the reference MgO level (bottom abscissa) and with respect to the Ag(001) level (top abscissa).

For type I defects shifts of −50 to −25 meV below the MgO level were observed. These significant shifts can be explained by the presence of positively charged defects with respect to the surrounding area resulting in a decrease of the local contact potential. The charge density distribution is significantly reduced at the positions of the defects compared with the surrounding MgO lattice. The presence of charges localized at defect sites induces a contact potential shift of the MgO/Ag(001) in analogy to the Helmholtz equation $\Delta\Phi = 4\pi e\mu\sigma$ [37]. Where μ is the dipole moment induced by the localized charge at the site of the defect and the screening charge in the Ag(001) substrate and σ is the surface concentration. However, the full complexity is not covered by the Helmholtz equation and detailed calculations are still desired. Defect type II shows a contact potential shift of $\approx +9$ meV. This shift can be assigned to an F^+. For an F^+ the overall charge is positive, but on a very local scale the single electron has a probability above the surface as derived by density functional theory calculations [31]. The charge density spills out of the defect's site and has therefore a probability above the surface. The spill out of the negative charge changes the local dipole moment such that the local contact potential increases compared with the MgO/Ag(001) reference level. The electron charge is symmetrically distributed along the surface normal with its charge maximum located in the center of the defect. Defect type III results in a shift of about +15 to +20 meV above the MgO level. The shift results from two charges present in a defect site and is thus attributed to an F^0 color center. An F^0 is neutral compared to the surrounding MgO lattice, but the two electrons have a large probability density above the surface due to Coulomb repulsion. The charges are as for type II symmetrically distributed and located in the center of the defect, see Figure 8c. Therefore, the charge does not belong to any Mg^{2+} site surrounding the defect. Thus, the oxidation state of the surrounding lattice is not affected by the trapped charges. The spill out of the charges results in a stronger dipole moment compared to defect type II and the measured shift is about twice as large as that for defect type II.

The strongest positive shift on the relative scale is that of type IV. The strong shift indicates that negative charges are involved. Therefore, this shift might result from divacancies (DV) or OH groups trapped at low coordinated Mg^{2+} sites. It is known that OH groups can trap electrons [38]. However, OH groups and other adsorbates can be excluded since all defects

occur only after high voltage and high current scanning and are not present on regular terraces and steps. With the above mentioned scan parameters, adsorbates would be removed from the scan area. Furthermore, the defects occur only within the high current scan frame and not outside. Favored candidates are, therefore, divacancies formed at step and corner sites since the formation energy at these sites is the lowest. The stability of divacancies and their electron affinity have been confirmed by DFT calculations [39]. A divacancy is neutral compared with the surrounding MgO, since a complete Mg-O unit is missing. Due to the electron affinity of 0.6–1 eV, electrons can be trapped by the DV from the tunneling junction and the DV becomes negatively charged. The trapped electron of the DV^- is strongly localized at the Mg^{2+} site due to the attractive Coulomb interaction. Since the DV^- is negatively charged with respect to the surrounding MgO area, the additional dipole moment will increase the work function resulting in the largest positive shift on the relative scale. The covered ranges in the maximum positions originate from different tip structures, however, the reproducibility for two subsequent measurements with the same microscopic tip is within ±2 meV. All defect types analyzed show a characteristic *fingerprint* due to different charge states.

The measurements based on NC-AFM are supported by complementary STS. For all defects the local density of states (LDOS) has been detected. The tunneling spectra measurements have been performed directly after the local contact potential measurements without moving the tip laterally, i.e., STS and KPFM have been performed with the same microscopic tip configuration. To prevent tip changes when carrying out STS at high voltages, the feedback on the tunneling current was switched on and dz/dU_{bias} was detected. The dz/dU_{bias} vs U_{bias} spectrum at constant tunneling current I_t is similar to the dI_t/dU_{bias} vs U_{bias} spectrum at constant height z, see [40].

The tunneling spectra measured on the defects are compared with MgO spectra on the terrace next to the defect. The MgO reference spectra show no peaks within the voltage regime due to the band gap (compare red lines in Figure 9). The spectra taken on the F^{2+} only show peaks in the unoccupied regime at voltages of $\approx +1$ V above the Fermi level (see Figure 9). The F^+ centers have both occupied and unoccupied electronic states within the band gap. The electronic states are located within the band gap of MgO. The occupied states are quite broadly distributed from −3.5 V to −2.0 V below the Fermi level, depending on the defect location on the film [32]. The empty states are at $\approx +1$ V above the Fermi level. Considering the F^0 color center, the doubly occupied state is higher in energy, approximately −1 V below the Fermi level, while the position of the unoccupied state is similar to F^+ centers.

The negatively charged divacancies only show a clear feature in the empty states at about +1 V. The corresponding occupied shallow state is expected to be very close to the Fermi level, i.e., in a region where the experiment cannot clearly detect states. However, F^0 and DV^- are equally frequent and represent $\approx$85% of the total defects. F^+ color centers are much less frequent and represent $\approx$10% and F^{2+} centers about 5%. These findings are in good agreement with the high formation energies of F^{2+} centers. By comparing the STS peak positions in Figure 9, it becomes obvious that F^{2+} and DV^- defects are hardly distinguishable by their electronic structure but show a significant difference in the local contact potential due to the effect of a locally trapped charge on the surface dipole. This demonstrates the great benefit of NC-AFM and KPFM in combination with STM and STS.

Line defects

Apart from point defects more complex structures like line defects are found on oxide surfaces. Line defects can be caused by step edges or grain boundaries that penetrate the surface. In thin oxide films line defects are often generated by domain boundaries. The structure at these line defects usually differs significantly from the defect-free domains. This is often associated with a change of electronic properties, which may significantly influence the surface chemistry.

Sample system: aluminum oxide on NiAl(110)

Thin film aluminum oxide on NiAl(110) is composed of two oxygen and two aluminum layers limiting the film thickness to 0.5 nm [41]. It is prepared in a reliable and simple two step oxidation procedure. After dosing 5×10^{-4} Pa oxygen at 550 K for

10 minutes, the sample is heated to 1050 K in vacuum to crystallize the oxide film. This process may be repeated to close open metal patches in the film. The preparation is explained in detail in [42]. The film grows in two reflection domains, A and B. The long edges of the parallelogram shaped unit cells (1.055 nm × 1.788 nm, α = 88.7°) are rotated by ±24° with respect to NiAl[1$\overline{1}$0].

Antiphase domain boundaries in aluminum oxide

The most common structural defects in the thin film aluminum oxide on NiAl(110), besides substrate induced step edges, are reflection domain boundaries (from domain A to B or vice versa) and antiphase domain boundaries (abbrev. APDBs; A-A or B-B). The latter are translation domain boundaries originating from strain relief and introduced into already existing oxide patches. For this film system their denotation as APDBs is common usage due to historical reasons and to distinguish them from boundaries between nucleation related translation domains. While the reflection domain boundaries occur less frequent, APDBs occur regularly, approximately every 8–10 nm to release stress in the aluminum oxide film that accumulates due to a small lattice mismatch with the NiAl(110) surface along the [1$\overline{1}$0] direction.

Different types of APDBs exist, the most common types are straight (type I) and zigzagged (type II) APDBs [43,44]. At straight APDBs the surface unit cell is extended parallel to the long edge of the aluminum oxide unit cell. At zigzagged APDBs both directions of the oxide unit cell are extended. For the sake of simplicity, we focus on straight APDBs in this section. A more comprehensive NC-AFM study of the ADPBs
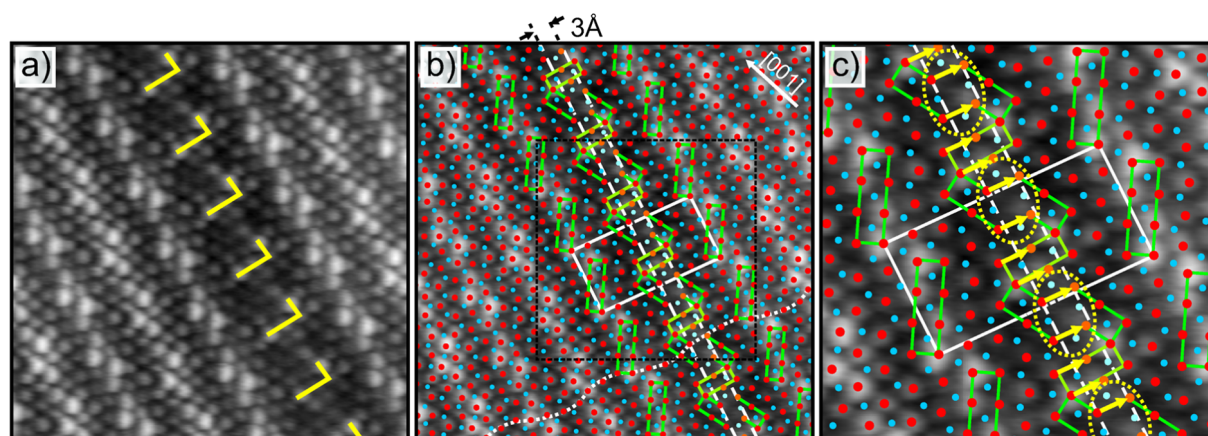
Figure 10: Atomic resolution NC-AFM image of a straight antiphase domain boundary (type I) in the aluminum oxide on NiAl(110). The scan area is 6.4 nm × 6.4 nm in (a) and (b). b) An adjusted model [47] has been superimposed. The unit cell is extended by 3 Å along the long edge of the unit cell. Inserted sites are given in lighter colors. Dashed lines indicate the extension. The dotted line highlights wave-like oxygen rows along the unit cell. c) shows an enlarged section of the image for better visibility (3.5 nm × 3.5 nm). Yellow arrows denote the direction and length (3 Å) of the Burgers vector. Yellow loops indicate spacious arrangements of oxygen sites that are different from all domain sites. Δf = −2.75 Hz, A_{osc} = 3.8 Å, U_{bias} = −220 mV.
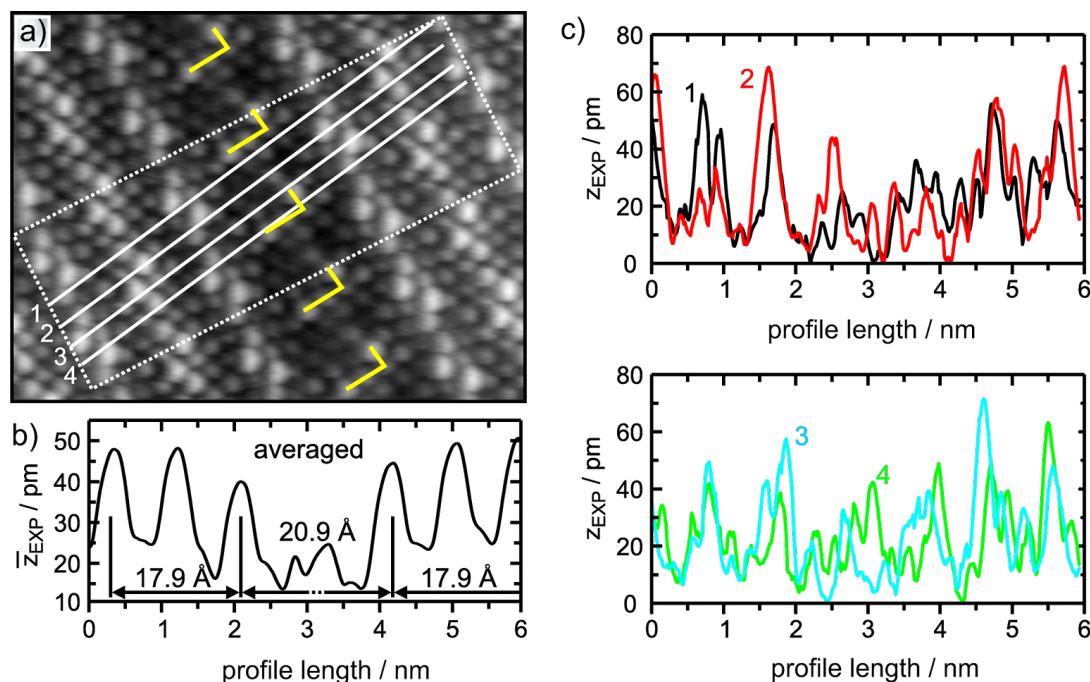
Figure 11: Height profiles. a) Cutout from Figure 10. White lines indicate positions where line profiles have been taken across the type I boundary. b) Averaged line profile taken within the rectangle (two unit cells in width) in the frame above. This emphasizes that such boundaries are reproduced as depressions within NC-AFM images. Averaging was performed over 167 line profiles. c) Single profiles along chains of O atoms across the APDB marked by white lines in the rectangle in (a). Such atom rows show heights different from average terrace height. Only the profile labeled 4 shows nearly no decrease in height over the APDB.

and other line defects on aluminum oxide in NiAl(110) can be found in [43,45,46]. By DFT calculations [47], the stoichiometry of the film with a straight APDB was determined to be $(NiAl)^{2-}_{substrate} (Al_{19}O_{28}Al_{28}O_{32})^{2+}$. An oxygen deficiency with unoccupied electronic states in the aluminum oxide band gap was proposed.

An atomically resolved NC-AFM image of a straight APDB (type B I) is shown in Figure 10. Clearly visible, the boundary is marked by a fairly wide linear depression. The adjusted model for the lateral positions at the APDB [47] is superimposed in Figure 10b and found to be in perfect agreement. From this we see that NC-AFM images the surface oxygen sites of the film with high accuracy. The model is based on a unit cell that has been split in the middle according to STM images. Important structural elements of the oxygen sub-lattice are highlighted as well as the extended unit cell and two equivalent lines between which the inserted new sites are visible. Inserted sites are marked in a slightly different color to distinguish them from the usual sites in the oxide unit cell: orange and light blue as compared to red and blue. In Figure 10c an enlarged section of the elongated unit cell at the APDB is given. In the middle of the APDB a broken block of 8 O atoms appears, which is of the type that is almost aligned with the NiAl[001] direction. A

particularly spacious arrangement of oxygen atoms in the shape of a quadrangle (yellow dotted loops) is formed at this block at the boundary. This is in agreement with DFT calculations [47], which assign an electronic defect state to this structure. Another deviation from the usual oxide unit cell is a rectangle of six oxygen sites which is derived from the bridging square groups indicated in light green in Figure 10c. These characteristic protrusions in the topography of the boundary form the shape of the letter 'L' as indicated by the yellow angle in Figure 10a.

The direction and the length of the lattice discrepancy generated by a dislocation in a crystal is given by the Burgers vector. At straight APDBs this vector measures 3 Å in length and is parallel to the long edge of the oxide unit cell as indicated by yellow arrows. At the same time the Burgers vector is also parallel to the overall direction of the wave-like rows of atoms within the surface aluminum and oxygen sub-lattices (dotted line in Figure 10b). Considering the topographic quality of the contrast, the domain boundary can finally be determined to be a depression. This is summarized in Figure 11. An averaged line profile across the APDB I covering the width of 2 unit cells, as indicated by the rectangle in Figure 11a, is shown in Figure 11b. In Figure 11c individual line profiles across oxygen rows are shown. These profiles have been taken along the white
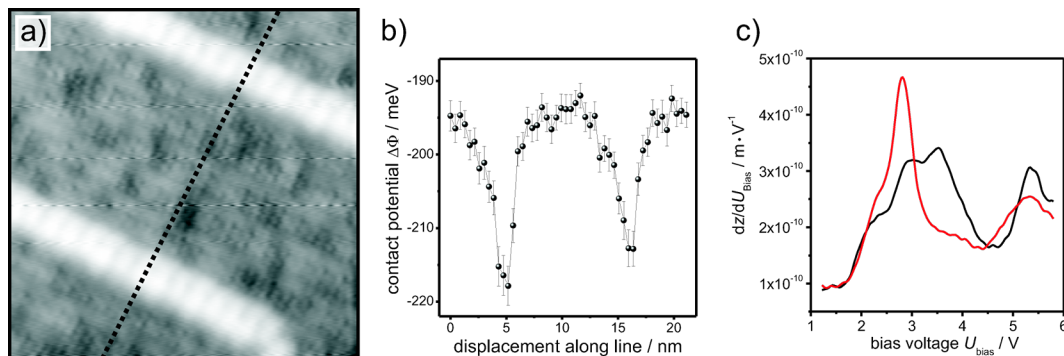
Figure 12: Spectroscopy on aluminum oxide. a) STM image of a thin film of aluminum oxide on NiAl(110), 18 nm × 18 nm. Two straight APDBs (bright) separating three A domains (dark) are visible. U_{bias} = +3 V and I_t = 100 pA. b) Effective contact potential, which was determined at the line shown in (a), decreases at the APDB by approximately 20 meV. The tip height was constant during the measurement and corresponds to a frequency shift of −1 Hz at −150 mV. The contact potentials were determined by fitting the frequency shift vs bias voltage curves with a quadratic term (see Equation 5). The error bars represent the accuracies by which the maxima were determined. c) STS curves taken at the domain (black) and the APDB (red).

lines 1, 2, 3, 4 in the image in (a). At the linear oxygen rows there exist sites with a mean height that is 10 pm lower than the average height of corresponding terrace sites (see Figure 11b).

Knowing the surface structure with highest accuracy, it is still very desirable to determine aspects of electronic structures to gain further insight. In Figure 12, the effective contact potential is plotted for positions along a line across three domains and two straight APDBs. The recorded contact potential at the APDB is approximately 20 meV smaller than at the regular domain, which was verified at many different sites [45]. This means the work function at the APDBs is reduced compared to that of the domain. Comparison of STS curves on domain and APDB shows significant differences in the electronic structures. At the domain boundary a pronounced unoccupied defect state appears at bias voltages between 2–3 V.

The real variation of contact potential may be even larger, since the recorded signal is a convolution of the actual contact potential difference with the tip geometry [48]. The depressions in the contact potential at the APDBs have approximately a full width at half minimum of 3 nm (see Figure 12b). The lateral extension of the APDBs is approximately 1.5 nm and the oxide unit cell is expanded by an additional row of oxygen atoms by 0.3 nm at that position [41]. Assuming the change of the contact potential to be approximately located in this range (between 0.3 and 1.5 nm), the recorded contact potential is broadened by a factor of 2 to 10 due to the convolution with the tip geometry. This means on the other hand, the contact potential difference is actually 2 to 10 times larger than recorded. Furthermore, we conclude that the tip is influenced by these defects over a distance of approximately 2–3 nm, which might be a reasonable estimation of the tip size. This gives also the lateral resolution

of the measurements. As shown in [36] and [49], the determined contact potential difference depends also on the tip-sample distance. In general, a smaller distance increases the size of the interaction and decreases the integration area, this means the determined difference of the contact potential increases. If the distance is too small, the probability that the tip restructures increases. Therefore, the tip-sample distance was set to a moderate value which corresponds to roughly 0.5–0.75 of the maximum absolute frequency shift.

Thin film aluminum oxide reduces the work function on NiAl(110) by approximately 0.5 eV from 4.8 eV for a pure NiAl(110) surface to 4.3 eV for the aluminum oxide film [50]. A further reduction of the work function at the APDBs may explain the higher reactivity at these linear defects. In [51], it has been shown that APDBs are preferred adsorption sites for different atoms and metal clusters. Furthermore, a particular chemical activity at the APDBs has been experimentally verified. For instance, nitric oxide decomposition on thin film aluminum oxide preferentially takes place at the APDBs [52].

It has been predicted by means of DFT calculations [47] that unoccupied defect states in the APDBs of the aluminum oxide film are associated with F^{2+}-like centers. In our NC-AFM measurements, we have recorded a shift of the local work function of approximately −20 meV at the APDB. This is in great agreement with the shift recorded at F^{2+} centers on MgO/Ag(001) (see Figure 9). As it has been shown above, a small shift of the contact potential difference is caused by the fact that the recorded contact potential depends on the tip-sample distance. The recorded change of the work function is in agreement with the DFT calculations, where a shift of the valence and the conduction band with a local band bending at the APDB

were predicted [47]. Thus, in the APDB F^{2+}-like centers, which have been predicted by DFT calculations, are now experimentally verified by NC-AFM.

Conclusion

Defects on surfaces of thin oxide films were studied by means of low temperature NC-AFM combined with STM in UHV. In addition to imaging the topography of the surface termination, STS and KPFM were employed for a deeper insight into the nature of the defects. The spectroscopy was performed with a very high spatial resolution in the order of 1 nm. For magnesium oxide on Ag(001), different point defects, which are the most frequently discussed ones in literature, were studied. Using contact potential measurements by KPFM in comparison to STS spectra and DFT calculations, the point defects on an MgO surface could be unambiguously identified for the first time. The point defects were distinguished as DV^-, F^0, F^+ and F^{2+} color centers. In addition, the electronic signature was measured and electronic defect states were determined within the band gap of the MgO surface. These color centers influence the surface chemistry by significantly increasing the reactivity of the almost inert surface of defect-free MgO. The NC-AFM investigation on aluminum oxide on NiAl(110) unveils the surface structure of the domain and at the APDBs with atomic resolution. Apart from the determined topography, F^{2+}-like centers, which have been predicted by DFT calculations, were experimentally verified for the APDBs. These studies show that NC-AFM in combination with STM can be successfully used beyond imaging the topography of the surface termination. The employed high resolution spectroscopy significantly improves our understanding of the surface chemistry of thin oxide films.

Acknowledgements

References

1. Ertl, G.; Knözinger, H.; Schüth, F.; Weitkamp, J., Eds. *Handbook of heterogeneous catalysis,* 2nd ed.; Wiley-VCH: Weinheim, Germany, 2008; Vol. 2.
2. Freund, H.-J. *Chem.–Eur. J.* **2010,** *16,* 9384–9397. doi:10.1002/chem.201001724
3. Plummer, E.; Matzdorf, R.; Melechko, A.; Zhang, J. *Prog. Surf. Sci.* **2001,** *67,* 17–44. doi:10.1016/S0079-6816(01)00014-4
4. Henrich, V. E.; Cox, P. A. *The surface science of metal oxides;* Cambridge University Press: Cambridge, U. K., 1996.
5. Nilius, N. *Surf. Sci. Rep.* **2009,** *64,* 595–659. doi:10.1016/j.surfrep.2009.07.004
6. Tilley, R. J. D. *Defect crystal chemistry and its applications;* Chapman and Hall: New York, U. S. A., 1987.
7. König, T.; Simon, G. H.; Rust, H.-P.; Heyde, M. *Appl. Phys. Lett.* **2009,** *95,* 083116. doi:10.1063/1.3189282
8. Heyde, M.; Simon, G. H.; Rust, H.-P.; Freund, H.-J. *Appl. Phys. Lett.* **2006,** *89,* 263107. doi:10.1063/1.2424432
9. Israelachvili, J. *Intermolecular & Surface Forces;* Academic Press: Burlington, MA, U. S. A., 1991.
10. Chen, C. J. *Introduction to scanning tunneling microscopy;* Oxford University Press: Oxford, U. K., 2008.
11. London, F. *Z. Phys.* **1930,** *63,* 245–279. doi:10.1007/BF01421741
12. Sader, J. E.; Jarvis, S. P. *Appl. Phys. Lett.* **2004,** *84,* 1801–1803. doi:10.1063/1.1667267
13. Nonnenmacher, M.; Oboyle, M.; Wickramasighe, H. *Appl. Phys. Lett.* **1991,** *58,* 2921–2923. doi:10.1063/1.105227
14. Jacobs, H.; Leuchtmann, P.; Homan, O.; Stemmer, A. *J. Appl. Phys.* **1998,** *84,* 1168–1173. doi:10.1063/1.368181
15. Filleter, T.; Emtsev, K. V.; Seyller, T.; Bennewitz, R. *Appl. Phys. Lett.* **2008,** *93,* 133117. doi:10.1063/1.2993341
16. Kawai, S.; Glatzel, T.; Hug, H.-J.; Meyer, E. *Nanotechnology* **2010,** *21,* 245704. doi:10.1088/0957-4484/21/24/245704
17. Kelvin, W. T. L. *Philos. Mag.* **1898,** *46,* 82–120.
18. Stomp, R.; Miyahara, Y.; Schaer, S.; Sun, Q.; Guo, H.; Grütter, P.; Studenikin, S.; Poole, P.; Sachrajda, A. *Phys. Rev. Lett.* **2005,** *94,* 056802. doi:10.1103/PhysRevLett.94.056802
19. Waser, R., Ed. *Nanoelectronics and Information Technology,* 2nd ed.; Wiley-VCH: Weinheim, Germany, 2005; pp 426–427.
20. Yang, K.-M.; Chung, J.-Y.; Hsieh, M.-F.; Lin, D.-S. *Jpn. J. Appl. Phys., Part 1* **2007,** *46,* 4395–4402. doi:10.1143/JJAP.46.4395
21. Palermo, V.; Palma, M.; Samorì, P. *Adv. Mater.* **2006,** *18,* 145–164. doi:10.1002/adma.200501394
22. Pacchioni, G. Theory of point defects at the MgO surface. In *Oxide surfaces;* Woodruff, D. P., Ed.; Chemical Physics Of Solid Surfaces, Vol. 9; Elsevier: Amsterdam, 2001; pp 94–135. doi:10.1016/S1571-0785(01)80023-7
23. Ferrari, A. M.; Pacchioni, G. *J. Phys. Chem.* **1995,** *99,* 17010–17018. doi:10.1021/j100046a029
24. Scorza, E.; Birkenheuer, U.; Pisani, C. *J. Chem. Phys.* **1997,** *107,* 9645–9658. doi:10.1063/1.475260
25. Barth, C.; Henry, C. R. *Phys. Rev. Lett.* **2003,** *91,* 196102. doi:10.1103/PhysRevLett.91.196102
26. Livshits, A. L.; Shluger, A. L.; Rohl, A. L.; Foster, A. S. *Phys. Rev. B: Condens. Matter Mater. Phys.* **1999,** *59,* 2436–2448. doi:10.1103/PhysRevB.59.2436
27. Sushko, P. V.; Shluger, A. L.; Catlow, C. R. A. *Surf. Sci.* **2000,** *450,* 153–170. doi:10.1016/S0039-6028(00)00290-9
28. Corneille, J. S.; He, J.-W.; Goodman, D. W. *Surf. Sci.* **1994,** *306,* 269–278. doi:10.1016/0039-6028(94)90071-X
29. Fang, C. S. A. *Surf. Sci.* **1990,** *235,* L291–L294. doi:10.1016/0039-6028(90)90098-S
30. Trevethan, T.; Shluger, A. *Nanotechnology* **2009,** *20,* 264019. doi:10.1088/0957-4484/20/26/264019
31. Giordano, L.; Martinez, U.; Pacchioni, G.; Watkins, M.; Shluger, A. L. *J. Phys. Chem. C* **2008,** *112,* 3857–3865. doi:10.1021/jp7108016
32. Sterrer, M.; Heyde, M.; Novicki, M.; Nilius, N.; Risse, T.; Rust, H.; Pacchioni, G.; Freund, H. J. *J. Phys. Chem. B* **2006,** *110,* 46–49. doi:10.1021/jp056306f
33. Sicolo, S.; Giordano, L.; Pacchioni, G. *J. Phys. Chem. C* **2009,** *113,* 16694–16701. doi:10.1021/jp905592c

34. Giordano, L.; Pacchioni, G. *Phys. Chem. Chem. Phys.* **2006,** *8,* 3335–3341. doi:10.1039/b604288k
35. König, T.; Simon, G. H.; Rust, H.-P.; Pacchioni, G.; Heyde, M.; Freund, H.-J. *J. Am. Chem. Soc.* **2009,** *131,* 17544–17545. doi:10.1021/ja908049n
36. König, T.; Simon, G. H.; Rust, H.-P.; Heyde, M. *J. Phys. Chem. C* **2009,** *113,* 11301–11305. doi:10.1021/jp901226q
37. Somorjai, G. A. *Introduction to Surface Chemistry and Catalysis;* John Wiley & Sons, Inc.: New York, 1994.
38. Napoli, F.; Chiesa, M.; Giamello, E.; Finazzi, E.; Di Valentin, C.; Pacchioni, G. *J. Am. Chem. Soc.* **2007,** *129,* 10575–10581. doi:10.1021/ja073114k
39. Ricci, D.; Pacchioni, G.; Sushko, P. V.; Shluger, A. L. *J. Chem. Phys.* **2002,** *117,* 2844–2851. doi:10.1063/1.1491405
40. Ziegler, M.; Néel, N.; Sperl, A.; Kröger, J.; Berndt, R. *Phys. Rev. B* **2009,** *80,* 125402. doi:10.1103/PhysRevB.80.125402
41. Kresse, G.; Schmid, M.; Napetschnig, E.; Shishkin, M.; Köhler, L.; Varga, P. *Science* **2005,** *308,* 1440–1442. doi:10.1126/science.1107783
42. Jaeger, R.; Kuhlenbeck, H.; Freund, H.-J.; Wuttig, M.; Hoffmann, W.; Franchy, R.; Ibach, H. *Surf. Sci.* **1991,** *259,* 235–252. doi:10.1016/0039-6028(91)90555-7
43. Simon, G. H.; König, T.; Rust, H.-P.; Heyde, M.; Freund, H.-J. *New J. Phys.* **2009,** *11,* 093009. doi:10.1088/1367-2630/11/9/093009
44. Kulawik, M.; Nilius, N.; Rust, H. P.; Freund, H. J. *Phys. Rev. Lett.* **2003,** *91,* 256101. doi:10.1103/PhysRevLett.91.256101
45. Heinke, L.; Lichtenstein, L.; Simon, G. H.; König, T.; Heyde, M.; Freund, H.-J. *Phys. Rev. B* **2010,** *82,* 075430. doi:10.1103/PhysRevB.82.075430
46. Heinke, L.; Lichtenstein, L.; Simon, G.; König, T.; Heyde, M.; Freun, H.-J. *ChemPhysChem* **2010,** *11,* 2085–2087. doi:10.1002/cphc.201000060
47. Schmid, M.; Shishkin, M.; Kresse, G.; Napetschnig, E.; Varga, P.; Kulawik, M.; Nilius, N.; Rust, H. P.; Freund, H. J. *Phys. Rev. Lett.* **2006,** *97,* 046101. doi:10.1103/PhysRevLett.97.046101
48. Zerweck, U.; Loppacher, C.; Otto, T.; Grafstrom, S.; Eng, L. *Phys. Rev. B* **2005,** *71,* 125424. doi:10.1103/PhysRevB.71.125424
49. Gross, L.; Mohn, F.; Liljeroth, P.; Repp, J.; Giessibl, F. J.; Meyer, G. *Science* **2009,** *324,* 1428–1431. doi:10.1126/science.1172273
50. Song, W.; Yoshitake, M. *Appl. Surf. Sci.* **2005,** *251,* 14–18. doi:10.1016/j.apsusc.2005.03.116
51. Bäumer, M.; Freund, H.-J. *Prog. Surf. Sci.* **1999,** *61,* 127–198. doi:10.1016/S0079-6816(99)00012-X
52. Schauermann, S.; Johánek, V.; Laurin, M.; Libuda, J.; Freund, H.-J. *Chem. Phys. Lett.* **2003,** *381,* 298. doi:10.1016/j.cplett.2003.09.101

Single-pass Kelvin force microscopy and d*C*/d*Z* measurements in the intermittent contact: applications to polymer materials

Sergei Magonov[*] and John Alexander

Abstract

We demonstrate that single-pass Kelvin force microscopy (KFM) and capacitance gradient (d*C*/d*Z*) measurements with force gradient detection of tip–sample electrostatic interactions can be performed in the intermittent contact regime in different environments. Such combination provides sensitive detection of the surface potential and capacitance gradient with nanometer-scale spatial resolution as it was verified on self-assemblies of fluoroalkanes and a metal alloy. The KFM and d*C*/d*Z* applications to several heterogeneous polymer materials demonstrate the compositional mapping of these samples in dry and humid air as well as in organic vapors. In situ imaging in different environments facilitates recognition of the constituents of multi-component polymer systems due to selective swelling of components.

Introduction

Atomic force microscopy (AFM) applications include high-resolution imaging, probing of local materials properties and compositional mapping of heterogeneous materials in different environments. In recent years the improvements in these fields have been associated with the development of oscillatory modes and multi-frequency approaches. Despite the continuing interest and progress in high-resolution imaging, the practical value of AFM is strongly related to compositional imaging. The high sensitivity of the AFM probe to various materials properties is behind such visualization of individual components of complex materials. So far, compositional imaging of heterogeneous polymer materials is primarily based on differences of local mechanical and adhesive properties of their constituents. These differences are best reflected in phase images in the amplitude modulation (AM) mode, which are obtained at elevated forces. Although the phase contrast is efficient in differentiating the rubbery, glassy and inorganic components of polymer blends and composites, its interpretation in terms of specific mechanical properties is extremely difficult. Furthermore, the quantitative analysis of local mechanical properties of even neat poly-

mers obtained in AFM experiments is rather intricate due to their frequency-dependent nature. An additional limitation of AFM-based nanomechanical studies is their sensitivity to materials with an elastic modulus below 10 GPa (polymers, biological specimen, etc.) that leaves rigid materials (metals, semiconductors, ceramics, etc.) out of reach.

In this situation AFM compositional imaging can be expanded by local electrical techniques that enable measurements of electrical properties (surface potential, dielectric permittivity, capacitance, etc.) at a tip–sample junction. Here we will demonstrate that single-pass Kelvin force microscopy (KFM) studies based on sensing of an electrostatic force gradient can be performed in the intermittent contact mode and provide high-resolution maps of surface potential. This approach will be shortly described and its functionality will be proved by the results obtained on model systems: Self-assemblies of fluoroalkanes and metal alloys. The verification of novel approaches is specifically important in the case of multifrequency AFM applications that give a researcher a multiple choice of experimental procedures. Furthermore, the initial efforts of compositional imaging using surface potential maps will be demonstrated by studies of individual polymers and polymer blends on different substrates. In some cases we will add complimentary capacitance gradient (dC/dZ) data that give hints on the local dielectric response of materials.

Finally, we would like to point out that the environmental AFM capabilities, which make this technique unique among the microscopic methods, has enormous potential for compositional mapping of organic materials and polymers. In the intermittent contact operation, proximity of the conducting probe to a sample helps in avoiding screening the sample's electrical response by a water layer when measurements are performed at high humidity. A selective swelling of individual components with water or organic solvents helps to distinguish them when the experiments are conducted in water and solvent vapors. We will show how environmental studies of polymer blends with AFM-based electric studies enhance compositional imaging of these heterogeneous materials.

Materials and Methods
Samples
The samples for KFM and dC/dZ measurements were prepared by depositing different materials on doped Si, graphite or conducting glass (ITO) substrates. Fluoroalkanes $F_{14}H_{20}$ were dissolved in perfluorodecalin and a droplet of its dilute solution (0.01 mg/mL) was spin cast on the substrates. Self-assembled $F(CF_2)_{14}(CH_2)_{20}H–F_{14}H_{20}$ structures (toroids, spirals and ribbons) and thin molecular layers were formed on these substrates. A piece of Bi/Sn alloy with a composition 40:60 was

squeezed between two flat Si plates at 200 °C and chilled to room temperature. One of the plates was removed afterwards, and a shiny surface of the alloy sheet was examined by AFM. Polymer films were prepared by the spin-casting of a droplet of a dilute solution of the polymer on the substrates. Thin films of poly(methyl methacrylate) (PMMA) and polymer blends PMMA with polystyrene (PS) and PS with poly(vinyl acetate) (PVAC) were prepared from their solutions in toluene. A thin film of a blend of PMMA with poly(vinyledenefluoride) (PVDF) blend was spin cast from its solution in 1-methyl-2-pyrrolidinone. The polymers with molecular weights in the 100–150 K range, solvents and ITO glass substrates were purchased from Sigma-Aldrich. The Bi/Sn alloy was purchased from Rotometals, Inc. We also used boron-doped Si wafers with 0.02–0.05 Ω·cm resistivity manufactured by Virginia Semiconductor, Inc. Fluoroalkane samples were courtesy of Prof. M. Moeller (DWI, Aachen, Germany).

Prior to AFM measurements, scratches were made on the polymer films by a sharp wooden stick and we verified that a substrate-specific morphology was present at the bottom of scratches. At the scratched locations one can measure the film thickness and a relative electrical response of the polymer and Si substrate. All prepared samples were glued to metal disks with epoxy glue. An electrical contact between the instrument and the samples was arranged with a wire, which was fixed to a side of the conducting substrate with a drop of silver glue.

For KFM and dC/dZ we used Pt-coated Si probes with a stiffness in the 3–40 N/m range and flexural resonance in the 60–300 kHz range. AC and DC voltages were applied to the probe whereas the sample was earthed. The sharper coated probes have a tip diameter around 25–30 nm. Some of the probes were specially made with larger tip size (50–60nm in diameter). In control measurements, we applied carbon nanotubes probes (generously provided by Carbon Design Innovations). The probes with small tip apex and tips with high aspect ratio provide higher spatial resolution of surface potential images whereas the probes with thicker tips have a better signal-to-noise ratio of the surface potential.

The majority of measurements were made in air at 20–25% humidity. An environmental chamber of the microscope was used for studies in humid air (2% < RH < 95%, as measured by a humidity meter) and also for experiments in organic solvent vapors. One or two milliliters of water, methanol or toluene was injected into the environmental chamber, and these liquids gradually evaporated to influence the samples. Because of differences in the boiling points of the liquids, methanol vapor affected a sample in a shortest time, i.e., only a few minutes.
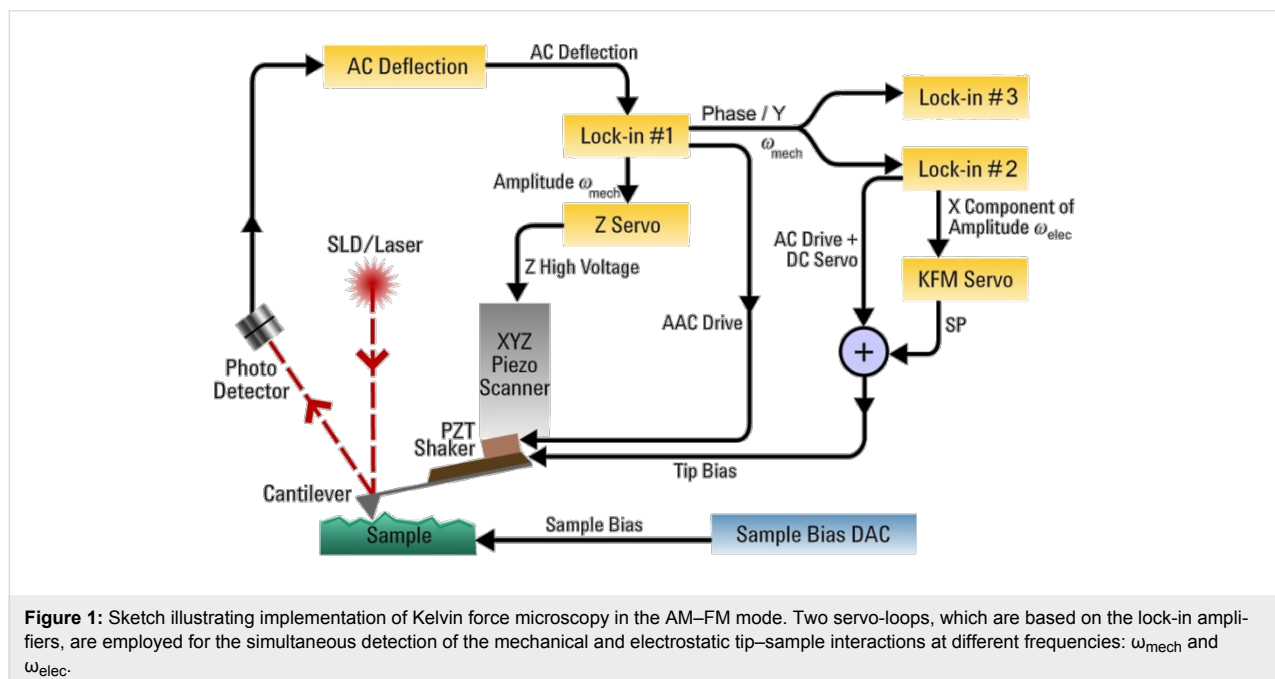
Electrostatic force measurements

The simultaneous use of the probe flexural resonance frequency (ω_{mech}) for sensing van der Waals or mechanical tip–sample interactions for surface profiling and a much lower frequency (ω_{elec}) for electrostatic force detection was suggested in 1988 [1]. For many years the single-pass approach has been mostly applied in UHV KFM studies, and such measurements are usually conducted in the non-contact mode. Under ambient conditions KFM is most often applied in the two-pass lift mode [2] that does not require the use of multiple lock-in amplifiers. In the lift mode, the long-range electrostatic force is sensed by a conducting probe, which is positioned 10–20 nm above the sample. This is done in the second pass by guiding the probe along the topography contour determined in the first pass whilst keeping away from the sample. Caution related to possible electrostatic force coupling with topography should still be taken into account. In many cases this method of separating the mechanical and electrostatic forces helps, however, measurements of the electrostatic force at remote tip–sample distances limit their sensitivity and, particularly, spatial resolution. Therefore, it may be advantageous to check the capabilities of single-pass KFM at ambient conditions because nowadays lock-in amplifiers are an essential part of the electronics in scanning probe microscopes.

AFM-based electrostatic force measurements were performed under ambient conditions with an Agilent 5500 scanning probe microscope equipped with a MAC III unit, which has three lock-in amplifiers (LIAs) enabling multi-frequency measurements. The MAC III has three dual phase LIAs converting the AC inputs to amplitude and phase. These digitally-controlled analog LIAs have a broad bandwidth (up to 6 MHz) that cover the operational bandwidth of the photodetector employed in the microscope. A signal access module provides a flexible routing of input and output signals of the LIAs. The software, which is flexible in routing signals back to the controller, supports two servo systems related to these LIAs.

The single-pass KFM operation can be realized in different combinations of AM and frequency modulation (FM) modes; AM–AM, AM–FM, FM–FM, FM–AM [3] where first abbreviation defines a surface tracking procedure and the second – detection of the electrostatic force. It is worth noting that AM is associated with force detection and FM with force gradient detection, and this difference appears to be essential for optimization of KFM imaging. The KFM operation can be described with the help of Figure 1. One of LIAs (LIA-1) was used for topography imaging, which was performed at the first flexural resonance of the probes, ω_{mech}, with free amplitude A_0 in the 1–100 nm range and set-point amplitude $A_{sp} = 0.6$–0.8 A_0. These imaging conditions correspond to the intermittent contact imaging when A_{sp} is chosen on the steep part of the amplitude-versus-distance curve. Another LIA (LIA-2), which is used for KFM, applies AC and DC voltages to the probe and detects the electrostatic response either directly from the photodetector (AM–AM) or from the LIA-1 (AM–FM). The latter block scheme configuration is shown in Figure 1. In the AM–FM, the electrostatic interactions are excited by an AC voltage applied to the probe at $\omega_{elec} = 3$–5 kHz, which is within the bandwidth of ω_{mech}. The electrostatic response, which is

Figure 1: Sketch illustrating implementation of Kelvin force microscopy in the AM–FM mode. Two servo-loops, which are based on the lock-in amplifiers, are employed for the simultaneous detection of the mechanical and electrostatic tip–sample interactions at different frequencies: ω_{mech} and ω_{elec}.

detected by the phase signal or *Y* component signal of the LIA-1, is seen at the heterodyne frequencies $\omega_{mech} \pm \omega_{elec}$. When the KFM servo is on, the heterodyne sidebands practically disappear and the DC voltage equals the contact potential difference. This AM–FM procedure is similar to one used for KFM in the non-contact regime [4] with the following variations. LIA-1 is used for both the AM topography servo and the demodulation of the side bands of the drive frequency. In [4] a separate PLL was used for the FM topography servo, and the drive out from the FM controller served as the reference input for LIA-1. In our case we used the internal reference of LIA-1 as the drive output to drive the cantilever shaker. There is a noise advantage in the use of the *Y* vector component as the input to the LIA-2 for the KFM servo because this excludes noise from the *X* vector component that would couple in through the phase calculation in the LIA-1.

The third LIA was used for recording the amplitude response at $2\omega_{elec}$ in two different configurations. In one configuration (shown in Figure 1) this amplifier was connected to the LIA-1. In this case the amplitude of $2\omega_{elec}$ satellite of the main amplitude peak at $2\omega_{mech}$ is recorded and it is proportional to the force gradient signal, and therefore to d^2C/dZ^2. In the second configuration, the third LIA is connected directly to the photodetector and in this case the detected amplitude at $2\omega_{elec}$ is proportional to the electrostatic force and therefore to dC/dZ. Both the dC/dZ and d^2C/dZ^2 signals are related to the local dielectric permittivity and we used these for compositional mapping. The interplay between the experimental measurements and theoretical studies is needed for a better understanding of the sensitivity of dC/dZ and d^2C/dZ^2 based dielectric studies, and for the extraction of quantitative permittivity data. In addition, we also recorded the phase response at $2\omega_{elec}$ that can be used for detection of complex dielectric response. In the following we will demonstrate that surface potential and dC/dZ data, which are measured simultaneously and independently of sample topography, can be used for compositional imaging.
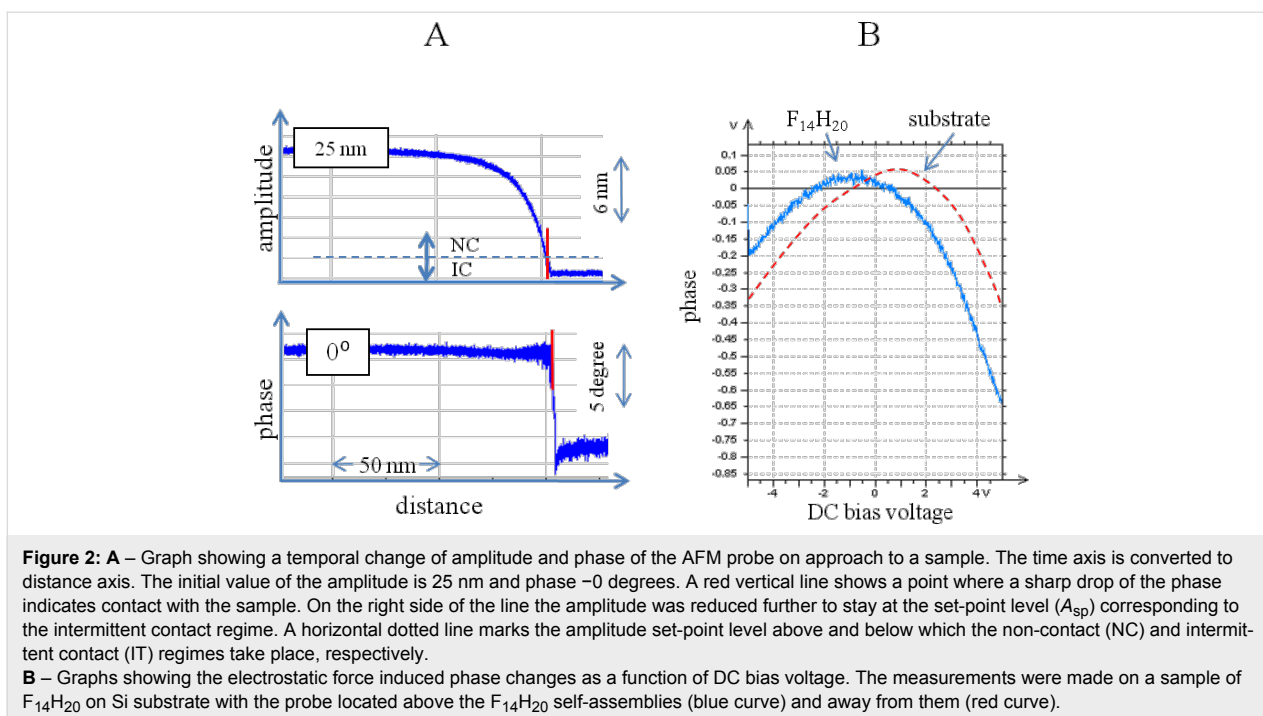
Results and Discussion
Studies of model samples
For the verification of our AFM-based electrostatic measurements, we have chosen two model systems: Self-assemblies of fluoroalkanes $F(CF_2)_{14}(CH_2)_{20}H$–$F_{14}H_{20}$ and the binary metal alloy Bi/Sn. The fluoroalkane molecules consist of fluorinated and hydrogenated parts that avoid each other in $F_{14}H_{20}$ self-assemblies (spirals, toroids, ribbons) on different substrates [5]. The $F_{14}H_{20}$ molecules have a dipole of 3.1 D oriented along the chain at the central $-CF_2-CH_2$-junction. Therefore, macroscopic Kelvin probe studies of Langmuir–Blodgett layers of different F_nH_m revealed a strong surface potential of −0.8 V [6,7] that is assigned to vertically oriented molecular chains

with fluorinated parts facing air. Therefore, the fluoroalkane structures are the useful models for the verification of KFM operations. The same is true for metal alloys because their surface potentials are directly defined by work function [8].

At the beginning we compare KFM imaging in the non-contact and intermittent contact modes. When the AFM probe, which is driven into an oscillation at its resonant frequency, approaches a sample, the probe amplitude gradually decreases, Figure 2A. This effect is caused by a squeezed air damping and attractive probe-sample force interactions. The latter are enhanced by electrostatic force interactions between the conducting probe and the sample as its counter electrode. The amplitude drop is accompanied by changes of the probe phase. On further approach of the probe to the sample, the amplitude changes are intensified and at some point a sharp drop (4–10 degrees) of the phase is observed. This signifies transition from non-contact situation to the intermittent contact regime. In other words, imaging at the set-point amplitude (A_{sp}) below its transition value will insure a profiling of surface topography, and at higher A_{sp} the imaging will proceed in the non-contact mode when the probe experiences long-range forces such as electrostatic forces. This is illustrated in Figure 2B which shows the dependence of phase changes as a function of DC bias voltage between a conducting probe and different locations of the $F_{14}H_{20}$ adsorbate on Si substrate. The phase-versus-DC-bias curve (colored blue) was detected when the probe was over a domain of the toroid-like self-assemblies. It shows a parabolic dependence of the phase response and demonstrates that the electrostatic force is fully compensated (nullified) at the bias voltage (about −1 V) and equals the difference in surface potential of the tip and the sample underneath. Similar phase-versus-DC-bias curve (red colored), which was recorded at a sample location free of the toroids, has been shifted on the DC bias axis due to a different surface potential at this location. The measurement of the phase or frequency responses to DC bias is the subject of electric force microscopy (EFM) whereas the mapping of bias voltages needed for nullification of the electrostatic is the main function of KFM.

The topography and surface potential images, which were recorded on the $F_{14}H_{20}$ adsorbate on Si substrate, are presented in Figure 3. These images were obtained with A_{sp} just above (Figure 3A) and below (Figure 3B) its value corresponding to the transition to the intermittent contact regime. The topography image recorded in the non-contact mode is practically featureless. At the conditions near the transition, it may be possible to detect weak cross-talk patterns, which are caused by the long-distance electrostatic interactions that are responsible for the bright domains in the corresponding surface potential images. The topography image changes drastically in the inter-

Figure 2: A – Graph showing a temporal change of amplitude and phase of the AFM probe on approach to a sample. The time axis is converted to distance axis. The initial value of the amplitude is 25 nm and phase −0 degrees. A red vertical line shows a point where a sharp drop of the phase indicates contact with the sample. On the right side of the line the amplitude was reduced further to stay at the set-point level (A_{sp}) corresponding to the intermittent contact regime. A horizontal dotted line marks the amplitude set-point level above and below which the non-contact (NC) and intermittent contact (IT) regimes take place, respectively.
B – Graphs showing the electrostatic force induced phase changes as a function of DC bias voltage. The measurements were made on a sample of $F_{14}H_{20}$ on Si substrate with the probe located above the $F_{14}H_{20}$ self-assemblies (blue curve) and away from them (red curve).

mittent contact regime and the elevated sub-micron domains of self-assemblies are clearly resolved. Related patterns are detected in the surface potential images obtained in both regimes. The signal-to-noise ratio of the surface potential pattern is higher in the intermittent contact operation due to the larger dC/dZ amplitude in immediate vicinity of the sample. A higher spatial resolution of the surface potential image obtained in the intermittent contact operation is also obvious. The averaged potential value is slightly larger (−0.79 V vs −0.75 V) in the image obtained in the intermittent contact regime. This statement can be extended to the 2-pass KFM measurements in the lift mode that actually present the results as a combination of the topography image in Figure 3B and surface potential image in Figure 3A.

In our experience the KFM measurements in the intermittent contact studies are most stable and reproducible with A_{sp} 70–80% of its value at the initial contact. The lowering of the set-point might cause a tip–sample discharge followed by sample and tip modifications. The fact that under ambient condition, KFM studies in the intermittent contact mode at moderate A_{sp} can be performed on pure metals such as Au [9] indicate that a short tip–sample force contact and a airborne contamination of surfaces prevents discharge between the tip and sample.

Here we would like to comment on a comparison of KFM results obtained in the AM–FM and AM–AM modes. The KFM images presented in Figure 3 were obtained in AM–FM mode.

Figure 3: Topography and surface potential images of $F_{14}H_{20}$ self-assemblies on Si substrate. The images in **A** were obtained in the non-contact regime with A_{sp} just above the transition level from the non-contact to the intermittent contact regime (see Figure 2A). The images in **B** were recorded in the intermittent contact regime with A_{sp} below the transition level. The contrast covers height variations in the 0–10 nm range in the topography images and potential changes in the 0–1 V range in the surface potential images. The averaged surface potential difference between the self-assemblies and the substrate is 0.75 V for the image in **A** and 0.79 V for the image in **B**.

The earlier KFM studies of $F_{14}H_{20}$ self-assemblies on different substrates revealed that the FM detection of the electrostatic forces provides the most accurate measurements of surface

potential (~0.8 V) and higher spatial resolution of surface potential images compared to AM detection [9-11]. This result is consistent with KFM studies of different samples in UHV [4,12] and with the theoretical considerations in [13]. In the latter paper, the authors have reported that compared to the electrostatic force changes, the force gradient variations are more confined to the probe apex and less sensitive to the force contributions of the cantilever and tip body. This hints at the advantage of FM detection compared to AM. We have also performed KFM studies in FM–FM mode using our microscope enhanced by adding PLL control. The surface images of $F_{14}H_{20}$ self-assemblies obtained in the FM–FM and AM–FM modes were practically identical when the measurements were performed in the intermittent contact mode. It is also important that the AM–FM and FM–FM measurements are typically performed at smaller stimulating AC voltages than AM–AM ones. This is essential for avoiding the possible electric field-induced changes of surface electric properties.

The KFM operation in the intermittent contact can be also performed in different gas environments. Importantly, the intermittent contact measurements were not affected by high humidity that screens surface potential when studies are performed in the non-contact mode [14]. Such environmental KFM studies of fluoroalkanes were performed in high humidity [10] and we extended these in a methanol vapor environment. A domain of self-assembled $F_{14}H_{20}$ structures is shown in Figure 4A, which demonstrates the topography, surface potential and dC/dZ images recorded in the single-pass operation. The cross-section profiles taken across the images in the direction marked with white arrows are presented underneath the images. The domain consists mostly of spiral self-assemblies around 4 nm in height as seen from the topography profile. The potential profile shows the negative surface potential of the spirals (approx. −0.8 V), which as mentioned before is caused by an almost vertical orientation of fluoroalkane chains whose fluorinated segments are facing air. The spirals also exhibit a darker dC/dZ contrast than the surroundings. The latter is formed by a thin fluoroalkane layer with molecules lying along the sample surface that makes them "invisible" in surface potential image. A few contaminating particles, which are marked with the red stars, are seen in the topography and dC/dZ images but not in surface potential image. The dC/dZ contrast correlates with variations of dielectric permittivity and the latter is related to averaged dipole values. A quantification of dC/dZ and permittivity changes is under development, and recent data [15] indicate that dC/dZ response increases with an increase of sample permittivity. This can explain the more negative dC/dZ contrast of the spirals. The images, which are shown in Figure 4B and related figures below, were recorded on the sample in methanol vapor. The change of the environment

caused a structural transformation of spirals to toroids and the height of these structures increased to ~5 nm. The latter is likely related to straightening of the chain molecules in the vertical direction. This slight change of the molecular alignment might be responsible for the increase of the negative surface potential from −0.8 V to (−1.0)–(−1.1) V. The methanol-induced changes in the dC/dZ image are responsible for the stronger difference between the contrast of the self-assemblies and the surroundings. Additionally, the toroids centers, a few nm in size, are visible in this image whereas the same toroids are seen as more bulky patterns in the surface potential image. The described height, surface potential and dC/dZ changes were reversible after the environmental chamber was opened to air. This is not related to the spirals-toroids conversion. There is no doubt that the electrostatic interaction of polar methanol molecules with fluroalkanes is responsible for these changes that initiate the structural transformation and small-scale surface transport on the substrate which is obvious from a comparison of the topography images shown in Figure 4.

The discussed images of $F_{14}H_{20}$ adsorbates also illustrate a high spatial resolution of surface potential and dC/dZ detection in the single-pass operation performed in the intermittent contact mode. A true spatial resolution of KFM is often determined as a width of a transition region between locations of different surface potential [4,12]. In a separate paper [16], we reported the measurements of the potential profile change at the steps of $F_{14}H_{20}$ self-assemblies on a Si substrate. When the Pt-coated probe was applied the step width was around 20–30 nm – a dimension that is similar to the tip's apex diameter. The same width was 4–5 nm on imaging with a carbon nanotube probe due to its high aspect ratio. In compositional mapping, the visualization of individual components is more important than obtaining the correct values of local mechanical or electrical properties. Therefore, the spatial resolution can be higher than the described above. In imaging of $F_{14}H_{20}$ ribbons on graphite, tiny bright slits of 2 nm in width were distinguished in between the individual ribbons. These are the locations where the probe "feels" the substrate.

A soldering material, an alloy of Bi and Sn, is another useful sample for KFM studies. The topography and surface potential images of this sample show its surface domain structure presented by different patterns (see Figure 5A). This finding suggests that the material is actually a partial solid solution. A comparison of these images shows that there is no a cross-talk between the topography and potential measurements. The surface potential contrast in the images at different magnifications shows four levels of contrast with the 200 mV span. These changes are close to the difference of surface potentials of Sn and Bi (~0.2 V). We found that sample preparation and its
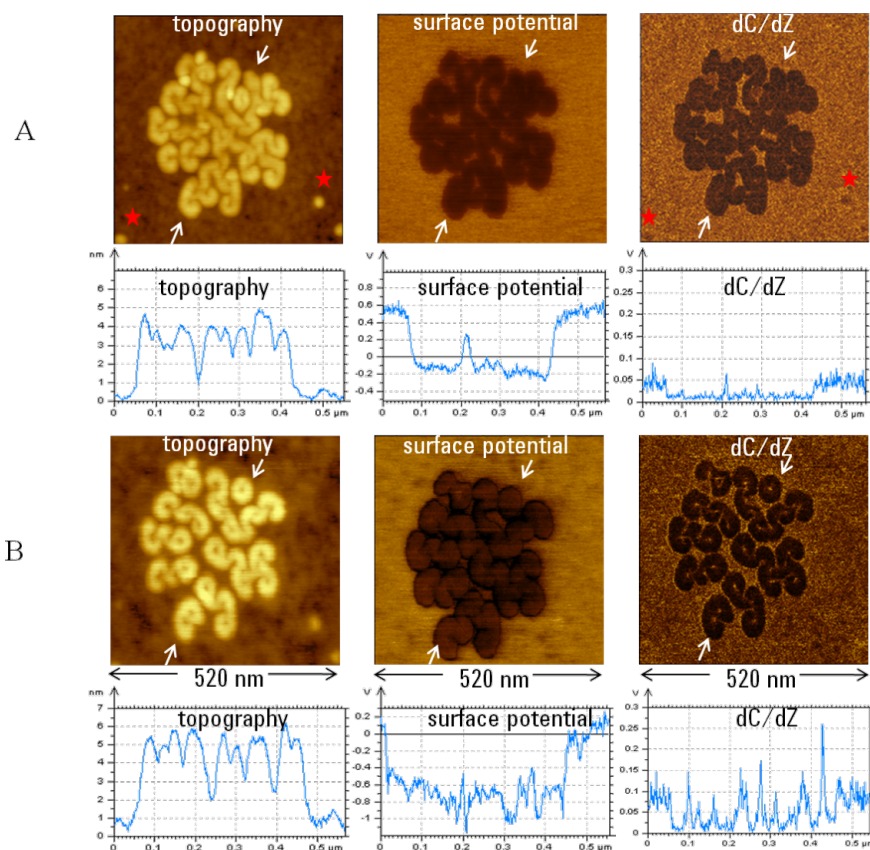
Figure 4: Topography, surface potential and dC/dZ images and cross-section plots obtained on a domain of $F_{14}H_{20}$ self-assemblies on the Si substrate. The plots, which are shown underneath the images, were taken along the directions indicated by the white arrows. The images in **A** were obtained during imaging in air. Two red stars indicate the contaminating particles, which are not seen in the surface potential image. The images in **B** were obtained during imaging in methanol vapor.
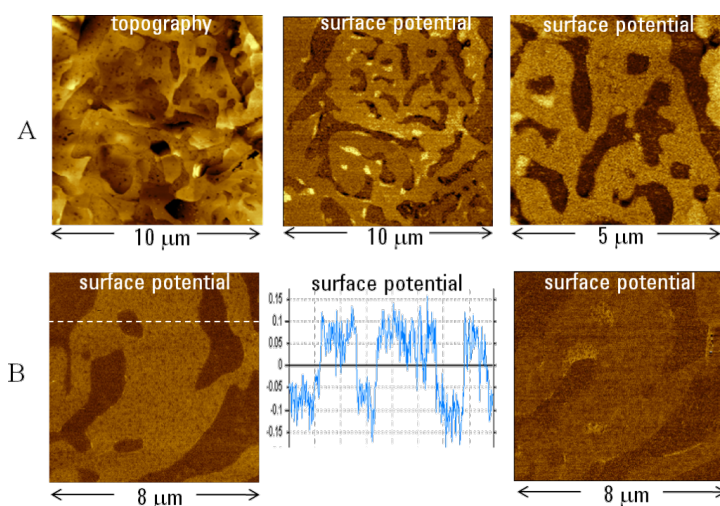
Figure 5: Topography and surface potential images recorded on two Bi/Sn samples. The images in **A** were obtained on the sample that is characterized by several levels of the surface potential contrast. The contrast covers the height corrugations in the 0–60 nm range in the topography image and the potential variations in the 0–0.4 V range in the surface potential images. The surface potential images in **B** were obtained on a freshly-prepared Bi/Sn sample (left) and the same sample after the overnight storage in air (right). The graph between the images displays the potential profile taken in the left image along the direction marked with a dashed white line.

storage are important factors influencing the surface potential contrast. The surface potential image of a freshly prepared sample, Figure 5B (left), shows only binary potential alternation of 0.2 V as seen from the cross-section profile in Figure 5B (middle). Therefore these domains can be assigned 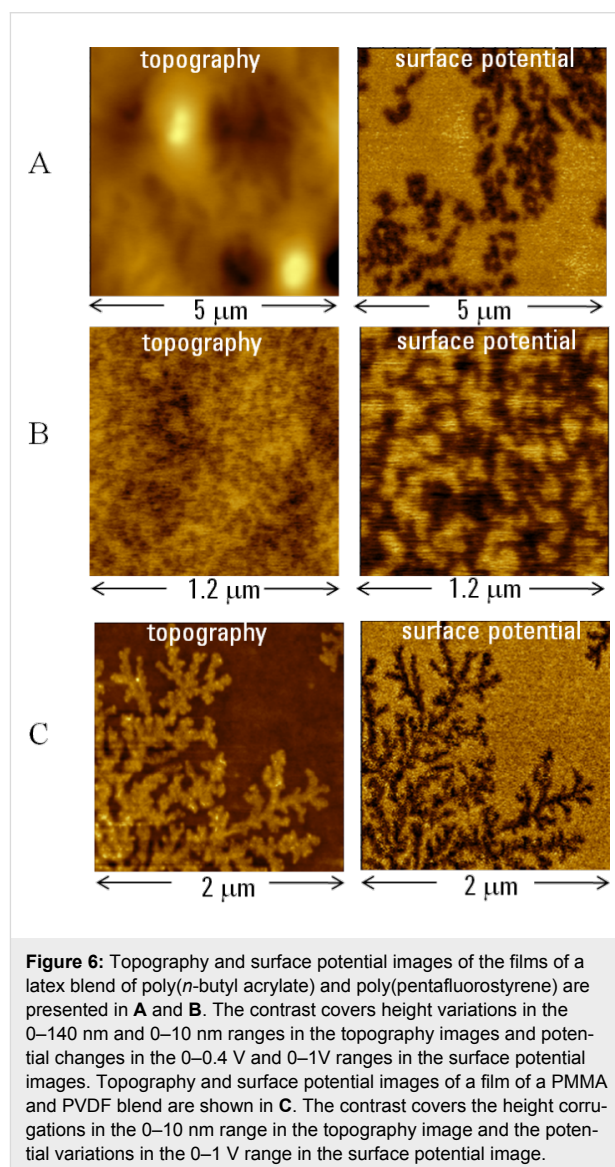to the individual metals Sn and Bi. The surface potential image of the same location after the sample was stored overnight in air is presented in Figure 5B (right). The contrast between the individual domains has worsened and bright patches have appeared in several locations. These changes are most likely caused by oxidation which is more progressive for Sn. This is an example of KFM compositional imaging of a stiff material. Other rigid materials that are beyond the range of phase imaging applications are semiconductors. The KFM inspection of local impurities and defects will benefit from higher-resolution studies in the intermittent contact regime.

KFM and d*C*/d*Z* mapping of polymer materials

Electrical and dielectric properties of polymer materials are studied by different methods, and their characterization at small scales and in confined geometries is an important and challenging task. The pathway to mapping of d*C*/d*Z* responses of polymers, which are directly related to local dielectric permittivity that depends strongly on frequency, has been initiated by studies of PVAC films [17]. In this work the frequency-dependent d*C*/d*Z* responses of this material, which was previously examined with dielectric spectroscopy [18], were studied with AFM probe at a single location. Furthermore, these studies were extended to d*C*/d*Z* mapping of a PVAC/PS blend at different temperatures in UHV [19] and to studies of a PVAC-based nanocomposite material [20]. We initiated KFM and d*C*/d*Z* measurements of the polymer objects having in mind several objectives. They included, but were not limited to, the use of these methods for compositional imaging of heterogeneous polymers and examination of polymer structures and behavior in different environments. In a wide variety of polymers those with a non-polar nature have a very low dielectric permittivity whilst polar polymer materials have permittivities around 7–9. Many polymers have dipole groups with molecular dipoles oriented along the chain backbone or perpendicular to it. In addition, the polymer response to an AC electric field is described by complex dielectric permittivity directly related with a spectrum of molecular motions and its dependence on temperature. Therefore the development of AFM-based electric techniques capable of examining these materials on a sub-micron scale and in a wide frequency range will open up a broad range of technologically and fundamentally important applications.

The first example is taken from studies of a binary latex blend of poly(*n*-butyl acrylate) and poly(pentafluorostyrene). The

images of the blend film at two locations are shown in Figure 6A and Figure 6B. The surface potential images reveal a bi-component composition of this material: The darker locations can most likely be assigned to the fluorinated component. The surface potential contrast between the constituents was relatively strong around 0.4 V. The micro-phase separated morphology is more homogeneous in the second location. It is worth noting that due to the softness of this polymer material, the images were recorded at a much lower A_{sp} at which the tip was partially imbedded in the sample. Therefore, the surface potential measurements can be carried out even in sub-surface layers. Another example of the materials with a fluorinated component is a thin film of a PMMA and PVDF blend. The relation between the polymer morphology and material performance is the key question for polymer technology that reinforces the importance of compositional imaging.

Figure 6: Topography and surface potential images of the films of a latex blend of poly(*n*-butyl acrylate) and poly(pentafluorostyrene) are presented in **A** and **B**. The contrast covers height variations in the 0–140 nm and 0–10 nm ranges in the topography images and potential changes in the 0–0.4 V and 0–1V ranges in the surface potential images. Topography and surface potential images of a film of a PMMA and PVDF blend are shown in **C**. The contrast covers the height corrugations in the 0–10 nm range in the topography image and the potential variations in the 0–1 V range in the surface potential image.

The film was prepared by spin-casting of PMMA and PVDF solutions, and the blend was formed during evaporation of the solvent and crystallization of PVDF. Therefore, dendritic structures observed on film surface represent crystalline PVDF. The dark surface potential contrast of the structures is consistent with the presence of a molecular dipole (~2.1 V) in this polymer and the preferential orientation of these dipoles is in the vertical direction. In crystalline polymer materials with a strong dipole moment, KFM might be a useful tool for correlating the molecular dipole orientation with chain orientation in lamellar structures.

In materials with strong dipole moments, the surface potential is directly related to the strength and orientation of the molecular dipole, as is the case in fluoroalkanes self-assemblies. In other materials surface potential correlates to the surface work function of metals, the doping level of semiconductors, the strength and orientation of molecular dipoles, and the presence of charges and interfacial and field-induced dipoles. In polar polymers, the situation can be much more complicated and the apparent surface potential of polymer molecules has to be discussed in connection with macroscopic Kelvin probe studies of thin PMMA films. These studies revealed that surface potential of PMMA films depends on the stereoregularity and molecular conformations of this polymer [21]. Therefore, PMMA

domains and blocks in multi-component polymer materials might exhibit a specific surface potential that can be examined with KFM. First of all, we studied the surface potential variations between PMMA and PS films of different thickness on a Si substrate. For this purpose, the images were collected in the scratched regions of the polymers with different thickness, Figure 7A. The cross-section profiles of the topography and surface potential images revealed that compared to the Si substrate, the surface potential of PS is rather small (~50 mV) in a film of thickness ~12 nm and twice as high in a film which is 140 nm thick. The surface potential difference between a 100 nm thick PMMA film and Si reaches 300 mV. Monitoring of the environmental effects was demonstrated by following the topography and surface potential changes of a thin PMMA film, Figure 7B. The study of swelling of PMMA film by different organic vapors [22] showed that methanol has a strong effect as shown by AFM. Indeed, swelling of PMMA with methanol induced changes not only in topography but also in surface potential. The surface potential changes are relative and the contrast of the film and the substrate reversed on sample exposure to methanol vapor: The difference of 200 mV between the PMMA film and Si became ca. −300 mV. These alterations proceed within 30–40 min, as the methanol vapor spread throughout the chamber and modified the sample. After the chamber was opened to air, the reverse changes of surface
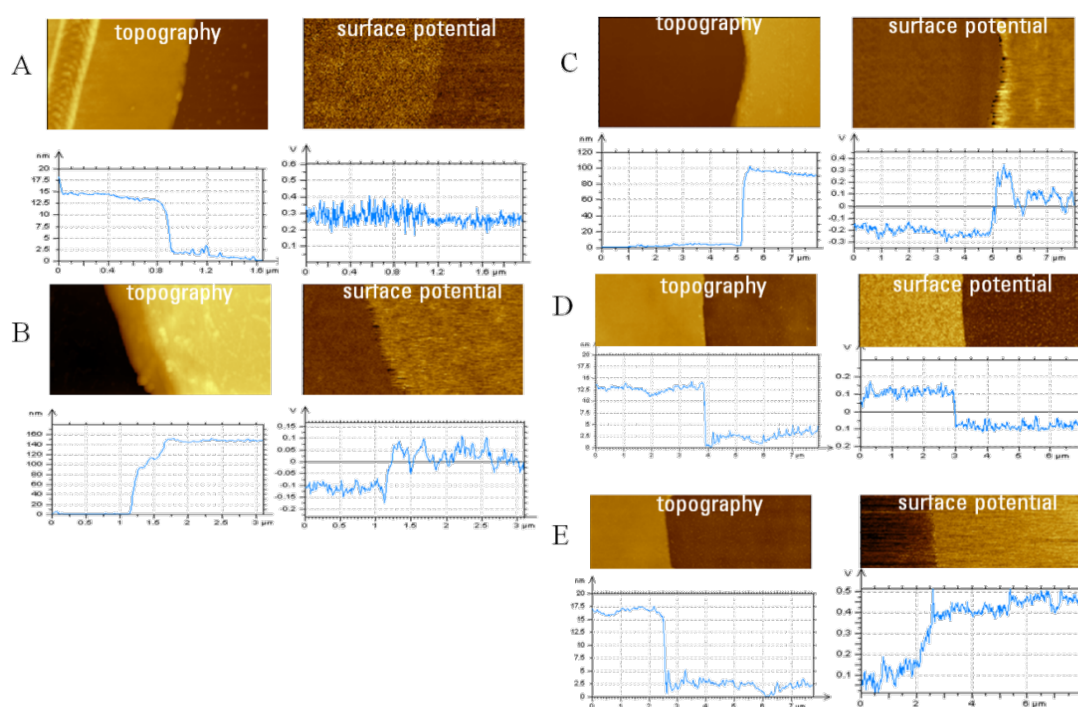

Figure 7: Topography and surface potential images, which were recorded at the scratch location in PS films of different thicknesses on a Si substrate, are presented in A and B. Similar images at the scratch location in PMMA films on Si are shown in **C–E**. The cross-section profiles, which were taken in the images, in the horizontal direction are shown under the images. The images in **A–D** were recorded with the sample in air and the image in **E** was recorded with the PMMA film in methanol vapor.

potential contrast happened practically immediately following methanol evaporation. This suggests that the methanol vapor affects only the top surface of the sample.

The analysis of KFM data obtained under ambient conditions in the intermittent contact mode on different samples shows that absolute values of surface potential might be influenced by a presence of occasional contaminants or modifications of the tip and the sample. This should be taken into account in comparing the surface potential data in Figure 7A and Figure 7B. A quantitative difference of surface potentials at dissimilar surface locations or sample components obtained in the same image is more reliable than absolute potential values.

KFM studies of PMMA and PS films were further extended by imaging of their blends with weight ratios of 3:7 (3M7S) and 7:3 (7M3S). Their topography and surface potential images, which were recorded at the scratches, are shown in Figure 8. According to the cross-section of the topography images, the films have a thickness of around 30 nm and the surface corrugations due to the elevated domains are in the 4–7 nm range. The averaged potential differences between the bright locations of the blends and the substrate were around 300 mV for 3M7S and 170 mV for 7M3S. On the blends' surface the differences between the brighter and darker locations were around 150–200 mV (3M7S) and 80 mV (7M3S). As can be seen, the surface potential patterns of the blends resemble their topography. However, a surface potential pattern with reversed contrast appeared when an AC bias was applied to the sample and not to the tip. The surface potential contrast of the blends was best seen at an AC bias of 6 V when the noise was much lower than at an AC bias of 1 V. In case of the 3M7S blend, as the AC bias was changed from 3 V to 6 V a substantial increase (80 mV to 150 mV) in surface potential difference between the bright and dark locations was observed. This might be considered as an indication of field-induced dipole effect.

The allocation of the surface potential features to the blend constituents is not a trivial task and a direct correlation with the results obtained on PS and PMMA films might be difficult due to unknown morphology inside the blend film. We assume that the bright and dark patches correspond to domains enriched in PMMA and PS. This assignment is tentatively supported by a correlation of the ratio of bright and dark areas to the composition of the blends as well as by the higher surface potential values recorded on PMMA films compared those with PS. Decisive support for this analysis was found in the images of the 7M3S blend obtained after the sample was exposed to high humidity (RH > 95%) overnight (Figure 8C). The surface potential image was unchanged but multiple droplets appeared inside the dimples in the topography image. Most likely these
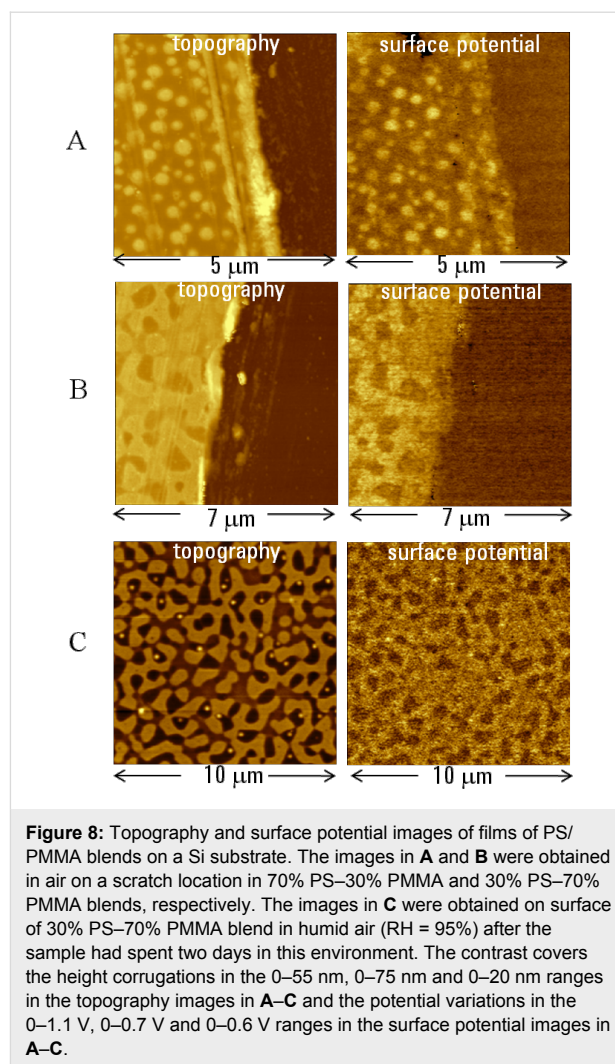

Figure 8: Topography and surface potential images of films of PS/PMMA blends on a Si substrate. The images in **A** and **B** were obtained in air on a scratch location in 70% PS–30% PMMA and 30% PS–70% PMMA blends, respectively. The images in **C** were obtained on surface of 30% PS–70% PMMA blend in humid air (RH = 95%) after the sample had spent two days in this environment. The contrast covers the height corrugations in the 0–55 nm, 0–75 nm and 0–20 nm ranges in the topography images in **A**–**C** and the potential variations in the 0–1.1 V, 0–0.7 V and 0–0.6 V ranges in the surface potential images in **A**–**C**.
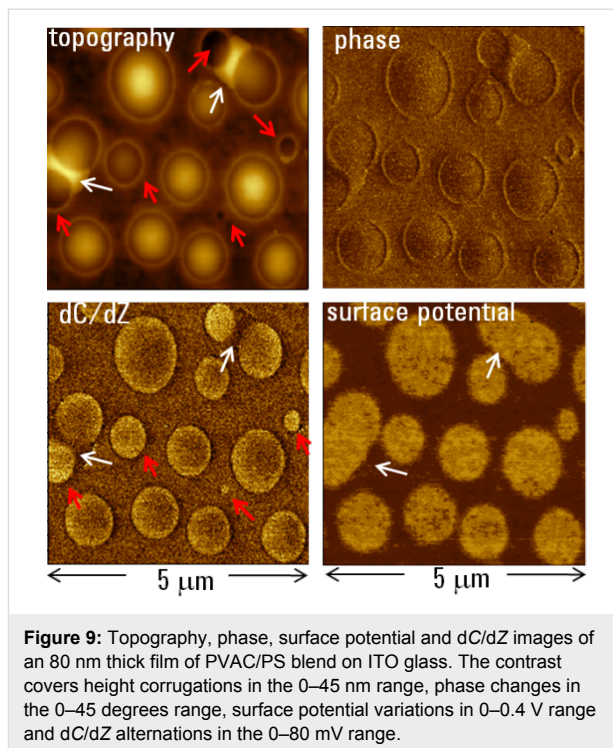
are due to condensed water droplets on hydrophobic surface of PS-enriched domains. The droplets are characterized by a relatively large wetting angle that indicates hydrophobicity of the underlying locations.

Compared to surface potential studies the use of dC/dZ measurements was relatively limited by studies of organic layers [23] and water adsorption [24,25]. Recently, the situation has changed and there is now an increasing interest in nanoscale dielectric studies. Our interest in PS-PVAC blends was brought about by recent efforts to measure its local dielectric properties by different EFM approaches [17,19,20,26]. The static dielectric permittivities of the blend components are quite different (2–3 for PS and ~7 for PVAC) as well as their dipole moments (~0.3 D for PS and 2.1 D for PVAC). This makes this material attractive for local electric measurements. In addition, the glass transition temperature of PVAC is quite low (35 °C) thus its complex permittivity can also be studied with comparative ease. The studies EFM-based local measurements [19] were

conducted at frequencies in the range 0.1–100 Hz range and at temperatures around 35 °C (glass transition of PVAC) where the dielectric response exhibits pronounced changes. Indeed, it was found that the dielectric contrast of the PVAC domains varied with temperature, and nanoscale mapping of the permittivity differences was demonstrated. These studies were done in UHV and the dC/dZ measurements were conducted in the non-contact mode.

In extending single-pass KFM and dC/dZ applications in the intermittent contact, we examined 80-nm thick film of the same blend on an ITO substrate. The topography, phase, dC/dZ and surface potential images of one of the locations are shown in Figure 9. The topography image revealed a morphology, which was characterized by sub-micron scale domains embedded into a matrix. The domains have a shape of a top part of sphere inserting into the surroundings. The elevated part of highest domains reached 30 nm where as few of domains are seen below the matrix. This morphology is similar to that described in [19] where the round-shape domains were assigned to PVAC and the matrix to PS. The topography image also shows well-resolved rims around the PVAC domains that most likely are a consequence of immiscibility of the components of this blend. The composition map of the blend is clearly presented in the surface potential image in which PVAC domains exhibit a 50–60 mV higher surface potential than the PS matrix. Their potential is also 130–140 mV higher than that of the ITO substrate as seen in surface potential image taken at the scratch in the film (not shown here). Remarkably, in a few surface regions the neighboring PVAC domains are connected by "bridges", which are marked with white arrows. According to the surface potential contrast, these bridges are formed from PVAC. The surface potential contrast reflects the larger dipole moment of PVAC and the positive value is caused by an average dipole orientation towards the substrate. In further speculation, we might point out that because the dipole moment of PVAC is oriented perpendicular to the molecular chain [27], a planar chain orientation could be the most preferable arrangement in the PVAC domains. High-resolution surface potential images (not shown here) emphasize that surface potential contrast is not uniform across the PVAC domains. This observation suggests a clustering of polymer chains into nanometer-scale blocks with different averaged molecular orientation.

The phase and dC/dZ images are quite different from that for surface potential. The phase image resembles the error signal image and the PVAC domains are not emphasized. At room temperature both polymers, PS and PVAC, are in glassy state therefore it would not be expected to observe a difference in their phase contrast. The dC/dZ contrast variations are more distinguished with PVAC domains being brighter than the

Figure 9: Topography, phase, surface potential and dC/dZ images of an 80 nm thick film of PVAC/PS blend on ITO glass. The contrast covers height corrugations in the 0–45 nm range, phase changes in the 0–45 degrees range, surface potential variations in 0–0.4 V range and dC/dZ alternations in the 0–80 mV range.

surrounding PS. There are two interesting aspects. The first is related to the contrast of individual domains. The domains, which are marked with a red arrow, have their top part just above the surface or below it. The dC/dZ patterns of these domains are uniform in bright contrast. The other elevated domains exhibit a different dC/dZ patterns with a central part darker that the perimeter. This suggests that at elevated locations only the tip apex is sensing the electrostatic force and a large part of the tip participates in the force interactions when the domains are lower. The second is related to the bridges between the PVAC domains (white arrows). The darker dC/dZ contrast as opposed to brighter surface potential contrast points to their assignment as PVAC. We might suggest that these bridges are formed by ultrathin PVAC films spreading between the two domains and that the dC/dZ contrast is more influenced by the underlying PS matrix than the surface potential contrast. This is only a tentative suggestion but it indicates the necessity of knowing the depth of the surface potential and dC/dZ measurements.

The studies of the PVAC/PS blend were continued at low and high humidity and also in methanol and toluene vapors. There are general similarities between the results obtained in high humidity and in the organic vapors. The images of the same location obtained in air and at high humidity are shown in Figure 10. The images obtained in air exhibit similar features to those seen in Figure 9. In addition to the topography, surface potential and dC/dZ amplitude signal, we were able to demon-
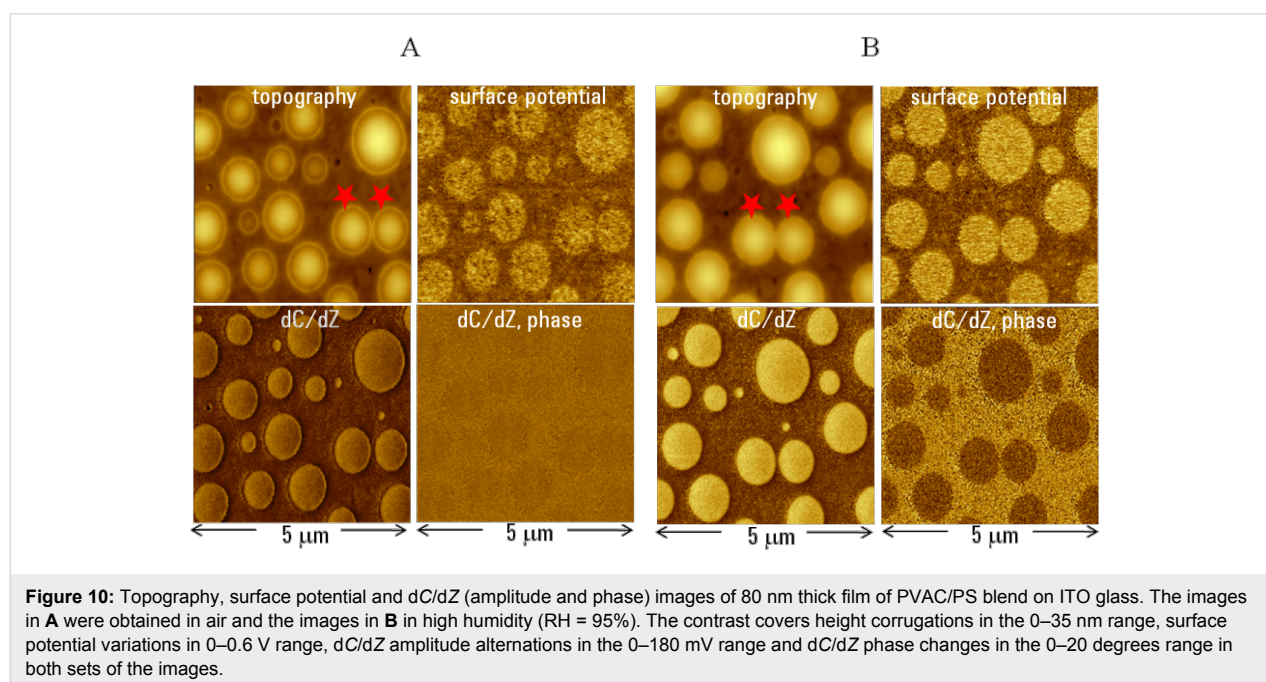
strate the d*C*/d*Z* phase image, which does not show much contrast in air. By changing air to humid environment, we expected selective action on the hydrophilic PVAC domains. The images, which were obtained after the sample was exposed high humidity for couple of hours, are presented in Figure 10B. The two red star marks placed near the same PVAC domains serve as the references in Figure 10A and Figure 10B. The humidity effect is pronounced in the topography and d*C*/d*Z* (amplitude and phase) images. Surface potential changes are less obvious. A selective swelling of PVAC domains with water vapor led to an increase in the volume of the domains and the disappearance of the circular rims. The height of the domains marked with the red stars increased from 20 to 25 nm. Simultaneously with the topography changes, the d*C*/d*Z* contrast increased 8-fold and a pronounced phase contrast (~20 degrees) was detected. These changes were reversible and the original contrast of all three images was restored after the environmental chamber was opened or purged with argon. The strong phase changes might serve as an indication of dynamic dielectric behavior that is common for polymers around glass transition point. The swelling of polymers with low-molecular agents effectively lowers their glass transition point and this effect is suspected. Ongoing d*C*/d*Z* studies of this blend at elevated temperatures will help address this question.

The d*C*/d*Z* contrast observed in the PVAC/PS blend and its environmental changes are not easy to understand. The static permittivity of PVAC is much higher than that of PS but it is difficult to assume that the contrast recorded at 3 kHz follows their low frequency difference. We also might suspect some environmental effects in our preliminary measurements at low humidity (3% RH) and in different gases (N$_2$, Ar) as revealed by the the contrast variations. The humidity-induced changes are very noticeable and well as those caused by methanol and toluene vapors. These observations might be also affected by dielectric absorbance of water or organic molecules that, being in GHz range, might also have direct or indirect lower frequency contributions. Therefore, the expansion of AFM-based d*C*/d*Z* measurements to broader (higher and lower) frequency ranges is quite desirable for a better understanding the local dynamic dielectric properties.

Conclusion

Single-pass KFM and d*C*/d*Z* studies in the intermittent contact regime were carried out and their value was verified in experiments with two model samples, i.e., self-assemblies of fluoroalkanes F$_{14}$H$_{20}$ on a Si substrate and films of the metal alloy Bi/Sn. The electrostatic force interactions were measured by force gradient changes. The results showed that sensitivity and spatial resolution of this approach is superior compared to use of the non-contact mode for KFM and d*C*/d*Z* detection. Furthermore, the single-pass measurements of several polymer materials demonstrate that KFM and d*C*/d*Z* mapping can be applied for compositional imaging of multi-component systems. These techniques have also been applied to samples in various environments (humidity, vapors of organic solvents, etc.), where the samples were subjected to partial swelling. Such measurements are helpful in the identification of individual constituents of complex materials and will further enhance compositional imaging. The d*C*/d*Z* measurements, which were

Figure 10: Topography, surface potential and d*C*/d*Z* (amplitude and phase) images of 80 nm thick film of PVAC/PS blend on ITO glass. The images in **A** were obtained in air and the images in **B** in high humidity (RH = 95%). The contrast covers height corrugations in the 0–35 nm range, surface potential variations in 0–0.6 V range, d*C*/d*Z* amplitude alternations in the 0–180 mV range and d*C*/d*Z* phase changes in the 0–20 degrees range in both sets of the images.

performed at a single frequency, gave rise to a number of intriguing questions regarding the origin of the image contrast. Expansion of these studies to a broad frequency range and at different temperatures will be essential for reliable interpretation of the dielectric data and will be the subject of nanoscale dielectric spectroscopy.

References

1. Martin, Y.; Abraham, D. A.; Wickramasinghe, H. K. *Appl. Phys. Lett.* **1988,** *52,* 1103–1105. doi:10.1063/1.99224
2. Elings, V. B.; Gurley, J. A. Scanning probe microscope using stored data for vertical probe positioning. U.S. Patent 5,308,974, March 5, 1994.
3. Nakamura, M.; Yamada, T. Electrostatic Force Microscopy. In *Roadmap 2005 of Scanning Probe Microscopy;* Morita, S., Ed.; Springer: Berlin, Germany, 2006; pp 43–51.
4. Zerweck, U.; Loppacher, C.; Otto, T.; Grafstroem, S.; Eng, L. M. *Phys. Rev. B* **2005,** *71,* 125424–125433. doi:10.1103/PhysRevB.71.125424
5. Mourran, A.; Tartsch, B.; Gallyamov, M.; Magonov, S.; Lambreva, D.; Ostrovskii, B. I.; Dolbnya, I. P.; de Jeu, W. H.; Moeller, H. *Langmuir* **2005,** *21,* 2308–2316. doi:10.1021/la048069y
6. El Abed, A.; Faure, M.-C.; Pouzet, E.; Abillon, O. *Phys. Rev. E* **2002,** *5,* 051603. doi:10.1103/PhysRevE.65.051603
7. Broniatowski, M.; Minores, J., Jr.; Dynarowicz-Latka, P. *J. Colloid Interface Sci.* **2004,** *279,* 552–558. doi:10.1016/j.jcis.2004.06.080
8. Michaelson, H. B. *J. Appl. Phys.* **1977,** *48,* 4729–4733. doi:10.1063/1.323539
9. Magonov, S.; Alexander, J. Advanced Atomic force microscopy: Exploring measurements of local electric properties. *Application Note 5989-9740EN,* Agilent Technologies Inc., December 15, 2008; S. Magonov, S.; Alexander, A. Compositional imaging of materials with single-pass Kelvin force microscopy. *Application Note 5990-0000EN,* Agilent Technologies Inc., March 4, 2010.
10. Alexander, J.; Magonov, S.; Moeller, M. *J. Vac. Sci. Technol., B: Microelectron. Nanometer Struct.–Process., Meas., Phenom.* **2009,** *27,* 903–911. doi:10.1116/1.3079675
11. Magonov, S.; Alexander, J.; Wu, S. Advancing characterization of materials with Atomic Force Microscopy – based electric techniques. In *Scanning Probe Microscopy of Functional Materials: Nanoscale Imaging and Spectroscopy;* Kalinin, S. V.; Gruverman, A., Eds.; Springer: Berlin, Germany, 2010; pp 1–77.
12. Krok, F.; Sajewicz, K.; Konior, J.; Goryl, M.; Piatkowski, P.; Szymonski, M. *Phys. Rev. B* **2008,** *77,* 235427–235435. doi:10.1103/PhysRevB.77.235427
13. Colchero, J.; Gil, A.; Baro, A. M. *Phys. Rev. B* **2001,** *64,* 245403–245414. doi:10.1103/PhysRevB.64.245403
14. Sugimura, H.; Ishida, Y.; Hayashi, K.; Takai, O.; Nakagiri, N. *Appl. Phys. Lett.* **2002,** *80,* 1459–1461. doi:10.1063/1.1455145
15. Fumagalli, L.; Gramse, G.; Esteban-Ferrer, D.; Edwards, M. A.; Gomilla, G. *Appl. Phys. Lett.* **2010,** *96,* 183107–183109. doi:10.1063/1.3427362
16. Magonov, S.; Alexander, J. *Microsc. Microanal,* in press.
17. Crider, P. S.; Majewski, M. R.; Zhang, J.; Okris, H.; Israeloff, N. E. *Appl. Phys. Lett.* **2007,** *91,* 013102–013104. doi:10.1063/1.2753539
18. Wagner, H.; Richert, R. *Polymer* **1997,** *38,* 255–261. doi:10.1016/S0032-3861(96)00524-1
19. Riedel, C.; Sweeney, R.; Israeloff, N. E.; Arinero, R.; Schwartz, G. A.; Alegria, A.; Tordjeman, P.; Colmenero, J. *Appl. Phys. Lett.* **2010,** *96,* 213110–213112. doi:10.1063/1.3431288
20. Labardi, M.; Prevosto, D.; Nguyen, K. H.; Capaccioli, S.; Lucchesi, M.; Rolla, P. *J. Vac. Sci. Technol., B: Microelectron. Nanometer Struct.–Process., Meas., Phenom.* **2010,** *28,* C4D11–C4D17. doi:10.1116/1.3368597
21. Kim, J.-J.; Jung, S.-D.; Hwang, W.-Y. *ETRI Journal* **1996,** *18,* 195–206. doi:10.4218/etrij.96.0196.0037
22. Tanaka, K.; Fujii, Y.; Atarashi, H.; Akabori, K.; Hono, M.; Nagamura, T. *Langmuir* **2008,** *24,* 296–301. doi:10.1021/la702132t
23. Fujihira, M. *Annu. Rev. Mater. Sci.* **1999,** *29,* 353–380. doi:10.1146/annurev.matsci.29.1.353
24. Hu, J.; Xiao, X. D.; Salmeron, M. *Appl. Phys. Lett.* **1995,** *67,* 476–478. doi:10.1063/1.114541
25. Salmeron, M. *Oil Gas Sci. Technol.* **2001,** *56,* 63–75. doi:10.2516/ogst:2001008
26. Riedel, C.; Arinero, R.; Tordjeman, P.; Leveque, G.; Schwartz, G. A.; Alegria, A.; Colmenero, J. *Phys. Rev. E* **2010,** *81,* 010801–010804. doi:10.1103/PhysRevE.81.010801
27. Stockmayer, W. H. *Pure Appl. Chem.* **1967,** *15,* 539–554. doi:10.1351/pac196715030539

Oriented growth of porphyrin-based molecular wires on ionic crystals analysed by nc-AFM

Thilo Glatzel[*1], Lars Zimmerli[1], Shigeki Kawai[1], Ernst Meyer[1], Leslie-Anne Fendt[2] and Francois Diederich[2]

Full Research Paper

Address:
[1]Department of Physics, University of Basel, Klingelbergstrasse 82, 4056 Basel, Switzerland and [2]Laboratory of Organic Chemistry, ETH Zurich, Wolfgang-Pauli-Str. 10, 8093 Zurich, Switzerland

Email:
Thilo Glatzel[*] - thilo.glatzel@unibas.ch

* Corresponding author

Abstract

The growth of molecular assemblies at room temperature on insulating surfaces is one of the main goals in the field of molecular electronics. Recently, the directed growth of porphyrin-based molecular wires on KBr(001) was presented. The molecule–surface interaction associated with a strong dipole moment of the molecules was sufficient to bind them to the surface; while a stabilization of the molecular assemblies was reached due to the intermolecular interaction by π–π binding. Here, we show that the atomic structure of the substrate can control the direction of the wires and consequently, complex molecular assemblies can be formed. The electronic decoupling of the molecules by one or two monolayers of KBr from the Cu(111) substrate is found to be insufficient to enable comparable growth conditions to bulk ionic materials.

Introduction

One of the main challenges of artificial photosynthesis and molecular electronics is the controlled growth of molecules on the nanometer scale in a certain direction. For the construction of electronic devices, nanowires are essential components which provide an efficient transport of electrons and/or excitons along specific directions. Compared to semiconductor based devices, self-assembled molecules provide some distinct advantages such as self-healing [1] and a decreased number of defects [2-4]. For some time, studies on molecular growth were limited

to metal substrates analyzed by scanning tunneling microscopy (STM) (for a few selected examples see [5-13]). Alkali halide thin insulating films on metal surfaces are often regarded as the model system for both testing experimental methodologies and validating new theories. In particular NaCl thin films have already proved their importance as homogeneous ultrathin spacer layers to separate single molecules from the metal substrate [14-16]. Nevertheless, complete electrical decoupling of such devices from the substrate requires bulk insulators or thick

insulating films. Several studies by non-contact atomic force microscopy (nc-AFM) were done on ionic crystals with adsorbed PTCDA [17-22], PTCDI [23] or C_{60} [24]. In the case of porphyrins, the growth [25-27] and electronic properties [28] of stable, monolayered molecular wires on KBr(001) with a length of up to several hundred nanometers have been observed at room temperature (rt). Even the contacting of self-ordering molecular wires by nanolithography was shown recently [29].

Controlled growth procedures of molecules on insulators are often hindered by the weak, unspecific interaction between the molecules and the insulating surfaces which leads to diffusion on the surfaces and assembly of disordered aggregates. One possibility to overcome this barrier is the use of a specific end group which induces an adequate directed dipole moment within the molecule [26,30]. Moreover, high resolution measurements of molecules on insulating surfaces were scarce due to a lack of suitable imaging techniques. However, recent progress in high resolution nc-AFM has given the opportunity to verify the proposed concept of directed growth of molecular wires on insulators [31-33]. Alkali halides offer some distinct advantages compared to other surfaces. Flat surfaces with monoatomic steps and large terraces are easily prepared and electron bombardment leads to well-structured surfaces [34]. Additionally, these materials have rather large unit cells which allow to obtain atomic resolution fairly easily [35,36].

In the work presented here we focus on the influence of the substrate on the growth process of *meso*-(4-cyanophenyl)-substituted Zn(II) porphyrin molecular wires self-assembled on KBr(001) and NaCl(001) studied by nc-AFM. We found that

the lattice spacing of the ionic crystal has a direct impact on the growth direction of the wires. Extending the studies, the self-assemblies of molecules onto thin ionic films deposited on Cu(111) revealed that the growth process is also strongly influenced by the metal substrate even for several monolayer of KBr which also indicates an imperfect electronic decoupling.

Results and Discussion

Cleaving KBr crystals in vacuum and annealing them at moderate temperatures results in the formation of wide terraces with step edges in [100] direction which can be as long as several hundred nanometers. Evaporating the cyano-porphyrins onto the bulk KBr(001) surface results, as also reported earlier [25,26], in the formation of molecular wires. Figure 1 shows a topographic measurement on a KBr(001) surface, decorated with cyano-porphyrines. The molecular monowires (1) are found to be more than 700 nm long mainly depending on the length of the step. Along one and two monolayer step edges, single molecular wires are found while at higher steps disordered aggregates of molecules (2) appear. Based on simple geometrical considerations and taking into account the strong dipole moment of the molecules, the special expansion of the aryl side groups and the enhanced electrostatic field at the step edge result in a basic model of the wire formation as presented in Figure 1b, Figure 1c and Figure 1d. Single molecules are highly mobile at rt at the surface. Due to an electrostatic interaction between the dipole moments of the molecules and the enhanced periodic electrostatic field at a step edge compared to the flat surface, the molecules are attracted towards the steps. A stabilization of the wire is enabled due to a π–π binding between the porphyrin cores of the molecules. Increasing the
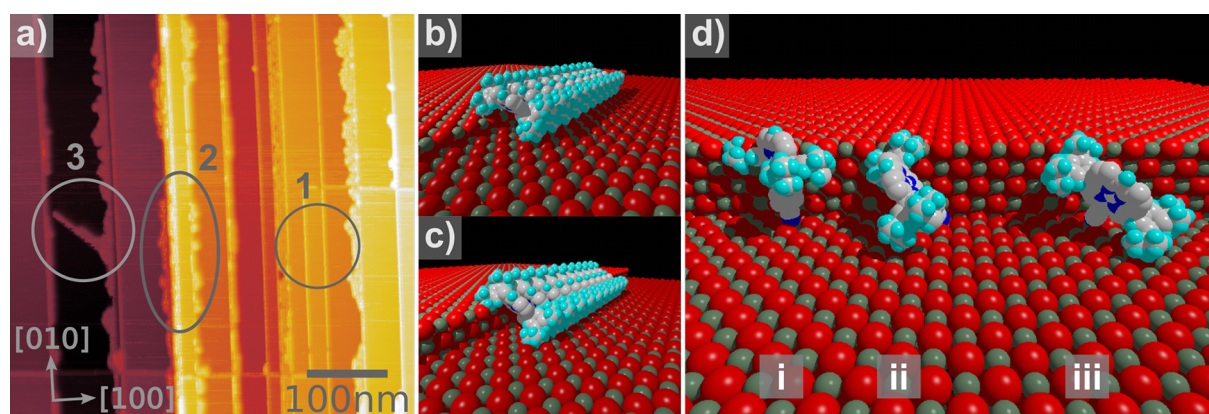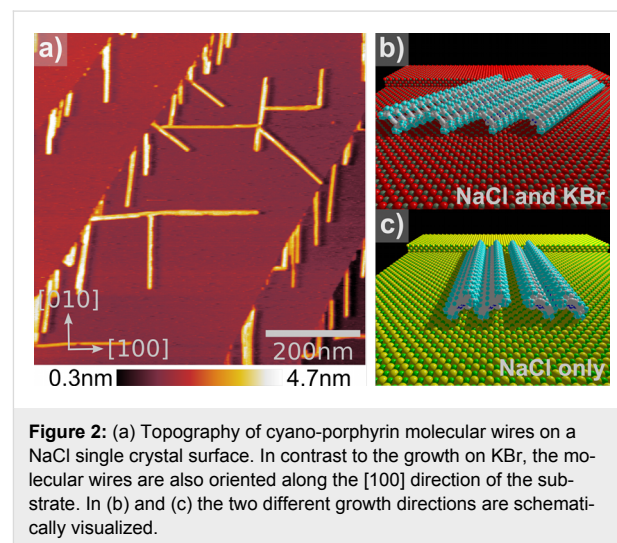

Figure 1: (a) Topographical measurement of molecular structures at KBr step edges showing monowires (1), unordered agglomerates (2) and multi-wires (3). Scan range = 500 × 500 nm^2, A_{1st} = 20 Hz, Δf_{1st} = −8 Hz. The arrangements estimated from height profiles along single and double steps are shown in (b) and (c), respectively. The tilt angle of the molecules has to adopt to fulfil geometrical conditions. Along a triple step, one dimensional wires were never observed. (d) Three different orientations of molecules at those edges. The leftmost molecule (i) in (d) is turned by 45° so that the core is oriented along the [110] direction. This orientation does not allow π–π stacking along the direction of the step edges. The molecule in the middle (ii) is tilted by 45° to the surface, making it fit geometrically to the step. (iii) combines those two angles and could be considered as a possible arrangement for the growth in the [110] direction.

step height changes the tilt angle of the molecules towards the surface which is inherently coupled with a weaker π–π inter-action and therefore a more fragile molecular wire.

The analysis of our measurements resulted in a wire height of 0.8−0.9 nm and of 1.2−1.3 nm for the one and two monolayer (1ML and 2ML) step edges, respectively. Assuming that the height of a single molecule from the cyanophenyl to the upper parts of the aryl groups is roughly 1.5 nm (the calculated height would be 14.989 Å plus the van der Waals radii of one hydrogen and one nitrogen atom) and that the molecules are not laterally tilted, this would lead to a tilt angle of roughly $57 \pm 5°$ for the 2ML and $35 \pm 5°$ for the 1ML step edge with respect to the substrate. Balaban et al. [37] showed that the distance between two molecules in the π–π plane is approximately 3.6 Å, which leads to a distance of 5.9 Å parallel to the surface for a tilt angle of 37° between the porphyrin core and the π–π direction. This angle is observed in crystallographic assemblies of those molecules as well as in former nc-AFM studies [25,26]. Taking also into account a vertical tilt angle, determined by the aryl groups (Figure 1b and Figure 1c), the measured height of the molecules results in a tilt angle in the π–π stack direction of 37° and 43° for the 1ML and the 2ML step, respectively. Both values indicate a stable π–π interaction, while for 3ML steps and higher no stable configurations can be found for a single molecular wire (see Figure 1d). As already visible in Figure 1a, the unordered agglomerates (3) are the source of multi-wire structures. These structures are parallel ordered single molecular wires growing in the $\langle 110 \rangle$ directions on KBr. High-resolution nc-AFM measurements of these structures [26] revealed a separation of the single wires by 2.4 ± 0.2 nm which corresponds to approximately five lattice spacings of the substrate. Pšenčík et al. determined distances between different bacteriochlorophyll stacks of 2.1–3.0 nm in natural chromosomes; the same order of magnitude as observed for the porphyrin assemblies [38]. Since the photon capture crosssection might be markedly increased, hence, leading to higher efficiencies with a broader wavelength range compared to silicon solar cells, such antennae systems are for example also of potential interest for hybrid solar cells that could operate under low or moderate light conditions. Furthermore, porphyrins are known to be very promising building blocks: They are not only very stable, inexpensive and quickly accessible, but also both the periphery and the central metal are very easy to modify. Therefore, such porphyrin wires can be tuned with a high degree of freedom.

FFT-analysis of measurements [26] showing simultaneous molecular and atomic resolution of the substrate revealed that, unlike at step edges in [100] direction, the molecule-to-molecule distance within a wire differs from the KBr lattice spacing. The molecule–molecule separation measures 5.6 Å, compared

to the distance of 4.6 Å between two K^+ ions along the $\langle 110 \rangle$ directions. This indicates that the dimensions of the molecule ask for a larger separation than the K^+ ions intervals could provide, rather corresponding to the spacings observed in the crystal lattice of Balaban et al. [37]. At the steps along the [100] direction, K^+ ions are alternating with Br^- ions creating attractive and repulsive sites for the partially negative charged cyanogroups and therefore forcing them into position. Diagonally across the lattice in $\langle 110 \rangle$ directions, the K^+ ions are evidently closer together and not interrupted by bromine ions, presumably creating a slightly delocalized positive charge distribution. The stacks are directed along one dimension but in contrast to the assemblies at the step edges, the single porphyrins are not located each directly above a potassium ion, but rather along the K^+ chain, keeping their thermodynamically preferred intermolecular spacing. The molecular wires are most likely inclined to the surface, with the cyano-groups pointing downwards and the big side groups standing out more on one side (Figure 2b). Heights between 1.5–2.0 nm were measured for multi-wires, depending on the tilt angle of the stacks respective to the surface.

Figure 2: (a) Topography of cyano-porphyrin molecular wires on a NaCl single crystal surface. In contrast to the growth on KBr, the molecular wires are also oriented along the [100] direction of the substrate. In (b) and (c) the two different growth directions are schematically visualized.

Looking at the spacing of 5.6 Å between the stacked molecules leads to the assumption that NaCl with a lattice constant of 5.65 Å is an ideal substrate to grow multi-wires on. NaCl is chemically and physically similar to KBr and is therefore a good sample to investigate the influence of the lattice distance of the substrate to the self-assemblies. Figure 2a shows an overview nc-AFM image of the molecular assemblies on NaCl(001). The step edges have no specific direction and show no ordered molecular decorations. Regions with steps in $\langle 100 \rangle$ directions show similar single-wire decoration as the KBr(001) surface did. Additionally, we observe a large amount of broader structures growing across the terraces which presumably start

growing from kink sites at the step edges. The main difference which was observed between self-assembly on KBr and NaCl is the tendency of the molecules to form crossing carpets or networks of wires. Figure 2a shows such a network of several wire-junctions. The angles between the structures are not only 90° as observed on KBr but also 45° indicating a growth oriented in all major crystallographic surface directions. The structures along the ⟨100⟩ directions do not differ in shape or thickness from the ones oriented in the ⟨110⟩ directions. The molecules along the ⟨100⟩ directions on NaCl are most certainly adsorbed at every sodium atom. That leads to an intermolecular distance of 5.65 Å making wire growth along this direction more favorable compared to KBr. However, wires along the ⟨110⟩ directions can still grow from kink sites or wire junctions. In Figure 2b and Figure 2c structural models for KBr(001) and NaCl(001) are presented.

To study the influence of a metal substrate on the formation of the molecular wires and assemblies, we evaporated the cyano-porphyrin molecules onto thin KBr films grown on Cu(111). In Figure 3, a series of topographical images can be seen. In (a) a 100×100 nm^2 overview of ordered cyano-porphyrin assemblies on single and double KBr layers is shown. KBr steps in ⟨100⟩ directions of the second ML are decorated by not only one single molecular wire as observed on the bulk material but with a multi-wire. Furthermore, Cu steps indicated by small arrows from the left to the right side of the image overgrown by KBr are also partially decorated by the molecules. Additionally, an assembly is originated from the underlying Cu step and grows towards the lower image edge. It is then interrupted by a conventional wire along a KBr island. Figure 3b and Figure 3c show a 30×30 nm^2 topography image of the assembly, already

revealing submolecular details as well as atomic resolution of the underlying KBr. First, the molecular assembly is not aligned along a certain substrate direction of the KBr layer. The rows are inclined by ≈10° to the [010] direction of the KBr layer. Second, submolecular contrast does not reveal a wire like configuration as observed for the multi-wires on bulk ionic crystals. The molecules lay rather flat on the surface since the whole structure is only 0.9–1.0 nm in height.

These measurements also reveal the relatively weak binding energy of the molecules to the substrate: Already during the change of the set point, parts of the layer on the left lower side were removed while scanning from bottom to top. The first few lines of Figure 3c were scanned with an increased frequency shift of $\Delta f_{1st} = -11$ Hz. After the removal of the first molecules, the set point was lowered to $\Delta f_{1st} = -10$ Hz again. Regardless of that, the tip continued to remove molecules thinning the structure to 50% of its original size. It is remarkable that even though the tip is removing molecules the scan remained absolutely stable and maintained a high resolution ability during all the performed manipulations. The amount of removed molecules and the shape of the resulting structure suggest that the molecules are arranged in a superstructure of about 6–8 nm width. Both columns visible in Figure 3b and Figure 3c show periodic and distinct features proving that they are real submolecular features. Nevertheless, suggesting an appropriate model of the molecular arrangement based only on these measurements has proven to be difficult. However, it can be concluded that the influence of the Cu(111) substrate on the molecular assemblies and wires hinders the formation of mono-and multi-wire cyano-porphyrin assemblies stabilized by an intermolecular π–π interaction.
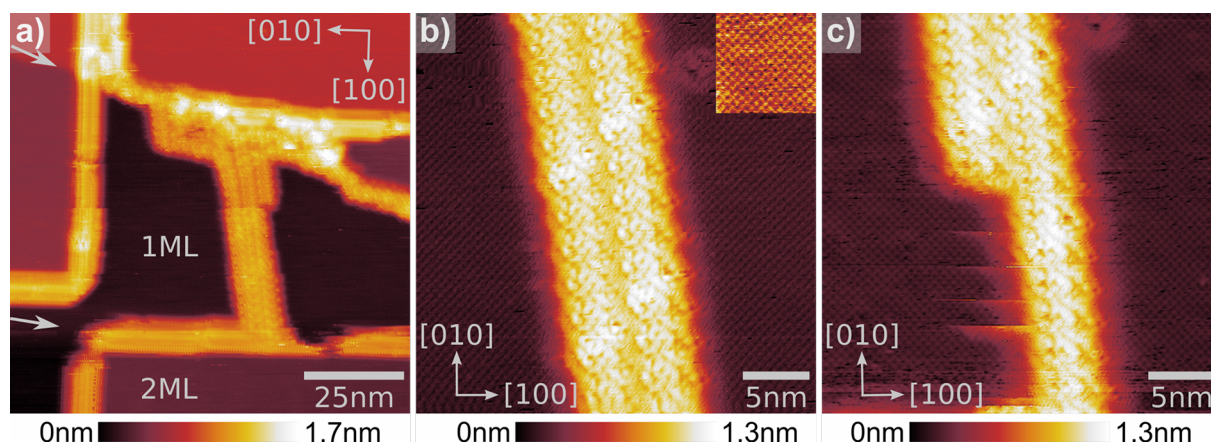

Figure 3: nc-AFM measurements of molecular assemblies grown on an ultrathin KBr layer on Cu(111). (a) 100×100 nm^2 overview of ordered cyano-porphyrin assemblies on single and double KBr layers. (b) and (c) 30×30 nm^2 zoom in of the free standing molecular assembly on a single KBr layer. Clear sub-molecular resolution as well as atomic resolution is observed. After decreasing the set-point, parts of the assembly are removed and the atomic corrugation below becomes visible.
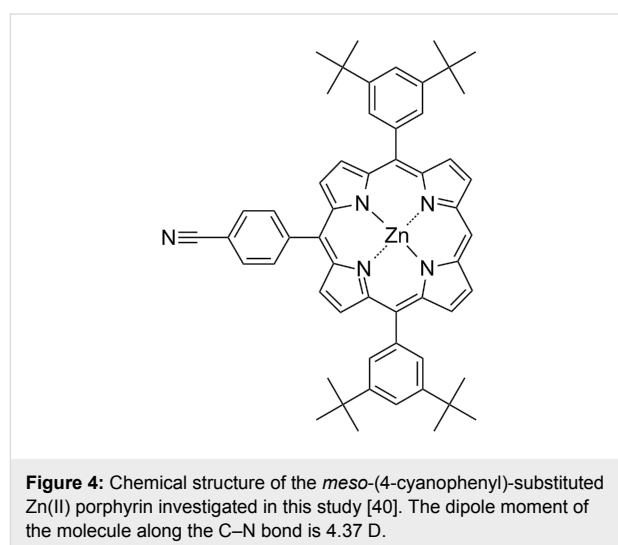
Conclusion

The adsorption of cyano-porphyrin molecules was studied for bulk KBr and NaCl samples and resulted in various reproducible assemblies on the surfaces. Especially step edges and kinks of the alkali halide crystals act as trapping points for the polar molecules, preventing them from diffusing freely over the surface. Simultaneously, intermolecular interactions force the cyano-porphyrins to form π–π stacks. These wires grow along the edges, forming long one-dimensional molecular structures. The growth is affected by the potential corrugation at the step edge which forces the negatively charged nitrogen atom of the cyano-porphyrin to sit on top of a positively charged ion. This results in an intermolecular distance corresponding to the lattice constant of the underlying substrate. At increased molecule coverages, two-dimensional arrays start to grow away from the steps across the terraces. The preferred growth orientation is the (110) direction on KBr while on NaCl also assemblies oriented in (100) direction are found. The different growth mode is directed by the lattice spacing of the underlying substrate and the equilibrium distance of the π–π interaction of the molecules. The absorption behavior of the cyano-porphyrins was also studied on ultrathin KBr films on Cu(111). We have shown that KBr thin films can be used as a substrate for the molecular assemblies at room temperature. Nevertheless, the first layers of KBr are still not sufficient to decouple the molecules completely from the underlying Cu substrate. On areas close to an underlying copper step, porphyrins grow in a hexagonal lattice structure and are probably adsorbed with their core more parallel to the surface loosing their intermolecular π–π stacking.

Experimental

Experiments were performed under ultrahigh vacuum (UHV) conditions with a base pressure below 10^{-10} mbar using a home built non-contact atomic force microscope operated at rt [39]. In the nc-AFM mode, the tip-sample distance is usually controlled by maintaining a constant shift of the first flexural resonance frequency f_{1st} with respect to the resonance far from the surface. Highly doped silicon cantilevers with integrated tips (Nanosensors, NCL), a typical resonance frequency $f_{1st} \approx 160$ kHz and a spring constant $k \approx 30$ N/m were employed as a force sensor. The typical oscillation amplitude measures about $A_{1st} \approx$ 5–20 nm. The cantilevers were annealed in UHV (30 min at 120 °C) and sputtered (1–2 min at 680 eV) with Ar$^+$ ions for cleaning. In the experiments reported here, *meso*-(4-cyanophenyl)-substituted Zn(II) porphyrin (cyano-porphyrin, Figure 4) was thermally evaporated from a Knudsen cell at 160 °C (with a rate of the order of 10 Å/min) onto bulk crystals of NaCl and KBr as well as on ultrathin KBr layers on a Cu(111) substrate. During evaporation the samples were held at 80 °C to enhance the diffusion of the molecules at the surface. The synthesis of the cyano-porphyrin molecules has been described in detail in [40]. The bulk crystals were cleaved in UHV followed by an annealing step at 150 °C to reduce surface charges. In our experiments we used additionally a Cu(111) surface which was prepared in UHV according to regular surface science techniques by several cycles of Ar$^+$ ion bombardment and subsequent annealing to 520 °C. KBr thin films were deposited on the clean Cu(111) substrates by sublimation, using a temperature controlled Knudsen cell. As a source material, crushed salt powder obtained from alkali halide single crystals was used. In order to obtain thin layers of KBr, choosing a very low evaporation rate of ≈0.2 Å/min proved to be successful.

Figure 4: Chemical structure of the *meso*-(4-cyanophenyl)-substituted Zn(II) porphyrin investigated in this study [40]. The dipole moment of the molecule along the C–N bond is 4.37 D.

Acknowledgements

References

1. Kawai, S.; Maier, S.; Glatzel, T.; Koch, S.; Such, B.; Zimmerli, L.; Fendt, L.-A.; Diederich, F.; Meyer, E. *Appl. Phys. Lett.* **2009,** *95,* 103109. doi:10.1063/1.3216057
2. Kay, E. R.; Leigh, D. A.; Zerbetto, F. *Angew. Chem., Int. Ed.* **2007,** *46,* 72–191. doi:10.1002/anie.200504313
3. Douglas, P. *Supramolecular chemistry: Concepts and perspectives;* VCH: Weinheim, Germany, 1996.
4. Whitesides, G. M.; Mathias, J. P.; Seto, C. T. *Science* **1991,** *254,* 1312–1319. doi:10.1126/science.1962191
5. Jung, T. A.; Schlittler, R. R.; Gimzewski, J. K. *Nature* **1997,** *386,* 696–698. doi:10.1038/386696a0
6. Bonifazi, D.; Spillmann, H.; Kiebele, A.; de Wild, M.; Seiler, P.; Cheng, F.; Güntherodt, H. J.; Jung, T.; Diederich, F. *Angew. Chem., Int. Ed.* **2004,** *43,* 4759–4763. doi:10.1002/anie.200460562

7. Schreiber, F. *Prog. Surf. Sci.* **2000,** *65,* 151–257.
doi:10.1016/S0079-6816(00)00024-1

8. De Feyter, S.; De Schryver, F. C. *Chem. Soc. Rev.* **2003,** *32,* 139–150.
doi:10.1039/b206566p

9. Rosei, F.; Schunack, M.; Naitoh, Y.; Jiang, P.; Gourdon, A.;
Laegsgaard, E.; Stensgaard, I.; Joachim, C.; Besenbacher, F.
Prog. Surf. Sci. **2003,** *71,* 95–146.
doi:10.1016/S0079-6816(03)00004-2

10. Tanaka, S.; Suzuki, H.; Inada, M.; Kamikado, T.; Mashiko, S.
Nanotechnology **2005,** *16,* S107–S111.
doi:10.1088/0957-4484/16/3/020

11. Tanaka, S.; Suzuki, H.; Kamikado, T.; Mashiko, S. *Thin Solid Films*
2003, *438–439,* 56–60. doi:10.1016/S0040-6090(03)00758-2

12. Yokoyama, T.; Yokoyama, S.; Kamikado, T.; Okuno, Y.; Mashiko, S.
Nature **2001,** *413,* 619–621. doi:10.1038/35098059

13. Spillmann, H.; Kiebele, A.; Stöhr, M.; Jung, T. A.; Bonifazi, D.;
Cheng, F.; Diederich, F. *Adv. Mater.* **2006,** *18,* 275–279.
doi:10.1002/adma.200501734

14. Repp, J.; Meyer, G.; Paavilainen, S.; Olsson, F. E.; Persson, M.
Science **2006,** *312,* 1196–1199. doi:10.1126/science.1126073

15. Gross, L.; Mohn, F.; Liljeroth, P.; Repp, J.; Giessibl, F. J.; Meyer, G.
Science **2009,** *324,* 1428–1431. doi:10.1126/science.1172273

16. Meyer, E.; Glatzel, T. *Science* **2009,** *324,* 1397–1398.
doi:10.1126/science.1175869

17. Nony, L.; Bennewitz, R.; Pfeiffer, O.; Gnecco, E.; Baratoff, A.;
Meyer, E.; Eguchi, T.; Gourdon, A.; Joachim, C. *Nanotechnology* **2004,**
15, S91–S96. doi:10.1088/0957-4484/15/2/019

18. Kunstmann, T.; Schlarb, A.; Fendrich, M.; Wagner, T.; Möller, R.;
Hoffmann, R. *Phys. Rev. B* **2005,** *71,* 121403.
doi:10.1103/PhysRevB.71.121403

19. Fendrich, M.; Kunstmann, T.; Paulkowski, D.; Möller, R.
Nanotechnology **2007,** *18,* 084004.
doi:10.1088/0957-4484/18/8/084004

20. Burke, S. A.; Ji, W.; Mativetsky, J. M.; Topple, J. M.; Fostner, S.;
Gao, H. J.; Guo, H.; Grütter, P. *Phys. Rev. Lett.* **2008,** *100,* 186104.
doi:10.1103/PhysRevLett.100.186104

21. Mativetsky, J. M.; Burke, S. A.; Fostner, S.; Grütter, P. *Nanotechnology*
2007, *18,* 105303. doi:10.1088/0957-4484/18/10/105303

22. Mativetsky, J. M.; Burke, S. A.; Fostner, S.; Grütter, P. *Small* **2007,** *3,*
818–821. doi:10.1002/smll.200600699

23. Fendrich, M.; Lange, M.; Weiss, C.; Kunstmann, T.; Möller, R.
J. Appl. Phys. **2009,** *105,* 094311. doi:10.1063/1.3122253

24. Burke, S. A.; Mativetsky, J. M.; Fostner, S.; Grütter, P. *Phys. Rev. B*
2007, *76,* 035419. doi:10.1103/PhysRevB.76.035419

25. Zimmerli, L.; Maier, S.; Glatzel, T.; Gnecco, E.; Pfeiffer, O.;
Diederich, F.; Fendt, L.; Meyer, E. *J. Phys.: Conf. Ser.* **2007,** *61,*
1357–1360. doi:10.1088/1742-6596/61/1/268

26. Maier, S.; Fendt, L.-A.; Zimmerli, L.; Glatzel, T.; Pfeiffer, O.;
Diederich, F.; Meyer, E. *Small* **2008,** *4,* 1115–1118.
doi:10.1002/smll.200701259

27. Glatzel, T.; Zimmerli, L.; Meyer, E. *Isr. J. Chem.* **2008,** *48,* 107–116.

28. Glatzel, T.; Zimmerli, L.; Koch, S.; Kawai, S.; Meyer, E.
Appl. Phys. Lett. **2009,** *94,* 063303. doi:10.1063/1.3080614

29. Gross, L.; Schlittler, R. R.; Meyer, G.; Fendt, L.-A.; Diederich, F.;
Glatzel, T.; Kawai, S.; Koch, S.; Meyer, E.
*J. Vac. Sci. Technol., B: Microelectron. Nanometer Struct.–Process., M
eas., Phenom.* **2010,** *28,* C4D34–C4D39. doi:10.1116/1.3292601

30. Schütte, J.; Bechstein, R.; Rohlng, M.; Reichling, M.; Kühnle, A.
Phys. Rev. B **2009,** *80,* 205421. doi:10.1103/PhysRevB.80.205421

31. Nony, L.; Gnecco, E.; Baratoff, A.; Alkauskas, A.; Bennewitz, R.;
Pfeiffer, O.; Maier, S.; Wetzel, A.; Meyer, E.; Gerber, C. *Nano Lett.*
2004, *4,* 2185–2189. doi:10.1021/nl048693v

32. Such, B.; Trevethan, T.; Glatzel, T.; Kawai, S.; Zimmerli, L.; Meyer, E.;
Shluger, A. L.; Amijs, C. H. M.; de Mendoza, P.; Echavarren, A. M.
ACS Nano **2010,** *4,* 3429–3439. doi:10.1021/nn100424g

33. Rahe, P.; Nimmrich, M.; Greuling, A.; Schutte, J.; Stara, I. G.;
Rybacek, J.; Huerta-Angeles, G.; Stary, I.; Rohlng, M.; Kühnle, A.
J. Phys. Chem. C **2010,** *114,* 1547–1552. doi:10.1021/jp911287p

34. Bennewitz, R.; Schär, S.; Barwich, V.; Pfeiffer, O.; Meyer, E.; Krok, F.;
Such, B.; Kolodzej, J.; Szymonski, M. *Surf. Sci.* **2001,** *474,* L197–L202.
doi:10.1016/S0039-6028(00)01053-0

35. Bammerlin, M.; Lüthi, R.; Meyer, E.; Baratoff, A.; Lü, J.;
Guggisberg, M.; Gerber, C.; Howald, L.; Güntherodt, H.-J.
Probe Microsc. **1997,** *1,* 3.

36. Bammerlin, M.; Lüthi, R.; Meyer, E.; Baratoff, A.; Lü, J.;
Guggisberg, M.; Loppacher, C.; Gerber, C.; Güntherodt, H.-J.
Appl. Phys. A: Mater. Sci. Process. **1998,** *66,* S293–S294.
doi:10.1007/s003390051148

37. Balaban, T. S.; Linke-Schaetzel, M.; Bhise, A. D.; Vanthuyne, N.;
Roussel, C.; Anson, C. E.; Buth, G.; Eichhöfer, A.; Foster, K.;
Garab, G.; Gliemann, H.; Goddard, R.; Javorfi, T.; Powell, A. K.;
Rösner, H.; Schimmel, T. *Chem.–Eur. J.* **2005,** *11,* 2267–2275.
doi:10.1002/chem.200400664

38. Pšencík, J.; Arellano, J. B.; Ikonen, T. P.; Borrego, C. M.;
Laurinmäki, P. A.; Butcher, S. J.; Serimaa, R. E.; Tuma, R. *Biophys. J.*
2006, *91,* 1433–1440. doi:10.1529/biophysj.106.084228

39. Howald, L.; Meyer, E.; Lüthi, R.; Haefke, H.; Overney, R.; Rudin, H.;
Güntherodt, H. J. *Appl. Phys. Lett.* **1993,** *68,* 117–119.
doi:10.1063/1.109732

40. Cheng, F.; Zhang, S.; Adronov, A.; Echegoyen, L.; Diederich, F.
Chem.–Eur. J. **2006,** *12,* 6062–6070. doi:10.1002/chem.200600126

Switching adhesion forces by crossing the metal–insulator transition in Magnéli-type vanadium oxide crystals

Bert Stegemann[*1,2], Matthias Klemm[3], Siegfried Horn[3] and Mathias Woydt[2]

Full Research Paper

Abstract

Magnéli-type vanadium oxides form the homologous series V_nO_{2n-1} and exhibit a temperature-induced, reversible metal–insulator first order phase transition (MIT). We studied the change of the adhesion force across the transition temperature between the cleavage planes of various vanadium oxide Magnéli phases (n = 3 … 7) and spherical titanium atomic force microscope (AFM) tips by systematic force–distance measurements with a variable-temperature AFM under ultrahigh vacuum conditions (UHV). The results show, for all investigated samples, that crossing the transition temperatures leads to a distinct change of the adhesion force. Low adhesion corresponds consistently to the metallic state. Accordingly, the ability to modify the electronic structure of the vanadium Magnéli phases while maintaining composition, stoichiometry and crystallographic integrity, allows for relating frictional and electronic material properties at the nano scale. This behavior makes the vanadium Magnéli phases interesting candidates for technology, e.g., as intelligent devices or coatings where switching of adhesion or friction is desired.

Introduction

Thermally controlled metal–insulator transitions (MIT) are observed in a large number of crystalline and amorphous semiconductors. Particularly among the transition metal oxides, there are numerous compounds with partially filled electron bands, which show insulator behavior at low temperatures, although they should be metals with respect to the band model. Well-known examples are Magnéli-type vanadium oxide compounds, which form the homologous series V_nO_{2n-1} ($3 \leq n \leq 10$) and which undergo an abrupt transition from metallic to insulating behavior and vice versa by a change of

external parameters such as doping, pressure or temperature, even although the global stoichiometry remains unchanged [1,2]. Thereby, the electrical resistance changes by many orders of magnitude. The physical reason for this metal–insulator transition (MIT) is the correlation of d band electrons of opposite spins as explained by the Mott–Hubbard model [3].

It was first recognized by Magnèli et al., that oxides of titanium and vanadium as well as those of molybdenum and tungsten form homologous series with planar faults of general formulae $(Ti,V)_nO_{2n-1}$ or $(W,Mo)_nO_{3n-1}$ [4-6]. In a simplified way, the Magnèli phase structure can be derived from a perfect V_2O_5 crystal, which has one missing oxygen layer, i.e., the (121) plane, which is called the crystallographic shear (CS) plane and compensates for the non-stoichiometry of the compounds. The different stoichiometries result from different spacings between the CS planes and appear to be stable at high temperature before dissolving as point defects. The CS planes interact over rather large distances ($\approx$100 Å or more) to form regular or nearly regular arrays in an otherwise perfect crystal. The overall stoichiometry of the resulting crystals depends upon the width of the particular crystallographic plane in which the CS occurs. As a consequence, a homologous series of structures is formed [7,8].

The special electrical as well as optical properties of the Magnèli phases are of great interest not only for basic research but also for future technological applications [9-11]. Therefore, materials with correlated electrons play a major role, e.g., for the construction of switches and sensors and, more generally, for the development of novel electronic devices and micro-electro-mechanical systems (MEMS). In this context, a great technological challenge in advancing miniaturization is to overcome the strong adhesive attractions between nanoscopic tribo-elements in order to realize technical systems with low friction [12,13].

The atomic force microscope (AFM) has become a powerful tool for measuring the forces interacting between a sharp tip and a solid sample surface, such as van der Waals forces and short-range chemical forces [14-17]. Typically, the AFM is used for a spatially resolved imaging of forces, which requires a tip with a sharp apex. However, such tips are disadvantageous for quantitative measurements of interfacial forces, because reliable and accurate determination of the tip geometry and also comparison with theoretical predictions are difficult. In contrast, utilizing a microsphere attached to the free end of the cantilever instead of a sharp tip provides a well-defined, theoretically controllable sphere versus flat surface geometry for the scaling of forces [18-21]. Furthermore, it allows customizing of the probe material and size. This method, also referred to as spherical-probe

or colloidal-probe AFM technique, is thus better suited for quantitative and comparative adhesion force measurements [22-24]. Previously, the applicability and the sensitivity of the AFM in the spherical probe configuration (i.e., with a microsphere as a probe tip) operated under ultrahigh vacuum conditions for the quantification of adhesion forces on metal single crystals was demonstrated [25].

In our approach, adhesion forces were assessed by sensing the force interaction between the cleavage planes of four different Magnèli-type vanadium oxide single crystals (V_nO_{2n-1}, $n = 3, 4, 6, 7$) and a micro-spherical titanium AFM probe as a function of the probe/sample separation under UHV conditions, where environmental influence is eliminated and advantage of surface preparation and analysis tools can be taken. The MIT was induced by appropriate variation of temperature. In particular, we report on the change of the adhesion force when crossing the MIT temperature and correlate this behavior to the corresponding phase transition.

Results and Discussion

Adhesion force measurements were carried out on the cleavage planes of the vanadium oxide both at room temperature (298 K) and at an appropriate temperature beyond the MIT. According to the measurement temperatures indicated in Figure 1, for V_4O_7 and V_6O_{11} a sample temperature of 120 K and for V_3O_5 a sample temperature of 540 K was chosen in order to cross the MIT temperature. As a reference, V_7O_{13} which exists solely in the metallic phase and which does not exhibit an MIT (i.e., $T_{MIT} = 0$ K) was measured at all three temperatures.
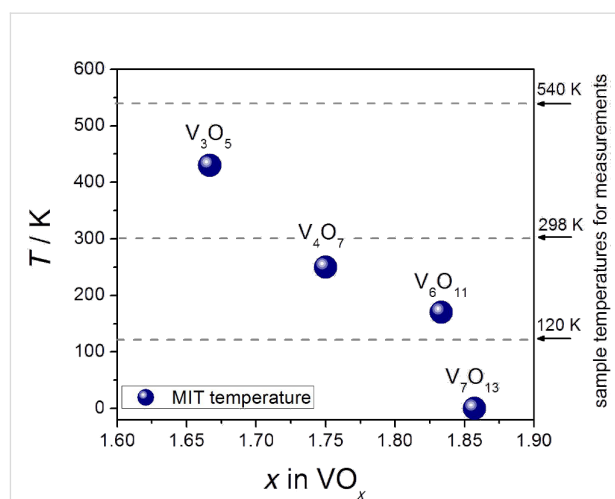

Figure 1: Metal–insulator transition (MIT) temperatures of the investigated Magnèli-type vanadium oxide crystals [1,26]. V_7O_{13} does not show an MIT. The right scale shows temperatures where force measurements were carried out to probe the metallic and the insulating state of each sample.

Before acquisition of the force–distance curves, the topography of the vanadium oxide cleavage was characterized by contact mode AFM using a conventional sharp tip. Topography is of importance for the study of adhesion forces since all realistic surfaces normally exhibit some degree of roughness. Surface roughness is expected to decrease the actual area of contact and reduce the measured adhesion force. However, Magnéli-type vanadium oxides possess a layered structure with a planar oxygen defect [2] and can be easily cleaved to provide atomically flat substrates. This is shown in Figure 2 for the case of the V_4O_7 cleavage plane, exhibiting atomically flat terraces with lateral extensions of up to several microns. A rough estimation of the apparent sphere/flat surface contact area according to the Hertzian theory of deformation by taking into account the deformation properties of the materials leads to a diameter of about 40 nm [18,27]. The terraces are by far wider than this value and, thus, well suited for reliable measurements of adhesion forces.
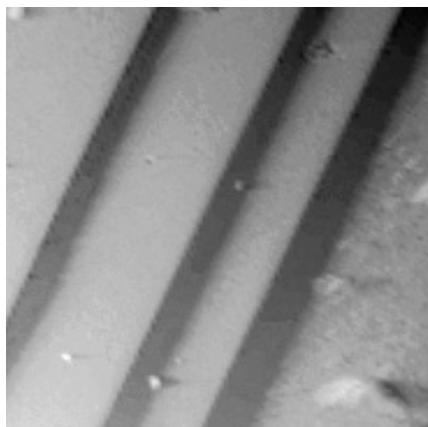

Figure 3: Typical force (*F*) vs distance (*x*) curves obtained on V_4O_7 for single measurements of a spherical Ti tip (diameter 7.2 µm) against the flat crystal plane at 120 K and 298 K. The curves show the force interaction during approach and retraction of the tip from the surface. The adhesion force corresponds to the pull-off force between the tip and sample surface.

Figure 2: Contact mode AFM topograph of the V_4O_7 crystal cleavage plane. Scanning size: 25 × 25 µm², z-range 1 µm.

Typical force–distance curves of single measurements obtained on V_4O_7 above and below the MIT temperature are shown in Figure 3. The plot shows the force interaction during approach and retraction of the spherical AFM tip from the sample surface. During retraction the tip adheres to the sample until the spring constant of the cantilever overcomes the adhesion force and the cantilever instantaneously jumps out of contact back into its equilibrium position. The force necessary to pull-off the cantilever represents, to a first approximation, the adhesion force [24,28].

The graphs in Figure 4 provide an analysis of the adhesion forces acquired at the V_4O_7 cleavage plane at 120 K (i.e., below the MIT temperature) and at 298 K (i.e., above the MIT temperature). Displayed are the sequences of the measured data
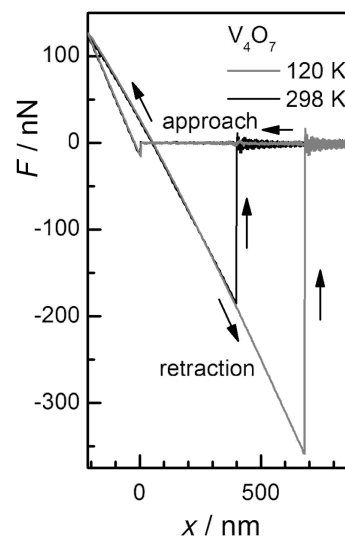
and the frequency distributions for both temperatures. Some 50 to 80 force measurements at different spots all over the surface were made. All measurements were carried out at intermediate retraction velocities and at low loads, so that the behavior of the contact is dominated by the action of surface forces [29,30]. Each data point was checked for reproducibility by at least two consecutive measurements.

It was found that throughout the measurements on the same surface spot the adhesion force remains rather constant, indicating that the tip did not change significantly during successive force curve acquisition. However, when acquiring force–distance curves at different positions on the surface plane there was some scatter in the data. This scatter might be explained by topographic effects, i.e., interaction with cleavage steps (cf. Figure 2) or slight surface heterogeneities resulting in variations of the interaction geometry. The values given in the graphs (right column) are the data averages and their standard deviations. By comparing these two curves, it is instantly obvious that the adhesion force below the MIT is significantly higher than above the MIT (cf. Figure 5a). Accordingly, the lower adhesion force corresponds to the metallic vanadium oxide phase. Since contact models of a sphere/flat surface geometry [19,20] predict a linear dependence of the adhesion force on the sphere radius, all measured adhesion forces are normalized in this graph to the value obtained above the MIT temperature – corresponding to the metallic phase. Thus comparison between measurements carried out with different micro-
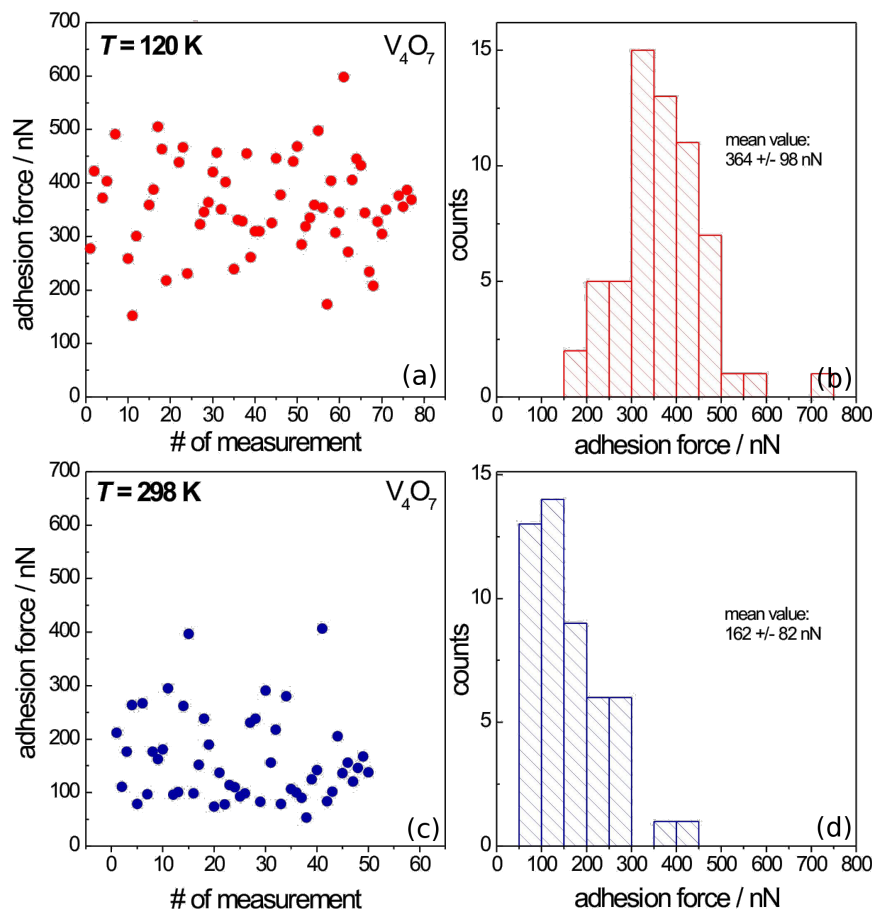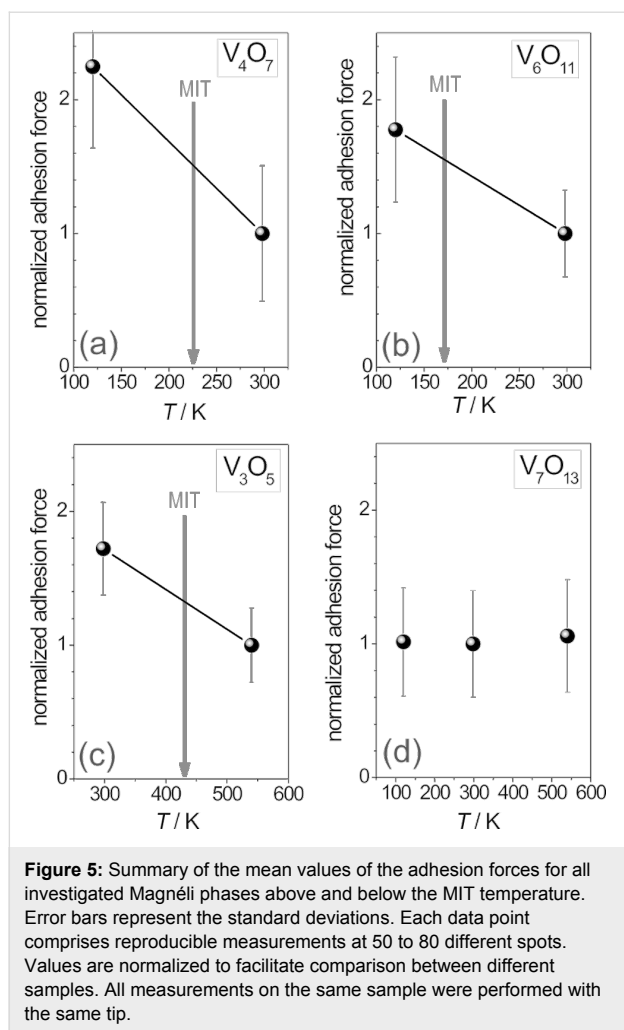
Figure 4: Statistical analysis of the adhesion forces acquired at the V_4O_7 cleavage plane at (a, b) 120 K and (c, d) 298 K. Displayed are (a, c) the sequences of data points acquired at different surface spots and (b, d) the normalized frequency distributions. The numbers given are the data averages and their standard deviations.

spherical tips is facilitated. Error bars correspond to the standard deviation of the mean value as obtained from the statistical data analysis (cf. Figure 4).

For the measurements on the cleavage plane of the V_6O_{11} crystal, as well as of the V_3O_5 and V_7O_{13} crystals, the same procedure of data acquisition and data evaluation was followed. The summary of the statistical analysis of the adhesion forces acquired on V_6O_{11} at 120 K and 298 K, respectively, is shown in Figure 5b. Again, there is a distinct jump in the adhesion going to low temperatures and crossing the MIT temperature. This is well in accord with the results on V_4O_7. According to Figure 2, for V_3O_5 the sample temperature had to be raised above 430 K in order to cross the MIT temperature. As shown in Figure 5c, in this case the adhesion force significantly drops, which is consistent to the observations on the previous samples because again the metallic phase exhibits the lower adhesion force. V_7O_{13} is known to undergo no phase transition neither when the sample is cooled down nor when heated up. Rather it

maintains its metallic state. Due to this feature the V_7O_{13} phase acted as reference sample in order to prove that the observed jump in the adhesion force is not simply a temperature-related artifact but rather due to the phase transformation in the crystal. The measurements reveal that in this case the adhesion force remains indeed constant when going to high or low temperatures (see Figure 5d). This behavior clearly indicates that the jump in the adhesion force is correlated to the change in the electronic properties of vanadium oxide crystals due the phase transformation when crossing the MIT temperature.

For the investigated Magnéli-type oxides with a MIT, the adhesion force of the insulating phase is roughly twice as high as in the metallic state. This behavior is in contrast to observations at the macroscale [31], but it can be related to the distortion of the crystal structure and the distinct change of conductivity occurring at the MIT. In theory, the interaction of an ideal sphere with an atomically flat surface is, e.g., described by the Derjaguin–Muller–Toporov (DMT) model [20] or the

Figure 5: Summary of the mean values of the adhesion forces for all investigated Magnéli phases above and below the MIT temperature. Error bars represent the standard deviations. Each data point comprises reproducible measurements at 50 to 80 different spots. Values are normalized to facilitate comparison between different samples. All measurements on the same sample were performed with the same tip.

Conclusion

The adhesion forces of Magnéli-type phases of vanadium oxide, acquired by means of force–distance measurements with a spherical AFM probe, show a distinct response to the temperature-induced metal–insulator transition. This behavior makes the vanadium Magnéli phases interesting candidates for technological applications where switching of adhesion or friction is desired, such as intelligent devices or coatings. At the nanoscale, these adhesion measurements displayed a lower adhesion force in the metallic state than in the non-metallic, ceramic state, which is in contrast to the macroscopic experience in tribology. In accord with several recent examples, this study indicates that tribological properties at the nanoscale cannot be predicted directly from macroscopic laws [35]. Detailed measurements are in progress to obtain a better understanding of the observed phenomenon. An extension of this study to further materials revealed consistent results: Comparative adhesion force measurements of the (0001) basal planes and the (10−10) prism planes of highly oriented pyrolytic graphite (HOPG) and MoS_2 also showed that the metallic state lowers the adhesion at the nanoscale [36].

Experimental
Vanadium oxide crystal preparation

Single crystals of the vanadium oxide Magnéli phases were grown in vacuum sealed quartz tubes in a gradient furnace. The chemical transport reaction, using $TeCl_4$ as a transport agent took nearly six weeks. The growth temperature was 600 °C. The different phases were prepared by adjusting the oxygen content by means of a definite mixture of the starting vanadium oxides V_2O_3 and VO_2 [37]. Under such conditions crystals of exclusively one Magnéli phase per tube could be obtained, several of which showed specular surfaces. X-Ray diffraction (XRD) and magnetic susceptibility measurements on representative crystals of all the batches were carried out to characterize the quality of the crystals. The MIT temperatures of the samples under study in the present work are displayed in Figure 1.

Spherical AFM probe preparation

The spherical AFM probes were prepared by attaching a microsphere of the desired size and material to the end of AFM cantilevers using an *x*-*y*-*z*-micromanipulator and an optical microscope. For the experiments presented here, titanium microspheres (Alfa Aesar GmbH) were conductively glued to the free end of tipless NSC12 cantilevers (Silicon-MDT Ltd.). The successful attachment of the spheres was verified by scanning electron microscopy (SEM), as shown in Figure 6. The titanium microspheres have a smooth surface and show normally an elastic response. In situ characterization of the spherical tips was performed by reverse tip imaging with the calibration grating TGT01 (Silicon-MDT Ltd.), which consists

Johnson–Kendall–Roberts (JKR) model [19]. These two models improved the Hertzian theory [18] by including the effect of adhesion and present the limiting cases of more general contact theories by Maugis [32]. Both models have in common that the pull-off-force is independent of the elastic material properties but is essentially a linear function not only of the sphere radius but also of the surface energy of the sample. At the MIT the crystal structure of the Magnéli phases is distorted resulting in a slightly higher density in the metallic phase [33] and an increase of the atomic density at the surface. A decrease of the surface energy [34] and hence a decrease of the adhesion force is expected, as was observed in the experiments.

Furthermore, the distinct increase of conductivity will lead to a better screening of trapped charge defects in the surface and therefore decrease the electrostatic contribution of the overall adhesion force. However, reference measurements with a silica microsphere on V_3O_5 showed the same qualitative behavior, i.e., a lower adhesion force in the metallic state. Accordingly, a possible tip-induced electrostatic contact charging is negligible.

of an array of sharp spikes [25,38,39]. Scanning this grating with a spherical AFM probe creates an image consisting of an array of spherical caps, i.e., the microsphere itself is imaged repeatedly by each spike in the scanning area. This technique allows the precise determination of the shape and radius of the microsphere. Moreover, there is the possibility of easy in situ re-examination of the spherical probe under UHV conditions to reveal shape deformation or material take-up possibly occurring during the experiment.
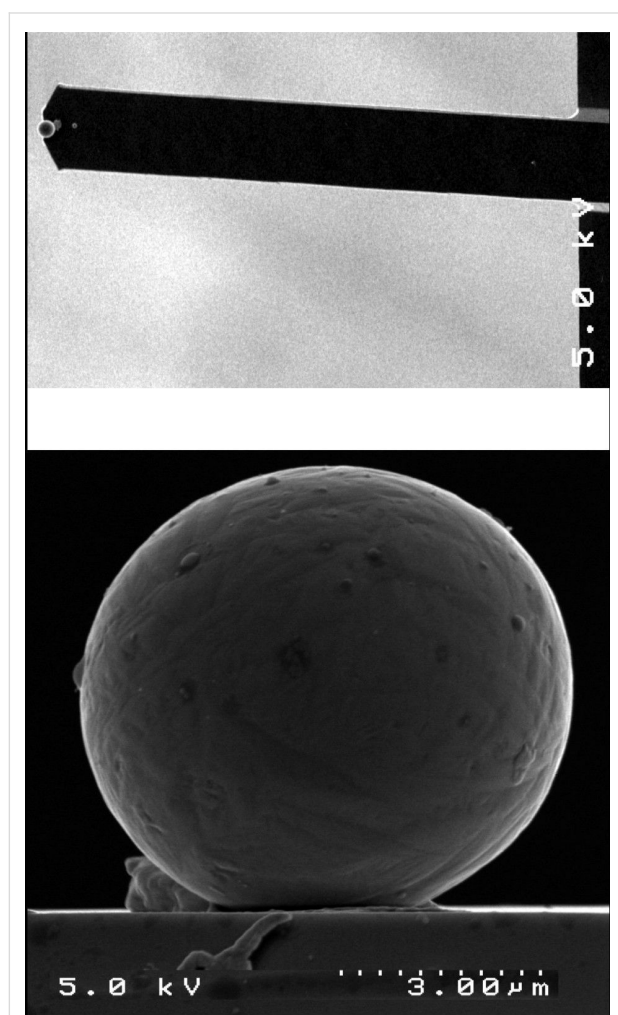

Figure 6: SEM images of a Ti microsphere (diameter 7.2 μm) attached at the free end of a single beam tipless AFM cantilever.

Adhesion force measurements

The crystals were cleaved under ambient conditions, then immediately transferred into the UHV apparatus and degassed for a few hours. The UHV apparatus consists of two directly coupled chambers with a base pressure of $<6 \times 10^{-11}$ mbar. The preparation chamber is equipped with sample heating and cleaning faculties. The analysis chamber houses a variable temperature scanning probe microscope (Omicron Nanotech-

nology, Germany), which allows AFM measurements at sample temperatures in the range from 120 K to 1000 K by either cooling with liquid N_2 or radiative heating. Temperature measurements were made with a thermocouple attached to the sample acceptance stage. The actual temperature of the sample plates is taken from a calibration curve with an accuracy of ±20 K as provided by the manufacturer.

The spring constant of the cantilevers with attached microsphere (typically 3.0 ± 0.2 N/m) was determined by means of the reference cantilever technique, where the cantilever under test was deflected in situ against a cantilever with a precisely known spring constant [40,41]. The spring constant of the reference cantilever (Park Scientific Instruments) was determined by a calculation based on geometrical dimensions and resonance frequency, as determined from SEM images and scanning laser vibrometry measurements, respectively.

For reliable comparison of the data acquired on a certain sample, only adhesion forces obtained with one and the same tip were taken into account. To facilitate comparison between different samples where different spherical tips had to be used, adhesion force values were normalized.

Acknowledgments

References

1. Brückner, W.; Oppermann, H.; Reichelt, W.; Terukow, J. I.; Tschudnowski, F. A.; Wolf, E. *Vanadiumoxide;* Akademie-Verlag: Berlin, 1983.
2. Schwingenschlögl, U.; Eyert, V. *Ann. Phys. (Weinheim, Ger.)* **2004,** *13,* 475–510. doi:10.1002/andp.200410099
3. Hubbard, J. *Proc. R. Soc. London, Ser. A* **1963,** *276,* 238–257. doi:10.1098/rspa.1963.0204
4. Magnéli, A. *Acta Crystallogr.* **1953,** *6,* 495–500. doi:10.1107/S0365110X53001381
5. Andersson, S.; Magnéli, A. *Naturwissenschaften* **1956,** *43,* 495–496. doi:10.1007/BF00632520
6. Magnéli, A.; Andersson, S.; Westmann, S.; Kihlborg, L.; Holmberg, B.; Åsbrink, S.; Nordmark, C. *Final technical report 1, DA-91-591-EUC-935;* Stockholms Universitet: Stockholm, 1959.
7. Woydt, M.; Skopp, A.; Dörfel, I.; Witke, K. *Wear* **1998,** *218,* 84–95. doi:10.1016/S0043-1648(98)00181-1
8. Surnev, S.; Ramsey, M. G.; Netzer, F. P. *Prog. Surf. Sci.* **2003,** *73,* 117–165. doi:10.1016/j.progsurf.2003.09.001
9. Babulanam, S. M.; Eriksson, T. S.; Niklasson, G. A.; Granqvist, C. G. *Sol. Energy Mater.* **1987,** *16,* 347–363. doi:10.1016/0165-1633(87)90029-3
10. Lopez, R.; Boatner, L. A.; Haynes, T. E.; Haglund, R. F.; Feldman, L. C. *Appl. Phys. Lett.* **2004,** *85,* 1410–1412. doi:10.1063/1.1784546

11. Perucchi, A.; Baldassarre, L.; Postorino, P.; Lupi, S. *J. Phys.: Condens. Matter* **2009,** *21,* 323202–323218. doi:10.1088/0953-8984/21/32/323202
12. Woydt, M. *Tribol. Lett.* **2000,** *8,* 117–130. doi:10.1023/A:1019170831371
13. DelRio, F. W.; de Boer, M. P.; Knapp, J. A.; Reedy, E. D., Jr.; Clews, P. J.; Dunn, M. L. *Nat. Mater.* **2005,** *4,* 629–634. doi:10.1038/nmat1431
14. Carpick, R. W.; Salmeron, M. *Chem. Rev.* **1997,** *97,* 1163–1194. doi:10.1021/cr960068q
15. Bhushan, B., Ed. *Handbook of Micro/Nanotribology,* 2nd ed.; CRC Press: Boca Raton, 1999.
16. Lantz, M. A.; Hug, H. J.; Hoffmann, R.; van Schendel, P. J. A.; Kappenberger, P.; Martin, S.; Baratoff, A.; Güntherodt, H.-J. *Science* **2001,** *291,* 2580–2583. doi:10.1126/science.1057824
17. Sugimoto, Y.; Pou, P.; Abe, M.; Jelinek, P.; Pérez, R.; Morita, S.; Custance, O. *Nature* **2007,** *446,* 64–67. doi:10.1038/nature05530
18. Hertz, H. *Journal für die reine und angewandte Mathematik* **1882,** *92,* 156–171. doi:10.1515/crll.1882.92.156
19. Johnson, K. L.; Kendall, K.; Roberts, A. D. *Proc. R. Soc. London, Ser. A* **1971,** *324,* 301–313. doi:10.1098/rspa.1971.0141
20. Derjaguin, B. V.; Muller, V. M.; Toporov, Y. P. *J. Colloid Interface Sci.* **1975,** *53,* 314–326. doi:10.1016/0021-9797(75)90018-1
21. Schwarz, U. D. *J. Colloid Interface Sci.* **2003,** *261,* 99–106. doi:10.1016/S0021-9797(03)00049-3
22. Ducker, W. A.; Senden, T. J.; Pashley, R. M. *Nature* **1991,** *353,* 239–241. doi:10.1038/353239a0
23. Kappl, M.; Butt, H.-J. *Part. Part. Syst. Charact.* **2002,** *19,* 129–143. doi:10.1002/1521-4117(200207)19:3<129::AID-PPSC129>3.0.CO;2-G
24. Butt, H.-J.; Cappella, B.; Kappl, M. *Surf. Sci. Rep.* **2005,** *59,* 1–152. doi:10.1016/j.surfrep.2005.08.003
25. Stegemann, B.; Backhaus, H.; Kloss, H.; Santner, E. Spherical AFM probes for adhesion force measurements on metal single crystals. In *Modern Research and Educational Topics in Microscopy, Series 3;* Méndez-Vilas, A.; Díaz, J., Eds.; Formatex: Badajoz, Spain, 2007; Vol. 2, pp 820–827.
26. Kachi, S.; Kosuge, K.; Okinaka, H. *J. Solid State Chem.* **1973,** *6,* 258–270. doi:10.1016/0022-4596(73)90189-8
27. Popov, V. L. *Contact Mechanics and Friction;* Springer: Berlin Heidelberg, 2010. doi:10.1007/978-3-642-10803-7
28. Burnham, N. A.; Colton, R. J.; Pollock, H. M. *Nanotechnology* **1993,** *4,* 64–80. doi:10.1088/0957-4484/4/2/002
29. Pashley, M. D.; Pethica, J. B.; Tabor, D. *Wear* **1984,** *100,* 7–31. doi:10.1016/0043-1648(84)90003-6
30. Gulbiński, W.; Suszko, T.; Pailharey, D. *Wear* **2003,** *254,* 988–993. doi:10.1016/S0043-1648(03)00304-1
31. Miyoshi, K. *Tribol. Int* **1999,** *32,* 605–616. doi:10.1016/S0301-679X(99)00093-6
32. Maugis, D. *J. Colloid Interface Sci.* **1992,** *150,* 243–269. doi:10.1016/0021-9797(92)90285-T
33. Kucharczyk, D.; Niklewski, T. *J. Appl. Crystallogr.* **1979,** *12,* 270–373. doi:10.1107/S0021889879012711
34. Vitos, L.; Ruban, A. V.; Skriver, H. L.; Kollár, J. *Surf. Sci.* **1998,** *411,* 186–202. doi:10.1016/S0039-6028(98)00363-X
35. Mo, Y.; Turner, K. T.; Szlufarska, I. *Nature* **2009,** *457,* 1116–1119. doi:10.1038/nature07748
36. Marwitz, C.; Stegemann, B.; Breitkreiz, M.; Kloss, H.; Woydt, M.; Sturm, H. *Surf. Sci.*, submitted.
37. Nagasawa, K.; Bando, Y.; Takada, T. *Jpn. J. Appl. Phys.* **1969,** *8,* 1262. doi:10.1143/JJAP.8.1262
38. Villarrubia, J. S. *J. Res. Natl. Inst. Stand. Technol.* **1997,** *102,* 425–454.
39. Neto, C.; Craig, V. S. J. *Langmuir* **2001,** *17,* 2097–2099. doi:10.1021/la001506y
40. Torii, A.; Sasaki, M.; Hane, K.; Okuma, S. *Meas. Sci. Technol.* **1996,** *7,* 179–184. doi:10.1088/0957-0233/7/2/010
41. Tortonese, M.; Kirk, M. *Proc. SPIE* **1997,** *3009,* 53–60. doi:10.1117/12.271229

Manipulation of gold colloidal nanoparticles with atomic force microscopy in dynamic mode: influence of particle–substrate chemistry and morphology, and of operating conditions

Samer Darwich[1], Karine Mougin[*1], Akshata Rao[2], Enrico Gnecco[2], Shrisudersan Jayaraman[3] and Hamidou Haidara[1]

Full Research Paper

Address:
[1]IS2M-CNRS, 15 Rue Jean Starcky, 68057 Mulhouse, France, [2]Institute of Physics, University of Basel, and NCCR "Nanoscale Science", Klingelbergstrasse 82, 4056 Basel, Switzerland and [3]Corning Incorporated, 1 Science Center Road, Corning, NY 14831, USA

Email:
Samer Darwich - sam.simones@hotmail.com; Karine Mougin[*] - karine.mougin@uha.fr; Akshata Rao - Akshata.Rao@stud.unibas.ch; Enrico Gnecco - enrico.gnecco@imdea.org; Shrisudersan Jayaraman - JayaramaS@corning.com; Hamidou Haidara - hamidou.haidara@uha.fr

* Corresponding author

Keywords:
atomic force microscopy; intermolecular interaction; manipulation; nanoparticles; precise positioning; self-assembled monolayers

Abstract

One key component in the assembly of nanoparticles is their precise positioning to enable the creation of new complex nano-objects. Controlling the nanoscale interactions is crucial for the prediction and understanding of the behaviour of nanoparticles (NPs) during their assembly. In the present work, we have manipulated bare and functionalized gold nanoparticles on flat and patterned silicon and silicon coated substrates with dynamic atomic force microscopy (AFM). Under ambient conditions, the particles adhere to silicon until a critical drive amplitude is reached by oscillations of the probing tip. Beyond that threshold, the particles start to follow different directions, depending on their geometry, size and adhesion to the substrate. Higher and respectively, lower mobility was observed when the gold particles were coated with methyl (–CH_3) and hydroxyl (–OH) terminated thiol groups. This major result suggests that the adhesion of the particles to the substrate is strongly reduced by the presence of hydrophobic interfaces. The influence of critical parameters on the manipulation was investigated and discussed viz. the shape, size and grafting of the NPs, as well as the surface chemistry and the patterning of the substrate, and finally the operating conditions (temperature, humidity and scan velocity). Whereas the operating conditions and substrate structure are shown to have a strong effect on the mobility of the particles, we did not find any differences when manipulating ordered vs random distributed particles.

Introduction

Nanotechnology, which aims at the ideal miniaturization of devices and machines down to atomic and molecular sizes has become a strategic topic with a promising future in high technology for the forthcoming century [1]. By the precise control of atoms, molecules, or nanoscale objects, new sensors and man-made materials, micromachines, organic integrated computers, microscale intelligence system, communication tools would be possible within the near future [2]. However, for new nanotechnology products, there are still many problems to be solved such as nanomanipulation which has a great impact on nanometer scale expertise. By manipulation of nanoscale objects (nano-objects), we mean using external force for positioning or assembling objects in two (2-D) or three (3-D) dimensions by twisting, bending, picking-and-placing, or pushing and pulling them [3]. Nanomanipulation is a complex 3-D problem. Because mechanical and chemical properties of substrates, probing tools and nano-objects (especially 'particles') are combined, different results are expected depending on the environmental and operating conditions. Numerous methods exist for the manipulation of nanostructures and can be classified into two categories as non-contact and contact manipulation systems. In the former, laser trapping (optical tweezers) or electrostatic or magnetic field forces are utilized. Thus, Yamomoto et al. [4] cut DNA using restriction enzymes on a laser trapped bead, Vonna et al. used magnetic tweezers and beads to stretch cell membranes [5] and Stroscio et al. [6] utilized electrical forces between a scanning tunneling microscopy (STM) probe tip and surface atoms for manipulating Xe or Ni atoms. More precisely, manipulation of nanoparticles (nanoscale metal particles (NPs)) in a non-contact mode was the first approach to manipulate these nano-objects. Historically, the first accurate manipulation studies of nanoparticles were performed by STM. In a pioneer experiment, Cuberes et al. moved single C_{60} molecules along the steps of a Cu(111) surface using an STM in UHV [7]. In addition, the majority of the STM experiments were performed at cryogenic temperatures [8]. Unfortunately, despite the accurate level of control obtained with STM, the energy dissipated in the manipulation process cannot be estimated by this technique. Recently, it has been shown that another scanning probe technique, atomic force microscopy (AFM), is capable of positioning single atoms or clusters even at room temperature, and has thus become popular as a simple manipulation tool [9,10]. Changing its function from only imaging to both imaging and manipulation, new challenging problems did arise. Three main modes are used in atomic force microscopy, i.e., non-contact (NC) mode, contact mode and intermittent tapping mode.

The first mode used in AFM was the contact mode. Manipulation of large C_{60} islands on NaCl was performed by Lüthi et al.

using contact AFM [11]. Even if the shear between islands and crystal surface can be derived from the frictional forces experienced by the AFM tip while scanning, the applicability of contact AFM to nanomanipulation was limited to relatively large objects (tens of nanometers in size). The latest results obtained by Custance et al. show that it is now possible to manipulate single atoms using NC-AFM [12]. Byungsoo Kim et al. [13] have also proposed a new explanation for the extraction and deposition of atoms using AFM. In the contact mode, different strategies, such as pushing and pulling, have been used to manipulate nanoclusters. Firstly, the tip can be used for positioning particles on a substrate by pushing or pulling operations [14,15]. For instance, M.C. Strus et al. have manipulated carbon nanotubes and estimated the flexural strain energy distributions and static frictional force between a carbon nanotube and a SiO_2 surface [16]. Nanometer scale antimony particles have been manipulated on an atomically flat graphite surface by atomic force microscopy techniques and quantitative information on interfacial friction was extracted from the lateral manipulation of these nanoparticles [17]. These particles were first *pushed* on a graphite surface by the AFM tips and then manipulated by placing the AFM tip *on top* of the particles. Above a certain lateral force threshold, particle sliding was observed, which has allowed the transition from static to kinetic friction to be quantified [18].

A compromise between the contact and non-contact AFM techniques is the intermittent mode, the so called tapping mode. In this mode the phase shift of the cantilever oscillations with respect to the external periodic excitation can be used to estimate the dissipated energy during manipulation. This method was recently used by Ritter and coworkers to manipulate antimony particles on a graphite surface in air [17,18]. Paollicelli et al. manipulated gold nanoparticles deposited on highly oriented pyrolitic graphite using AFM in tapping mode. NPs were selectively moved as a function of their size varying from 24 up to 42 nm in diameter and the energy detachment threshold of NPs was estimated accordingly [19]. Sitti and coworkers have also manipulated nanoscale latex particles positioned on Si substrates with an accuracy of about 30 nm [20] whilst Mougin et al. manipulated as-synthesized and functionalized gold nanoparticles on silicon substrates with dynamic AFM [21]. In all these techniques, the major difficulties that arise are related to the quantification of the dynamical processes occurring during manipulation, i.e., collisions between probing tips and particles, friction between particles and substrates, electrostatic interactions among all of them, etc.

For this reason, colloidal particles have appeared as model nano-objects because they can be produced in various well-

controlled sizes and from various materials such as metals or semiconductors. Of particular interest has been the use of metal nanoparticles, which have been applied to the development of highly sensitive nanoparticle-based detection assays that utilize electrical or optical detection (colorimetric and surface enhanced Raman spectroscopy (SERS)). For different reasons gold particles are particularly attractive in this field. For instance, they are ideal electrodes for molecular electronics [22]. Gold clusters below 5 nm in size deposited onto thin metal oxides also exhibit unexpected highly catalytic activity (not obtained with bulk metal) for different types of reactions, e.g., combustion, hydrogenation, reduction etc. [23,24]. Coated with organic molecules, gold nanoparticles can be used for DNA assays in genomics [25,26], as signal amplifiers for biological recognition or as quantitation of tags in biological assays. To utilize and optimize the chemical and physical properties of gold NPs, a great deal of research has been done regarding the control of size [27,28], shape [29,30], surface chemistry [31,32] and aggregation morphology of nanoparticles as isolated clusters [33], or as single- or multilayer coatings [34]. The manipulation of nanoparticles, especially colloidal gold NPs, by AFM can be influenced by the structural characteristics of the particle, tip and surface, in particular the intermolecular interactions between tip and particle or particle and surface. In addition, both the physical structure of the substrate (topography) and the operating conditions (environmental conditions and scan velocity of the tip [35]) determine to a large extent the tip–particle–substrate interactions and behavior. Furthermore, the fundamental understanding of the different types of particle motion during manipulation, such as sliding, rolling, stick-slip and spinning, is crucial since the mode of motion of particles determines the energy loss and wear in the contacting surfaces.

In this paper, the sensitivity of those critical parameters on the mobility of gold nanoparticles during their manipulation using AFM in tapping mode has been investigated. In particular, the effects of the size, shape and coating of the nanoparticles, the lateral scan velocity, the particle-surface interactions and the environmental conditions, especially temperature *T* and relative humidity *RH*%, are presented and discussed. The dependency of the energy dissipation during the manipulation was particularly studied as a function of size, coating of particles, substrate and temperature. Finally, interpretation of the physico-chemical mechanisms involved at both interfaces – tip–particle and particle–surface – during the movement of the particle was proposed and partially verified by modeling; nevertheless additional investigations are still needed.

Results and Discussion

Spherical and asymmetrical gold nanoparticles were synthesized as described in the Experimental section and deposited

onto flat and patterned surfaces. Accurate manipulation was performed using AFM in tapping mode as it provides indirect access to dissipation energy during particle movement [21]. Since the same microscope is used to either image or manipulate at a given instant, imaging is almost impossible while pushing the nanoparticle. To face this problem, imaging is carried out before and after manipulation using a fixed reference to locate the final position of the particle.

The first part of the discussion will focus on the influence of the size and shape of the particle on manipulation. Then, we will examine the effect of functional (hydrophilic vs hydrophobic) molecules grafted on the Au nanoparticles on their mobility. In addition, we will address the important issue of environmental conditions (*T*, *RH*%), surface topography and tip scan velocities on the manipulation performance of gold nanoparticles. Finally, conclusions with discussions and future directions are given in the last paragraph.

1. Influence of size and shape of the particle
A. Influence of the size of the spherical Au particle

Sizes of gold spherical nanoparticles(NPs) were tuned from 5 nm up to 65 nm according to the synthesis procedure described in the Experimental section. "As-synthesized" Au NPs, meaning NPs covered with citrate stabilizing group (COO^-), referred to as "reference NPs" were deposited onto bare and hydrophobized (CH_3-terminated coating) silicon wafers, and manipulated using AFM in tapping mode. During manipulation, the oscillation amplitude of the tip, A_{set}, was kept constant by a feedback loop. In such cases, the power dissipation accompanying the tip-sample interaction can be determined from the following relationship [21-36]:

$$P_{dis} = -\pi k f_0 \left(A_{piezo} A_{set} \sin\varphi - \frac{A_{set}^2}{Q} \right) \qquad (1)$$

where A_{piezo} is the oscillation amplitude of a piezo-element coupled to the cantilever, f_0, k and Q are the resonance frequency, the spring constant and the quality factor of the free cantilever, respectively, and φ is the phase shift caused by the interaction between the tip and the underlying particles or surface.

The calculation of the dissipated power (P_{dis}) was performed for 5 sizes of Au colloidal particles whose radius (*R*) was varied from 5 up to 65 nm. Figure 1a and Figure 1b show a logarithmic plot of the dissipated power normalized by the radius of the nanoparticle as a function of the particle radius, on bare and hydrophobic coated silicon wafers, respectively. These plots actually can be fitted using an approximation of a friction model

for NPs rolling and sliding on the substrate [37,38]. The red curves describe simulated dynamic behavior of the nanoparticles according to pure sliding (Figure 1a) and rotation (Figure 1b) models of the nanoparticle in a typical AFM tapping mode manipulation as described by Sitti [37,38]. According to this model, the force brought by the tip to the particle should be higher than a threshold value given by

$$\frac{\tau_{ps} C_{ps}}{\sin\alpha - \mu_{ps}\cos\alpha},$$

for sliding and

$$\frac{\tau_{ps} C_{ps} + \tau_{tp} C_{tp}}{R(\sin\alpha + \cos\beta) + \mu_{tp}\sin\beta - \mu_{ps}\cos\alpha},$$

for rolling of the NP. In these expressions, μ is the friction coefficient, τ is the shear strength, C the contact area, and α and β are the angles which are defined in Scheme 1. The subscripts tp and ps as of τ, C and μ represent the tip–particle and particle–substrate contacts, respectively.

These results thus display the dependence of the movement of the particle on, both, their size and the substrate–surface chemistry, underscoring in particular the importance of the particle–substrate interactions on the mobility and behavior of nano-objects on manipulation.

Although crucial, these particles–substrate interactions actually represent one parameter among other important physical parameters. Indeed small and large particles do not undergo the same trajectory during manipulation. This size-dependence of the particle trajectory under manipulation can thus provide a way to fractionate or to separate a mixture of nano-objects. In Figure 2a and Figure 2b, we can observe that large (a few dozens of nanometers) particles move at a small angle with respect to the normal of the tip's fast scan direction, until they reach the bottom of the scan area, whereas smaller ones slide to the edge of the scan area using a shorter path. From this observation it is possible to fractionate and separate small from big particles adsorbed on a substrate. This size-dependence of the particle trajectory was explained by a simulation which shows that the trajectory of the particle at the same time depends on i) the operating parameter which is the scanning path used by AFM (zigzag or scattered one, Figure 3), ii) the density of scan lines and, iii) the parameter R_{tot} which corresponds to the sum of the radii of the tip and the particle [39].

Indeed, it has been observed (Figure 2b) that two particles that collide at a point and move together can be considered as a single particle. If we compare two consecutive trajectories of
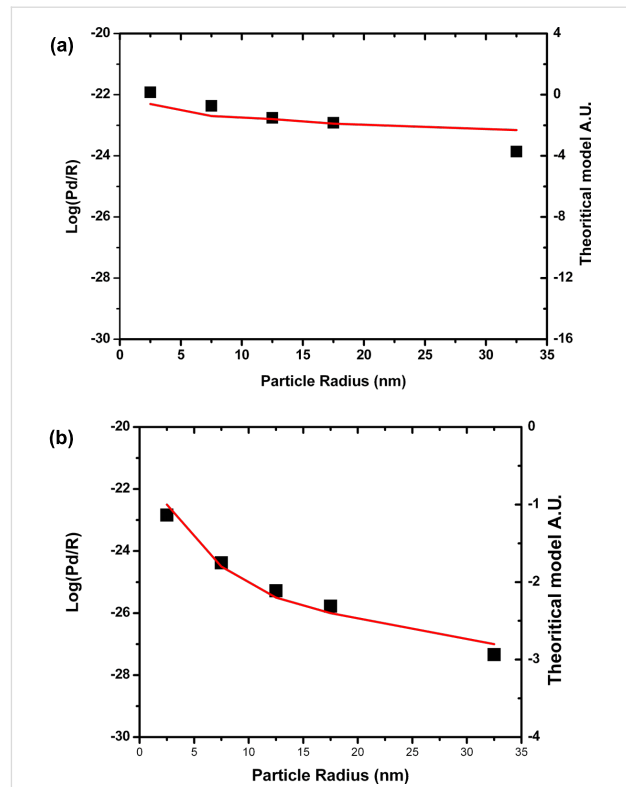

Figure 1: Evolution of the logarithm of the dissipated power normalized by the radius (*R*) as a function of (a) as-synthesized spherical Au nanoparticles on bare silicon wafer versus the particle radius *R* (squares: experimental data; solid line: theoretical data) corresponding to a pure sliding model and (b) spherical Au nanoparticles on silicon wafer coated with –CH$_3$ terminated groups (hydrophobic coating) versus the particle radius *R* (squares: experimental data, solid line: theoretical data) corresponding to a pure rotation model. Both after the tap of a tip in a typical AFM tapping mode manipulation as described by Sitti [37,38].
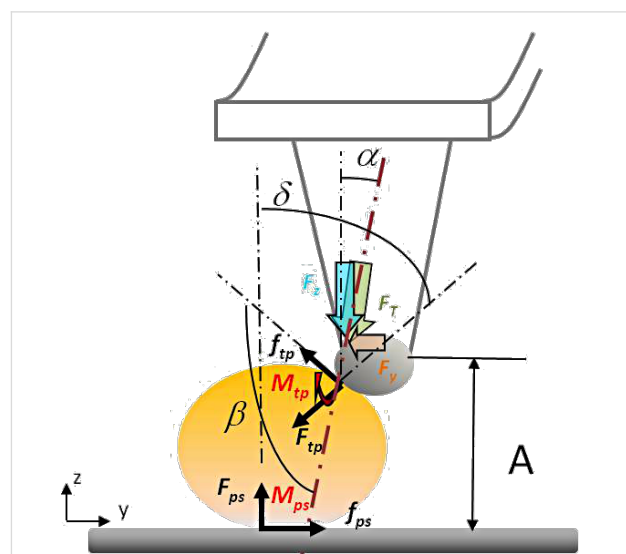
Scheme 1: Scheme presenting the different forces during tip–particle and particle–substrate interactions, and the angles α, β and δ.
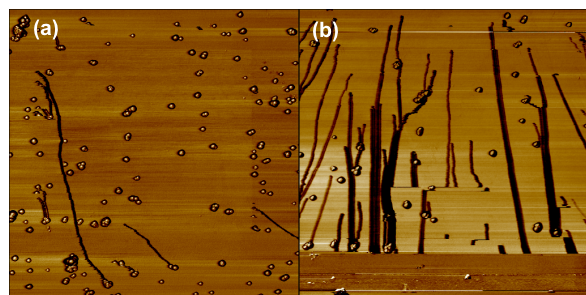
Figure 2: Typical trajectories of bare gold nanoparticles (20 nm diameter) on a silicon substrate when the probing tip moves along a zigzag path: (a) low drive amplitude, (b) high drive amplitude. Scan size: 5 μm.

Figure 3: Typical scan patterns used in AFM: (a) raster scan path used by Nanosurf (b) zigzag scan path used by Veeco. *Top view:* the grey disk corresponds to the position of the tip on the surface and the yellow, blue and red disks are the positions of spherical particles pushed by the tip along its scan path.

the particle before and after collision, the single Au particle (thinner line) moves at a smaller angle, as compared to the case where it meets another particle (thicker line). In this case, the variation of the trajectory can be explained by the variation of the radius of the average cluster R_{tot} (different sizes move at different angles).

Moreover, the modeling of the NPs trajectory addresses a relation between the frictional forces acting on spherical nanoparticles, and the trajectories predicted. This model can also be used to interpret the trajectory fluctuations and the apparent discontinuities observed when spherical gold particles are manipulated on rigid substrates by AFM.

B. Influence of the shape

The manipulation of spherical and asymmetrical nanoparticles by AFM represents a way to understand and control the motion of complex shaped nanoparticles. For instance, manipulation of elongated objects such as rigid Au nanorods induces mainly
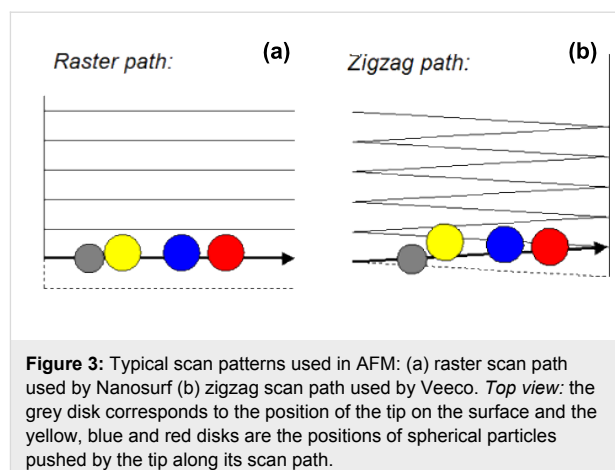
sliding and rolling of the nano-objects, and this movement varies with the different stages of nanomanipulation time scale. As shown in Figure 4, the rods first tend to move perpendicular to their principal direction of motion and then wobble along their longitudinal axis. The average orientation of the rod is perpendicular to its direction of motion. According to theoretical simulation and experience, the torque applied by the tip to the rods results in a wobbling motion, which has no determining influence on the overall direction of the nanoparticles [39].

For triangular and flower shaped nanoparticles, the nano-objects mostly evolve through a translation movement, as well as a rotation along their main perpendicular axis during the manipulation, as shown in Figure 4. While asymmetric particles wobble around a fixed angle, they do follow a well defined path with a specific angle. Simulation of the trajectory of these different particles is still under progress [40] and may lead to a better understanding of how to induce a well-defined direction
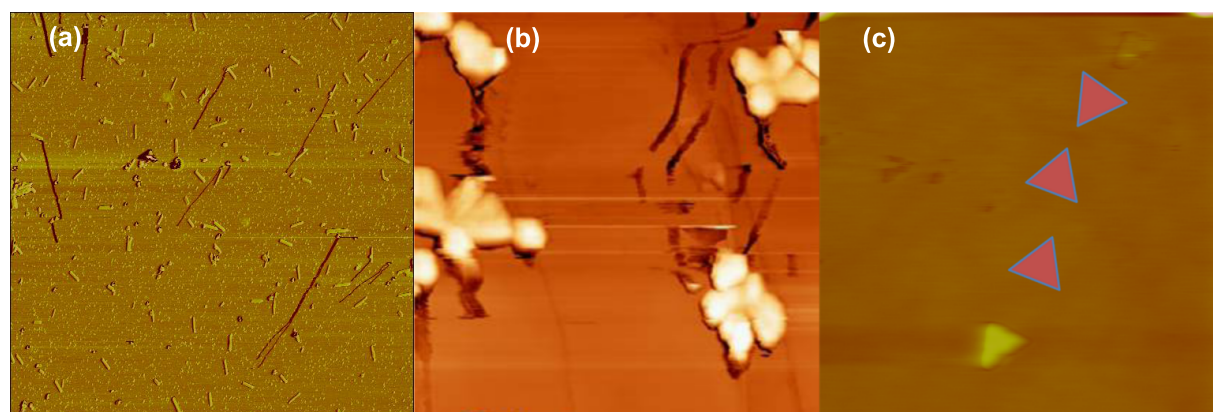

Figure 4: AFM images of nanocluster movement during their manipulation (a) gold nanorods deposited onto silicon wafer, scan size: 12 μm; (b) antimony islands on HOPG, scan size: 1.5 μm; (c) Au nanotriangles on silicon wafer. Middle triangles have been intentionally colored in to illustrate the trajectory of the Au nanoparticles during manipulation, scan size: 5 μm.

of motion to nanoparticles by adjusting the operating parameters of the AFM. Besides the shape and the size of the particles, the chemistry of the functional grafting surrounding the particle also strongly affects their movement and trajectory during nanomanipulation.

2. Influence of the chemistry of the particles on a flat substrate

Because real surfaces are often heterogeneous in their chemical composition, functionalized nanoparticles provide good model systems to study and tune the mobility of nano-objects on these substrates. As a next step, the role of the hydrohilicity and hydrophobicity of the functional grafting on spherical Au nanoparticles is illustrated in Figure 5a. This series of experiments was performed on a Veeco AFM whose tip follows a zigzag scan path.

The role of the hydrophobic or hydrophilic character of the interface in the manipulation process was investigated, using gold nanoparticles bearing OH- and CH$_3$-terminated thiol groups (as described in the Experimental section) and moving these particles against a flat bare silicon substrate. The results are summarized in Figure 5 which displays the average power dissipation required to induce the motion of the particles. The first observation that arises directly from this figure is that the presence of a hydrophobic interface significantly enhances the mobility of the particles. The energy required to move OH-coated nano gold particles was found to be at least 10 times higher than that for CH$_3$-coated particles. We also observed that

the manipulation of hydrophilic coated nanoparticles often results in a damage to the tip due to the high particle–substrate adhesion force. This strong adhesion between silicon substrate and hydrophilic coated nanoparticles primarily arises from intermolecular interactions. It may also involve a contribution from capillary bridges between the substrate and the NPs on one hand and between the closest NPs on the other hand (see below, subsection 5). In contrast, it has already been observed that the thin adsorbed water film formed on the silicon wafer acts as a lubricant when confined between the hydrophobized CH$_3$-coated nanoparticles and the (hydrophilic) substrate [41-43].

As we can see here, the eventual role of relative humidity (*RH*%) which is an environmental parameter, strongly depends on the chemistry of the NP–substrate interface. Another environmental parameter, namely temperature, also affects the mobility of the nanoparticles. The influence of extrinsic (environmental) parameters is discussed in the following paragraph.

3. Influence of the temperature

Figure 5a shows a histogram of the raw values of power dissipation vs the temperature for temperatures ranging from 20 to 150 °C. These results clearly show that the power dissipation involved in the motion decreases with the temperature. This effect appears to be stronger on hydrophilic particles. Intuitively, one could expect this result since the higher thermal energy (k_BT) impedes the formation of stable intermolecular bonds and water bridges between particles and substrate, reducing the adhesion between them. Similar thermal effects
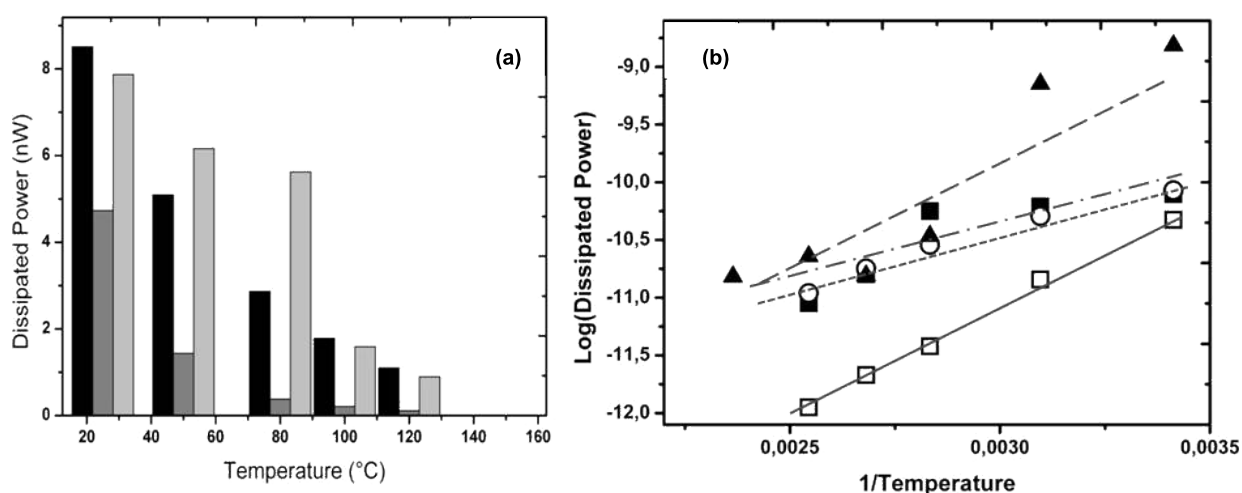
Figure 5: (a) Average power dissipation accompanying the onset of motion of as-synthesized and coated nanoparticles on silicon in air vs temperature. *Black columns*: as-synthesized NPs that are uniformly distributed on the substrate, *dark gray columns*: CH$_3$-coated NPs, *light gray columns*: as-synthesized NPs randomly distributed on the substrate. (b) Logarithm of the dissipated power in moving as-synthesized and coated NPs on silicon wafer vs reciprocal temperature. *Closed squares*: as-synthesized nanoparticules, *open circles*: as-synthesized nanoparticles ordered organized, *open squares*: CH$_3$-coated nanoaprticles, *closed triangles*: OH-coated nanoparticles.

have been recognized in friction on hydrophilic surfaces measured with different scan velocities [42]. It is worth noting that during this temperature dependent manipulation no evident damage was observed on working areas.

Figure 5b shows a logarithmic plot of the dissipated power as a function of the reciprocal temperature. The experimental data of all NP–substrate couples can be fitted well using a linear regression (r² > 0.90), except the data of as-synthesized NPs for which r² is ~0.78. This linear behavior of [log(dissipated power)] vs (1/T) actually corresponds to an exponential decay of the dissipated power with T which points to a thermally activated process [44]. The slopes of these linear fits correspond to $(\Delta E_{act}/k_B)$, where ΔE_{act} represents an activation energy barrier with respect to a reference state E_0: $\Delta E_{act} = (E_0 - E_{act})$ where $E_{act}(T)$ is the energy input involved in the motion of the particle. This energy variation (slope) is high for the CH_3-hydrophobized NPs, indicating a strong decrease of the input energy with the temperature which would be expected for low adhesion strength between nanoparticle and substrate. Surprisingly, a quite similar behavior in, both, trend and activation barrier of the temperature-dependent mobility is observed for the hydrophilic OH-coated NPs. An explanation for this result may come at least partly from the complex behavior of the adsorbed (structural) water depending on temperature in the hydrophilic system. Beyond the observed – and rather reasonable – general trend, the strong decrease with the temperature of the energy required for particle movement, the magnitude of the activation barrier for essentially hydrophilic and hydrophobic contacts will certainly need further confirmation experiments, as well as a more extensive interpretation. Indeed, we assumed in our treatment (Figure 5b) ideal Arrhenius behavior where the activation energy is independent of the temperature in both systems. This is an assumption which may not be the case for the complex water bridging hydrophilic contact.

4. Organization effects

The first and third columns of the series shown in Figure 5a show the threshold power dissipation for the motion of randomly and ordered organized distribution of nanoparticles (see Figure 6), obtained as described in the Experimental section.

The power dissipation at different temperatures is comparable in both cases. This result can be explained by the average distance between the nano-objects, which is 70 nm for the random distribution and 100 nm for the ordered one. At such a scale, the interparticular forces are of the order of long range interactions. The mobility of particles is essentially affected by electrostatic interactions arising from residues from the synthesis (citric acid) that may be adsorbed on the particles. It is thus normal, in
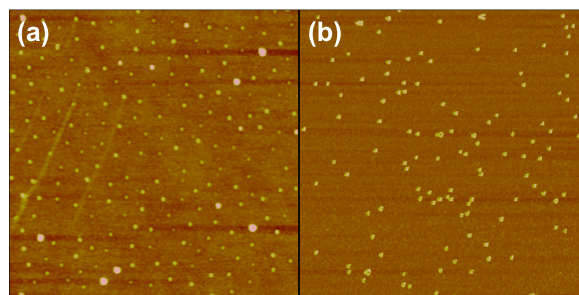

Figure 6: AFM images of 25 nm diameter gold nanoparticles deposited onto a silicon wafer. (a) Ordered organization as described in the Experimental section, (b) random distribution. Frame sizes: 3 μm and 1 μm, respectively.
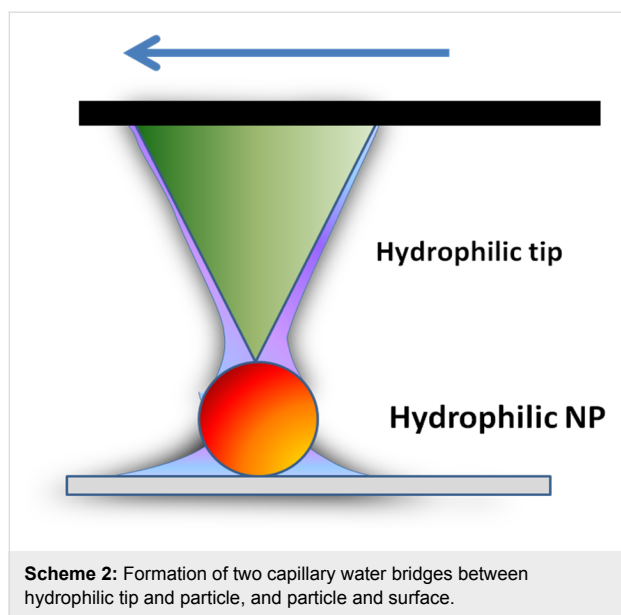
the absence of both physical contact and notable intermolecular forces between the particles, that their mobility is independent of their organization (random or ordered). In other words, this result means that as long as the particle number density n_p is such that the interparticle distance $d_p \sim (n_p)^{-1/2}$ is larger than the range of short-ranged forces [45], their mobility is not affected by their mutual intermolecular binding and is thus independent of their organization. It is worth noting that this absence of true intermolecular binding does not exclude possible particle–particle interaction through capillary forces arising from nanosized condensation films connecting particles at these separations.

5. Influence of humidity and vacuum environment
A. Effect of relative humidity

The presence of surface contaminants (dust or water) affects the mobility of nanoparticles as this directly changes the intermolecular interactions between the nanoparticles and the surface. As it has been discussed in subsection 2, a contribution from capillary bridges has also a strong influence on the mobility of spherical Au nanoparticles during their manipulation. Indeed, capillary forces of water films between both interfaces, nanoparticle–surface and tip–nanoparticle, will depend on the volume of liquid condensate present at the interface, as well as the interface geometry [46] (see Scheme 2). The presence of the water meniscus at both interfaces will increase the adhesive forces and lower the mobility of the NPs.

In this section we describe our studies on the mobility of as-synthesized Au spherical NPs and CH_3-coated ones. The diameter of the Au nanoparticle is about 20 nm. The ambient (*RH* = 33%) and higher relative humidity results displayed in Table 1 illustrate how the adsorption of water on nanoparticles can affect the adhesion and friction forces at, both, tip–nanoparticle and nanoparticle–surface contacts. Independently of the

Scheme 2: Formation of two capillary water bridges between hydrophilic tip and particle, and particle and surface.

Scheme 3: Formation of two water layer films between hydrophilic tip–hydrophobic particle, and hydrophobic particle–hydrophilic surface, respectively.

environmental conditions, manipulation of nanoparticles on a surface requires that they are loosely attached in order to be able to move them.
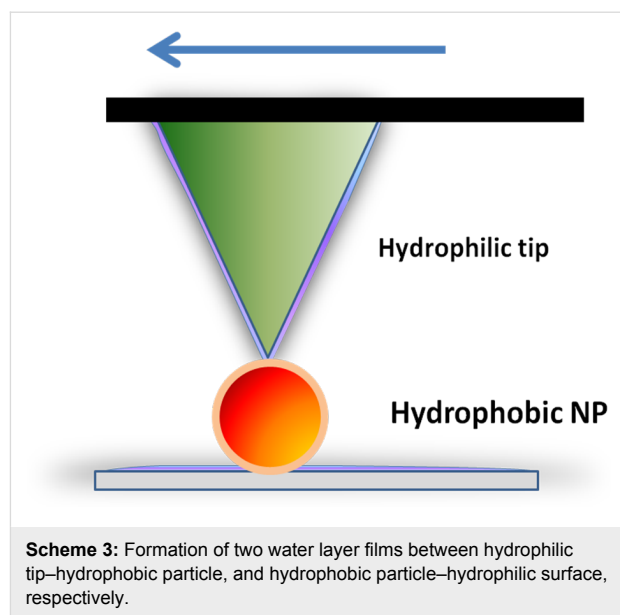
Table 1: Mobilities of spherical Au nanoparticles (hydrophilic and hydrophobic) versus humidity rate during their manipulation using an AFM in tapping mode (zigzag scan path).

Relative humidity (%)	33 (ambient conditions)	43	53
as-synthesized Au NPs	movement	fixed	fixed
CH$_3$-coated Au NPs	movement	movement	movement

The decrease of relative humidity from 53 down to 33% has a strong impact on the mobility of the hydrophilic Au NPs. Above RH = 43%, the adsorbed Au particles do not move, because the energy transferred from the tip to the particle during the tap is not high enough to break the capillary bridges formed at both interfaces. As a consequence, the overall energy does not reach the threshold barrier to move the particle and is completely dissipated in the system.

However, this process does not affect strongly the mobility of hydrophobic Au NPs. They move whatever the environment. This difference can be explained by the existence and the local shape of a liquid condensate (Scheme 2 and Scheme 3) around the tip–substrate contact [47].

In a humid environment, the magnitude of friction and adhesion forces is strongly dependent on the capillary force that is related to the intrinsic wetting properties of the interfacial system. As a consequence, the resulting water meniscus (or layer) can either increase friction through increased adhesion in the contact zone (hydrophilic interfaces) or reduce it through the lubricating effect of a water layer.

Further experiments should also prove that the bigger the particles are, the higher the capillary effect will be as has previously been observed in contact mode [35-48].

B. Vacuum environment

The environment is a crucial parameter in manipulation (tribological) experiments. The adhesive and frictional results are directly dependent on the humidity and temperature of the surrounding medium. Concerning the influence of humidity (or more exactly the absence of humidity), we have investigated how the nanomanipulation process is affected in ultra high vacuum (UHV) environment. The topography image in Figure 7 shows the gold particles on a silicon substrate after the sample was transferred into UHV without any further treatment, which could have changed the organization of the particles. The shape of the particles is well defined, and the structure of some aggregates can be recognized, due to the absence of convolution effects that usually arise from the water layer which may cover the particles under ambient conditions. This image thus shows that the transfer into UHV by itself does not affect the shape of the NPs or their organization. When manipulated under UHV conditions, the particles could not be moved, even when imaged at the maximum magnification available with our system (in the order of 100 nm). Even in contact mode, with forces of a few nanonewtons applied to the particles, no motion was observed. This UHV result particularly illustrates the important lubri-
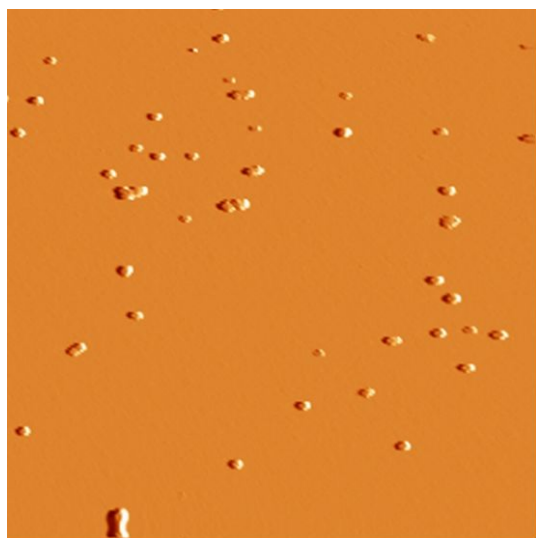
Figure 7: As-synthesized Au particles on silicon in ultra-high vacuum. Frame size: 3 μm.
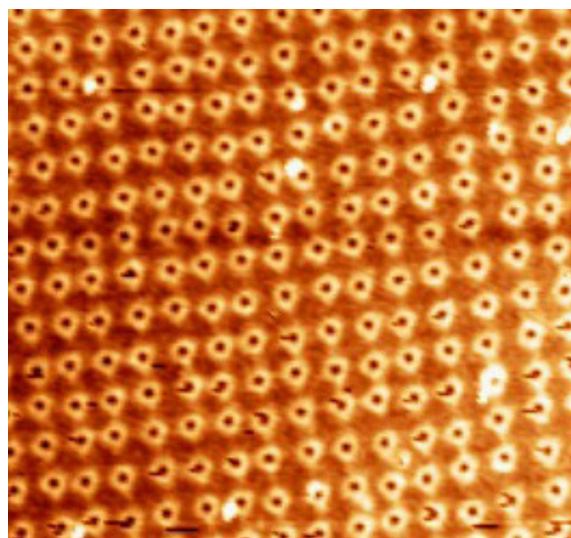

Figure 8: AFM image of nanopatterned surface exhibiting Si pits: Frame size: 3 μm.

cating role of the adsorbed water layer between the particle and the substrate in both the free (Brownian) and externally-driven motion of nanoparticles.

The previous sections have demonstrated the influence of the morphological, environmental and chemical parameters on the mobility and movement of the particle. The following addresses the influence of the topography of the substrate.

6. Influence of the topography of the substrate

Manipulation of gold nanoparticles was investigated on flat bare silicon wafers, as well as on nanostructured (or nanopatterned) silicon wafers, i.e., silicon substrates that are patterned on the nanoscale.

The following experiences were performed using a raster scan path of the tip mounted on a Nanosurf AFM. On flat bare silicon wafer, the direction of motion of the 25 nm diameter gold nanoparticles was initially well defined, but changed after acquiring a couple of images. This makes it much more difficult to move the particles, even for higher values of the drive amplitude, possibly because of tip contamination. Hence, the idea to modify the topography of the surface was chosen to study the effect of the geometrical surface confinement on the mobility and trajectory of the nanoparticles. Nanopatterned substrates shown in Figure 8 were chosen for that purpose.

The surface patterns consist of an array of nanopits created by the focused ion beam (FIB) milling technique. The width and depth of the pits are 650 nm and 5 nm, respectively, and the

spacing between two adjacent pits is 125 nm. On the patterned surface, the mean direction of motion remains identical (on average), even after a long acquisition time. This stability of the direction of the particle movement observed here on the nanopatterned substrates can be attributed to "self-cleaning" of the tip when it crosses the shallow pits. Considering that the pits have only a small influence on the particle direction (Figure 9), which means that all the particles follow the same direction, this parameter could be ignored for determining the deflection angle. As a result, patterned surfaces were chosen for this determination, rather than the flat bare silicon surfaces. The influence of the spacing *b* separating two scan paths on the deflection angle has been shown by simulation of these experiments [39-49]. Figure 9b and Figure 9c display the change in angle for the same surface and identical particles for b = 16 nm and 3.9 nm, respectively. The trend of adopting higher angles with lower spacing is clear from these results. To confirm the topographical effect, as-synthesized Au NPs were also manipulated on different substrates such as nanopatterned silicon wafers presenting grooves, and steeped HOPG surfaces [40].

Manipulation experiments were repeated to check the influence of the deep grooves (either on Si wafers or on HOPG) on the trajectory of the moving particles. It was found that the deep grooves slightly influence the direction of movement of the particles as particles tend to follow their preferential angle during movement.

Finally, the last important and technological parameter of AFM nanomanipulation is the effect of scan velocity on the movement of the nanoparticles.
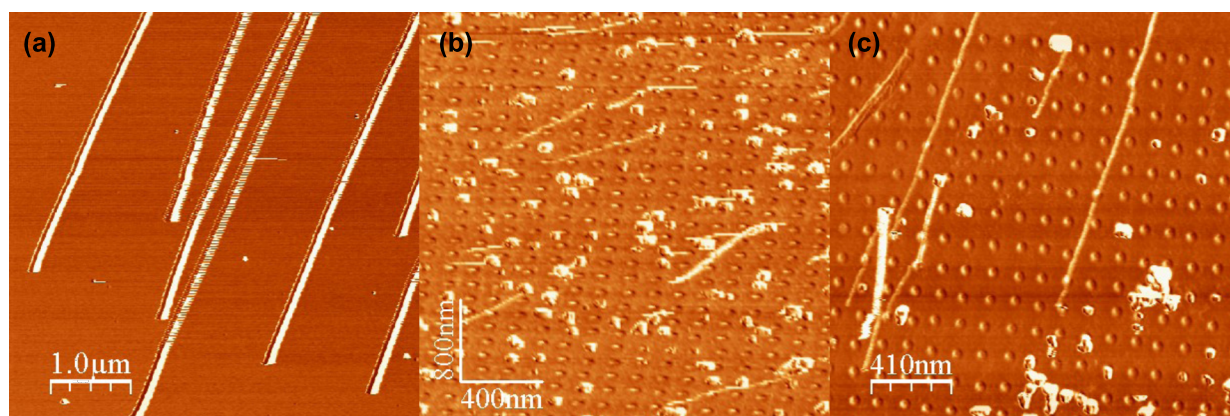
Figure 9: Manipulation of as-synthesized Au nanoparticles on (a) a flat silicon wafer with a spacing of 9.7 nm and (b) a nanopatterned one with a spacing 16 nm, and (c) a patterned wafer with a spacing of 3.9 nm.

7. Influence of scan velocity

The influence of the sliding velocity on friction, which accounts, at least partly, for the dynamical response of the boundary layer, can be exploited to gain insight into the manipulation of nano-objects [41].

Spherical particles (as-synthesized Au NPs) of 35 nm and 60 nm in diameter were moved in tapping mode with Veeco AFM following the previous procedure described in subsection 1. The drive amplitude threshold to move the particle was recorded as well as the phase shift to estimate the loss of energy during the movement of the particles. These experiments were repeated for different scan tip velocities ranging from 0.1 up to 10 $\mu m \cdot s^{-1}$ on three model substrates, i.e., a cleaned silicon wafer (SiO_2), and two other ones, coated with either hydrophilic ($-NH_2$) or hydrophobic ($-CH_3$) self-assembled monolayers.
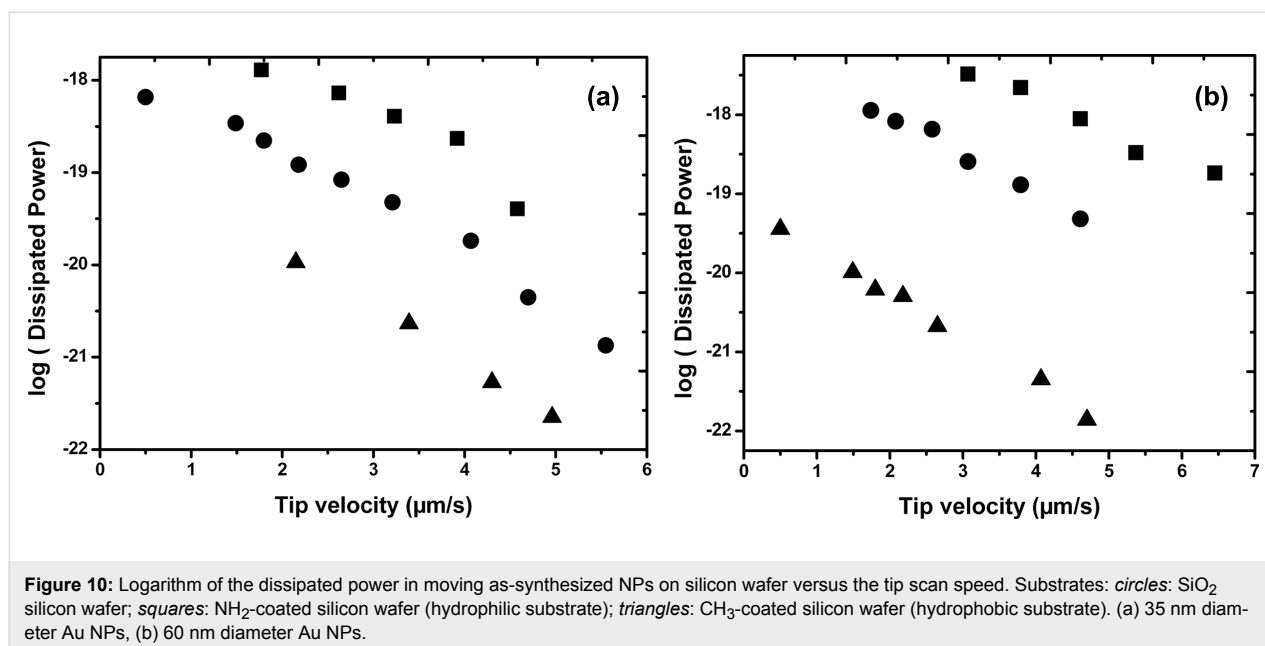
The results of the velocity-dependence of the dissipated power are plotted in Figure 10. The dissipated power has been plotted on a logarithmic scale to allow a more usual comparison with the literature [14,21,42]. To ensure that the measured power dissipation was representative of the spherical gold nanoparticles motion, several particles (at least 10) were moved under similar conditions.

Our results in Figure 10 show that for both nanoparticle sizes (35 and 60 nm), the dissipated power during the tip–particle contact depends on the chemical nature of the substrate. The magnitude of the dissipated energy gradually and significantly increases from the more hydrophobic to the more hydrophilic substrate as one could expect from the intermolecular interactions involved at the different interfaces. This dissipated power

also increases with the diameter of the nanoparticles as expected from the increase of the NPs–substrate contact area.

At the more hydrophobic substrate (CH_3), the interactions with the hydrophilic nanoparticles (as-synthesized citrate stabilized NPs) mainly involve London dispersion forces that have a much lower magnitude as compared to the polar, hydrogen and electrostatic bonds involved in the adhesion of these citrate-stabilized nanoparticles, with more hydrophilic (SiO_2 and NH_2) substrates. The maximum dissipated power appears for the more polar substrates. It is worth noting that this value can involve a contribution from the capillary water bridges which readily form on more hydrophilic systems under ambient conditions as previously discussed in subsection 5A. It is also worth noting that we also verified here that both the surface and the particle were free of any observable damage after each manipulation.

However, independent of the nature of the intermolecular interactions exchanged between tip and nanoparticles or nanoparticles and surface, and independent of the size of the spherical particles, the logarithm of the dissipated power during the manipulation systematically decreases linearly, when the scan velocity increases. This linear dependence is generally attributed to a decrease of the energy dissipation in the contact as the velocity increases, in a way similar to the velocity (frequency)-dependent viscoelastic and/or plastic dissipation in polymers (as well as metals), as is described for instance through the time-temperature superposition principle for polymers [50-52]. However, from this discussion, it appears that further investigations regarding the velocity dependence of the dissipated power are still necessary on both experimental and theoretical

Figure 10: Logarithm of the dissipated power in moving as-synthesized NPs on silicon wafer versus the tip scan speed. Substrates: *circles*: SiO_2 silicon wafer; *squares*: NH_2-coated silicon wafer (hydrophilic substrate); *triangles*: CH_3-coated silicon wafer (hydrophobic substrate). (a) 35 nm diameter Au NPs, (b) 60 nm diameter Au NPs.

levels. This work is now under investigation and we hope to be able to give an additional and detailed explanation regarding the mechanisms from our experimental results.

Conclusion

The manipulation of nano-objects is still a relatively rare operation. Because micro/nanomechanics has not been completely well-developed, two-dimensional positioning of nanometer-size particles on a substrate at ambient conditions remains a difficult operation and depends on several critical physical, mechanical and chemical parameters. However, advances have enabled better control in nanoscale manipulation. In this paper, we have described manipulation of gold colloidal nanoparticles using AFM in tapping mode. The influence of structural characteristics of the particle (chemistry, size, shape) and the substrate (chemistry and topography) have been investigated. It has been shown that the mobility of the particles was significantly affected by the nature of intermolecular tip–particle and particle–surface interactions, the particle shape and size, the operating environment conditions (relative humidity *RH*% and temperature *T*), as well as the tip scan velocity. The dissipated power during manipulation was quantified under various operating conditions (*RH*%, *T*, tip scan speed). Our experiments show that the velocity dependence of the dissipated power at these nanoscale contacts is far more complex than what one could predict, based on the sole contribution of the tap energy and capillary liquid bridging adhesive force. Indeed, the thermal energy produced within the tip–substrate contact can induce molecular excitations and structural transitions in the topmost contacting layers, the magnitude of which also increases with the sliding velocity. Direct access to the nanoscale contact

between tip and nanoparticle, and nanoparticle and surface are limited with the current device, thus any quantitative analysis of these results remain at this stage scientifically debatable. The second difficulty is naturally related to the yet insufficiently understood size effects that show up in nanoscale friction and strongly affect the results. In addition, real-time monitoring of the manipulation process is almost impossible. Most of the time, imaging is *offline* and the unexpected problems during pushing cannot be detected. Another way is utilizing the force feedback information during pushing for reliable manipulation. This is currently being seriously investigated and correlated to theoretical studies [20]. Because of potential improvements in the mechanical and theoretical fields, more complex and precise manipulations of particles, molecules and single atoms at surfaces using AFM will become achievable and nanoscale manipulations may be of fundamental importance for the realization of nanoscale devices in the future.

Experimental

Gold nanoparticles were adsorbed onto silicon wafers and manipulated in AFM tapping mode. They were either bare or coated with self-assembled monolayers terminated with hydrophobic (methyl, $-CH_3$) or hydrophilic groups (hydroxyl, $-OH$).

Bare gold nanoparticles

The colloidal suspension was made by reduction of an aqueous solution of nanogold particles, $HAuCl_4 \cdot 3H_2O$ supplied by ABCR, Karlsruhe, Germany. The suspension was stabilized with citric acid trisodium salt (Aldrich), which, by reducing $HAuCl_4$, imparts the negative charge of the citrate ions to the

gold nano-particle surface [27,28]. The average size of these nanogold particles, as determined from transmission electron microscopy (TEM) images, was 25 ± 5 nm (Figure 11).
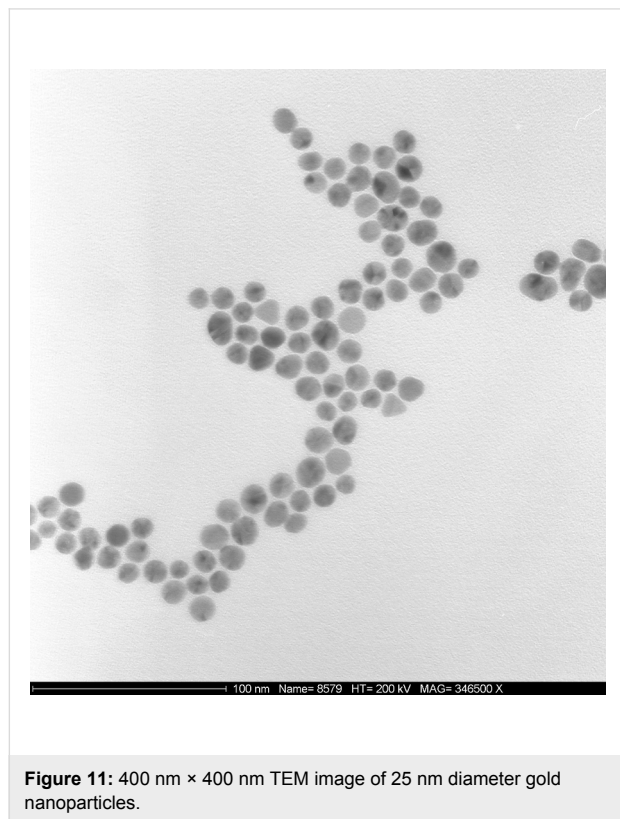

Figure 11: 400 nm × 400 nm TEM image of 25 nm diameter gold nanoparticles.

Coated gold nanoparticles

Dodecanethiol for methyl terminated monolayers and 11-mercapto-1-undecanol for hydroxyl terminated monolayers were obtained from Sigma-Aldrich and used as received. Hydroxyl or methyl-thiol-stabilized gold nanoparticles were synthesized according to a modified version of two common syntheses [21]. The as-synthesized nanosphere solution [27,28] was centrifuged at 7000 rpm for 20 min to pellet the nanoparticles, decanted, and then re-suspended in 1 mL of deionized water to reduce the citric acid concentration. The nanoparticles were then purified from excess surfactant and other reactants by dialysis for one week. Finally, the dialyzed solution was centrifuged and particles were re-dispersed in tetrahydrofuran. 300 µL of the appropriate thiol (methyl- or hydroxyl-terminated) was added to the solution, sonicated and stirred for approximately 2 h to allow the grafting reaction to reach completion. The yellow colored solution slowly became colorless was stored at 4 °C until required. The average diameter of the synthesized nanoparticles is 25 ± 5 nm.

Nanoparticles adsorption
Random adsorption

For the adsorption experiments, a concentration of 0.03 wt % of nanoparticles in the aqueous or organic dispersion was used. The experimental protocol basically involved the particle adsorption by immersing the samples for about 20 minutes in the suspension, whose temperature was maintained at 20 ± 1 °C. After this initial adsorption stage, the samples were removed from the bath, and the thick dispersion film remaining at the substrates was allowed to dry.

Ordered organisation

Samples were provided by McFarland's group at UCSB. Au nanoparticles (25 nm diameter) were synthesized as described previously [27,28]. The Au NPs coated silicon wafer was prepared using a micelle encapsulation method [53,54]. Au nanoparticles were encapsulated by diblock copolymer poly(styrene)-*block*-poly(2-vinylpyridine). The solution was deposited onto silicon wafer and dried under a nitrogen flow. After being dip-coated, the polymer was removed by oxygen plasma treatment (see Figure 6).

Self-assembled monolayer coated silicon wafer

The molecular surfaces were prepared by self-assembling organosilane molecules onto silicon wafers Si(111) with a native thin oxide (SiO_2) layer of ~1.5 nm. The organosilane compounds were methyl terminated hexadecyltrichlorosilane ($-CH_3$), and the amine terminated 6-aminohexylaminopropyl-trimethoxysilane ($-NH_2$). Homogeneous films were obtained by vapor-phase deposition in a dynamically evacuated chamber (1 h at 10^{-3} torr), using a mineral oil as dispersing solvent for the molecules. This consists of mixing the organosilanes in paraffin oil before evacuating the atmosphere in the dessicator enabling the molecules to pass into the vapor phase and stick to the substrate placed above the mixture [33-50].

Manipulation Setup
In-air measurements

The images in air were acquired with two commercial AFMs (Multimode, Nanoscope IV from Veeco and Mobile S from Nanosurf). Rectangular silicon cantilevers with resonance frequencies f_0 around 120 kHz and 190 kHz, quality factors of around 800 and 600, and nominal spring constants of 5 and 48 N/m (respectively, MPP12100 from Veeco and PPP-NCLR from Nanosensors) were used. During manipulation, the oscillation amplitude of the tip, A_{set}, was kept constant by a feedback loop. In this case, the power dissipation accompanying the tip–sample interaction can be determined from Equation 1 [36].

UHV measurements

The images in UHV were acquired with a custom built AFM available at the University of Basel [21]. The base pressure was below 10^{-9} mbar. Due to the high quality factor in UHV, the out-of-contact-resonance frequency shift was used as the imaging parameter instead of the tip's oscillation amplitude (NC-AFM). We have also performed measurements in contact mode, where the set point is determined by the normal load acting between tip and sample. PPP-NCLR and CONT cantilevers from Nanosensors were used in both cases.

Acknowledgements

References

1. Kottas, G. S.; Clarke, L. I.; Horinek, D.; Michl, J. *Chem. Rev.* **2005,** *105,* 1281. doi:10.1021/cr0300993

2. Storhoff, J. J.; Marla, S. S.; Bao, P.; Hagenow, S.; Mehta, H.; Lucas, A.; Garimella, V.; Patno, T.; Buckingham, W.; Cork, W.; Müller, U. R. *Biosens. Bioelectron.* **2004,** *19,* 875. doi:10.1016/j.bios.2003.08.014

3. Schaefer, D.; Reifenberger, R.; Patil, A.; Andres, R. P. *Appl. Phys. Lett.* **1995,** *66,* 1012. doi:10.1063/1.113589

4. Yamamoto, Y.; Kurosawa, O.; Kabata, H.; Shimamoto, N.; Washizu, M. Molecular surgery of DNA based on electrostatic micromanipulation. In *Thirty-Third IAS Annual Meeting, 1998,* The 1998 IEEE Industry Applications Conference, St. Louis, MO, USA, Oct 12–15, 1998; 1998; pp 1933 ff. doi:10.1109/IAS.1998.729860

5. Vonna, L.; Wiedemann, A.; Aepfelbacher, M.; Sackmann, E. *J. Cell Sci.* **2003,** *116,* 785. doi:10.1242/jcs.00230

6. Stroscio, J. A.; Eigler, D. M. *Science* **1991,** *254,* 1319. doi:10.1126/science.254.5036.1319

7. Cuberes, M. T.; Schlitter, R. R.; Gimzewski, J. K. *Appl. Phys. Lett.* **1996,** *69,* 3016. doi:10.1063/1.116824

8. Eigler, D. M.; Schweizer, E. K. *Nature* **1990,** *344,* 524. doi:10.1038/344524a0

9. Sitti, M.; Hashimoto, H. *Seisan Kenkyu* **1999,** *51,* 651.

10. Nazin, G. V.; Qiu, X. H.; Ho, W. *Science* **2003,** *302,* 77. doi:10.1126/science.1088971

11. Lüthi, R.; Meyer, E.; Haefke, H.; Howald, L.; Gutmannsbauer, W.; Güntherodt, H.-J. *Science* **1994,** *266,* 1979. doi:10.1126/science.266.5193.1979

12. Oyabu, N.; Sugimoto, Y.; Abe, M.; Custance, O.; Morita, S. *Nanotechnology* **2005,** *16,* S112. doi:10.1088/0957-4484/16/3/021

13. Kim, B.; Putkaradze, V.; Hikihara, T. *Phys. Rev. Lett.* **2009,** *102,* 215502. doi:10.1103/PhysRevLett.102.215502

14. Schirmeisen, A.; Schwarz, U. D. *ChemPhysChem* **2009,** *10,* 2373. doi:10.1002/cphc.200900378

15. Baur, C.; Bugacov, A.; Koel, B. E.; Madhukar, A.; Montoya, N.; Ramachandran, T. R.; Requicha, A. A. G.; Resch, R.; Will, P. *Nanotechnology* **1998,** *9,* 360. doi:10.1088/0957-4484/9/4/011

16. Strus, M. C.; Lahiji, R. R.; Ares, P.; Lopez, V.; Raman, A.; Reifenberger, R. *Nanotechnology* **2009,** *20,* 385709. doi:10.1088/0957-4484/20/38/385709

17. Dietzel, D.; Mönninghoff, T.; Jansen, L.; Fuchs, H.; Ritter, C.; Schwarz, U. D.; Schirmeisen, A. *J. Appl. Phys.* **2007,** *102,* 084306. doi:10.1063/1.2798628

18. Ritter, C.; Heyde, M.; Stegemann, B.; Rademann, K.; Schwarz, U. D. *Phys. Rev. B* **2005,** *71,* 085405. doi:10.1103/PhysRevB.71.085405

19. Paolicelli, G.; Rovatti, M.; Vanossi, A.; Valeri, S. *Appl. Phys. Lett.* **2009,** *95,* 143121. doi:10.1063/1.3238320

20. Sitti, M.; Hashimoto, H. *IEEE-ASME Trans. Mechatron.* **2000,** *5,* 199. doi:10.1109/3516.847093

21. Mougin, K.; Gnecco, E.; Rao, A.; Cuberes, M. T.; Jayaraman, S.; McFarland, E. W.; Haidara, H.; Meyer, E. *Langmuir* **2008,** *24,* 1577. doi:10.1021/la702921v

22. Adams, D. M.; Brus, L.; Chidsey, C. E. D.; Creager, S.; Creutz, C.; Kagan, C. R.; Kamat, P. V.; Lieberman, M.; Lindsay, S.; Marcus, R. A.; Metzger, R. M.; Michel-Beyerle, M. E.; Miller, J. R.; Newton, M. D.; Rolison, D. R.; Sankey, O.; Schanze, K. S.; Yardley, J.; Zhu, X. *J. Phys. Chem. B* **2003,** *107,* 6668. doi:10.1021/jp0268462

23. Haruta, M. *CATTECH* **2002,** *6,* 102. doi:10.1023/A:1020181423055

24. Valden, M.; Lai, X.; Goodman, D. W. *Science* **1998,** *281,* 1647. doi:10.1126/science.281.5383.1647

25. Wang, J. *Anal. Chim. Acta* **2003,** *500,* 247. doi:10.1016/S0003-2670(03)00725-6

26. Penn, S. G.; He, L.; Natan, M. J. *Curr. Opin. Chem. Biol.* **2003,** *7,* 609. doi:10.1016/j.cbpa.2003.08.013

27. Frens, G. *Nature (London)* **1973,** *241,* 20.

28. Grabar, K. C.; Allison, K. J.; Baker, B. E.; Bright, R. M.; Brown, K. R.; Freeman, R. G.; Fox, A. P.; Keating, C. D.; Musick, M. D.; Natan, M. J. *Langmuir* **1996,** *12,* 2353. doi:10.1021/la950561h

29. Nikoobakht, B.; El-Sayed, M. A. *Chem. Mater.* **2003,** *15,* 1957. doi:10.1021/cm020732l

30. Nehl, C. L.; Liao, H.; Hafner, J. H. *Nano Lett.* **2006,** *6,* 683. doi:10.1021/nl052409y

31. Brust, M.; Walker, M.; Bethell, D.; Schiffrin, D. J.; Whyman, R. *J. Chem. Soc., Chem. Commun.* **1994,** 801. doi:10.1039/C39940000801

32. Sun, S.; Mendes, P.; Critchley, K.; Diegoli, S.; Hanwell, M.; Evans, S. D.; Leggettt, G. J.; Preece, J. A.; Richardson, T. H. *Nano Lett.* **2006,** *6,* 345. doi:10.1021/nl052130h

33. Mougin, K.; Haidara, H.; Castelein, G. *Colloids Surf., A* **2001,** *193,* 231. doi:10.1016/S0927-7757(01)00744-0

34. Mougin, K.; Haidara, H. *Langmuir* **2002,** *18,* 9566. doi:10.1021/la020491w

35. Palacio, M.; Bushan, B. *Nanotechnology* **2008,** *19,* 315710. doi:10.1088/0957-4484/19/31/315710

36. Anczykowski, B.; Gotsmann, B.; Fuchs, H.; Cleveland, J. P.; Elings, V. B. *Appl. Surf. Sci.* **1999,** *140,* 376. doi:10.1016/S0169-4332(98)00558-3

37. Tafazzoli, A.; Sitti, M. In *Proceedings of the ASME International Mechanical Engineering Congress and Exposition,* ASME International Mechanical Engineering Congress and Exposition, Anaheim, CA, Nov 13–19, 2004; ASME International: New York, 2004.

38. Sumer, B.; Sitti, M. *J. Adhes. Sci. Technol.* **2008,** *22,* 481. doi:10.1163/156856108X295527

39. Rao, A.; Gnecco, E.; Marchetto, D.; Mougin, K.; Schoenenberger, M.; Valeri, S.; Meyer, E. *Nanotechnology* **2009,** *20,* 115706. doi:10.1088/0957-4484/20/11/115706

40. Rao, A. Controlled Manipulation of Nanoparticles: Scanning Probe Measurements and Modelling of Trajectories and Dissipative Effects. Ph.D. Thesis, University of Basel, Switzerland, 2009.
41. Bhushan, B.; Liu, H. *Phys. Rev. B* **2001,** *63,* 245412. doi:10.1103/PhysRevB.63.245412
42. Riedo, E.; Lévy, F.; Brune, H. *Phys. Rev. Lett.* **2002,** *88,* 185505. doi:10.1103/PhysRevLett.88.185505
43. Liu, Y.; Evans, D. F.; Song, Q.; Grainger, D. W. *Langmuir* **1996,** *12,* 1235. doi:10.1021/la950504o
44. Meredith, J. C.; Smith, A. P.; Karim, A.; Amis, E. J. *Macromolecules* **2000,** *33,* 9747. doi:10.1021/ma001298g
45. Israelachvili, J. *Intermolecular and Surface Forces;* Academic Press: San Diego, CA, 1992.
46. Dickinson, J. T.; Hariadi, R. F.; Scudiero, L.; Langford, S. C. *Tribol. Lett.* **1999,** *7,* 113. doi:10.1023/A:1019129622285
47. Bushan, B. Nanotribology, Nanomechanics, and Materials Characterization. In *Springer Handbook of nanotechnology;* Bushan, B., Ed.; Springer: Heidelberg, Germany, 2004; pp 789–856.
48. Stifter, T.; Marti, O.; Bhushan, B. *Phys. Rev. B* **2000,** *62,* 13667. doi:10.1103/PhysRevB.62.13667
49. Rao, A.; Wille, M.-L.; Gnecco, E.; Mougin, K.; Meyer, E. *Phys. Rev. B* **2009,** *80,* 193405. doi:10.1103/PhysRevB.80.193405
50. Mougin, K.; Castelein, G.; Haidara, H. *Tribol. Lett.* **2004,** *17,* 11. doi:10.1023/B:TRIL.0000017413.60354.bc
51. Bouhacina, T.; Aime, J. P.; Gauthier, S.; Michel, D.; Heroguez, V. *Phys. Rev. B* **1997,** *56,* 7694. doi:10.1103/PhysRevB.56.7694
52. Zwoerner, O.; Hoelscher, H.; Schwarz, U. D.; Wiesendanger, R. *Appl. Phys. A* **1998,** *66,* S263. doi:10.1007/s003390051142
53. Jaramillo, T. F.; Baeck, S.-H.; Cuenya, B. R.; McFarland, E. W. *J. Am. Chem. Soc.* **2003,** *125,* 7148. doi:10.1021/ja029800v
54. Cuenya, B. R.; Baeck, S. H.; Jaramillo, T. F.; McFarland, E. W. *J. Am. Chem. Soc.* **2003,** *125,* 12928. doi:10.1021/ja036468u

License and Terms

The role of the cantilever in Kelvin probe force microscopy measurements

George Elias[*1], Thilo Glatzel[2], Ernst Meyer[2], Alex Schwarzman[1], Amir Boag[1] and Yossi Rosenwaks[*1]

Full Research Paper

Address:
[1]School of Electrical Engineering, Faculty of Engineering, Tel-Aviv University, Ramat-Aviv 69978, Israel and [2]Department of Physics, University of Basel, Basel 4056, Switzerland

Email:
George Elias[*] - georgeel@post.tau.ac.il;
Yossi Rosenwaks[*] - yossir@eng.tau.ac.il

* Corresponding author

Keywords:
boundary elements method; cantilever; convolution; Kelvin probe force microscopy; point spread function

Abstract

The role of the cantilever in quantitative Kelvin probe force microscopy (KPFM) is rigorously analyzed. We use the boundary element method to calculate the point spread function of the measuring probe: Tip and cantilever. The calculations show that the cantilever has a very strong effect on the absolute value of the measured contact potential difference even under ultra-high vacuum conditions, and we demonstrate a good agreement between our model and KPFM measurements in ultra-high vacuum of NaCl monolayers grown on Cu(111). The effect of the oscillating cantilever shape on the KPFM resolution and sensitivity has been calculated and found to be relatively small.

Introduction

The effect of the measuring probe in electrostatic force based microscopies, such as Kelvin probe force microscopy (KPFM) [1], is very large because the measured forces are long range. This effect has been studied and analyzed by several groups [2-9], who invariably focused on the contribution of the tip while neglecting the effect of the cantilever or took it into account using various approximations. Hochwitz et al. [10] and Belaidi et al. [11] estimated the entire cantilever contribution to the overall electrostatic force as a function of the probe–sample distance and cantilever–sample angle. They concluded that the cantilever may impose a limitation on the maximal probe–sample distance that can be used to obtain high lateral resolution. Colchero et al. [12] calculated the influence of the cantilever on the KPFM resolution, and several groups [13-15] derived analytic expressions for the cantilever electrostatic force. To the best of our knowledge, despite the above studies, the accurate role of the cantilever in general, and in high resolution ultra-high vacuum (UHV) KPFM measurements in particu-

lar, has not been reported. In this work we use the boundary element method (BEM) [7] to calculate the point spread function (PSF) of the measuring probe: Tip and cantilever. The probe PSF analysis shows that the cantilever has a very strong effect on the absolute value of the measured contact potential difference (CPD) even under UHV conditions, and we demonstrate a good agreement between our model and KPFM measurements.

Experimental
Electrostatic model

In order to calculate the full probe configuration, we extended our previous model [7] to solve the entire probe–surface electrostatic system, including the cantilever. The model assumes a conducting probe and a sample that is represented by an infinitely thin dipole layer on top of an earthed plane; variations in the dipole density account for the inhomogeneous sample surface potential. Both the probe and the sample were divided into boundary elements in order to calculate their surface charge density. Unlike our previous work [7], where the probe was divided into conical and spherical elements, here we used commercial software (MSC/Patran®) in order to perform fast automatic meshing of an arbitrary probe geometry, including the cantilever as required in this work.

The probe charge density was used as the unknown quantity to be determined in order to calculate subsequently the PSF. We use the following notations: (a) A matrix $\mathbf{G}$ which is a discrete representation of the Green's function between two probe boundary elements; (b) a matrix $\mathbf{D}$ which represents the discretized influence of the dipole layer (representing the sample) on each probe mesh element; (c) a diagonal matrix $\mathbf{B}$ with diagonal elements equal to the z components of the normal area vectors of the probe boundary elements divided by $2\varepsilon_o$, and (d) the vector $\vec{V}_{CPD}(\mathbf{r})$, which is a discrete representation of the surface potential, corresponding to a probe centered at $\mathbf{r} = (x,y,z)$. Matrices $\mathbf{G}$, $\mathbf{D}$, $\mathbf{B}$ and vector $\vec{V}_{CPD}(\mathbf{r})$ were previously defined in [7] and are explained again in the Appendix section.

The probe–sample system was solved by dividing the mutual interactions into homogeneous and inhomogeneous parts. The homogeneous part represents a system with a probe above an infinite earthed plane, while the inhomogeneous part accounts for the contribution of the sample surface potential to the electrostatic force acting on the probe; the total potential is a sum of the two parts. In addition, we define $\vec{C}_h = \mathbf{G}^{-1}\vec{I}$, and $\mathbf{C}_{inh} = \mathbf{G}^{-1}\mathbf{D}$ where $\mathbf{G}^{-1}$ is the inverse of $\mathbf{G}$, and $\vec{I}$ is a vector with all elements equal to 1. The vector $\vec{C}_h$ represents the capacitance density (capacitance per unit area) between two probe elements and the matrix $\mathbf{C}_{inh}$ represents the mutual capacitance

density between every pair of surface and probe elements. By inserting the charge density distribution into the Maxwell stress tensor, replacing the probe potential with $V_{dc}(\mathbf{r}) + V_{ac}\sin(\omega t)$, and extracting the force, we obtained the following expression for the electrostatic force acting on the entire probe in the z direction at frequency ω:

$$F_{z,\omega}(\mathbf{r}) = 2V_{ac}\left(V_{dc}(\mathbf{r})\underbrace{\vec{C}_h^t\mathbf{B}\vec{C}_h}_{H_h} - \underbrace{\vec{C}_h^t\mathbf{B}\mathbf{C}_{inh}}_{\vec{H}_{inh}^t}\vec{V}_{CPD}(\mathbf{r}) \right) \quad (1)$$

where H_h is the coefficient of the homogeneous force component, and $\vec{H}_{inh}$ scales the relative contribution of each sample element to the inhomogeneous force; the superscript t denotes the transpose vector. The distinction between the homogeneous and inhomogeneous parts of the force is not merely mathematical; while the homogeneous force depends on the applied voltage, V_{dc}, the inhomogeneous force is proportional to a weighted average of the sample potential. These weights are due to the contributions from areas at different distances from the probe, and therefore will determine the KPFM spatial resolution.

Equation 1 calculates the force for a specific probe–sample distance. In practice, almost all UHV KPFM measurements use the single pass method. In this method, the cantilever oscillates at its first resonance frequency in order to measure the surface topography, while the oscillations due to the electrostatic force (in amplitude modulated AM-KPFM at the second resonance or in frequency modulated FM-KPFM at several hundred Hz [16]) are nullified by adjusting $V_{dc}(\mathbf{r})$. The first resonance oscillations have a strong effect on the measured CPD, especially at probe–sample distances smaller than 10 nm, where the electrostatic force varies strongly with the distance [17]. Since in most cases the KPFM feedback circuit time constant is much larger than the period of the first resonance oscillations, the force minimization condition must be applied to the average force. This leads to the following relation between the measured potential and the sample potential: $V_{dc}\big|_{\bar{F}_{z,\omega}=0}(\mathbf{r}) = \bar{H}_h^{-1}\bar{\bar{H}}_{inh}^t\vec{V}_{CPD}(\mathbf{r})$, where $\bar{F}_{z,\omega}$ is the averaged force. In addition, $\bar{\bar{H}}_{inh}$ and $\bar{H}_h$ represent, respectively, the time averaged of $\vec{H}_{inh}$ and H_h, which are defined in Equation 1 for a certain time, i.e., for a given probe height; the product $\bar{H}_h^{-1}\bar{\bar{H}}_{inh}^t$ is the PSF of the system. The time averaged force was calculated by sampling the sinusoidal movement at K time points uniformly covering an oscillation period T_0, so that $t_k = (T_0/K)\cdot k$ (where k is an integer between zero and K) and the probe–sample distance is $d(t_k) = A\sin(2\pi t_k/T_0)+A_0$, where A is the oscillation amplitude and A_0 is the average height. The

charge density on the probe was calculated for each probe–sample distance independently.

The magnitude of the cantilever effect on the measured potential can be explained as follows. Since the cantilever is located more than 10 μm above the sample surface, and its total lateral displacement during a high resolution scan is about 0.2 μm, its maximal angular movement relative to an axis perpendicular to the surface is on the order of 1°. Due to their large separation, the potential due to the surface dipole layer at the cantilever location can be expanded using the spherical harmonics series [18] (multipole expansion). As the angular span of the cantilever is very small during the scan, only terms with high multipole orders, (tens and higher), produce discernable angular variations. However, each multipole term decays as $1/r^n$ where r is the cantilever distance from the multipole origin, and n is the multipole order. Thus, these higher order terms in the multipole series are negligible at the cantilever location, since they decay as the reciprocal of the corresponding high power of the cantilever–sample distance. Therefore, we assumed, to a very good approximation, that the cantilever senses a constant potential during the entire scan.

To emphasize the cantilever role, we calculated separately the cantilever and tip contributions to the total vertical electrostatic force. The average force of a given geometrical model x (tip or cantilever) can be expressed using the calculated expected potential: $\bar{F}^x_{z,\omega}(\mathbf{r}) = 2V_{ac}\bar{H}^x_h\left(V_{dc}(\mathbf{r}) - V^x_{dc}\big|_{\bar{F}^x_{z,\omega}=0}(\mathbf{r})\right)$; where $\bar{H}^x_h$ is the averaged homogeneous force coefficient and $V^x_{dc}\big|_{\bar{F}^x_{z,\omega}=0}(\mathbf{r})$ is the nullifying force potential of the specific model x. Neglecting the mutual electrostatic interaction between the cantilever and the tip, the total force on the probe is $F^{tot}_{z,\omega}(\mathbf{r}) = F^{tip}_{z,\omega}(\mathbf{r}) + F^{cant}_{z,\omega}(\mathbf{r})$. Based on the conclusion from the previous paragraph, we approximated $V^{cant}_{dc}\big|_{\bar{F}^{cant}_{z,\omega}=0}(\mathbf{r})$, which is the potential after nullifying only the cantilever force, by a constant. Then, by minimizing the total force we obtained:

$$V^{tot}_{dc}\bigg|_{\bar{F}^{tot}_{z,\omega}=0}(\mathbf{r}) = \frac{\bar{H}^{tip}_h}{\left(\bar{H}^{tip}_h + \bar{H}^{cant}_h\right)}V^{tip}_{dc}\bigg|_{\bar{F}^{tip}_{z,\omega}=0}(\mathbf{r}) + \text{const.} \quad (2)$$

Equation 2 shows that the constant force of the cantilever introduces a factor of $\bar{H}^{tip}_h\big/\left(\bar{H}^{tip}_h + \bar{H}^{cant}_h\right)$ relative to a model that takes into account only the tip. In addition, since only a scaling factor is introduced in Equation 2, the cantilever does not affect the lateral resolution, but may strongly affect the CPD absolute value, even in high resolution UHV KPFM measurements, as we demonstrate below. It should be noted that our model does not include signal-to-noise considerations, which may reduce the lateral resolution due to the above scaling.

Results and Discussion
Cantilever influence on the system PSF and force analysis

The influence of the cantilever was calculated for two different geometries: One comprising only a tip normal to the sample surface composed of a sphere under a cone enclosed with a spherical cap, and the other containing the entire cantilever tilted relative to the surface. The first shape does not include a tilt since it is a reference model describing a widely used geometry [3,4]. Figure 1a and Figure 1b illustrate the used variables as well as the connection between cantilever and tip cone which has a rounded shape to avoid an infinite charge density distribution on sharp edges. Figure 1c shows the calculated cantilever contribution to the total homogeneous force on the probe as a function of the probe–sample distance for two different tilt angles: β = 20° (solid line) and β = 10° (dashed line). For a probe–sample distance of 30 nm, which is frequently used in ambient KPFM, and β = 10°, the cantilever contributes around 60% of the total homogeneous force. It was observed that the cantilever influence increases with the probe–sample distance, or for smaller tilt angles, as expected.
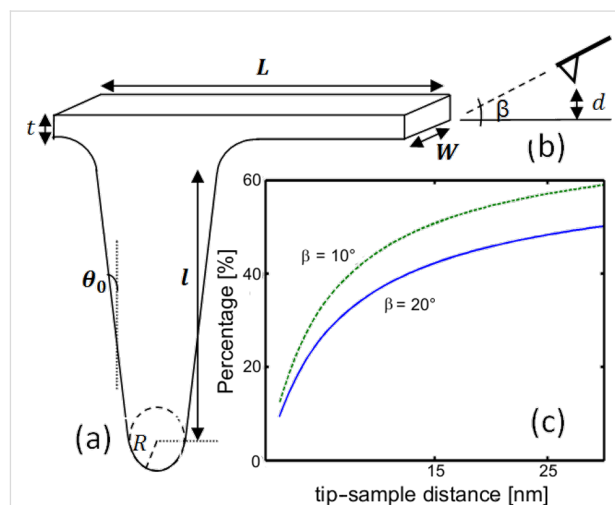

Figure 1: (a) Geometrical model of a tip, with cone length *l*, half-aperture angle θ_0, spherical apex radius *R*, and cantilever width, length and thickness *W, L* and *t*, respectively. (b) Probe–sample cross section for a probe distance *d* from the surface, tilted at an angle β. (c) Cantilever homogeneous force contribution relative to the total homogeneous force, as a function of the probe–sample distance for two tilt angles: β = 20° (solid line) and β = 10° (dashed line), with cantilever width of *W* = 40 μm. These and all the following results were calculated for the parameter values: *R* = 30 nm, θ_0 = 17.5°, *l* = 14 μm, *L* = 225 μm and *t* = 7 μm.

The effect of the cantilever on the PSF is demonstrated in Figure 2 for two different probe–sample distances with and without the cantilever, represented by the dashed and solid lines, respectively. For a probe–sample distance of 1.2 nm (Figure 2a), the maximum value of the cantilever PSF decreased

by about 85% compared to the tip PSF. At a probe–sample distance of 17.8 nm, the presence of the cantilever reduced the PSF peak by almost a factor of 3 compared to the PSF computed without the cantilever. The horizontal lines represent the full width at half maximum (FWHM) for the two cases and demonstrate the conclusion that the cantilever hardly affects the measurement resolution. It should be emphasized that the difference between the two cases stems not only from the cantilever, but also from the tilt of the probe relative to the surface.

Figure 2: One dimensional PSF calculated for two different probe–sample distances with and without the cantilever, represented by the dashed and solid lines respectively. The model with the tip only uses β = 0° (normal to the surface) while the other one uses β = 10°. (a) Tip–sample distance of 1.2 nm, (b) tip–sample distance of 17.8 nm. The horizontal lines in (b) represent the FWHM for a probe–sample distance of 17.8 nm. The simulations were performed using W = 40 μm.
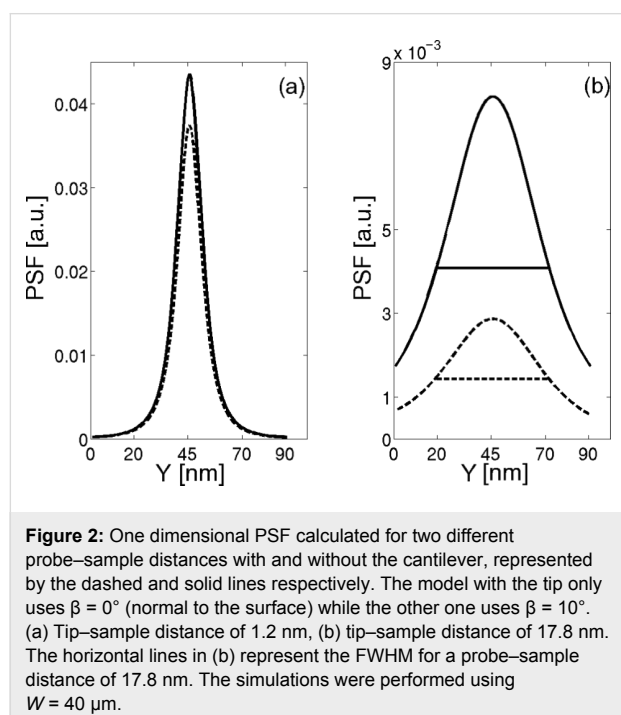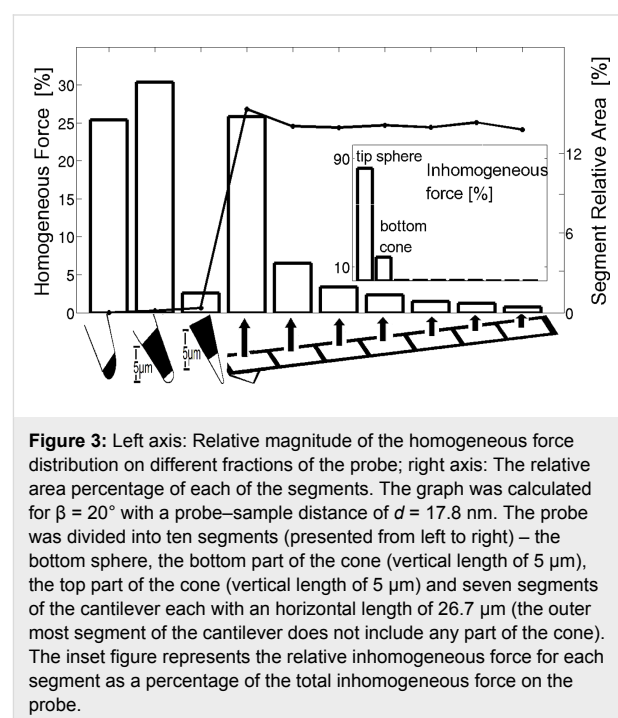
Figure 3 displays the relative homogeneous force contribution of the various parts of the probe normalized to the total homogeneous force (left axis), for a probe located 17.8 nm above the surface. Each bar corresponds to a different part of the probe defined as follows (from left to right): The bottom sphere of the tip, the bottom and top parts of the cone (each having a vertical length of 5 μm), and seven segments of the cantilever each with an equal length of 26.7 μm, with the first segment located closest to the tip. The spherical tip apex and the bottom part of the cone contribute 25% and 30% to the overall homogeneous force, respectively. The rest of the force stems mostly from the cantilever, especially from the two segments which are nearest to the tip which contribute 25.8% and 6.5% each. The effect of the cantilever segments decreases the further away each segment is from the tip. This is due to the tilt of the cantilever which increases the distance of each segment from the sample surface as we move along the cantilever away from the tip. Nevertheless, since the cantilever area is very large even the

remaining five outermost segments contribute about 9.2% of the total force. The right axis in Figure 3 presents the relative area of each part of the probe out of the total probe surface area. The area of the first two parts is significantly smaller than that of the cantilever. In addition, though the upper part of the cone has a much larger surface area than the lower one, it has a very small effect on the overall force, since its surface area is not large enough to compensate for the decay in the force – which is a result of the increasing distance from the sample.

Figure 3: Left axis: Relative magnitude of the homogeneous force distribution on different fractions of the probe; right axis: The relative area percentage of each of the segments. The graph was calculated for β = 20° with a probe–sample distance of *d* = 17.8 nm. The probe was divided into ten segments (presented from left to right) – the bottom sphere, the bottom part of the cone (vertical length of 5 μm), the top part of the cone (vertical length of 5 μm) and seven segments of the cantilever each with an horizontal length of 26.7 μm (the outer most segment of the cantilever does not include any part of the cone). The inset figure represents the relative inhomogeneous force for each segment as a percentage of the total inhomogeneous force on the probe.
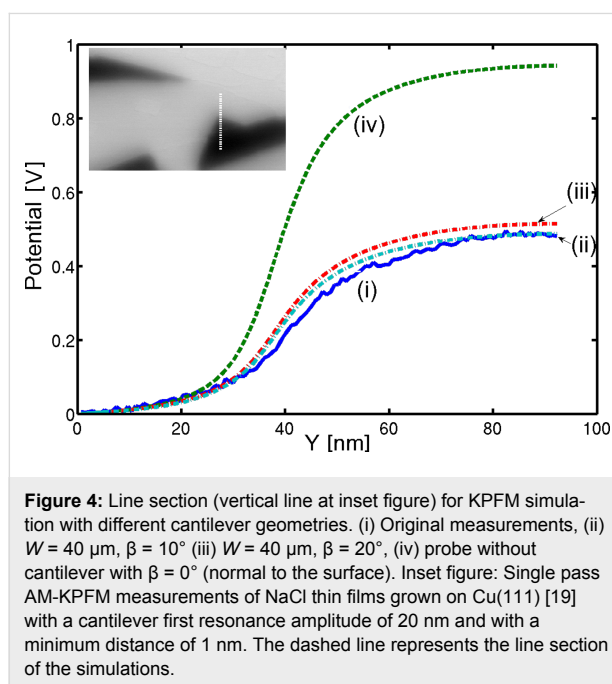
The inset of Figure 3 shows the relative inhomogeneous force magnitude distribution along the probe using the same segments. The force was calculated for a square sample (192 nm by 192 nm) having a potential difference of 1V relative to an infinite earthed substrate around it. It was observed that the spherical apex of the tip and the bottom part of the cone contribute 82.7% and 17.2%, respectively, of the inhomogeneous force, while the contribution of the rest of the probe was negligible. This demonstrates the profound effect of the tip apex on the KPFM resolution and, consequently, the minor influence of the cantilever.

Further calculations showed that at smaller probe sample distances the homogenous force contribution of the tip apex is higher. At a probe–sample distance of 1.2 nm (a typical distance in ultra-high vacuum measurements) the tip apex contributes 83% to the homogenous force, the cone lower segment contributes 7.3%, and the entire cantilever contributes only 8.4%.
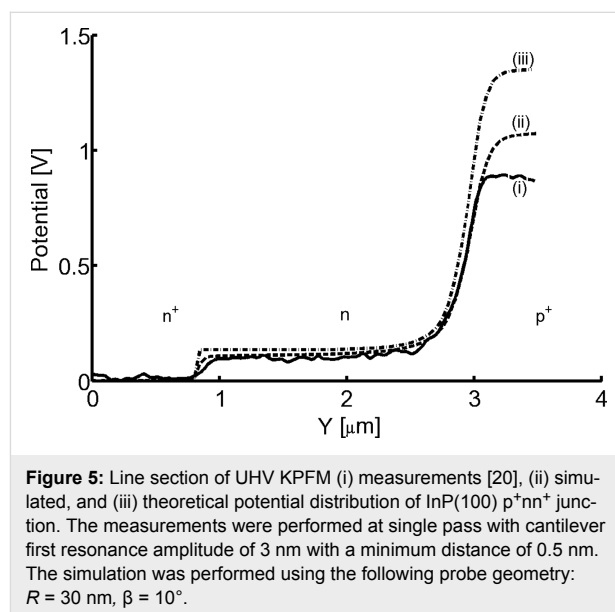
Comparison with experimental results

The above analysis was applied to high resolution UHV KPFM measurements of NaCl thin films grown on Cu(111) [19]. The simulation was performed by convolving the two-dimensional PSF with the theoretical surface potential difference between Cu and NaCl, where we assumed that the actual CPD landscape is approximately identical to the measured topography. Therefore, we used the measured topography as a rough estimate for the theoretical surface potential. Figure 4 shows a comparison between the measured CPD curve (i) and the simulated potential along a single line section (dashed line in the inset image). Curves (ii) and (iii) were calculated for a probe that includes a cantilever with two different tilt angles, and curve (iv) corresponds to a vertical tip. The calculation that included the cantilever shows a good agreement with the measurements both in terms of the resolution and the absolute CPD value. Comparison of curve (ii) to curve (iii), which represent tilt angles of 10° and 20°, respectively, shows that the exact angle has a weak effect. The model that includes only the tip shows a good agreement in terms of spatial resolution, but is about a factor of 2 larger than the absolute CPD value. Additional simulations show that changing the cantilever width may have a large effect on the results.

Figure 4: Line section (vertical line at inset figure) for KPFM simulation with different cantilever geometries. (i) Original measurements, (ii) $W = 40$ μm, $\beta = 10°$ (iii) $W = 40$ μm, $\beta = 20°$, (iv) probe without cantilever with $\beta = 0°$ (normal to the surface). Inset figure: Single pass AM-KPFM measurements of NaCl thin films grown on Cu(111) [19] with a cantilever first resonance amplitude of 20 nm and with a minimum distance of 1 nm. The dashed line represents the line section of the simulations.

We also demonstrate the effect of the cantilever on UHV KPFM measurements of a cleaved InP(100) p^+nn^+ junction [20]. As observed in Figure 5, the measured potential difference across the p^+n part of the junction (i) is ~0.9 V, which is smaller than the theoretical difference of around 1.35 V (iii) (calculated assuming an absence of surface states). Curve (ii) is the poten-

tial profile obtained by convoluting the theoretical junction potential (iii) with the PSF of the specific probe used in the experiments. It was observed that even far from the junction, i.e., deep inside the p^+ InP, the cantilever induced a potential offset of about 22% relative to the theoretical profile. This is in agreement with our analysis that the cantilever has a large influence on the absolute CPD value even above a relatively large equipotential area. The difference of ~0.15 V between the measurement and the convoluted profile may be attributed either to surface states or to a slightly different cantilever geometry.

Figure 5: Line section of UHV KPFM (i) measurements [20], (ii) simulated, and (iii) theoretical potential distribution of InP(100) p^+nn^+ junction. The measurements were performed at single pass with cantilever first resonance amplitude of 3 nm with a minimum distance of 0.5 nm. The simulation was performed using the following probe geometry: $R = 30$ nm, $\beta = 10°$.

The role of the cantilever oscillations

The analysis in the previous sections assumed that the cantilever shape is rigid during the measurement. In practice, the cantilever bends according to its mechanical properties. This has two implications on the force analysis presented above: The first is related to a different probe–sample distance profile which stems from the cantilever first resonance shape, while the second is a result of the change in the cantilever shape in its second resonance mode; this leads to a differentially weighted effect of the electrostatic forces along the cantilever. These two effects were analyzed and are discussed below.

The effect of the first resonance

In either the single or dual pass KPFM methods the cantilever oscillates at the frequency of its first resonance in order to measure the surface topography in the non-contact mode. In the previous sections the cantilever was considered rigid, meaning that during the calculation of $\vec{H}_{inh}$ and H_h of Equation 1 along the vertical tip movement, only the minimal probe–sample distance changed while the cantilever geometry was considered

constant. In practice the cantilever beam oscillates according to the boundary conditions of a clamp-free beam. The cantilever was modeled as a rectangular prismatic beam with one end restrained and the other one free. We used the beam fundamental mode formula, while neglecting deformations that may be introduced by the presence of the tip load at the end of the cantilever or by additional forces between the sample and the tip. This was done in order to evaluate the main influence of the oscillation without adding unnecessary complexity. Assuming that the cantilever is clamped at $y' = 0$, the vertical deformation along the y axis, and as a function of time, is given by [21]:

$$Z_n^{'}(y',t) = \frac{A}{2} \left\{ \begin{array}{l} \cos\left(\frac{B_n y'}{L}\right) - \cosh\left(\frac{B_n y'}{L}\right) \\ + \alpha_n \left[\sin\left(\frac{B_n y'}{L}\right) - \sinh\left(\frac{B_n y'}{L}\right) \right] \end{array} \right\} \cos\left(\frac{2\pi t}{T_0}\right) \quad (3)$$

where for the first mode (n = 1) $B_1 = 1.975$, $\alpha_1 = -0.731$, L is the cantilever length and, as before, T_0 is the oscillation period and A is the oscillation amplitude. The y' and z' axes are rotated by β degrees relative to the main coordinates (y, z) (see also Figure 7).

As before, the oscillatory movement was uniformly sampled; for each discrete time sample an entirely new geometry was established according to the deformation of Equation 3 and the average probe–sample height, A_0. For each configuration, the tip was positioned perpendicular to the free edge of the cantilever and the clamped edge of the cantilever was always at the same position. All these geometries were created using Patran's® command language (PCL) used to create automatically the entire geometry and mesh at any given time.

The influence of the beam deflection is shown in Figure 6. In all the three plots, the cantilever PSF (dashed lines) is compared to the rigid cantilever (solid lines); both were calculated for a cantilever oscillating with an amplitude of 20 nm and a minimum probe–sample distance of 1 nm. Figure 6b and Figure 6c present a comparison for a probe positioned at distances of 1.2 nm and 11.9 nm, respectively, above the surface. The inset figures illustrate the shape and position of rigid (solid line) and deformed (dashed line) cantilevers, emphasizing that the comparison is performed while maintaining the same minimum probe–sample distance in both cases. Figure 6b shows that at the lowest point of the oscillation there is a weak influence of the cantilever deformation on the PSF. Close to the equilibrium point, shown in Figure 6c, the significant difference between the two PSFs is that they are shifted, which clearly visible by comparing the peak positions. This offset of about 5 nm results from the change in the cantilever

shape which changes the tip angle. The averaged PSF, which is the average over the entire oscillation cycle, is presented for both cases in Figure 6a. It can be seen that the overall impact of the cantilever deformation, both on the average PSF and at any given probe–sample distance, is negligible. Therefore, we conclude that a simple model of a rigid cantilever is an adequate approximation.
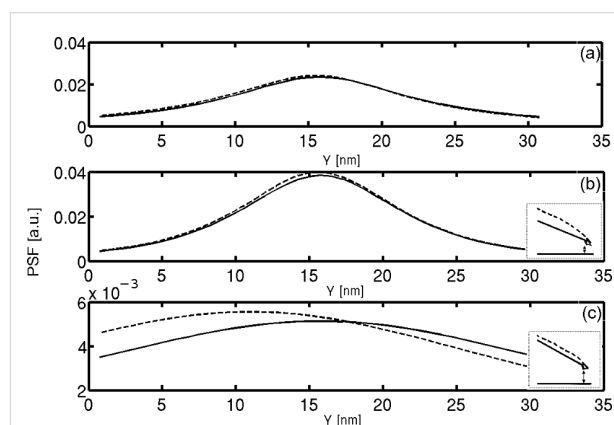

Figure 6: Beam deflection influence on PSF. The dashed line represents the PSF of a deflected beam while the solid one is for a stiff cantilever. Simulation was performed with cantilever first resonance amplitude of 20 nm with a minimum distance of 1 nm. (a) PSF comparison after averaging; (b) comparison for a probe located at a distance of 1.2 nm above the surface; (c) comparison for a probe located at a distance of 11.9 nm above the surface. Inset figures at (b) and (c) illustrate the deflected and stiff beams that were used for the calculations.

The effect of the second resonance

In most AM-KPFM single pass measurements an external AC bias, at a frequency ω of the second resonance of the beam, is applied to the entire probe. This oscillation, shown in Figure 7, is minimized by applying an additional DC bias to give the CPD. In the previous sections this was modeled by nullifying the entire electrostatic force acting on the probe. However, this analysis is not accurate since the electrostatic forces at different points along the cantilever have a different effect on the beam edge amplitude. As an example, consider a point along the cantilever which has zero amplitude (e.g., the end point which is held mechanically fixed). The forces acting at this point do not affect the amplitude measured by the detector, and therefore should not be considered in the electrostatic force minimization.

We first assumed that at a frequency ω (the second mechanical resonance) the beam is always deformed according to its second harmonic movement. We can assume that this is the only relevant mode, since it is the only frequency passed by the filter before the KPFM feedback circuit. Assuming, once again, that the beam deflection is purely harmonic, its deflection is given
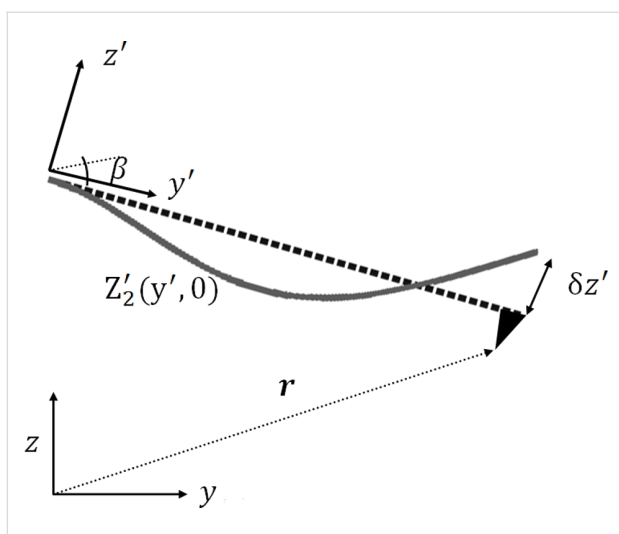
Figure 7: Second harmonic deflection relative to the cantilever at its rest position. The free edge deflection of the cantilever is δz'. All the other amplitude values along the cantilever are calculated relative to this deflection.

by Equation 3 with the coefficients $B_2 = 4.69$, $\alpha_2 = -1.018$, corresponding to the second mode (n = 2). In order to analyze the influence of the second resonance, we use the concept of virtual displacement [22] which states that the system equilibrium is obtained when the total external (virtual) work acting on the beam is zero. For a given time $t = 0$, assuming that the free edge of the cantilever $(y' = L)$ undergoes a small (virtual) displacement δz', we can determine the relative displacements of every point along the cantilever by using $A = \delta z'$ in Equation 3. In this situation, the entire virtual work $W_z(\mathbf{r})$ done by the external electrostatic forces in the z direction, for a probe positioned at $\mathbf{r}$, is given by

$$
W_z(\mathbf{r}) = \iiint_{\text{cantilever}} \cos\beta Z_2'(y',0) \cdot f_{z,\omega}^{\text{cant}}(\mathbf{r}',\mathbf{r})d\mathbf{r}'
$$
$$
+ \iiint_{\text{tip}} \cos\beta Z_2'(L,0) \cdot f_{z,\omega}^{\text{tip}}(\mathbf{r}',\mathbf{r})d\mathbf{r}' \qquad (4)
$$

where $f_{z,\omega}^{\text{cant}}(\mathbf{r}',\mathbf{r})$ and $f_{z,\omega}^{\text{tip}}(\mathbf{r}',\mathbf{r})$ are the local forces acting at point $\mathbf{r}'$ on the cantilever and the tip, respectively, when the probe is located at $\mathbf{r}$. In addition, $\mathbf{r}'$ corresponds to the rotated coordinate system (x', y', z'). Since the tip is located at the end of the beam, it experiences a constant amplitude. Figure 7 illustrates the second harmonic bending described by the function $Z'_2(y', 0)$ with an edge amplitude of $A = \delta z'$ relative to a probe tilted at an angle β and positioned at $\mathbf{r}$ in the main fixed coordinate system.

The steady state is reached when $W_z(\mathbf{r})$ is minimized instead of the total electrostatic force. This is achieved by multiplying the force over each boundary element by its relative virtual dis-

placement. We define a diagonal matrix **Z** whose diagonal elements are equal to the relative displacement for each cantilever element and equal to 1 for each tip element. The overall virtual work function may then be written as

$$
W_{z,\omega}(\mathbf{r}) = \delta z' \cos\beta\; 2V_{\text{ac}}
$$
$$
\times \left(V_{\text{dc}}(\mathbf{r})\vec{C}_h^t \mathbf{BZ}\vec{C}_h - \vec{C}_h^t \mathbf{BZC}_{\text{inh}} \vec{V}_{\text{CPD}}(\mathbf{r}) \right) \qquad (5)
$$

By nullifying the above expression we may achieve the new PSF of the system, similar to the process described in the Experimental section.

Figure 8 shows the effect of the second harmonic oscillations on the calculated PSF, for a probe–sample distance of 11.4 nm (a) and for an average PSF calculated for a first resonance movement with a minimal probe–sample distance of 1 nm and amplitude of 20 nm (b). The figure shows that the introduction of the second harmonic weighting has changed only the PSF height and not its shape, since it influences only the cantilever. In addition, it caused the PSF to increase by around 20% and 10% for a probe–sample distance of 11.4 nm and for the averaged PSF, respectively. The impact of the second harmonic oscillations is limited, since as shown in Figure 3, the dominant contribution of the cantilever to the homogeneous force stems from the areas closest to the tip. These areas resonate with similar amplitudes to that of the tip and therefore their relative displacement will be close to one. This additional refinement of the model does not have an entirely negligible influence on the PSF. However, since most of the impact of the cantilever remains the same, as in the model with a rigid cantilever, using such a model may
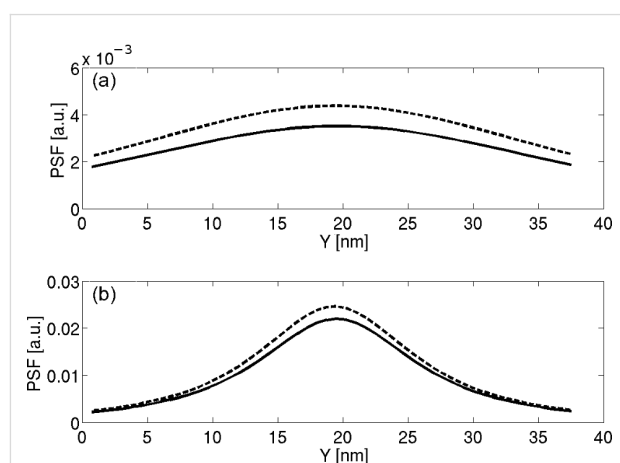

Figure 8: Second harmonic weighting influence on the PSF. Dashed lines: PSF calculated with the second harmonic displacement, using virtual work equilibrium. Solid lines: PSF calculated for a rigid cantilever. (a) Probe–sample distance d = 11.4 nm; (b) averaged PSF for amplitude of 20 nm with a minimum distance of 1 nm. For both cases the cantilever parameters were W = 40 μm, β = 20°.

provide a sufficiently accurate approximation. It should be noted that the above analysis will be different in the dual pass technique, since the applied bias frequency usually differs from the second resonance of the beam.

Conclusion

We have used the BEM method to calculate the cantilever contribution in KPFM measurements. By analyzing the force expression, we showed that although the cantilever may have little effect on the measurement resolution, it has a profound influence on the absolute CPD value. The influence of the cantilever has a direct relation to the probe–sample distance and an inverse relation to the probe–surface angle. It was found that even at probe–sample distances in the range of several nanometers, the absolute CPD may change by as much as 50% if the cantilever contribution is neglected. We have applied our analysis to UHV KPFM measurements and obtained good agreement both in the resolution and in the absolute value of the measured potential. This suggests that the cantilever must be taken into account in quantitative surface potential measurements. Longer tips or FM-KPFM will reduce the cantilever contribution and improve the measurement precision.

In the second part of this paper, we calculated the influence of the cantilever deformations on the measured KPFM. It was found that the exact cantilever shape in its first resonance has a very small effect, while the second resonance deformation has a larger effect on the PSF and thus should be considered where high surface potential accuracy is required.

Appendix – full matrix definitions

In this appendix we explicitly define the matrices that are used in the paper.

We define $\hat{\mathbf{z}}$ as the unit vector pointing in the z direction and $\mathbf{r}_i$ as the location of the center of the ith boundary element of the probe's surface. Each probe element is assumed to have a constant surface charge density. The ijth element of matrix **G** is given by

$$G_{ij} = \frac{1}{4\pi\varepsilon}\left(\int_{\Delta S_j} \frac{1}{|\mathbf{r}_i - \mathbf{r}'|} - \frac{1}{|\mathbf{r}_i - \tilde{\mathbf{r}}'|} ds'\right), \qquad (6)$$

where $\tilde{\mathbf{r}}'$ is the location of the image charge of the probe's jth element relative to an infinite earthed plane, so that if $\mathbf{r}' = (x', y', z')$ then $\hat{\mathbf{n}}_i = (x', y', -z')$. The integral is performed over the jth surface element of the probe. The diagonal of matrix **B** is defined as

$$B_{ii} = \frac{\hat{\mathbf{n}}_i \cdot \hat{\mathbf{z}}}{2\varepsilon}\int_{\Delta S_i} ds \qquad (7)$$

where $\hat{\mathbf{n}}_i$ is the outward normal unit vector to the ith surface element. The integral is performed over the probe's ith surface element.

The sample surface potential is discretized using uniform square elements according to the resolution of the scan, denoted Δ. The center of the kth surface element is located at $\mathbf{r}_k = (k_x\Delta, k_y\Delta)$ where both k_x and k_y are integers. The ikth element of matrix **D** is described as

$$D_{ik} = \frac{1}{2\pi}\int_{\Delta S_k} \frac{(\mathbf{r}_i - \mathbf{r}') \cdot \hat{\mathbf{z}}}{|\mathbf{r}_i - \mathbf{r}'|^3} ds' \qquad (8)$$

where the integral is performed over the kth element of the sample surface.

The kth element of the vector $\vec{V}_{CPD}(\mathbf{r})$ is obtained as

$$V_{CPD_k}(\mathbf{r}) = V_{CPD}(\mathbf{r} - \mathbf{r}_k) \qquad (9)$$

where $V_{CPD}(\mathbf{r})$ is the continuous CPD function of the sample and $\mathbf{r}$ represents the lateral position of the probe.

The measured potential over the probe for each location $\mathbf{r}$, $V_p(\mathbf{r})$, is a superposition of the potential induced by the charge distribution over the probe and the potential induced by the sample:

$$V_p(\mathbf{r})\vec{I} = \mathbf{G}\vec{\sigma} + \mathbf{D}\vec{V}_{CPD}(\mathbf{r}) \qquad (10)$$

where $\vec{\sigma}$ is a vector representing the charge distribution on each boundary element of the probe and $\vec{I}$ is a vector whose elements are equal to one. The probe's charge density is extracted using this equation. By inserting the charge density into the Maxwell stress tensor, we obtain Equation 1.

Acknowledgements

References

1. Weaver, J. M. R.; Abraham, D. W.
   J. Vac. Sci. Technol., B: Microelectron. Nanometer Struct.–Process., Meas., Phenom. **1991,** *9,* 1559–1561. doi:10.1116/1.585423
2. Rosenwaks, Y.; Glatzel, T.; Sadewasser, S.; Shikler, R. *Phys. Rev. B* **2004,** *70,* 085320. doi:10.1103/PhysRevB.70.085320
3. Hudlet, S.; Saint Jean, M.; Guthmann, C.; Berger, J. *Eur. Phys. J. B* **1998,** *2,* 5–10. doi:10.1007/s100510050219
4. Jacobs, H. O.; Leuchtmann, P.; Homan, O. J.; Stemmer, A.
   J. Appl. Phys. **1998,** *84,* 1168. doi:10.1063/1.368181
5. Belaidi, S.; Lebon, F.; Girard, P.; Leveque, G.; Pagano, S.
   Appl. Phys. A **1998,** *66,* S239–S243. doi:10.1007/s003390051138
6. Sadewasser, S.; Glatzel, T.; Shikler, R.; Rosenwaks, Y.;
   Lux-Steiner, M. C. *Appl. Surf. Sci.* **2003,** *210,* 32–36.
   doi:10.1016/S0169-4332(02)01475-7
7. Strassburg, E.; Boag, A.; Rosenwaks, Y. *Rev. Sci. Instrum.* **2005,** *76,* 083705. doi:10.1063/1.1988089
8. Bocquet, F.; Nony, L.; Loppacher, C.; Glatzel, T. *Phys. Rev. B* **2008,** *78,* 035410. doi:10.1103/PhysRevB.78.035410
9. Law, B. M.; Rieutord, F. *Phys. Rev. B* **2002,** *66,* 035402.
   doi:10.1103/PhysRevB.66.035402
10. Hochwitz, T.; Henning, A. K.; Levey, C.; Daghlian, C.; Slinkman, J.
    J. Vac. Sci. Technol., B: Microelectron. Nanometer Struct.–Process., Meas., Phenom. **1996,** *14,* 457. doi:10.1116/1.588494
11. Belaidi, S.; Girard, P.; Leveque, G. *J. Appl. Phys.* **1997,** *81,* 1023.
    doi:10.1063/1.363884
12. Colchero, J.; Gil, A.; Baro, A. M. *Phys. Rev. B* **2001,** *64,* 245403.
    doi:10.1103/PhysRevB.64.245403
13. Koley, G.; Spencer, M.; Bhangale, H. R. *Appl. Phys. Lett.* **2001,** *79,* 545. doi:10.1063/1.1384004
14. Bonaccurso, E.; Schonfeld, F.; Butt, H. J. *Phys. Rev. B* **2006,** *74,* 085413. doi:10.1103/PhysRevB.74.085413
15. Guriyanova, S.; Golovko, D. S.; Bonaccurso, E. *Meas. Sci. Technol.* **2010,** *21,* 025502. doi:10.1088/0957-0233/21/2/025502
16. Glatzel, T.; Sadewasser, S.; Lux-Steiner, M. C. *Appl. Surf. Sci.* **2003,** *210,* 84–89. doi:10.1016/S0169-4332(02)01484-8
17. Kawai, S.; Glatzel, T.; Hug, H. J.; Meyer, E. *Nanotechnology* **2010,** *21,* 245704. doi:10.1088/0957-4484/21/24/245704
18. Jackson, J. D. *Classical Electrodynamics,* 3rd ed.; John Wiley & Sons: New York, 1998.
19. Glatzel, T.; Zimmerli, L.; Koch, S.; Such, B.; Kawai, S.; Meyer, E.
    Nanotechnology **2009,** *20,* 264016.
    doi:10.1088/0957-4484/20/26/264016
20. Schwarzman, A. Nanoscale Electrical Characterization of Semiconductors Using Ultra High Vacuum Kelvin Probe Force Microscopy. Ph.D. Thesis, Tel-Aviv University, Israel, 2007.
21. Young, D.; Felgar, R. P., Jr. *Tables of characteristic functions representing normal modes of vibration of a beam;* University of Texas Publication: Austin, Texas, 1949.
22. Becker, R. A. *Introduction of Theoretical Mechanics,* 1st ed.; McGraw-Hill: New York, 1954.

Distinguishing magnetic and electrostatic interactions by a Kelvin probe force microscopy–magnetic force microscopy combination

Miriam Jaafar[1,2], Oscar Iglesias-Freire[1], Luis Serrano-Ramón[3,4], Manuel Ricardo Ibarra[3,4,5], Jose Maria de Teresa[3,4,5] and Agustina Asenjo[*1]

Full Research Paper

Address:
[1]Instituto de Ciencia de Materiales de Madrid, CSIC, Madrid, 28049, Spain, [2]Dpto. Física de la Materia Condensada, Universidad Autónoma de Madrid, Madrid, 28049, Spain, [3]Instituto de Ciencia de Materiales de Aragón, Universidad de Zaragoza-CSIC, Zaragoza, 50009, Spain, [4]Dpto. Física de la Materia Condensada, Universidad de Zaragoza-CSIC, Zaragoza, 50009, Spain and [5]Laboratorio de Microscopías Avanzadas (LMA), Instituto de Nanociencia de Aragón (INA), Universidad de Zaragoza, Zaragoza, 50018, Spain

Email:
Agustina Asenjo[*] - aasenjo@icmm.csic.es

* Corresponding author

Abstract

The most outstanding feature of scanning force microscopy (SFM) is its capability to detect various different short and long range interactions. In particular, magnetic force microscopy (MFM) is used to characterize the domain configuration in ferromagnetic materials such as thin films grown by physical techniques or ferromagnetic nanostructures. It is a usual procedure to separate the topography and the magnetic signal by scanning at a lift distance of 25–50 nm such that the long range tip–sample interactions dominate. Nowadays, MFM is becoming a valuable technique to detect weak magnetic fields arising from low dimensional complex systems such as organic nanomagnets, superparamagnetic nanoparticles, carbon-based materials, etc. In all these cases, the magnetic nanocomponents and the substrate supporting them present quite different electronic behavior, i.e., they exhibit large surface potential differences causing heterogeneous electrostatic interaction between the tip and the sample that could be interpreted as a magnetic interaction. To distinguish clearly the origin of the tip–sample forces we propose to use a combination of Kelvin probe force microscopy (KPFM) and MFM. The KPFM technique allows us to compensate in real time the electrostatic forces between the tip and the sample by minimizing the electrostatic contribution to the frequency shift signal. This is a great challenge in samples with low magnetic moment. In this work we studied an array of Co nanostructures that exhibit high electrostatic interaction with the MFM tip. Thanks to the use of the KPFM/MFM system we were able to separate the electric and magnetic interactions between the tip and the sample.

Introduction

The most valuable asset of scanning force microscopy (SFM) is its versatility for studying a variety of interactions between the tip and the sample surface [1-3]. The SFM techniques can be used to detect different short, medium and long range interactions with high sensitivity and lateral resolution. The spreading of this technique was possible thanks to the development of specific operation modes and to the functionalization of the probes. Thus, regarding the mode employed, SFM can be used to characterize the topography of organic and inorganic materials and to study chemical (composition), mechanical (including friction and stiffness, etc.), electrical (surface potential, work function), magnetic (domain structure) or biological (specific recognition) properties. A priori, the unknown contribution of every kind of force to the total force measured leads to serious problems for obtaining quantitative information from the measurements [4].

Among those SFM techniques, magnetic force microscopy (MFM) [5] was developed to characterize the domain configuration of ferromagnetic thin films, rather than the surface of the bulk materials, and it has been intensively used to characterize magnetic nanostructures. However, MFM is nowadays proposed as a valuable technique to characterize more complex systems such as organic nanomagnets [6], magnetic oxide films [7], superparamagnetic particles [8,9] and carbon based materials [10,11]. In general, these materials present low magnetic moment at room temperature. In addition, since the substrate and the nanomagnets present quite different electronic behavior, the sample can exhibit large surface potential differences, which cause heterogeneous electrostatic interactions between the tip and sample along the surface [12,13]. Notice that all of the tip–sample interactions provoke changes in the total force, i.e., they modify the cantilever state. In MFM it is a usual procedure to separate the topography and the magnetic signal by scanning at a certain height such that that the long range tip–sample interactions dominate. An additional problem appears if several different long range interactions are present between the tip and sample. In such cases, two different methods to distinguish clearly the origin of the forces can be proposed: (i) By applying in situ a magnetic field during the MFM operation [14-16]; (ii) performing a combination of Kelvin probe force microscopy (KPFM) [17,18] and MFM to compensate the electrostatic contribution to the frequency shift signal. In the first method the evolution of the MFM signal with the magnetic field is a signature of the magnetic character of the sample. In addition, by means of variable field MFM [19], the changes in the signal as a function of the external magnetic field can be utilized either to evaluate the coercivity of the MFM probes [20,21] or to analyze the magnetic behavior of micro- and nanostructures [22,23], depending on the values of both the

tip and sample coercive fields (H_{tip} and H_{sample}) and the maximum external magnetic field applied (H_{max}). Notice that the MFM measurements under an external magnetic field allow us to state the origin of the interaction but cannot remove other interactions from the magnetic signal in the case that they exist. However, the second method proposed, the KPFM/MFM combination, which was recently used to obtain an upper bound for the force gradient produced by a possible magnetic signal in graphite [24], allows us to nullify the main electrostatic interaction between the tip and the sample. Few works have been published on this topic despite its crucial importance in the study of new nanomagnet elements with weak magnetic signal and where, in general, the surface presents heterogeneous composition and electrical behavior.

Tip–sample interactions

When a magnetic (and in general conductive) tip approaches the sample, different mutual interactions are possible [25]: Long range electrostatic (F_e) and magnetic forces (F_m), medium range van der Waals interactions (F_{vdW}), or short range chemical interactions. Assuming that the short range interactions are negligible at the distances used for MFM, the total force between the tip and the sample (F_t) is:

$$F_t = F_{vdW} + F_e + F_m \tag{1}$$

The van der Waals [26] force between a spherical tip and a semi-infinite flat sample can be written as:

$$F_{vdW} = -\frac{A_H R}{6z^2} \tag{2}$$

where A_H is the Hamaker constant that depends on the material, R is the tip radius and z is the tip–sample distance. When both the tip and the sample are conductive and there is an electrostatic potential difference (U) between them, the electrostatic force [27,28] is

$$F_e = -\frac{\pi \varepsilon_0 R U^2}{z} \tag{3}$$

where R is the radius of the metallic part of the spherical tip, ε_0 is the permittivity of free space and z is the effective tip–sample distance taking into account the oxide layer. Regarding the magnetic force, there are widely used models for the magnetic tip–sample interaction, which can be fitted to the experimental data [29], but no simple, well-established function. We can obtain an order of magnitude estimation simply by modeling both the tip and the sample as magnetic dipoles and, hence, the magnetic force is proportional to the magnetic

moment of both the tip and sample (m_{tip} and m_{sam}) [22] and decays with the distance as z^4 [30].

Typical values of the three components of the force for three tip–sample distances are displayed in Table 1. The values have been calculated using Equation 2 and Equation 3 and the equation in [30]. For the van der Waals forces we assume a tip radius of 30 nm and A_H of about 10^{-19} J. The electrostatic interaction is calculated for a tip with an electrical radius slightly smaller due to the existence of an oxide layer 2 nm thick and a contact potential between tip and sample of 1 V [25]. We calculate the magnetic interaction of two Co spheres with a radius of 20 nm. The values in Table 1 show that at short distances all the interactions are on the same order of magnitude, although van der Waals interaction dominates at distances below 1 nm. At the typical tip–sample distance during the MFM imaging, around 30 nm, the F_{vdW} can be negligible but the F_e and F_m remain comparable.

Table 1: Values of the F_{vdW}, F_e and F_m for three different tip–sample distances, d^a.

	F_{vdW} [nN]	F_e [nN]	F_m [nN]
d = 30 nm	5.0×10^{-4}	2.3×10^{-2}	5.7×10^{-2}
d = 2 nm	1.2×10^{-1}	1.3×10^{-1}	4.4×10^{-1}
d = 1 nm	5.0×10^{-1}	1.6×10^{-1}	4.9×10^{-1}

^{a}The value of z corresponds to d in the case of F_{vdW}; for the F_e case $z = d + 2$ nm due to the existence of an oxide layer; and for F_m $z = d + 40$ nm due to the position of the dipole centers.

To avoid a contribution of the short and medium range interactions to the total tip–sample force in MFM, the images are recorded at a given distance from the surface using the so-called lift mode [31] or retrace mode [32]. Typical distances for this second scan are between 20 nm and 50 nm. However, in order to improve both the lateral resolution and sensitivity, especially when dealing with materials with weak magnetization (either of the tip or the sample), it is crucial to keep the tip–sample distance as small as possible. Thus, a balance has to be found in order to avoid the van der Waals contribution and to simultaneously improve the magnetic signal. Another important issue, that has conveniently been neglected so far, is how to distinguish between the magnetic and the electrostatic interaction in certain kinds of samples. These long range interactions can have similar values in the range of a few tens of nanometers, as shown in Table 1. Since, in a first approximation, the magnetic force is proportional to the sample and tip magnetic moments, samples with high magnetization generate stronger stray fields and the magnetic interaction dominates over the electrostatic one. In such cases, the electrostatic force can be neglected,

which is the usual procedure in standard MFM measurements [5]. However, it is well known that an electrostatic interaction is present whenever tip and sample exhibit a different work function. For homogeneous samples, the work function difference can be compensated by applying an appropriate bias voltage and, hence, an unambiguous magnetic image can be obtained [33]. Sometimes, this effect induces superposition of magnetic and topographic contrast in a MFM image [34]. In the heterogeneous sample case, it is impossible to compensate the electrostatic force with a single fixed bias voltage since it depends on the (x,y) position, and it is then necessary to use KPFM techniques. If the electrostatic interactions are not compensated, an incorrect interpretation of the MFM could be made. This is especially problematic in samples with low magnetic moment where it is crucial to distinguish clearly the origin of the interaction for a correct interpretation of the results [10].

Results and Discussion

In the present work we have studied cobalt nanowires grown by focused-electron-beam-induced deposition (FEBID). The sample growth was performed in a commercial dual beam® equipment using a field emission scanning electron microscope with $Co_2(CO)_8$ as gas precursor. The substrate material used in all the samples studied in this paper is As-doped (n-type) Si(111). Different nano- or submicrometric structures were grown for this experiment: (i) Co straight wires 5 μm long, 500 nm wide and a thickness ranging from 10 nm to 400 nm; (ii) Co L-shaped wires with long arm of 10 μm and short arm of 5 μm, the width of the wires varies between 125 nm and 2 μm, and the thickness between 50 nm and 200 nm.

An appropriate selection of the growth parameters leads to high-purity deposits (over 95% Co) with magnetic properties similar to those of bulk cobalt [35] and good domain wall conduit behavior [36]. All the structures presented in this study were deposited with an electron beam current of 2.1 nA, an acceleration voltage of 10 kV and 1 μs dwell time. The nanowires grown by this technique are polycrystalline with grain sizes of a few nanometers oriented randomly, thus shape anisotropy is the main magnetic energy contribution [37] that controls their domain wall structure and magnetization reversal process [38].

As we were using a semiconductor material as a substrate, we expected that some charging effects would appear where the electron beam was scanned. The secondary electrons generated when the electron beam impinges on the substrate may not have enough energy to overcome the work function of the surface and penetrate the bulk and as a consequence they will become trapped in the neighboring area of the wires. During the FEBID deposition process some secondary electrons reach the sub-

strate surface near the scanning area, even at distances of more than 1 μm, with energy enough to partially decompose the precursor gas molecules, producing a parasitic deposit, or a so-called "halo". The number of secondary electrons that reach the surface near the sample area is less than in the scanning area, and on average less energetic. Therefore, the decomposition of the precursor gas ($Co_2(CO)_8$) in the halo is not complete. As a consequence, the halo is an insulating material of which the major components are C and O (the Co content in the halo is lower than 20% in our system). Previous works have reported similar results with respect to the Co content of the halo [39]. Secondary electrons generated during the growth may get trapped in the halo, increasing the surface potential. On the other hand, a thin native oxide layer covers the Co thin film the moment the samples are exposed to the atmosphere, with a thickness of around 2 nm. These insulating side effects enhance the accumulation of charge in the area of the deposits, thus changing the electrostatic potential of the area close to where the electron beam has been scanned.

The measurements were performed with a commercial magnetic force microscope from Nanotec Electronica S. L., and the images were processed with WSxM [40]. This system has been

conveniently modified to apply in situ in-plane and out-of-plane magnetic fields [14]. Since the electric field can also be varied continuously, this system can be used to obtain high resolution SPM images of individual nanostructures under continuously applied electric and/or magnetic fields. The probes used in this experiment are commercial Si cantilevers (nanosensors PPP-FMR, k = 1.5 N/m and f = 75 kHz) coated with a Co/Cr sputtered thin film. The thickness of the Co coating (25 nm) was selected to prevent the influence of the tip stray field on the magnetic state of the sample. Before each experiment the probes were magnetized along their pyramidal axis and their magnetic behavior was analyzed under an in situ magnetic field [21]. In this particular case, we have prepared probes with an in-plane coercive field higher than the magnetic field values to be applied in the experiments. In addition, micromagnetic simulations have been performed by means of the object oriented micromagnetic framework (OOMMF) code [41] and with the polycrystalline cobalt values [37] and a cell size of 5 nm.

As usual procedure in MFM, we record two images simultaneously, the topography, obtained at small tip–sample distance, and the frequency shift, which is obtained at a retrace distance of 30 nm. Figure 1a and Figure 1b shows the topography and
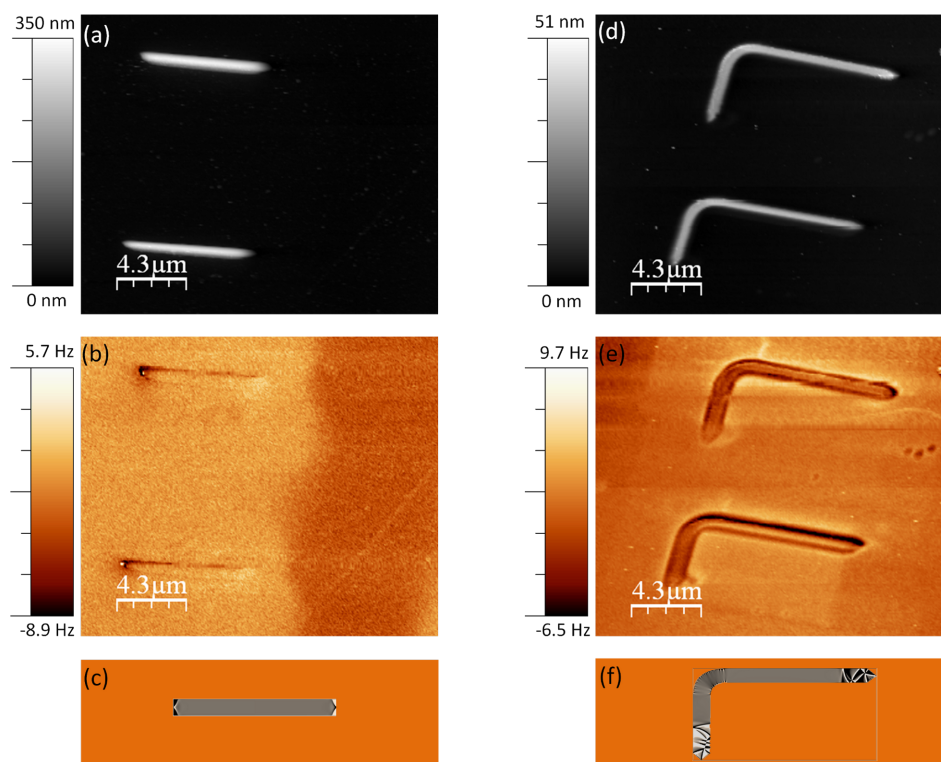

Figure 1: (a) Topography and (b) frequency shift images corresponding to the Co wires; (d) topography and (e) frequency shift images corresponding to the L-shape nanostructure. The frequency shift images were acquired at a retrace distance of 30 nm with V_{bias} = 0V. Cantilever amplitude: (a–b) A = 5 nm and (d–e) A = 8.5 nm. Simulated maps of the magnetization distribution (divM) obtained by OOMMF code of the Co wire (c) and L-shape Co nanostructure (f) in the remanent state after saturation along the main axis of the elements.

the frequency shift images of the Co wires. Figure 1c corresponds to the magnetization divergence (DivM) obtained by OOMMF. Such a magnetic distribution, the so-called "dipolar contrast", is for a remanent state after saturating the wire by applying 10 kOe along the axis. This contrast, which is still observed on the images of the Co wires in Figure 1b, is typical of the single domain structures. Surprisingly, the image corresponding to the experimental magnetic signal shows an additional area of high signal surrounding the wire that should not correspond to any kind of magnetic interaction since it is measured outside of the Co nanostructure. Co L-shape nanostructures were also studied by MFM (Figure 1e) and modeled by OOMMF code (Figure 1f). Yet again, the frequency shift image displayed in Figure 1e does not correspond to the expected MFM image, which should be similar to the divM map in Figure 1f. Moreover, the magnetic signal seems to be completely masked by other long range interactions, i.e., the electrostatic forces. These kinds of images can be erroneously interpreted as magnetic contrast in the case of complex magnetic materials.

In order to determine the origin of this contrast we varied the electric field between the tip and the sample. Instead of recording images at different bias voltage, we use a more useful technique to characterize the electrostatic behaviour of the samples, the so-called 3D modes [42]. This mode is based on measuring a signal (or a set of signals) while two parameters vary along the fast and slow scans. In our case, we measured the frequency shift (at 30 nm above the surface) while keeping the tip scanning along a selected profile (fast scan; all along the main axis of the wire marked in Figure 2a) and varying the bias voltage (slow scan). Figure 2b shows the frequency shift signal measured along a Co wire (with an MFM probe) as the bias voltage was varied between ±1.5 V. The vertical profiles measured on the Co nanowire (black line) and on the substrate (red line) are shown in Figure 2c. Notice the parabolic dependence of the frequency shift versus voltage, which corresponds to an electrostatic interaction between the tip and the sample [43]. The bias voltage at the apexes of those parabolas, measured in different regions of the sample, corresponds to the contact potential between the tip and the selected region of the sample. The respective maxima of the curves in Figure 2c are shifted to about +320 mV when the tip is on top of the Co wire and to about −320 mV in the case of the Si substrate. Thus, according to these results, by measuring the frequency shift on top of the Co wire at V_{bias} = 320 mV (horizontal black dashed line) we should detect only the magnetic signal without any electrostatic interaction between the tip and this particular region of the sample. Indeed, this measurement is represented in Figure 2d. In this curve we observe the typical dipolar contrast (positive in
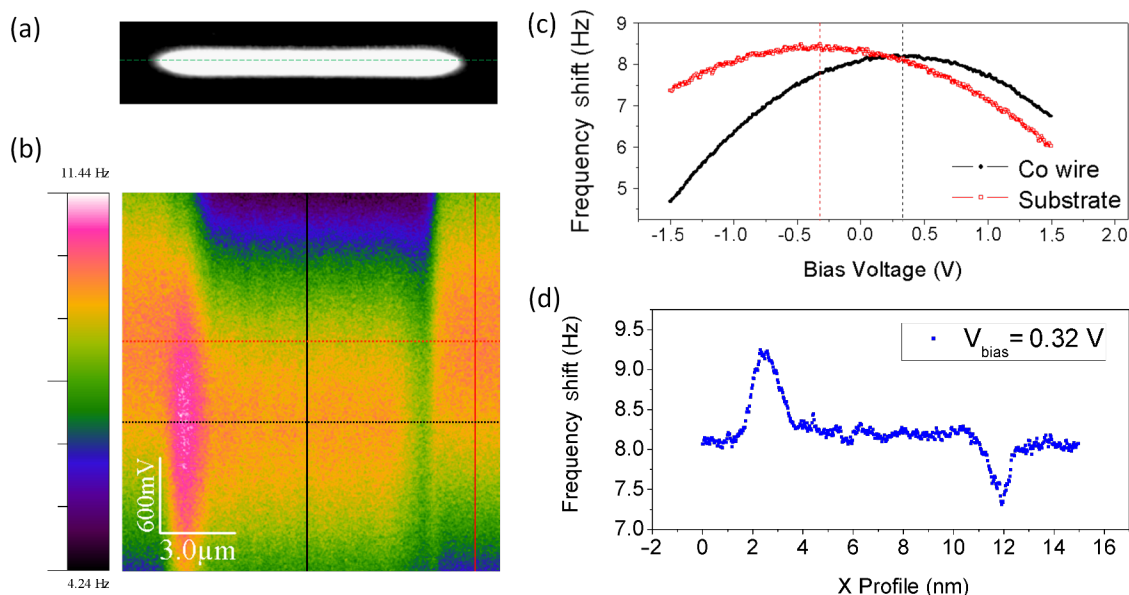

Figure 2: (a) Topography of the Co wire. The dashed line corresponds to continuous scanning along the profile while varying the bias voltage. (b) Frequency shift signal measured in the 3D mode (acquired at a distance of 100 nm). The fast scan corresponds to the *x*-axis scan all along the main axis of the Co wire and the slow scan is the bias voltage applied between the tip and the sample. (c) Frequency shift curves measured along the vertical profiles marked in (b) that correspond to the Co wire (black line) and substrate (red line). (d) Frequency shift measured along the wire at V_{bias} = 320 mV (horizontal dashed black line marked in Figure 2b). The oscillation amplitude was *A* = 7 nm and the scan rate was 1 Hz.

one extreme and negative in the opposite one) corresponding to a single domain nanostructure.

The 3D mode technique presented in this work is a highly valuable method to ascertain the electrostatic origin of some component of the frequency shift signal measured on magnetic elements. However, in this kind of system it is impossible to cancel the electrostatic force everywhere during scanning at a single, fixed bias voltage. Nevertheless, KPFM allows us to cancel the electrostatic force at every point of the image by applying the correct compensation voltage (V_{dc}) at each (x,y) position, and hence it is the only method that can be used to unambiguously measure the magnetic signal. The KPFM/MFM results are presented in Figure 3. The images in Figure 3a and Figure 3e (similar to the data in Figure 1a and Figure 1c) correspond to the topography of the nanowires. The frequency shift images shown in Figure 3b and Figure 3f (zooms of the Figure 1b and Figure 1d respectively) were measured at 30 nm without the KPFM bias correction. Notice that the magnetic

information is largely masked by the electrostatic signal. However, by using the KPFM/MFM combination, that is, activating the KPFM bias correction during the MFM operation, we were able to separate the electrostatic contribution (Figure 3c and Figure 3g) and the magnetic signal (shown in Figure 3d and Figure 3h).

It is important to note that the electrostatic interaction can also affect the topographic images [44]. In the experiments presented here for these rather thick structures this effect was not significant. Height differences less than 1 nm (a deviation about 2%) were found when we measured the topography of the same structure with and without activation of the KPFM mode (more details in Supporting Information File 1). After removing the electrostatic interaction from the MFM signal, we can apply a magnetic field to study the magnetization process of a single structure. As an example, in Supporting Information File 2 we present a combination of KPFM/MFM under in situ magnetic field on a single L-shaped nanostructure. The initial state of the
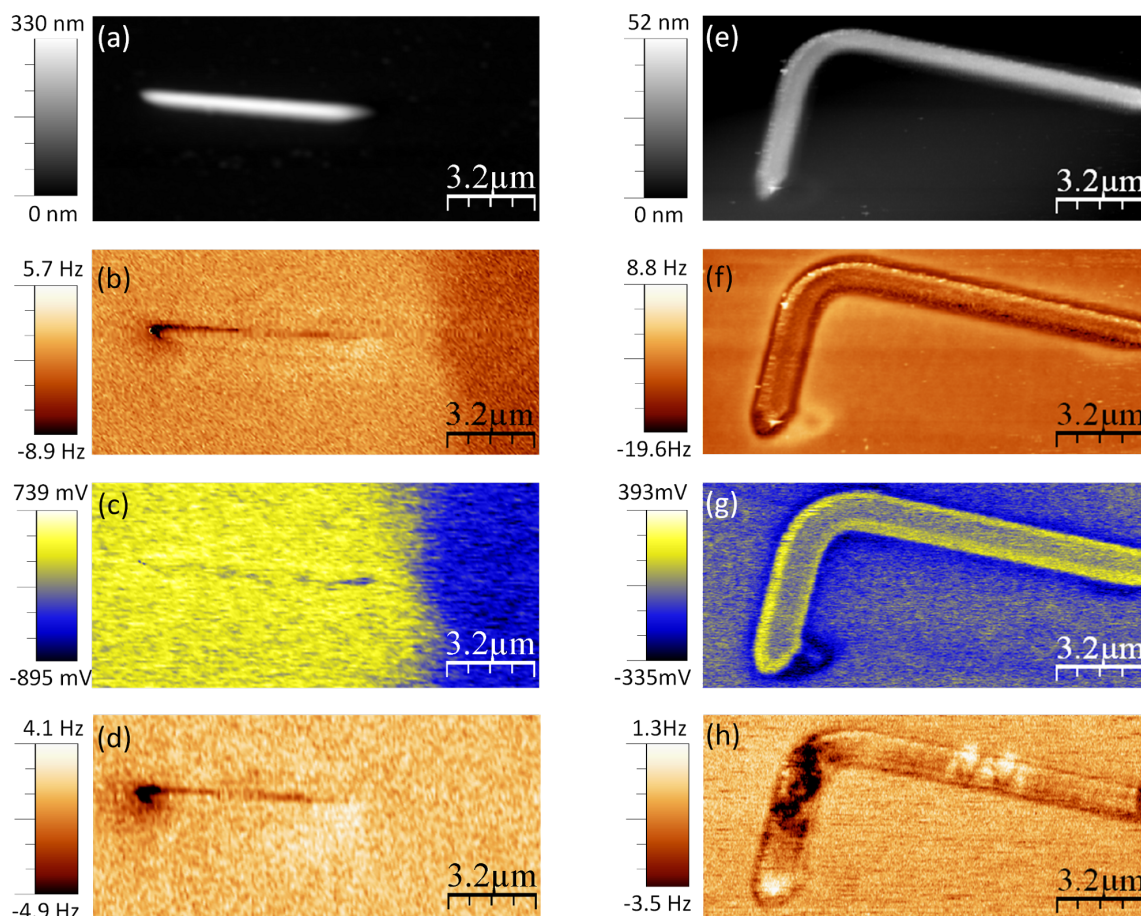

Figure 3: Topography of (a) Co nanowires and (e) L-shaped Co nanostructure. (b) and (f) frequency shift images measured without KPFM acquired at a retrace distance of 30 nm and 25 nm respectively. (c) and (g) surface potential images obtained by the KPFM technique. (d) and (h) MFM images (frequency shift) of the Co nanostructures measured when the KPFM bias correction was switched on. The oscillation amplitudes were (a–d) $A = 5$ nm and (e–h) $A = 8.5$ nm.

sample which corresponds to the images in Figure 3 is "as-prepared". Similar L-shaped structures were previously studied through the Magneto-Optical Kerr Effect [36] and good domain wall conduit was found (lower domain-wall propagation field than nucleation field). Using this technique, it has therefore been possible to obtain additional valuable information about the type of domain walls that form and propagate along the wires.

Conclusion

In this work we have shown that different tip–sample interactions are present when a magnetic (and also conductive) tip approaches the magnetic sample. These interactions have comparable values regarding the electric and magnetic properties of the system at the same tip–sample distances. When a heterogeneous sample (as is the case of nanostructures deposited on a substrate) is studied, and especially in the case of low magnetic moment materials, it is necessary to be aware of this problem in order to prevent incorrect image interpretation, examples of which can indeed be found in the literature.

To avoid mistakes in the interpretation of the MFM images it is crucial to distinguish between the separate contributions to the frequency shift signal by varying the external magnetic and electric fields. These methods allow us to elucidate the origin of the signal or the presence of different components. However, only by means of KPFM and MFM in combination is it possible to cancel the electrostatic interaction between the tip and sample at every point in the image, thus obtaining a pure magnetic signal. Thus, the KPFM/MFM combination is a powerful technique that allows us to obtain unambiguous magnetic images of low magnetic moment materials.

Experimental

In Figure 4a a schematic of the experimental system is presented. The tip–sample forces can be evaluated simply by
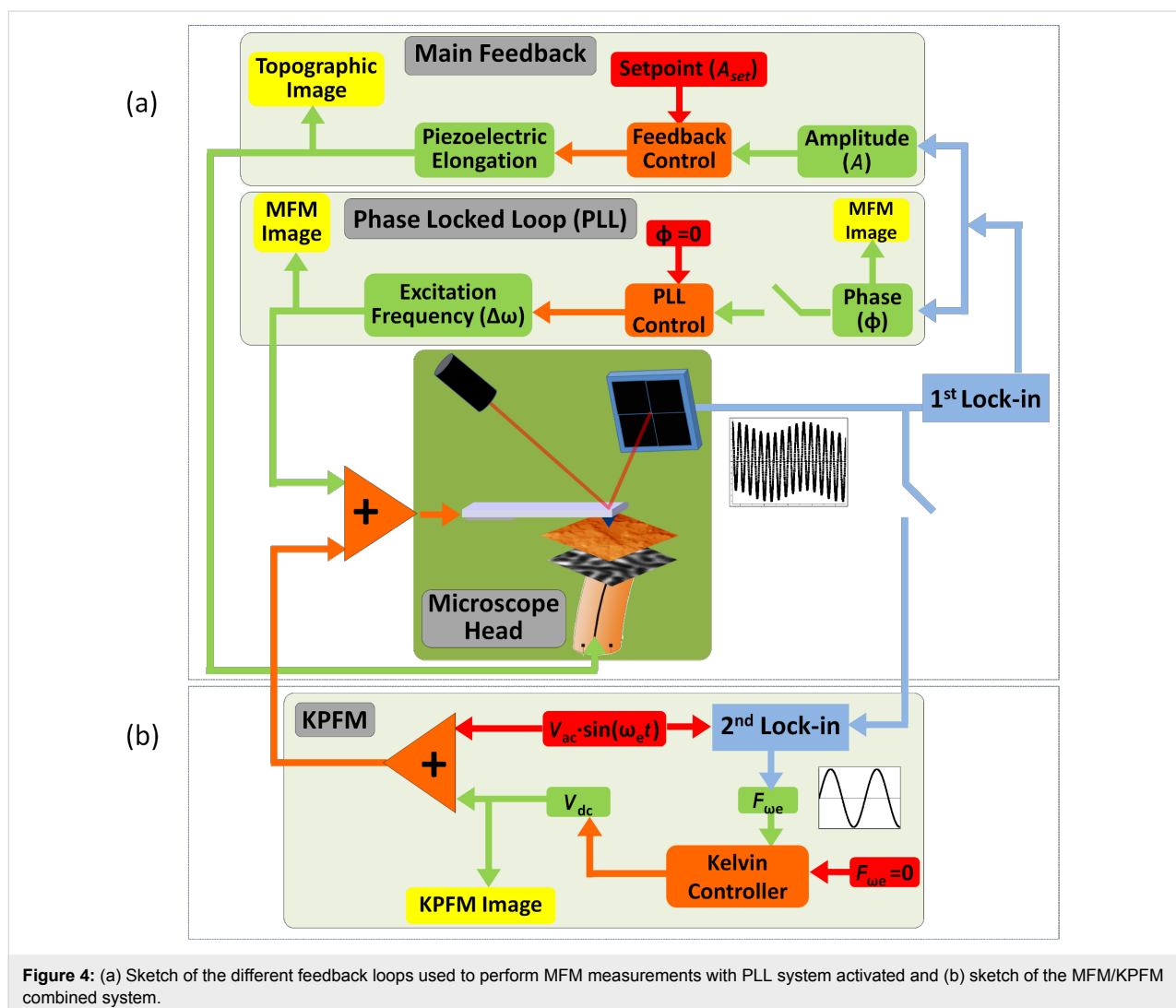

Figure 4: (a) Sketch of the different feedback loops used to perform MFM measurements with PLL system activated and (b) sketch of the MFM/KPFM combined system.

measuring the cantilever deflexion. However, dynamic modes are used to improve the sensitivity and resolution of the MFM signal. In any dynamic mode the interaction is evaluated through the force gradient, although the force can be recovered from the curve of frequency shift versus distance [45]. The interpretation of the interaction is more complicated in the case of dynamical modes. The tip–cantilever system oscillates at a certain frequency with a given amplitude. Due to the presence of an interaction between the tip and the sample, the amplitude and the phase of the oscillation change. In our experiments we use a PLL (Phase Locked Loop) system to keep the phase constant while the excitation frequency varies (see the sketch in Figure 4a). Both the amplitude and the frequency shift depend on the force gradient. It is well established that the changes in amplitude are related to dissipative process while changes in the frequency shift are associated with conservative interactions. In the amplitude modulation mode, the amplitude is the main feedback parameter and thus the movement of the piezoelectric is used to build the topography image. The frequency shift changes are recorded at a certain distance to build the magnetic image, thus the MFM images were obtained in the so-called "retrace mode". During the first scan the oscillation amplitude is kept constant as well as the phase of the oscillation (thanks to the PLL feedback system). The retrace scan is then performed at a selected tip–sample distance, following the topography recorded in the first scan (i.e., with the main feedback switched off).

The frequency shift results from a convolution between the tip–sample force gradient and a weight function. For low oscillation amplitudes, the frequency shift of the cantilever, at a retrace distance large enough to avoid van der Waals interactions, is proportional to the total force gradient (that can be composed of magnetic and/or electrostatic interactions).

The experiments in the present work were performed in ambient conditions, in the non-contact dynamic mode (with low amplitude modulation) and with the PLL feedback activated. In addition, KPFM [17] was used in combination with MFM to adjust the tip bias voltage to minimize electrostatic forces between the tip and the sample at every point on the sample (Figure 4b). In both of the scans (main scan and retrace mode), the normal force, amplitude, phase, frequency shift and surface potential (in the KPFM mode) signals can be recorded simultaneously.

In KPFM, an ac bias voltage ($V_{ac} \sin(\omega_e t)$, where $V_{ac} = 0.5$ V and $\omega_e = 7$ kHz) is added to the V_{dc} bias voltage. In order to cancel the electrostatic interaction between the tip and the sample, the component of the force that oscillates with $F_e (\omega_e)$ is nullified by applying the appropriate V_{dc} at each tip position; this is the output of the Kelvin feedback.

Supporting Information

Supporting Information File 1
Topography of the nanostructure.
[http://www.beilstein-journals.org/bjnano/content/supplementary/2190-4286-2-59-S1.pdf]

Supporting Information File 2
MFM images.
[http://www.beilstein-journals.org/bjnano/content/supplementary/2190-4286-2-59-S2.pdf]

Acknowledgements

References

1. Weisendanger, R. *Scanning Probe Microscopy and Spectroscopy: Methods and Applications;* Cambridge University Press: Cambridge, U.K., 1994.
2. Meyer, E.; Hug, H. J.; Bennewitz, R. *Scanning Probe Microscopy: The Lab on a Tip;* Springer-Verlag: Berlin, Germany, 2004.
3. Eaton, P.; West, P. *Atomic Force Microscopy;* Oxford University Press: Oxford, U.K., 2010.
4. Palacios-Lidón, E.; Colchero, J. *Nanotechnology* **2006,** *17,* 5491. doi:10.1088/0957-4484/17/21/033
5. Sáenz, J. J.; García, N.; Grütter, P.; Meyer, E.; Heinzelmann, H.; Wiesendanger, R.; Rosenthaler, L.; Hidber, H. R.; Güntherodt, H.-J. *J. Appl. Phys.* **1987,** *62,* 4293. doi:10.1063/1.339105
6. Gómez-Segura, J.; Kazakova, O.; Davies, J.; Josephs-Franks, P.; Veciana, J.; Ruiz-Molina, D. *Chem. Commun.* **2005,** 5615. doi:10.1039/B509282E
7. Wu, Y.; Suzuki, Y.; Rüdiger, U.; Yu, J.; Kent, A. D.; Nath, T. K.; Eom, C. B. *Appl. Phys. Lett.* **1999,** *75,* 2295. doi:10.1063/1.124995
8. Neves, C. S.; Quaresma, P.; Baptista, P. V.; Carvalho, P. A.; Araújo, J. P.; Pereira, E.; Eaton, P. *Nanotechnology* **2010,** *21,* 305706. doi:10.1088/0957-4484/21/30/305706
9. Schreiber, S.; Savla, M.; Pelekhov, D. V.; Iscru, D. F.; Selcu, C.; Hammel, P. C.; Agarwal, G. *Small* **2008,** *4,* 270. doi:10.1002/smll.200700116
10. Červenka, J.; Katsnelson, M. I.; Flipse, C. F. J. *Nat. Phys.* **2009,** *5,* 840. doi:10.1038/nphys1399
11. Esquinazi, P.; Spemann, D.; Höhne, R.; Setzer, A.; Han, K.-H.; Butz, T. *Phys. Rev. Lett.* **2003,** *91,* 227201. doi:10.1103/PhysRevLett.91.227201
12. Schmidt, R.; Schwarz, A.; Wiesendanger, R. *Nanotechnology* **2009,** *20,* 264007. doi:10.1088/0957-4484/20/26/264007
13. Femenia, M.; Canalias, C.; Pan, J.; Leygraf, C. *J. Electrochem. Soc.* **2003,** *150,* B274. doi:10.1149/1.1572482

14. Engel-Herbert, R.; Hesjedal, T.; Mohanty, J.; Schaadt, D. M.; Ploog, K. H. *Phys. Rev. B* **2006,** *73,* 104441. doi:10.1103/PhysRevB.73.104441
15. Foss, S.; Merton, C.; Proksch, R.; Skidmore, G.; Schmidt, J.; Dahlberg, E. D.; Pokhil, T.; Cheng, Y.-T. *J. Magn. Magn. Mater.* **1998,** *190,* 60. doi:10.1016/S0304-8853(98)00274-1
16. Asenjo, A.; García, D.; García, J. M.; Prados, C.; Vázquez, M. *Phys. Rev. B* **2000,** *62,* 6538. doi:10.1103/PhysRevB.62.6538
17. Nonnenmacher, M.; O'Boyle, M. P.; Wickramasinghe, H. K. *Appl. Phys. Lett.* **1991,** *58,* 2921. doi:10.1063/1.105227
18. Glatzel, T.; Sadewasser, S.; Lux-Steiner, M. C. *Appl. Surf. Sci.* **2003,** *210,* 84. doi:10.1016/S0169-4332(02)01484-8
19. Jaafar, M.; Gómez-Herrero, J.; Gil, A.; Ares, P.; Vázquez, M.; Asenjo, A. *Ultramicroscopy* **2009,** *109,* 693. doi:10.1016/j.ultramic.2009.01.007
20. Schwarz, A.; Wiesendanger, R. *Nano Today* **2008,** *3,* 28. doi:10.1016/S1748-0132(08)70013-6
21. Jaafar, M.; Asenjo, A.; Vázquez, M. *IEEE Trans. Nanotechnology* **2008,** *7,* 245. doi:10.1109/TNANO.2008.917785
22. Zhu, X.; Grütter, P.; Metlushko, V.; Ilic, B. *Appl. Phys. Lett.* **2002,** *80,* 4789. doi:10.1063/1.1489720
23. Endo, Y.; Fujimoto, H.; Kumano, S.; Matsumura, Y.; Sasaki, I.; Kawamura, Y.; Yamamoto, M.; Nakatani, R. *J. Appl. Phys.* **2008,** *103,* 07D918. doi:10.1063/1.2836681
24. Martínez-Martín, D.; Jaafar, M.; Pérez, R.; Gómez-Herrero, J.; Asenjo, A. *Phys. Rev. Lett.* **2010,** *105,* 257203. doi:10.1103/PhysRevLett.105.257203
25. Giessibl, F. J. Principle of NC-AFM.. In *Noncontact Atomic Force Microscopy;* Morita, S.; Wiesendanger, R.; Meyer, E., Eds.; Springer: Berlin, Heidelburg, New York, 2002; pp 11–46.
26. Israelachvili, J. N. *Intermolecular and Surface Forces,* 2nd ed.; Academic Press: London, 1991.
27. Hao, H. W.; Baró, A. M.; Sáenz, J. J. *J. Vac. Sci. Technol., B: Microelectron. Nanometer Struct.-Process., Meas., Phenom.* **1991,** *9,* 1323. doi:10.1116/1.585188
28. Olsson, L.; Lin, N.; Yakimov, V.; Erlandsson, R. *J. Appl. Phys.* **1998,** *84,* 4060. doi:10.1063/1.368618
29. Hartmann, U. *Annu. Rev. Mater. Sci.* **1999,** *29,* 53. doi:10.1146/annurev.matsci.29.1.53
30. $F_m = - 3\, \mu_0\, m_{tip}\, m_{sam} / 2\pi\, z^4$, where μ_0 is the permeability of free space, m_{tip} and m_{sam} are the magnetic moment of the tip and sample respectively and z is the distance between both dipoles.
31. Bruker AXS. http://www.bruker-axs.com/atomicforcemicroscopy.html (accessed July 15, 2011).
32. Nanotec Electronica S.L.. http://www.nanotec.es/ (accessed July 15, 2011).
33. Yu, J.; Ahner, J.; Weller, D. *J. Appl. Phys.* **2004,** *96,* 494. doi:10.1063/1.1757029
34. Yu, J.; Ahner, J.; Weller, D. *Appl. Phys. Lett.* **2003,** *83,* 4208. doi:10.1063/1.1627940
35. Fernández-Pacheco, A.; De Teresa, J. M.; Córdoba, R.; Ibarra, M. R. *J. Phys. D: Appl. Phys.* **2009,** *42,* 055005. doi:10.1088/0022-3727/42/5/055005
36. Fernández-Pacheco, A.; De Teresa, J. M.; Córdoba, R.; Ibarra, M. R.; Petit, D.; Read, D. E.; O'Brien, L.; Lewis, E. R.; Zeng, H. T.; Cowburn, R. P. *Appl. Phys. Lett.* **2009,** *94,* 192509. doi:10.1063/1.3139068
37. Fernández-Pacheco, A.; De Teresa, J. M.; Szkudlarek, M. A.; Córdoba, R.; Ibarra, M. R.; Petit, D.; O'Brien, L.; Zeng, H. T.; Lewis, E. R.; Read, D. E.; Cowburn, R. P. *Nanotechnology* **2009,** *20,* 475704. doi:10.1088/0957-4484/20/47/475704
38. Jaafar, M.; Serrano-Ramón, L.; Iglesias-Freire, O.; Fernández-Pacheco, A.; Ibarra, M. R.; De Teresa, J. M.; Asenjo, A. *Nanoscale Res. Lett.* **2011,** *6,* 407. doi:10.1186/1556-276X-6-407
39. Lau, Y. M.; Chee, P. C.; Thong, J. T. L.; Ng, V. *J. Vac. Sci. Technol., A* **2002,** *20,* 1295. doi:10.1116/1.1481040
40. Horcas, I.; Fernández, R.; Gómez-Rodríguez, J. M.; Colchero, J.; Gómez-Herrero, J.; Baro, A. M. *Rev. Sci. Instrum.* **2007,** *78,* 013705. doi:10.1063/1.2432410
41. The Object Oriented MicroMagnetic Framework (OOMMF) project at ITL/NIST. http://math.nist.gov/oommf/ (accessed July 15, 2011).
42. Gómez-Navarro, C.; Gil, A.; Álvarez, M.; De Pablo, P. J.; Moreno-Herrero, F.; Horcas, I.; Fernández-Sánchez, R.; Colchero, J.; Gómez-Herrero, J.; Baró, A. M. *Nanotechnology* **2002,** *13,* 314. doi:10.1088/0957-4484/13/3/315
43. Colchero, J.; Gil, A.; Baró, A. M. *Phys. Rev. B* **2001,** *64,* 245403. doi:10.1103/PhysRevB.64.245403
44. Sadewasser, S.; Lux-Steiner, M. C. *Phys. Rev. Lett.* **2003,** *91,* 266101. doi:10.1103/PhysRevLett.91.266101
45. Giessibl, F. J. *Appl. Phys. Lett.* **2001,** *78,* 123. doi:10.1063/1.1335546

The atomic force microscope as a mechano–electrochemical pen

Christian Obermair[*1], Andreas Wagner[1] and Thomas Schimmel[1,2]

Full Research Paper

Abstract

We demonstrate a method that allows the controlled writing of metallic patterns on the nanometer scale using the tip of an atomic force microscope (AFM) as a "mechano–electrochemical pen". In contrast to previous experiments, no voltage is applied between the AFM tip and the sample surface. Instead, a passivated sample surface is activated locally due to lateral forces between the AFM tip and the sample surface. In this way, the area of tip–sample interaction is narrowly limited by the mechanical contact between tip and sample, and well-defined metallic patterns can be written reproducibly. Nanoscale structures and lines of copper were deposited, and the line widths ranged between 5 nm and 80 nm, depending on the deposition parameters. A procedure for the sequential writing of metallic nanostructures is introduced, based on the understanding of the passivation process. The mechanism of this mechano–electrochemical writing technique is investigated, and the processes of site-selective surface depassivation, deposition, dissolution and repassivation of electrochemically deposited nanoscale metallic islands are studied in detail.

Introduction

The controlled, patterned, electrochemical deposition of metals at predefined positions on the nanometer scale is of great interest for numerous applications including in the fields of microelectronics, nanoscale electronics and nano-electro-mechanical systems (NEMS). Considerable progress was achieved recently in the field of self-organized electrochemical patterning of nanowires. In thin-film electrolytes, regular arrays of nanowires were grown in flat electrochemical cells at reduced temperatures. A dramatic increase of the mechanical yield strength of the nanowires of more than one order of magnitude as compared to bulk values was reported recently [1-3]. Significant progress was also achieved in the field of the controlled electrochemical deposition of metals for the fabrication of atomic-scale contacts and switches. By electrochemical
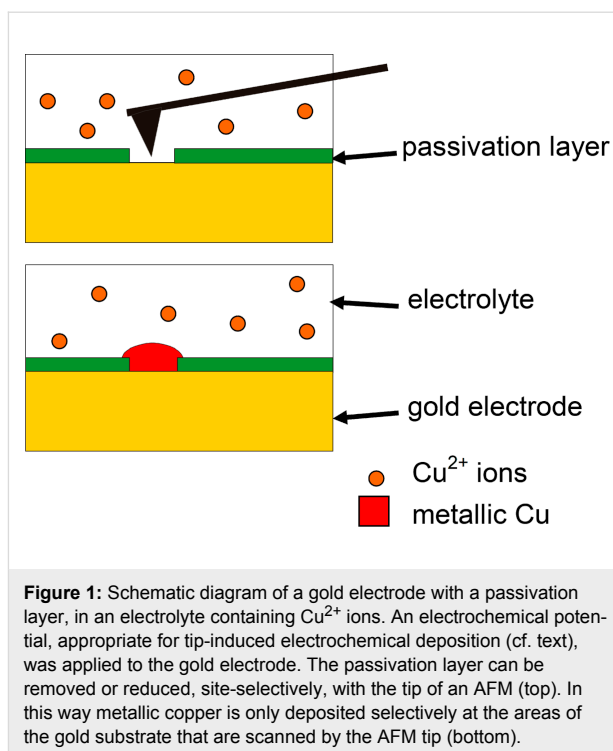
deposition of nanoscale silver contacts and subsequent electrochemical cycling, an electrically controllable single-atom relay was demonstrated, which allows the controlled switching of an electrical current by the control-voltage-induced movement of just a single atom [4-7]. In this way, a single-atom transistor was demonstrated as a quantum electronic device operating reproducibly at room temperature. At the same time, the scanning tunneling microscope (STM) and the atomic force microscope (AFM) represent techniques that allow surface manipulation on the nanometer scale and even on the atomic scale [8-21]. As shown in Don Eigler's pioneering work [8], the tip of an STM allows the assembling of structures on a surface, atom by atom. Early experiments demonstrated that the tip of an electrochemical STM can also be used for local electrochemical deposition. Material electrochemically deposited on an STM tip was subsequently transferred to the surface [22,23], allowing controlled metallic nanopatterning of surfaces. Improvements of STM-based techniques also include the use of elaborate voltage-pulse sequences [24,25].

While much work was performed using the STM as a tool for electrochemical patterning, only a few attempts exist utilizing the AFM as a tool for controlled site-selective electrochemical deposition of metals on surfaces. Initial experiments performed by LaGraff and Gewirth [26,27] demonstrated that the influence of the scanning tip can lead to both reduction or enhancement of copper deposition on the surface of copper single crystals. In further work we demonstrated the local electrochemical deposition of metal islands mechanically induced with the tip of an AFM [28]. Herein, we demonstrate that by combined passivation/depassivation of surfaces, complex metallic nanostructures can be selectively deposited by using the tip of an AFM as a mechano–electrochemical pen in the sense that it allows the local mechanical depassivation of a formerly passivated substrate surface for local electrochemical deposition.
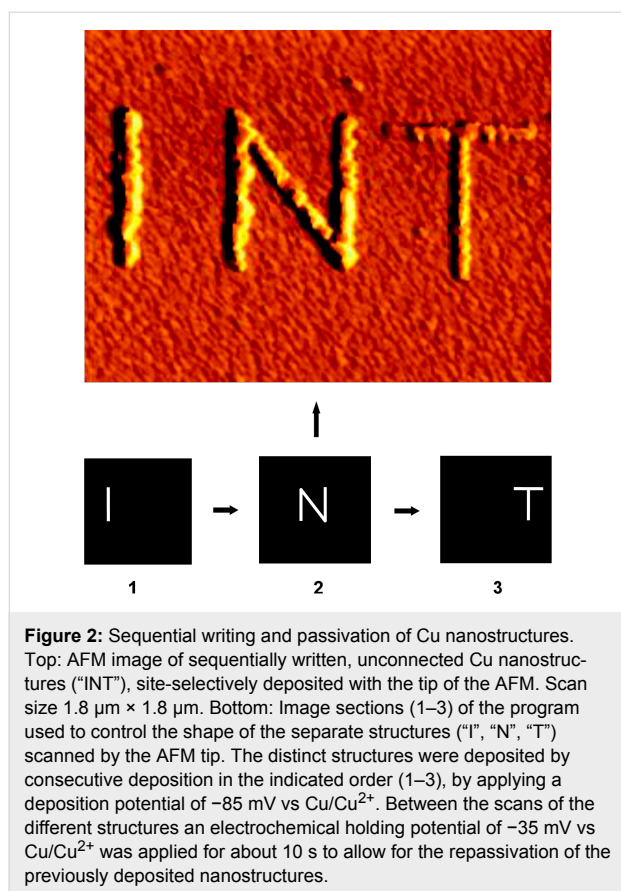
Results and Discussion

The basic principle of the structuring process applied in our experiments is illustrated in the schematic diagram in Figure 1. The gold substrate, which serves as the working electrode, is covered by a native passivation layer. This passivation layer consists of oxo-anions of the electrolyte, such as sulphate or hydrogen sulfate, which are well known from literature to cover metal films in their presence [29-33]. Alternatively, thiol molecules were used in our experiments as an organic passivation layer. These thiol molecules have a higher adhesion to the substrate but are not necessary for a precise deposition and are therefore not discussed in any more detail below.

While an electrochemical potential appropriate for tip-induced electrochemical deposition is applied to the gold electrode,

Figure 1: Schematic diagram of a gold electrode with a passivation layer, in an electrolyte containing Cu^{2+} ions. An electrochemical potential, appropriate for tip-induced electrochemical deposition (cf. text), was applied to the gold electrode. The passivation layer can be removed or reduced, site-selectively, with the tip of an AFM (top). In this way metallic copper is only deposited selectively at the areas of the gold substrate that are scanned by the AFM tip (bottom).

simultaneously the passivation layer is partially removed, site-selectively, with the tip of an AFM. The appropriate electrochemical potential is determined by cyclic voltammetry, and a cathodic potential is selected so as to be too low to lead to an overall growth of the metal film in spite of the passivation layer. Thus, metal is *only* deposited at the areas of the gold substrate that were scanned by the AFM tip and where, therefore, the passivation layer inhibiting the electrochemical deposition is locally destroyed. The method described above is not limited to the deposition of single nanostructures activated with the tip of an AFM. We found that if the gold electrode is exposed to the electrolyte at a neutral potential for deposition (holding potential), the surface is again re-covered by a passivation layer, including coverage of the newly deposited structures. By this mechanism of self-passivation, previously deposited structures do not continue to grow when the deposition potential is applied again. Rather, we find that after a short time of approximately 10–20 s after stopping the deposition, the newly deposited structures are passivated. This means that if we deposit a metal nanostructure in the way described above and we wait for 10–20 s after finishing deposition, this structure will not grow further when we apply a deposition potential again after this 10–20 s pause. On the other hand, if we start scanning these structures again with the AFM tip at the forces mentioned above, on the order of 10 nN, electrochemical growth continues as long as the deposition potential is applied and the scanning continues. This provides important information concerning the mechanism of the passivation, depassivation and repassivation.

Figure 2: Sequential writing and passivation of Cu nanostructures. Top: AFM image of sequentially written, unconnected Cu nanostructures ("INT"), site-selectively deposited with the tip of the AFM. Scan size 1.8 μm × 1.8 μm. Bottom: Image sections (1–3) of the program used to control the shape of the separate structures ("I", "N", "T") scanned by the AFM tip. The distinct structures were deposited by consecutive deposition in the indicated order (1–3), by applying a deposition potential of −85 mV vs Cu/Cu^{2+}. Between the scans of the different structures an electrochemical holding potential of −35 mV vs Cu/Cu^{2+} was applied for about 10 s to allow for the repassivation of the previously deposited nanostructures.

It gives the time scale of the repassivation process, which for the electrochemical conditions given in our experiment is on the order of 10 s. The results also indicate that when scanning at tip–sample forces on the order of 10 nN, passivated surfaces of the deposited copper are again depassivated, and that repassivation is efficiently prohibited locally within the scanning area of the AFM tip.

At the same time these results open possibilities for the controlled *sequential* writing of several independent nanostructures on the same substrate chip: After one copper nanostructure has been deposited and after the electrodeposition as well as the AFM scanning process has subsequently been stopped, it is sufficient to wait for just 10–20 s. After this time, the surface of the copper appears to be passivated, and one can write a new structure neighboring the first one without inducing further growth of the previously written structure. To demonstrate this sequential deposition process for the example of three separate nanostructures, an appropriate electrochemical deposition potential of −85 mV for tip-induced deposition was applied to the gold electrode. Then the shape of the letter "I" was scanned 50 times with the AFM tip (tip speed: 8 μm/s). Subsequently a holding potential of −35 mV was applied for a period of 10 s. After that, the letters "N" and "T" were scanned in a similar

way with a holding-potential period between the structuring cycles for each letter. Figure 2 (bottom) shows the image sections (1–3) of the program used to control the shape of the separate structures. Subsequent AFM imaging leads to the image in Figure 2 (top) (scan size 1.8 μm × 1.8 μm). Three unconnected Cu nanostructures ("INT") were deposited successively and site-selectively based on the "activation" or de-passivation by the scanning tip of the AFM.

A further example of this method is given in Figure 3a. Here an even more complex structure was produced following the same procedure. All the separate nanostructures have nearly the same height, indicating that during the holding-potential period the surface, including the previously deposited nanostructures, repassivates and does not continue growing during further deposition. The AFM image of Figure 3b shows the Cu nanostructure of Figure 3a at a larger scan size, demonstrating the selectivity of the tip-induced deposition process. The scan size is 2.5 μm × 2.5 μm in a) and 6 μm × 6 μm in b), respectively. Even at the larger scan size of Figure 3b, not one single Cu island is found outside the locations depassivated by the AFM tip during deposition. The above experiments demonstrate that electrodeposition can be induced locally with the tip of an AFM. As no potential was applied to the tip of the AFM and the experiments were reproduced both with insulating and with electrically conducting tips, the locally selective deposition is most likely related to the mechanical interaction between tip and sample during the scanning process. This is further supported by the observation that the mere presence of the tip in contact with the sample does not lead to locally selective deposition. The scanning process, i.e., the movement of the tip relative to the sample, is necessary to induce local electrodeposition.

Obviously, the scanning AFM tip mechanically activates deposition sites and/or nucleation centers for local copper deposition. A possible explanation for the observed phenomena is the assumed presence of a passivating layer on the gold surface that prevents deposition of copper on the gold surface at values of the overpotential between −60 mV and 0 V. Due to the mechanical interaction between the tip and sample, this passivating layer is disrupted locally. This would explain the selective local copper deposition along the lines were the tip was scanned. This explanation is also in agreement with the observation that lateral forces occurring between tip and sample during the scanning process can be used to induce rupture of chemical bonds mechanically [17,18]. As the experiments have been performed under environmental conditions, especially in the presence of oxygen, the formation of a surface layer on the gold substrate involving copper oxide/hydroxide and/or other compounds such as thiols is possible.
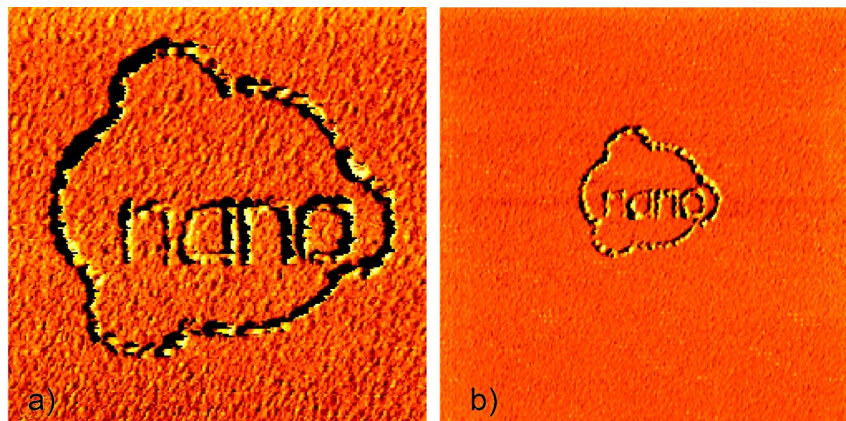
Figure 3: In situ AFM image demonstrating the selectivity of the tip-induced electrochemical copper deposition ("nano" + ring) from a Cu^{2+} electrolyte onto a polycrystalline gold substrate. a) Cu island structure deposited by sequential writing (deposition potential: −60 mV vs Cu/Cu^{2+}). Between writing the separate structures an electrochemical holding potential of −35 mV vs Cu/Cu^{2+} was applied for a period of 10 s. b) AFM image of the same Cu nanostructure at larger scan size, demonstrating the selectivity of the tip-induced deposition process; that is, no Cu islands are found in the surface areas that were not activated by the AFM tip during deposition. Scan size: a) 2.5 µm × 2.5 µm, b) 6 µm × 6 µm.

The alternative explanation that the tip induces defects within the gold surface itself, which, in turn, could possibly act as nucleation sites for the subsequent copper deposition, may well explain a somewhat enhanced copper deposition within the scanning area of the tip. Such a mechanism, however, cannot explain our experimental results for several reasons:

1. No damage was found on the gold surfaces after tip-induced deposition and subsequent dissolution of the deposited copper.
2. No memory effect is observed, when a further deposition experiment is performed on the same area of the gold surface after such a dissolution of the copper deposited in the first deposition experiment. This indicates that the gold surface is still intact and that there is no prepatterned sequence of nucleation centers due to defects induced during the first deposition experiment.
3. Furthermore, it is difficult to explain the high selectivity of the deposition process by merely assuming a substrate-defect-nucleated deposition mechanism. The substrate for deposition in our experiments is not a metal single crystal, but rather thermally evaporated polycrystalline gold, which was not annealed and which even before interaction with the AFM tip would exhibit a high density of defects (steps, kinks, dislocations, etc.). In our experiments, metal deposition was observed selectively only at the positions were the AFM tip was scanned.

Finally, tip-induced defects on the gold surface cannot explain the effects of repassivation and depassivation of the once-passivated copper structures described above.

Conclusion

To conclude, we have reported the controlled and site-selective electrochemical deposition of metallic nanopatterns, which were induced with the tip of an atomic force microscope used as a "mechano–electrochemical pen". The deposition led to the controlled writing of metallic patterns and lines, with line widths between 5 nm and 80 nm, depending on the structuring parameters. The process is highly selective, leading to electrochemical deposition only within the areas activated by the AFM tip. The mechanism can be explained as a mechanical depassivation of the substrate surface by the scanning tip, leading to local deposition in the depassivated area. If the tip is scanned repeatedly along a given line pattern while a deposition potential is applied, this will result in the site-selective deposition along the scanning path of the AFM tip. The results, which include the sequential writing and subsequent in situ repassivation of newly written structures, open perspectives for novel lithographic processes mechanically activated with the tip of an AFM.

Experimental

Electrochemical AFM setup: We used a home-built AFM with a tube scanner and a beam-deflection detection system with a four-quadrant photodetector, allowing the simultaneous detection of topography and lateral forces. The AFM was used in the contact mode both for lithography and for imaging. Contact-mode V-shaped silicon nitride cantilevers with pyramidal tips, and with force constants between 0.03 N/m and 0.1 N/m, were used. Within each experiment, the same AFM cantilever tip was used both for nanolithography and for subsequent AFM imaging. The position of the tip was controlled by a lithog-

raphy mode of our software, which at the same time allows control of the electrochemical potential. All AFM images were taken in situ under the electrolyte within the electrochemical cell. All images represent original raw data without filtering or image processing.

Electrochemical cell and controller: The experiments were performed in an electrochemical cell approximately 20 mm in diameter, with Cu reference and counter electrodes (copper wires of 0.5 mm diameter, Goodfellow) and a glass substrate with an evaporated gold film as the working electrode. The electrochemistry was controlled by a home-built, low-noise potentiostat, which was controlled by a computer. Cyclic voltammograms were measured both before and after each experiment. Aqueous solutions of 50 mM H_2SO_4 (Suprapur, Merck) with 1 mM $CuSO_4$ (p.a., Merck) were used as electrolytes. The potentials given in this article were measured against Cu/Cu^{2+} electrodes. Electrochemical deposition was performed at an overpotential of −60 mV. This potential was applied while the surface was locally mechanically depassivated with the AFM tip, resulting in the site-selective, local copper deposition.

Sample preparation: Glass slides of approximately 20 mm in diameter were used as samples, and were rinsed and sonicated, first in acetone and subsequently in ethanol. Prior to evaporation of a 50 nm gold film, a 3–4 nm Cr film was evaporated as an adhesion layer. The layer thickness was measured in situ in the vacuum chamber during evaporation by means of a quartz microbalance, and the base pressure in the vacuum chamber during evaporation was in the range of 10^{-6} mbar.

Acknowledgements

References

1. Zhong, S.; Dupeyrat, P.; Groeger, R.; Wang, M.; Koch, T.; Schimmel, T. *J. Nanosci. Nanotechnol.* **2010,** *10,* 6144–6149. doi:10.1166/jnn.2010.2565
2. Zhong, S.; Wang, D.; Koch, T.; Wang, M.; Walheim, S.; Schimmel, T. *Cryst. Growth Des.* **2010,** *10,* 1455–1459. doi:10.1021/cg9012747
3. Zhong, S.; Koch, T.; Wang, M.; Scherer, T.; Walheim, S.; Hahn, H.; Schimmel, T. *Small* **2009,** *5,* 2265–2270. doi:10.1002/smll.200900746
4. Xie, F.-Q.; Nittler, L.; Obermair, C.; Schimmel, T. *Phys. Rev. Lett.* **2004,** *93,* 128303. doi:10.1103/PhysRevLett.93.128303
5. Xie, F.-Q.; Maul, R.; Brendelberger, S.; Obermair, C.; Starikov, E. B.; Wenzel, W.; Schön, G.; Schimmel, T. *Appl. Phys. Lett.* **2008,** *93,* 043103. doi:10.1063/1.2955521
6. Xie, F.-Q.; Maul, R.; Augenstein, A.; Obermair, C.; Starikov, E. B.; Schön, G.; Schimmel, T.; Wenzel, W. *Nano Lett.* **2008,** *8,* 4493–4497. doi:10.1021/nl802438c
7. Xie, F.-Q.; Maul, R.; Obermair, C.; Schön, G.; Schimmel, T.; Wenzel, W. *Adv. Mater.* **2010,** *22,* 2033–2036. doi:10.1002/adma.200902953
8. Crommie, M. F.; Lutz, C. P.; Eigler, D. M. *Science* **1993,** *262,* 218–220. doi:10.1126/science.262.5131.218
9. Eigler, D. M.; Schweizer, E. K. *Nature* **1990,** *344,* 524–526. doi:10.1038/344524a0
10. Meyer, G.; Repp, J.; Zöphel, S.; Braun, K.-F.; Hla, S. W.; Fölsch, S.; Bartels, L.; Moresco, F.; Rieder, K. H. *Single Mol.* **2000,** *1,* 79–86. doi:10.1002/(SICI)1438-5171(200004)1:1<79::AID-SIMO79>3.0.CO;2-R
11. Moresco, F.; Meyer, G.; Rieder, K. H.; Tang, H.; Gourdon, A.; Joachim, C. *Appl. Phys. Lett.* **2001,** *78,* 306–308. doi:10.1063/1.1339251
12. Fuchs, H.; Schimmel, T. *Adv. Mater.* **1991,** *3,* 112–113. doi:10.1002/adma.19910030212
13. Schimmel, T.; Fuchs, H.; Akari, S.; Dransfeld, K. *Appl. Phys. Lett.* **1991,** *58,* 1039–1045. doi:10.1063/1.104416
14. Irmer, B.; Blick, R. H.; Simmel, F.; Gödel, W.; Lorenz, H.; Kotthaus, J. P. *Appl. Phys. Lett.* **1998,** *73,* 2051–2053. doi:10.1063/1.122364
15. Schumacher, H. W.; Keyser, U. F.; Zeitler, U.; Haug, R. J.; Eberl, K. *Appl. Phys. Lett.* **1999,** *75,* 1107–1112. doi:10.1063/1.124611
16. Popp, V.; Kladny, R.; Schimmel, T.; Küppers, J. *Surf. Sci.* **1998,** *401,* 105–111. doi:10.1016/S0039-6028(97)00917-5
17. Mullins, B. J.; Pfrang, A.; Braddock, R. D.; Schimmel, T.; Kasper, G. *J. Colloid Interface Sci.* **2007,** *312,* 333–340. doi:10.1016/j.jcis.2007.03.051
18. Lenhert, S.; Brinkmann, F.; Laue, T.; Walheim, S.; Vannahme, C.; Klinkhammer, S.; Xu, M.; Sekula, S.; Mappes, T.; Schimmel, T.; Fuchs, H. *Nat. Nanotechnol.* **2010,** *5,* 275–279. doi:10.1038/nnano.2010.17
19. Heß, C.; Borgwarth, K.; Ricken, C.; Ebling, D. G.; Heinze, J. *Electrochim. Acta* **1997,** *42,* 3065–3073. doi:10.1016/S0013-4686(97)00154-0
20. El-Giar, E. M.; Said, R. A.; Bridges, G. E.; Thomson, D. J. *J. Electrochem. Soc.* **2000,** *147,* 586–591. doi:10.1149/1.1393237
21. Li, W.; Hsiao, G. S.; Harris, D.; Nyffenegger, R. M.; Virtanen, J. A.; Penner, R. M. *J. Phys. Chem.* **1996,** *100,* 20103–20113. doi:10.1021/jp962328d
22. Kolb, D. M.; Ullmann, R.; Ziegler, J. C. *Electrochim. Acta* **1998,** *43,* 2751–2755. doi:10.1016/S0013-4686(98)00016-4
23. Ziegler, J. C.; Engelmann, G. E.; Kolb, D. M. *Z. Phys. Chem.* **1999,** *208,* 151–166. doi:10.1524/zpch.1999.208.Part_1_2.151
24. Pötzschke, R. T.; Staikov, G.; Lorenz, W. J.; Wiesbeck, W. *J. Electrochem. Soc.* **1999,** *146,* 141–149. doi:10.1149/1.1391577
25. Schindler, W.; Hofmann, D.; Kirschner, J. *J. Electrochem. Soc.* **2001,** *148,* C124–C130. doi:10.1149/1.1343107
26. LaGraff, J. R.; Gewirth, A. A. *J. Phys. Chem.* **1994,** *98,* 11246–11250. doi:10.1021/j100095a003
27. LaGraff, J. R.; Gewirth, A. A. *J. Phys. Chem.* **1995,** *99,* 10009–10018. doi:10.1021/j100024a050
28. Obermair, C.; Müller, M.; Klinke, C.; Schimmel, T. *Chin. Phys. (Beijing, China)* **2001,** *10,* S151–156.
29. Nakamura, M.; Endo, O.; Ohta, T.; Ito, M.; Yoda, Y. *Surf. Sci.* **2002,** *514,* 227–233. doi:10.1016/S0039-6028(02)01634-5
30. Toney, M. F.; Howard, J. N.; Richer, J.; Borges, G. L.; Gordon, J. G.; Melroy, O. R.; Yee, D.; Sorensen, L. B. *Phys. Rev. Lett.* **1995,** *75,* 4472–4475. doi:10.1103/PhysRevLett.75.4472

31. Lucas, C. A.; Markovic, N. M.; Ross, P. N. *Phys. Rev. B* **1997,** *56,* 3651–3654. doi:10.1103/PhysRevB.56.3651

32. Wilms, M.; Broekmann, P.; Stuhlmann, C.; Wandelt, K. *Surf. Sci.* **1998,** *416,* 121–140. doi:10.1016/S0039-6028(98)00550-0

33. Spaenig, A.; Broekmann, P.; Wandelt, K. *Z. Phys. Chem.* **2003,** *217,* 459–477. doi:10.1524/zpch.217.5.459.20454